Laser Chemistry

# Chemical and Physical Changes Induced in Optical Materials under High-Intensity Laser Irradiation

Guest Editors: Stavros Pissadakis, Saulius Juodkazis, and Jacques Albert

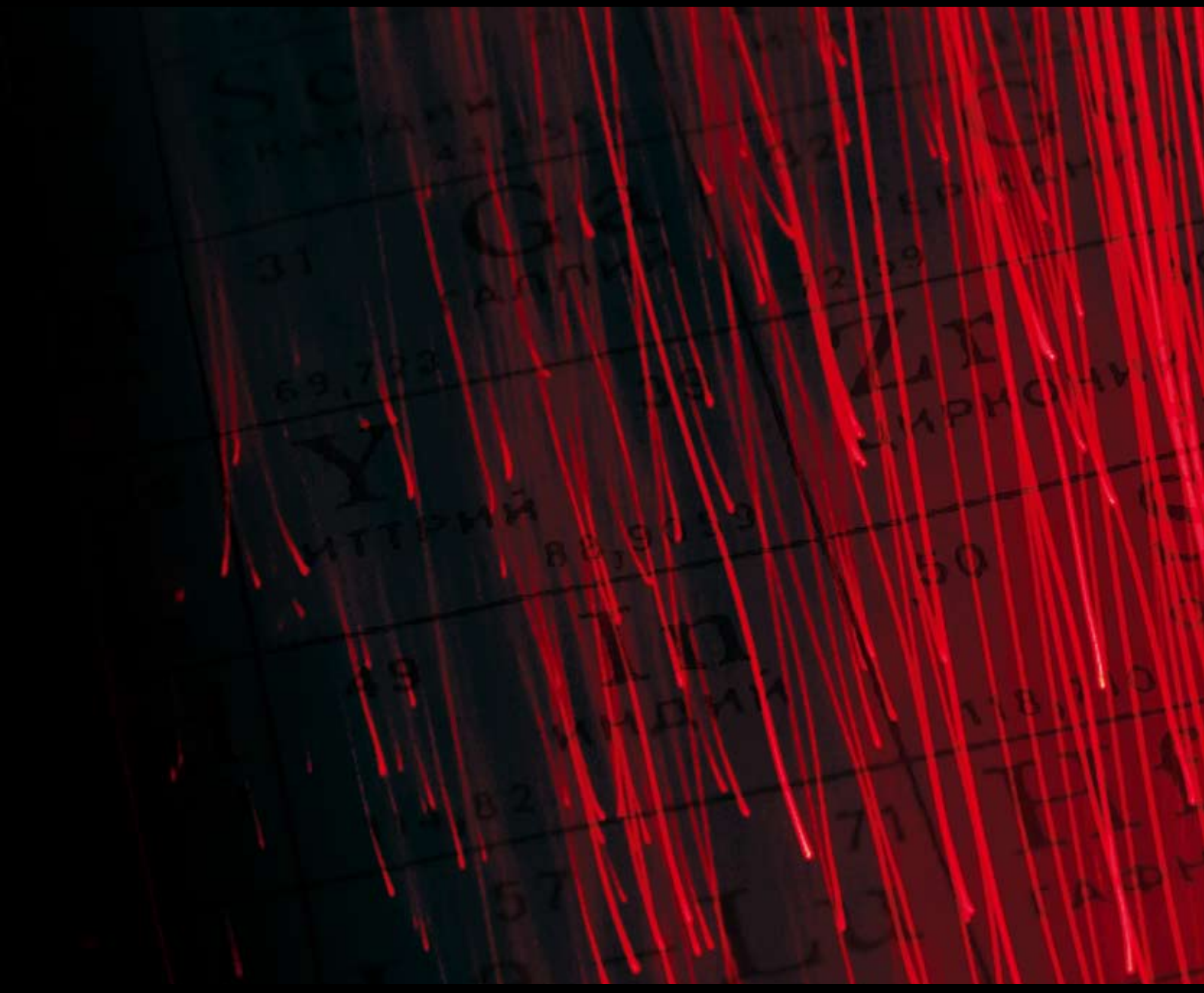

# Chemical and Physical Changes Induced in Optical Materials under High-Intensity Laser Irradiation

# Chemical and Physical Changes Induced in Optical Materials under High-Intensity Laser Irradiation

Guest Editors: Stavros Pissadakis, Saulius Juodkazis, and Jacques Albert

# Contents

**Chemical and Physical Changes Induced in Optical Materials under High-Intensity Laser Irradiation**, Stavros Pissadakis, Saulius Juodkazis, and Jacques Albert
Volume 2008, Article ID 839315, 2 pages

**Two-Photon Polymerization of Hybrid Sol-Gel Materials for Photonics Applications**, A. Ovsianikov, A. Gaidukeviciute, B. N. Chichkov, M. Oubaha, B. D. MacCraith, I. Sakellari, A. Giakoumaki, D. Gray, M. Vamvakaki, M. Farsari, and C. Fotakis
Volume 2008, Article ID 493059, 7 pages

**Gratings in Structured Optical Fibres**, John Canning, Nathaniel Groothoff, Kevin Cook, Cicero Martelli, Alexandre Pohl, John Holdsworth, Somnath Bandyopadhyay, and Michael Stevenson
Volume 2008, Article ID 239417, 19 pages

**Induced Bragg Gratings in Optical Fibers and Waveguides Using an Ultrafast Infrared Laser and a Phase Mask**, Stephen J. Mihailov, Dan Grobnic, Christopher W. Smelser, Ping Lu, Robert B. Walker, and Huimin Ding
Volume 2008, Article ID 416251, 20 pages

**Laser-Induced Backside Wet Etching of Transparent Materials with Organic and Metallic Absorbers**, K. Zimmer and R. Böhme
Volume 2008, Article ID 170632, 13 pages

**Ultrafast Four-Wave Optical Parametric Amplification in Transparent Condensed Bulk Media**, Audrius Dubietis, Gintaras Tamošauskas, Gintaras Valiulis, and Algis Piskarskas
Volume 2008, Article ID 534951, 9 pages

**Physical and Spectroscopic Properties of $Yb^{3+}$-Doped Fluorophosphate Laser Glasses**, Shujiang Liu and Anxian Lu
Volume 2008, Article ID 656490, 6 pages

**Processing of Dielectric Optical Coatings by Nanosecond and Femtosecond UV Laser Ablation**, J. Ihlemann, J. Békési, J.-H. Klein-Wiele, and P. Simon
Volume 2008, Article ID 623872, 6 pages

**Three-Dimensional Residue-Free Volume Removal inside Sapphire by High-Temperature Etching after Irradiation of Femtosecond Laser Pulses**, Shigeki Matsuo, Kensuke Tokumi, Takuro Tomita, and Shuichi Hashimoto
Volume 2008, Article ID 892721, 4 pages

**Photosensitivity of the Er/Yb-Codoped Schott IOG1 Phosphate Glass Using 248 nm, Femtosecond, and Picosecond Laser Radiation**, Stavros Pissadakis and Irini Michelakaki
Volume 2008, Article ID 868767, 7 pages

**Three-Dimensional Modeling of the Heat-Affected Zone in Laser Machining Applications**, Martynas Beresna, Titas Gertus, Rolandas Tomašiūnas, Hiroaki Misawa, and Saulius Juodkazis
Volume 2008, Article ID 976205, 6 pages

Hindawi Publishing Corporation
Laser Chemistry
Volume 2008, Article ID 839315, 2 pages
doi:10.1155/2008/839315

*Editorial*

# Chemical and Physical Changes Induced in Optical Materials under High-Intensity Laser Irradiation

**Stavros Pissadakis,[1] Saulius Juodkazis,[2] and Jacques Albert[3]**

[1] *Institute of Electronic Structure & Laser (IESL), Foundation for Research and Technology - Hellas (FORTH), P.O. Box 1385, 71 110 Heraklion Crete, Greece*
[2] *Research Institute for Electronic Science, Hokkaido University, North 21 - West 10, CRIS Building, Kita-ku, Sapporo 001-0021, Japan*
[3] *Department of Electronics, Carleton University, 1125 Colonel By Drive, Ottawa, ON, Canada K1S 5B6*

Correspondence should be addressed to Stavros Pissadakis, pissas@iesl.forth.gr and Jacques Albert, jacques_albert@carleton.ca

Received 30 October 2008; Accepted 4 November 2008



The laser-driven processes of surface structuring and photosensitivity in optical materials have been widely investigated during the last three decades. These accumulated efforts have promoted the understanding of the underlying physical processes involved and, also, prompted the optimal exploitation of the products of these processes in the photonics and micromanufacturing industry. The scientific research in these fields is mostly focused on the investigation of a fundamental problem "how the physical mechanisms and the products of high-intensity laser irradiation are correlated with specific exposure conditions." In such a basic approach, the high-intensity laser beam plays a twofold role, being simultaneously a precision tool for structuring or modifying the materials and an advanced probe for exploring and monitoring the physical processes occurring in the exposed optical material.

The above two broad scientific interest fields followed a rather parallel and similar evolution trend over the years, exhibiting a strong dependency on the available laser sources, especially their wavelengths and intensities. The $CO_2$ and YAG lasers era occurred in the 1970s and early 1980s, and was succeeded by excimer lasers period which lasted until the beginning of 1990s. This is when the terms "laser micromachining, ablation, and refractive index engineering" were established. However, after then, both fields were revolutionised with the emergence and commercialisation of the femtosecond laser sources, defining a new area that lasts up till today. These laser sources provided unprecedented field intensities of TW/$cm_2$ magnitude, at pulse durations below a few femtoseconds and at several emission wavelengths. The triggering of "cold," high-order multiphoton interactions opened new horizons in the science and technology of surface structuring and photosensitivity, settling several problems and doubts related to the physics yield and the exploitation potential of these optical material processing approaches. Femtosecond laser technology enabled processes such as the 3D structuring and refractive index engineering of high bandgap optical materials or the complex submicron photopolymerisation manufacturing, manufacturing methods which were considered as exotic only a few years ago.

We believe that launching this special issue is rather timely, since numerous and high impact findings have been presented over the last few years by several research groups. A priority objective of such special interest publication is to bring the communities of photosensitivity and laser processing closer together, thereby strengthening common codes of communication and establishing a parallel scientific vision. The contributions published herein cover a diverse number of research topics and applications in both fields, illustrating both experimental and fundamental aspects of those laser-matter interactions. Among the topics presented are filamentation effects, laser backside etching methods, Bragg grating recording in standard, microstructured optical fibres and thin films using ultrafast laser sources, etching of crystalline materials, photo-polymerisation and basic physics studies in photosensitivity and high intensity material modification.

Hopefully, this volume will constitute a useful reference guide for the researchers that work in fundamental investigations as well as engineers that utilise laser radiation for developing devices in the sectors of planar and fibre photonics, microoptics, and microfluidics.

*Stavros Pissadakis*
*Saulius Juodkazis*
*Jacques Albert*

Hindawi Publishing Corporation
Laser Chemistry
Volume 2008, Article ID 493059, 7 pages
doi:10.1155/2008/493059

*Research Article*

# Two-Photon Polymerization of Hybrid Sol-Gel Materials for Photonics Applications

**A. Ovsianikov,[1] A. Gaidukeviciute,[1] B. N. Chichkov,[1] M. Oubaha,[2] B. D. MacCraith,[2] I. Sakellari,[3,4] A. Giakoumaki,[3,5] D. Gray,[3] M. Vamvakaki,[3,5] M. Farsari,[3] and C. Fotakis[3,4]**

[1] *The Laser Zentrum Hannover e.V., 30419 Hannover, Germany*
[2] *The Optical Sensors Laboratory, National Centre for Sensor Research, Dublin City University, Dublin 9, Ireland*
[3] *Institute of Electronic Structure and Laser, Foundation for Research and Technology - Hellas, P.O. Box 1527, 711 10 Heraklion, Greece*
[4] *Department of Physics, University of Crete, 71003 Heraklion, Crete, Greece*
[5] *Department of Materials Science and Technology, University of Crete, 710 03 Heraklion, Crete, Greece*

Correspondence should be addressed to B. N. Chichkov, b.chichkov@lzh.de

Received 24 April 2008; Accepted 12 July 2008

Recommended by Saulius Juodkazis

Two-photon polymerization of photosensitive materials has emerged as a very promising technique for the fabrication of photonic crystals and devices. We present our investigations into the structuring by two-photon polymerization of a new class of photosensitive sol-gel composites exhibiting ultra-low shrinkage. We particularly focus on two composites, the first containing a zirconium alkoxide and the second a nonlinear optical chromophore. The three-dimensional photonic crystal structures fabricated using these materials demonstrate high resolution and clear bandstops in the near IR region.



## 1. Introduction

Nonlinear optical stereolithography is a laser technique which allows the direct-writing of high-resolution three-dimensional (3D) structures. The technique is based on the two-photon polymerization (2PP) of photosensitive materials; when the beam of a femtosecond infrared laser is tightly focused within the volume of such a material, the polymerization process can be initiated by nonlinear absorption within the focal volume. By moving the laser focus through the resin in the three dimensions, 3D structures can be fabricated. A variety of acrylate [1–7] and epoxy [8, 9] materials have been used to make components and devices such as photonic crystals templates [10], mechanical devices [11, 12], plasmonic structures [13, 14], biomolecule scaffolds [15, 16], and microscopic models [17, 18]. The highest resolution reported to date is 65 nm [19].

The first materials employed in 2PP were acrylic photopolymers and the negative photoresist SU8 [8, 9, 18]; more recently, photosensitive sol-gel hybrid materials [20] such as the commercially available ORMOCER [21, 22] have been used. These materials benefit from straight-forward preparation, modification, and processing and in combination with their high optical quality, postprocessing chemical and electrochemical inertness, and good mechanical and chemical stability, they are emerging as a very useful class of materials for multiphoton polymerization [23]. The process is based on the phase transformation of a sol obtained from metallic oxide or alkoxide precursors. This sol is first hydrolyzed and condensed at a low temperature to form a wet gel. It is subsequently polymerized through radical photopolymerization to give a product similar to glass.

In this paper, we report our investigations into the structuring by two photon polymerization of two composite sol-gel materials. The first material is a zirconium/silicon composite; we show that by changing the zirconium/silicon ratio, we can tune the refractive index of the material. The second material is a copolymer of a photosensitive silicon alkoxide with a nonlinear optical (NLO) alkoxysilane; this is used to make 3D photonic crystals containing an NLO chromophore. These materials share the characteristic of minimal shrinkage during photopolymerization.

## 2. Experimental

### 2.1. Materials Synthesis and Preparation

A photosensitive sol-gel process usually involves the catalytic hydrolysis of sol-gel precursors and the heat-activated polycondensation of the hydrolyzed products followed by the photopolymerization of the organic moieties to form a macromolecular network structure of hybrid sol-gel materials. The material is generally formed through a 4-step process.

(1) The first step is the hydrolysis and condensation in which precursors or monomers such as metal oxides or metal alkoxides are mixed with water and then undergo hydrolysis and condensation to form a porous interconnected cluster structure. Either an acid such as HCl or a base like $NH_3$ can be employed as a catalyst.

(2) The second step includes gelation, where the solvent is removed and a gel is formed by heating at low temperature. Hydrolysis and condensation do not stop with gelation; it is at this stage that solvents are removed and any significant volume loss occurs.

(3) Thirdly, the process moves to photopolymerization. Because of the presence of the double bonds and provided that a photoinitiator has been added to the gel, the photoinduced radicals will cause polymerization only in the area in which they are present. At this step, there is no material removal and no volume loss; the reaction that occurs is the cleavage of the pendant carbon-carbon double bonds by a free-radical process to form the organic polymer backbone.

(4) Finally comes the development step; the sol-gel is immersed in an appropriate solvent and the area of the sol-gel that is not photopolymerized is removed.

In this work, the sol-gel process has been used to prepare two different photosensitive composites, a zirconium containing hybrid and an NLO hybrid. The synthesis of these materials is described below.

### 2.2. Zirconium Composite Synthesis

The material was fabricated from methacryloxypropyltrimethoxysilane (MAPTMS, Polysciences Inc.) and methacrylic acid (MAA, Sigma-Aldrich), both of which possess photopolymerizable methacrylate moieties. Zirconium n-propoxide $Zr(OPr)_4$, (ZPO, 70% solution in 1-propanol, Sigma-Aldrich) was used as an inorganic network former. The molar ratio of MAPTMS to ZPO was varied from 10 : 0 to 5 : 5, in order to investigate the processability and the refractive index variation of the resulting copolymer.

MAPTMS was firstly hydrolyzed by adding HCl, (concentration 0.01 M) at a 1 : 0.75 ratio and the mixture was stirred for 30 minutes. ZPO was chelated by adding MAA (molar ratio ZPO:MAA, 1 : 1), an equal volume of 1-PrOH was then added, and the sol was stirred for 30 minutes. The MAPTMS sol was added drop-wise to the stirred ZPO sol. Following another 45 minutes, water was added to this mixture with a final 2.5 : 5 MAPTMS:$H_2O$ molar ratio. 4,4′-Bis(diethylamino)benzophenone (Sigma-Aldrich), 1% to the final product was used as a photoinitiator (PI). The photoinitiator Irgacure 369 was obtained from Ciba Speciality Chemicals. After stirring for 24 hours, the materials were filtered using 0.22 $\mu$m filters.

The samples were prepared by spin-coating or drop-casting onto glass substrates, and the resultant films were dried on a hotplate at 100°C for 1 hour before the photopolymerization. The heating process resulted in the condensation of the hydroxy-mineral moieties and the formation of the inorganic matrix. In a subsequent processing step, the material, which was not exposed to the laser radiation, was removed by developing in 1-propanol (Sigma-Aldrich).

The transmission spectra of thin films of this material were measured using a UV-Vis (Perkin-Elmer) spectrometer. Thin films were prepared by spin-coating and drying on a hotplate at 100°C for 1 hour. Figure 1 shows the difference in the absorption spectra induced by the addition of ZPO and photoinitiator. It can be seen that in the presence of photoinitiator even the addition of only 1% ZPO causes the absorption region to extend from 420 nm to 500 nm. A further increase in the amount of ZPO also causes an increase of the absorption around 470 nm; however, as also reported by Bhuian et al. [23], the extension of the absorption band disappears when no PI is added to the sol-gel composite; it also disappears when the composite is in solution. This behavior indicates an interaction between the ZPO and the PI which requires molecular proximity; a possible explanation is a charge transfer between the two composites.

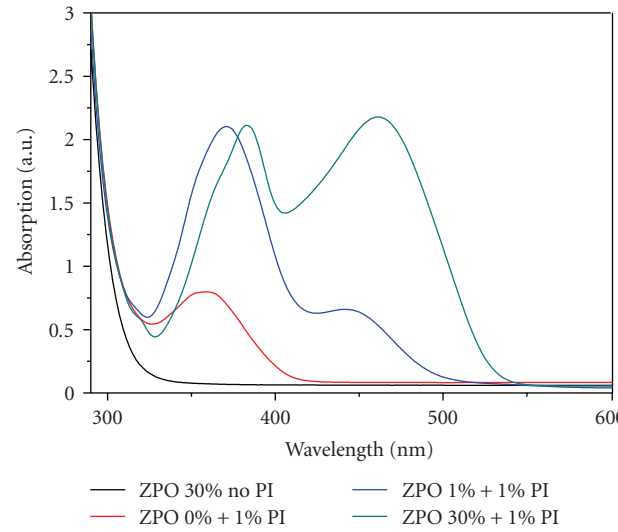


Figure 1: Transmission spectra for the material with varying ZPO and photoinitiator (PI) content. PI alone results in absorption around 360 nm. Addition of PI to ZPO containing material extends the absorption region from 420 nm to 500 nm.

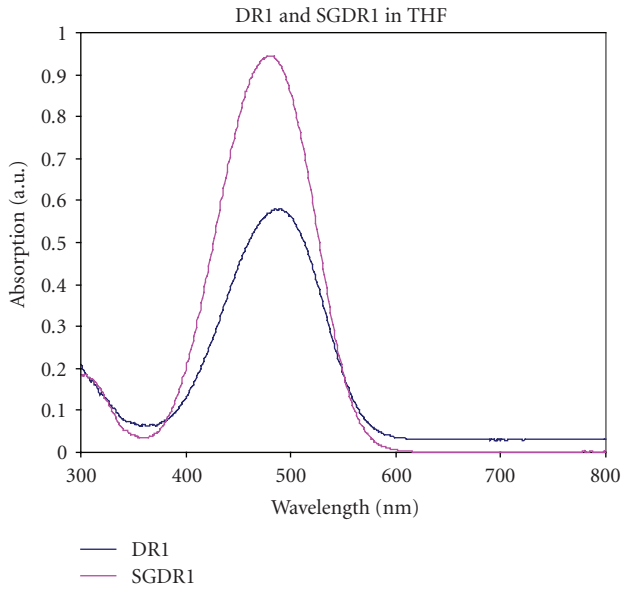


Figure 2: Absorption spectrum of DR1 and SGDR1 in THF.

## 2.3. NLO Hybrid Synthesis

The second material prepared consisted of the second-order NLO chromophore DR1 (Disperse Red 1, Sigma-Aldrich), which was firstly reacted with (3-isocyanatopropyl) triethoxysilane to form a functionalized silicon alkoxide precursor (SGDR1); SGDR1 was subsequently mixed with MAPTMS and the PI.

(3-isocyanatopropyl) trimethoxysilane and dibutyltin dilaurate (DBTDL) were purchased from Sigma-Aldrich and used without further purification. DR1 was recrystallized twice from ethanol before use. The synthesis of the NLO-active triethoxysilane was carried out according to [24]. (3-isocyanatopropyl) trimethoxysilane and DR1 at a 2 : 1 mole ratio were dissolved in anhydrous tetrahydrofuran (THF) under a nitrogen atmosphere. Next, 1 wt% DBTDL was added to the reaction flask and the solution was refluxed for 4 hours. The resultant solution was reduced to about half its initial volume under vacuum, followed by precipitation of the product as a red solid in hexane. The final product (SGDR1) was dried in a vacuum oven at 60°C for 24 hours and subsequently stored under vacuum until use. The product was characterized by $^1$H NMR spectroscopy which verified the successful synthesis of SGDR1.

To obtain the photosensitive gel, SGDR1 was first dissolved in toluene and stirred for 24 hours. Then MAPTMS was added to the SGDR1 solution (SGDR1 up to 40% w/w) and the mixture was hydrolyzed by the addition of HCl (pH = 1). After stirring for 1 hour, Irgacure 369 (up to 3.3 wt% to MAPTMS) was added and the mixture was stirred for a further 1 hour. To remove any aggregates, the solution was filtered through a 0.22 $\mu$m pore size Millipore syringe filter. After filtration, the solution remained clear without any sign of further particle aggregation for several weeks. Thermogravimetric analysis of the composite showed that it was stable up to 250°C, above which temperature it started to decompose.

The absorption spectra of both DR1 and SGDR1 are shown in Figure 2. Due to the presence of the DR1 azobenzene rings, the composite material absorbs very strongly in the spectral region 400–550 nm, but it is completely transparent at 600–800 nm and has a window of transparency in the spectral region 300–400 nm. These properties make SGDR1 ideal for two-photon polymerization using a Ti:Sapphire laser. The IR transparency allows focusing the laser within the volume of the material, while the relatively high UV transparency means that there will be two-photon absorption mostly by the PI, and not by the NLO chromophore.

Films were prepared by drop-casting the above mixture on 100 $\mu$m thick glass substrates, and the resultant films were baked at 100°C for 1 hour, to condense the silanol moieties and remove any residual solvent. After the completion of the photopolymerization process, the sample was developed for three minutes in THF and rinsed in isopropanol.

## 3. Experimental Techniques

### *Refractive Index Measurements*

The refractive index of the sol-gel films at 632.8 nm was determined from an m-line prism coupling experiment [25], using He-Ne laser. A thin film of the material was first made by spin-coating and subsequent curing under a UV lamp. A Schott Glass SF6 prism, as a higher refractive index medium, was used to couple light into the TE modes of the material waveguide; the sample was then mounted on a high-resolution rotation stage. The laser beam was directed toward the sample, and the transmitted light was detected with a photodiode. The coupling angles were then determined, and from the prism angle and refractive index the mode could then be determined. From the crossing point of the modes supported by the thin film, both the thickness and the refractive index of the film could be then calculated, using the mode equation [16, 26].

## 4. 3D Microfabrication by Two-Photon Polymerization

The experimental setup for the fabrication of three-dimensional microstructures by two-photon polymerization is shown in Figure 3. In the present work, two different Ti:Sapphire femtosecond lasers were used; for the processing of the MAPTMS:SGDR1 composite, the laser characteristics were 60 fs, 90 MHz, <450 mW, 780 nm, while for the MAPTMS:ZPO composite, it was 140 fs, 80 MHz, 780 nm. A 100X microscope objective lens (Zeiss, Plan Apochromat, N.A. = 1.4) was used to focus the laser beam into the volume of the photosensitive material. The photopolymerized structure was generated in a layer-by-layer format, by using an $x$-$y$ galvanometric mirror scanner. Movement on the $z$-axis was achieved using a high resolution linear stage.

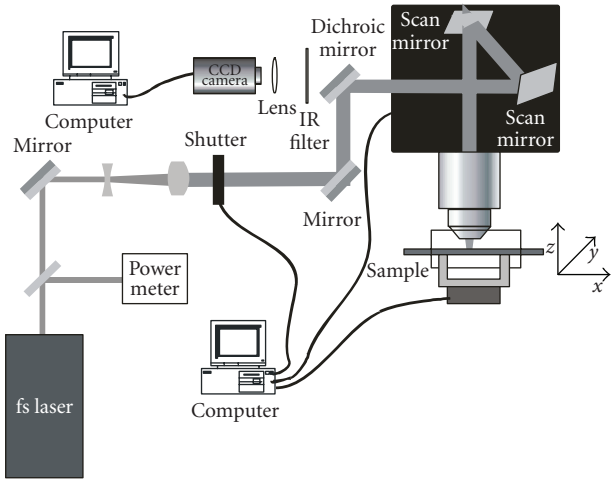


Figure 3: Experimental setup for two-photon polymerization.

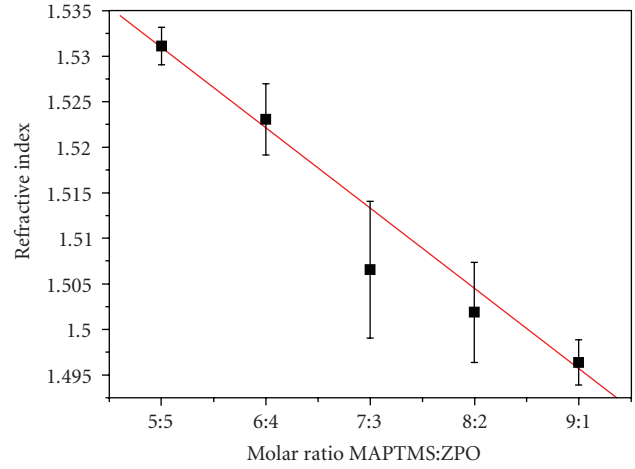


Figure 4: Refractive index variation of the MAPTMS:ZPO complex.

For the online monitoring of the photopolymerization process, a CCD camera was mounted behind a dichroic mirror. As the refractive index of the photopolymer changes during polymerization, the illuminated structure becomes visible during the building process.

## 5. Results

### *Refractive Index Measurements*

In the case of the MAPTMS:SGDR1 composite, the refractive index of the material was measured for 10% w/w SGDR1 content and was found to be $n = 1.497 \pm 0.006$.

In the case of the zirconium-containing sol-gel, by varying the molar ratio of MAPTMS and ZPO, the refractive index of the composite could be modified (Figure 4). It can be seen that as the ZPO content increases, so does the material's refractive index. The fact that this increase is linear greatly simplifies the material design criteria, as typically such increases are saturating so that the doping concentration becomes very critical. However, in this concentration range, no such limitation is apparent.

## 6. Two-Photon Fabrication of Photonic Crystals

For the fabrication of the photonic crystals, the woodpile geometry was chosen. It consists of layers of one-dimensional rods with a stacking sequence that repeats itself every four layers. The distance between four adjacent layers is "$a$" and within each layer, the axes of the rods are parallel to each other with a distance "$d$" between them. The adjacent layers are rotated by 90°. Between every other layer, the rods are shifted relative to each other by "$d/2$." For the case of "$a/d$" $= \sqrt{2}$, the lattice can be derived from a face-centred-cubic (fcc) unit cell with a basis of two rods. A constant "$a/d$" ratio of 1.34 was applied for all the woodpile structures presented here.

### *SGDR1 Photonic Crystals*

Photonic crystals are considered to be an optical equivalent of semiconductors, since they modify the properties of light in the same way as semiconductors do for electrons. However, in contrast to electrons, photon energy cannot be easily tuned. Therefore, fabrication of photonic crystals made of nonlinear materials, whose optical response depends on propagating light intensity, is important.

Figure 5(a) shows a microscope image of an array of photonic crystals; they have the bright red color of Disperse Red 1. Figure 5(b) shows a scanning electron microscope (SEM) image of a DR1-containing photonic crystal fabricated by the 2PP method using a laser fluence of 44 mJ/cm$^2$ and a beam scanning speed of 20 $\mu$m/s. As it can be seen, SGDR1 can be structured very accurately and without defects. The smallest lateral feature size that was experimentally obtained with this material is 250 nm. The refractive index of the material was found to be $n = 1.497 \pm 0.006$ (10% w/w SGDR1 content).

### *ZPO Photonic Crystals*

Figure 6 shows one of the fabricated woodpile photonic crystal structures exhibiting a bandstop in the near-IR region; in this case, the employed material had an 8 : 2 MAPTMS:ZPO molar ratio. As the material exhibits negligible distortion due to photopolymerization, no additional efforts such as precompensation or mechanical stabilization to avoid structural distortions are necessary.

FTIR measurements (Equinox, Bruker Optics) of the reflection and the transmission spectra of woodpile structures with rod distances between 1.2 $\mu$m and 1.8 $\mu$m indicate clear bandstops with the central frequency shifting to shorter wavelengths as the rod distance is reduced (see Figure 7). In addition, the spectra show the appearance of higher order bandstops in all samples, indicating the high quality of the fabricated structures. The observed bandstop positions are blue shifted when compared to the values estimated from

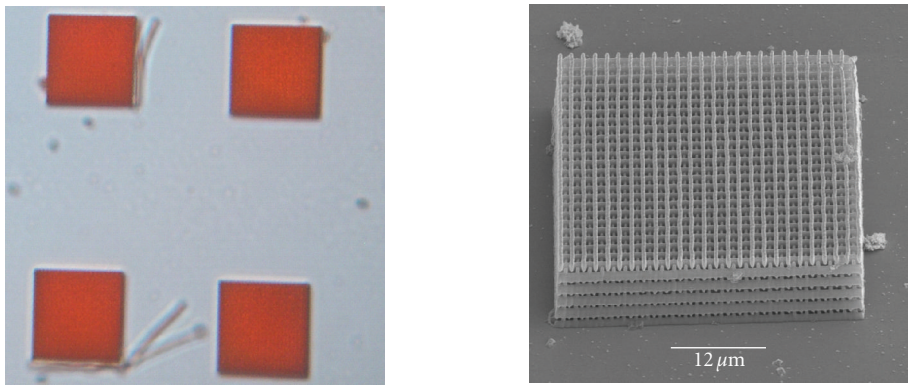


(a) (b)

Figure 5: Optical microscope (a) and SEM (b) images of photonic crystals by MAPTMS:SGDR1.

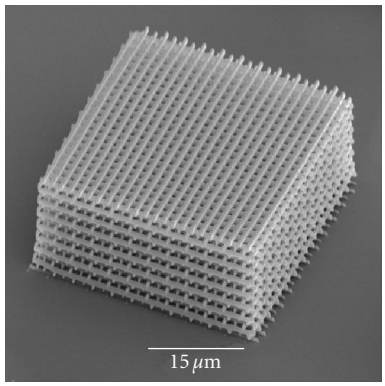


Figure 6: SEM image of Zr-containing photonic crystal structure (applied material MAPTMS:ZPO ratio is 8 : 2).

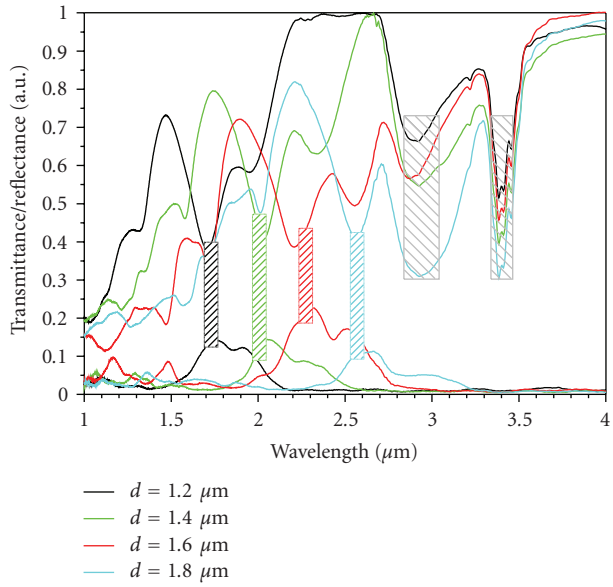


Figure 7: FTIR spectra of zirconium-containing photonic crystal structures with rod spacings 1.2 $\mu$m–1.8 $\mu$m (applied material MAPTMS:ZPO ratio is 8 : 2).

Bragg's condition or obtained from theoretical simulations. There are two additional bands at 3 $\mu$m and 3.4 $\mu$m whose origin is the absorption of the material, as confirmed by measurements of transmission through flat, unstructured layers. Also in this case, material with 8 : 2 MAPTMS:ZPO molar ratio was used. The material has no natural absorption in the spectral region 550–2700 nm, which makes it suitable for structuring by 2PP using a 780 nm laser and for making photonic crystal structures at telecommunication wavelengths.

The observed splitting of the absorption and transmission peaks as well as blue shift of the bandstops central position can be explained by taking a closer look at the experimental setup used for the FTIR transmission measurements. In order to focus the beam on the size of the fabricated photonic crystal, a Cassegrain reflective optical assembly is used. In contrast to the ideal case, when the measuring beam is perpendicular to the surface of the structure, this assembly provides illumination of the structure with a hollow light cone having an acceptance angle between 15° and 30°. Previous studies on 3D photonic crystal systems have shown that scattering of the measuring beam entering the photonic crystal at a large angle leads to the reflection peak splitting and a blue shift of its central position [27–29] Theoretical simulations have also confirmed these observations [30].

An approach taken by many groups is the templating of photonic crystals by inversion, infiltrating them with another, higher refractive index material [8, 18]. The materials described here also can be used for template fabrication. Like most hybrids, their organic components decompose at relatively low temperatures (approx. 220°C). The inorganic components, however, which are dominant after condensation in the materials described here, are very resistant to high temperatures. It should be possible to remove them by HF acid, in order to obtain the inverse structures, as has been demonstrated in similar material systems [31].

## 7. Conclusions

We have presented our investigations into two sol-gel hybrid photosensitive materials which can be structured accurately by two-photon polymerization. The first is a zirconium containing sol-gel; by varying its zirconium content, we have shown it is possible to "tune" its refractive index. The second material contains the nonlinear optical chromophore Disperse Red 1; it is a first step towards the fabrication of nonlinear three-dimensional photonic crystal devices using the two-photon polymerization technique.

As neither materials shrinks during photopolymerization, it was possible to fabricate photonic crystals with bandstops in the near IR region without any precompensation for structure distortions induced by the material shrinkage, or any support structures for their mechanical stabilization.

## Acknowledgments

This work was supported by the Marie Curie Transfer of Knowledge project "NOLIMBA" (MTKD-CT-2005-029194) and by the UV Laser Facility operating at IESL-FORTH under the European Commission "Improving Human Research Potential" program (RII3-CT-2003-506350). The authors would like to thank group of Professor Martin Wegener for valuable assistance in optical characterisation of photonic crystals. Travel between Crete, Greece and Hannover, Germany, was supported by an IKYDA/DAAD travel grant.

## References

[1] S. Maruo, O. Nakamura, and S. Kawata, "Three-dimensional microfabrication with two-photon-absorbed photopolymerization," *Optics Letters*, vol. 22, no. 2, pp. 132–134, 1997.

[2] S. Kawata, H.-B. Sun, T. Tanaka, and K. Takada, "Finer features for functional microdevices," *Nature*, vol. 412, no. 6848, pp. 697–698, 2001.

[3] X.-M. Duan, H.-B. Sun, K. Kaneko, and S. Kawata, "Two-photon polymerization of metal ions doped acrylate monomers and oligomers for three-dimensional structure fabrication," *Thin Solid Films*, vol. 453-454, pp. 518–521, 2004.

[4] D. McPhail, M. Straub, and M. Gu, "Optical tuning of three-dimensional photonic crystals fabricated by femtosecond direct writing," *Applied Physics Letters*, vol. 87, no. 9, Article ID 091117, 3 pages, 2005.

[5] L. H. Nguyen, M. Straub, and M. Gu, "Acrylate-based photopolymer for two-photon microfabrication and photonic applications," *Advanced Functional Materials*, vol. 15, no. 2, pp. 209–216, 2005.

[6] M. Straub and M. Gu, "Near-infrared photonic crystals with higher-order bandgaps generated by two-photon photopolymerization," *Optics Letters*, vol. 27, no. 20, pp. 1824–1826, 2002.

[7] S. H. Wu, M. Straub, and M. Gu, "Single-monomer acrylate-based resin for three-dimensional photonic crystal fabrication," *Polymer*, vol. 46, no. 23, pp. 10246–10255, 2005.

[8] M. Deubel, G. von Freymann, M. Wegener, S. Pereira, K. Busch, and C. M. Soukoulis, "Direct laser writing of three-dimensional photonic-crystal templates for telecommunications," *Nature Materials*, vol. 3, no. 7, pp. 444–447, 2004.

[9] T. Kondo, S. Matsuo, S. Juodkazis, V. Mizeikis, and H. Misawa, "Multiphoton fabrication of periodic structures by multibeam interference of femtosecond pulses," *Applied Physics Letters*, vol. 82, no. 17, pp. 2758–2760, 2003.

[10] H.-B. Sun, S. Matsuo, and H. Misawa, "Three-dimensional photonic crystal structures achieved with two-photon-absorption photopolymerization of resin," *Applied Physics Letters*, vol. 74, no. 6, pp. 786–788, 1999.

[11] P. Galajda and P. Ormos, "Complex micromachines produced and driven by light," *Applied Physics Letters*, vol. 78, no. 2, pp. 249–251, 2001.

[12] H.-B. Sun, K. Takada, and S. Kawata, "Elastic force analysis of functional polymer submicron oscillators," *Applied Physics Letters*, vol. 79, no. 19, pp. 3173–3175, 2001.

[13] R. Kiyan, C. Reinhardt, S. Passinger, et al., "Rapid prototyping of optical components for surface plasmon polaritons," *Optics Express*, vol. 15, no. 7, pp. 4205–4215, 2007.

[14] C. Reinhardt, S. Passinger, B. N. Chichkov, C. Marquart, I. P. Radko, and S. I. Bozhevolnyi, "Laser-fabricated dielectric optical components for surface plasmon polaritons," *Optics Letters*, vol. 31, no. 9, pp. 1307–1309, 2006.

[15] R. J. Narayan, C. Jin, A. Doraiswamy, et al., "Laser processing of advanced bioceramics," *Advanced Engineering Materials*, vol. 7, no. 12, pp. 1083–1098, 2005.

[16] R. J. Narayan, C. Jin, T. Patz, et al., "Laser processing of advanced biomaterials," *Advanced Materials & Processes*, vol. 163, no. 4, pp. 39–42, 2005.

[17] M. Straub, L. H. Nguyen, A. Fazlic, and M. Gu, "Complex-shaped three-dimensional microstructures and photonic crystals generated in a polysiloxane polymer by two-photon microstereolithography," *Optical Materials*, vol. 27, no. 3, pp. 359–364, 2004.

[18] J. Serbin, A. Ovsianikov, and B. N. Chichkov, "Fabrication of woodpile structures by two-photon polymerization and investigation of their optical properties," *Optics Express*, vol. 12, no. 21, pp. 5221–5228, 2004.

[19] W. Haske, V. W. Chen, J. M. Hales, et al., "65 nm feature sizes using visible wavelength 3-D multiphoton lithography," *Optics Express*, vol. 15, no. 6, pp. 3426–3436, 2007.

[20] A.-L. Pénard, T. Gacoin, and J.-P. Boilot, "Functionalized sol-gel coatings for optical applications," *Accounts of Chemical Research*, vol. 40, no. 9, pp. 895–902, 2007.

[21] R. Houbertz, L. Fröhlich, M. Popall, et al., "Inorganic-organic hybrid polymers for information technology: from planar technology to 3D nanostructures," *Advanced Engineering Materials*, vol. 5, no. 8, pp. 551–555, 2003.

[22] J. Serbin, A. Egbert, A. Ostendorf, et al., "Femtosecond laser-induced two-photon polymerization of inorganic organic hybrid materials for applications in photonics," *Optics Letters*, vol. 28, no. 5, pp. 301–303, 2003.

[23] B. Bhuian, R. J. Winfield, S. O'Brien, and G. M. Crean, "Investigation of the two-photon polymerisation of a Zr-based inorganic-organic hybrid material system," *Applied Surface Science*, vol. 252, no. 13, pp. 4845–4849, 2006.

[24] D. H. Choi, J. H. Park, T. H. Rhee, N. Kim, and S.-D. Lee, "Improved temporal stability of the second-order nonlinear optical effect in a sol-gel matrix bearing an active chromophore," *Chemistry of Materials*, vol. 10, no. 3, pp. 705–709, 1998.

[25] S. Monneret, P. Huguet-Chantôme, and F. Flory, "m-lines technique: prism coupling measurement and discussion of accuracy for homogeneous waveguides," *Journal of Optics A*, vol. 2, no. 3, pp. 188–195, 2000.

[26] P. K. Tien, G. Smolinsky, and R. J. Martin, "Thin organosilicon films for integrated optics," *Applied Optics*, vol. 11, no. 3, pp. 637–642, 1972.

[27] S. G. Romanov, T. Maka, C. M. S. Torres, et al., "Diffraction of light from thin-film polymethylmethacrylate opaline photonic crystals," *Physical Review E*, vol. 63, no. 5, Article ID 056603, 5 pages, 2001.

[28] S. G. Romanov, M. Bardosova, D. E. Whitehead, I. M. Povey, M. Pemble, and C. M. S. Torres, "Erasing diffraction orders: opal versus Langmuir-Blodgett colloidal crystals," *Applied Physics Letters*, vol. 90, no. 13, Article ID 133101, 3 pages, 2007.

[29] M. Deubel, M. Wegener, S. Linden, and G. von Freymann, "Angle-resolved transmission spectroscopy of three-dimensional photonic crystals fabricated by direct laser writing," *Applied Physics Letters*, vol. 87, no. 22, Article ID 221104, 3 pages, 2005.

[30] A. V. Lavrinenko and S. G. Romanov, "The finite-difference time-domain modeling of bi-directional transmission spectra in thin 3-dimensional opal-based photonic crystals," in *Proceedings of the International Symposium on Photonic and Electromagnetic Crystal Structures (PECS '07)*, Monterey, Calif, USA, April 2007.

[31] Y. Jun, P. Nagpal, and D. J. Norris, "Thermally stable organic-inorganic hybrid photoresists for fabrication of photonic band gap structures with direct laser writing," *Advanced Materials*, vol. 20, no. 3, pp. 606–610, 2008.

Hindawi Publishing Corporation
Laser Chemistry
Volume 2008, Article ID 239417, 19 pages
doi:10.1155/2008/239417

*Review Article*

# Gratings in Structured Optical Fibres

**John Canning,[1] Nathaniel Groothoff,[1] Kevin Cook,[1] Cicero Martelli,[1,2] Alexandre Pohl,[1,3] John Holdsworth,[1,4] Somnath Bandyopadhyay,[1,5] and Michael Stevenson[1]**

[1] *Interdisciplinary Photonics Laboratories, School of Chemistry, University of Sydney, Sydney, NSW 2006, Australia*
[2] *Mechanical Engineering Department, Pontifical Catholic University of Rio de Janeiro-PUC-Rio, Rio de Janeiro 22453-900, Brazil*
[3] *Federal University of Technology-Paraná, Curitiba 80230-901, Brazil*
[4] *School of Mathematical and Physical Sciences, Faculty of Science and Information Technology, Newcastle University, Newcastle, NSW 2308, Australia*
[5] *Central Glass and Ceramic Research Institute, Kolkata-700032, India*

Correspondence should be addressed to John Canning, j.canning@usyd.edu.au

Received 10 June 2008; Accepted 18 August 2008

Recommended by Stavros Pissadakis

Grating writing in structured optical fibres and their properties and applications are reviewed. To date, most gratings have been written in a straightforward manner into structured fibres containing a photosensitive germanosilicate step-index core. However, gratings have also been written directly into single material, structured silica fibres and into air-clad cores using two and higher-photon processes with both UV and near IR pulsed (nanosecond-femtosecond) light. Given the intrinsic-added functionality possible within a structured optical fibre, structured fibre gratings offer further capabilities for sensors, diagnostics, lasers, and devices.



## 1. Introduction

Structured optical fibres such as suspended core fibres [1], photonic crystal fibres [2], and Fresnel fibres [3] introduce a new degree of functionality hitherto not possible. For example, the composite properties of a structured optical fibre can be tailored by adding materials into the holes. This opens up a range of new possibilities, from zero temperature-dependent fibres and components, including gratings [4], to advanced functionality possible by superposing multiple properties; an example is an optical fibre white light source made by superposing the properties of individual dye molecules that are spatially separated to avoid quenching [5]. Access to the evanescent field over long lengths had enabled direct evanescent field spectroscopy of silica interfaces, revealing new bands not possible without resonant techniques [6].

Adding spectral selectivity to extend with similar ease the possible applications using laser written components such as fibre Bragg gratings demands a new level of engineering in grating writing since structured fibres introduce several challenges to grating writing not present in conventional fibres. These include high levels of scattered light arising from multiple interface reflections and, more critically, rotationally variant symmetry. Nevertheless, straightforward conventional single-photon Bragg grating writing has been demonstrated with 244 nm, 266 nm (nanosecond and femtosecond pulsed), 193 nm and in various structured fibres that contain conventional step index germanosilicate cores [7–12]. Unfortunately, for many applications, the advantages of having a surrounding structured cladding are lost when conventional step cores are inserted. Further in many applications, such as $Er^{3+}/Yb^{3+}$-codoped lasers, germanium present in the core is undesirable. Hydrogen loading is one approach for writing gratings using 193 nm in nongermanosilicate structured optical fibres [9]. Alternatively, two-photon absorption directly into the core has also been used to write gratings in pure silica core conventional step index fibres with a fluorinated cladding [13] and in all-silica, single material-structured fibres including photonic crystal fibre [14] and Fresnel fibres [15]. The generic nature of two-photon excitation

allowed gratings to be written into structured fibres for laser applications both as distributed Bragg reflector (DBR) elements and as phase-shifted distributed feedback (DFB) cavities [16–18]. The fibre in these cases was an $Er^{3+}$-doped aluminosilicate core photonic crystal fibre. Using two-photon absorption into the band edge avoids the need for hydrogen loading. The specific need of fibre lasers has also seen the inscription of both single-photon [19] and multiple-photon Bragg gratings [20] within Yb-doped core air-clad nanostructured optical fibres specifically fabricated for high-power fibre lasers. This work has been complemented in photonic crystal fibres by higher-exponent processes made possible using femtosecond lasers [21]. An updated review on photosensitivity in general is given in [22].

Although grating writing has been demonstrated in a range of structured optical fibres, the rotational variance of these fibres, however, leads to variations in the writing intensity across the core from the side during subsequent grating writing, posing serious challenges to reproducibility and predictability. Unlike conventional fibre grating writing, these must be considered if the process is to be brought under control. This surrounding structure leads to scattering, diffractive in the case of regular or quasicrystalline structures, which actually carries information regarding the structure of that fibre—indeed, such a property has been proposed as a simple photonic encryption key [23]. For grating writing, an obvious solution is to fill the holes with index matching fluids which can be subsequently removed [8]. However, for shorter wavelengths such as 193 nm solutions with appropriate transmission are not readily available. Higher-photon effects, both in the UV and in the near IR, are also unable to access the core without significant absorption and heating within the liquid itself, which can damage the fibre. If the structure is sufficiently removed from the step-index core, this problem can be overcome [20]. Here, we review the progress to date on grating writing within structured optical fibres and discuss some of the challenges and directions to further extending the capability of structured fibres using gratings. We also elaborate some of the unique properties and applications of structured optical fibres using Bragg gratings.

## 2. Scattering from the Structured Cladding

Typical structured optical fibres into which gratings have been successfully inscribed are illustrated in Figure 1. Each serves a purpose, ranging from gas and liquid sensing, biodiagnostics, novel components, and fibre lasers, which can be enhanced with gratings, as outlined in the figure caption. Structured optical fibres include two main types: (1) step-index analoges, where the cladding made up of air holes has an average index lower than that of the core, and (2) diffractive fibres, or Fresnel fibres, which includes Bragg fibres, omniwaveguides, and other photonic bandgap fibres exploiting crystal and quasicrystal symmetry [2, 3, 24]. In practice, structured step-index fibres also have significant diffractive effects particularly as the wavelength becomes shorter [25]. Within these categories, there are even finer details. When light strikes the structured cladding layers, both the light which is able to reach the core and the light which reaches beyond the other side of the fibre are dependent on the regularity of the lattice, hole size, hole number, lattice period, and interstitial hole spacing [26–31]. For example, a normal triangular lattice photonic crystal fibre will have repeating angular structure every 30–60°. Such crystal lattices can also act as lenses which may offset scattered light by focussing the light that gets through into the core, or which at another rotation angle leads to complete defocusing of light out of the core, depending on the parameters of the cladding structure [28].

There are two approaches to studying the scattered light: (1) examine the signature of the scattered light through and beyond the structured lattice in the far field; or (2) study the light reaching the core of the structured optical fibre. Each case is considered briefly.

### 2.1. Measuring Scattered Light through the Structured Fibre

Far-field measurements of scattered light can provide information about the structured cladding, particularly periodicity [23]. Figure 2 shows the experimental setup that was employed to investigate scattered light from the side. A five wavelength tunable HeNe laser is used as a flexible optical source. The beam is directed perpendicularly to the fibre sample and the scattered light is project on a CCD camera (CCD-1) at a distance $d$ from the fibre sample. The beam spot size is at least three times bigger than the fibre external diameter and the intensity is adjusted using a neutral density filter to be the same for all wavelengths in all measurements ($P = 0.7\,\mu$W). The fibre sample holder is placed on a rotation stage that controls the fibre angular orientation. An $xy$ stage set is used to position the fibre at the center of the rotation stage. The structured fibre angular position is determined by imaging its end face with an objective lens and projecting the image on a CCD camera (CCD-2) connected to a TV monitor. An example of the interference pattern generated by sending HeNe light at 543 nm through the side of a four-ring-structured optical fibre recorded by CCD-1 is, along with an SEM cross-section of the fibre, also shown. The scattered pattern is easily correlated to the regular lattice structured determined by the four rings.

The number of fringes displayed within a defined angle range is directly proportional to the fibre diameter and can be written as [23]

$$N = \frac{2b}{\lambda}\left\{\begin{array}{l}\left[\sin\dfrac{\theta_2}{2} + \left(m_1^2 + 1 - 2m_1\cos\dfrac{\theta_2}{2}\right)^{1/2}\right] \\ -\left[\sin\dfrac{\theta_1}{2} + \left(m_1^2 + 1 - 2m_1\cos\dfrac{\theta_1}{2}\right)^{1/2}\right]\end{array}\right\}, \tag{1}$$

where $b$ is the fibre radius, $m_1$ is the fibre cladding refractive index, $\theta_1$ = incident angle to the ΓK direction, and $\theta_2$ = scattered angle. Hence the number of fringes within the angle range is also a function of the laser wavelength. The

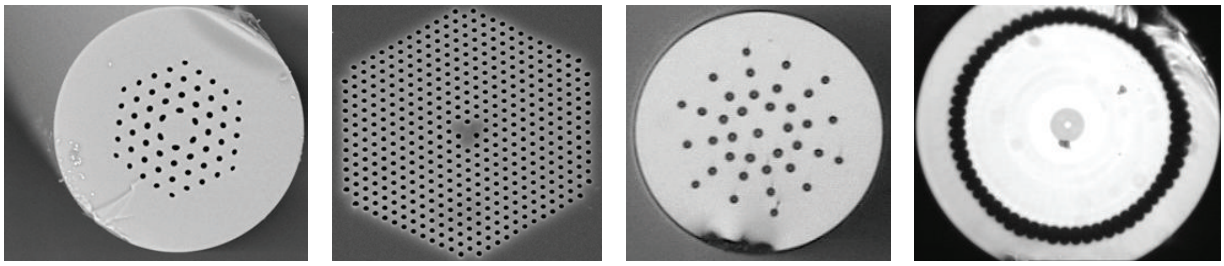

(a) (b) (c) (d)

Figure 1: Typical structured optical fibres into which gratings have been written: (a) low-loss (<4 dB/km) 4-ring all-silica photonic crystal optical fibre; (b) 12-ring photonic crystal fibre with triangular core and photosensitive, high-NA step-index germanosilicate center; (c) simple Fresnel fibre; and (d) air-clad fibre with $Yb^{3+}$-doped core.

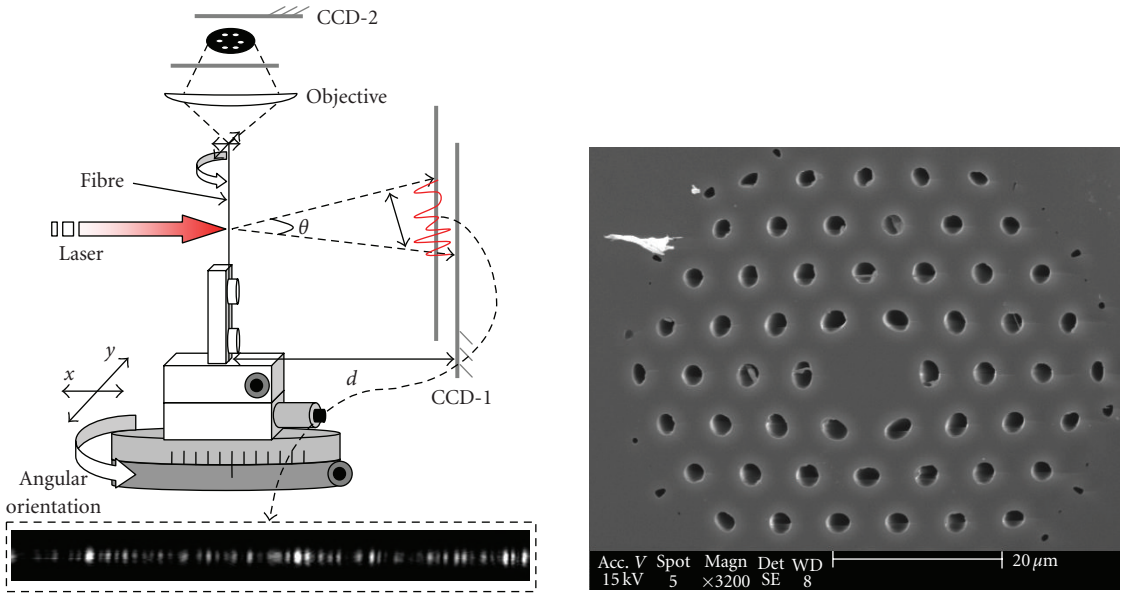


(a) (b)

Figure 2: (a) Experimental setup used to produce the interference patterns and example of the recorded pattern obtained from a 4-ring photonic crystal fibre; (b) SEM cross-section of 4-ring, single material (silica) photonic crystal fibre ($\Phi_{\text{ext diameter}} \sim 100\,\mu$m, $\phi_{\text{hole}} \sim 4.5\,\mu$m, and $\Lambda \sim 8.5\,\mu$m). More details in [23].

system is calibrated analyzing the fringe pattern of *fibre1* (a standard step-idnex fibre which is single mode at 632 nm) four different wavelengths (543, 594, 604, and 633 nm). Since the fibre diameter was known, the number of fringes was used as an evaluation parameter. The calculated and measured number of fringes is the same and the results presented in Table 1.

The patterns at each wavelength generated with the 4-ring-structured fibre similar to that in Figure 1(a) are presented in Figures 3(a)–3(c). The FFT plot of one interference pattern at 543 nm (Figure 3(b)) shows a broad frequency distribution, consistent with no obvious periodic pattern. The intensity plot at 543 nm shows a random distribution of peaks (Figure 3(c)). The calculated frequency using the previous equation is consistent with the peak of the broad FFT spectrum and we interpret this to mean that most of the rays reflect at the cladding air interface. The intensity plot

Table 1: Measured and calculated number of fringes for four wavelengths [23].

| Wavelength (nm) | No. of Figures (measured) | No. of Figures (calculated) |
|---|---|---|
| 543 | 86 | 86 |
| 594 | 79 | 79 |
| 604 | 77 | 77 |
| 633 | 74 | 74 |

of the scattering pattern has basically two components: (1) fringe component with higher frequency which is dependent on the refracted and reflected rays that do not cross the fibre core; and (2) a lower frequency component that modulates the fringes caused by interference between the refracted ray that traverses the core and the one that goes through the

cladding only. This component can potentially be used to evaluate the fibre core parameters (e.g., refractive index and diameter). In general, the unique signature produced by such scattering is what makes the use of structured fibres as optical encoding keys promising [23]. Unfortunately, this complexity makes monitoring of the scattered signature from the side to monitor alignment and rotation for other applications unnecessarily challenging and complicated since phase information becomes critical. It is possible by taking this information and feeding it to a wavefront encoder (e.g., an array of liquid crystals or micromechanical (MEMs) mirrors) to manipulate the phase front of the incident light, the intensity at the center of the core can be actively maximized. Such a feedback system has allowed a random Ag based paint deposited onto a glass slide to focus light [32]. A simpler approach may be to perform alignment and rotation by monitoring a process within the core of the optical fibre.

## 2.2. Measuring the Light Reaching the Core of the Structured Optical Fibre

The object when inscribing gratings is to illuminate the core of the fiber with sufficient power density to induce the required refractive index change within the core glass in spite of this scatter. A preliminary analysis of the likely impact of scattering can be obtained through computer simulation. To date, an idealized 4-ring structure such as shown in Figure 1(a) has been simulated using ray trace software [26] and with finite difference time domain (FDTD) software [28]. A previous model [27] which examined grating inscription with multiple IR photons required a very tight 4 $\mu$m focus of the light cone directly into the fibre core to generate the power density necessary to induce refractive index change in the core glass. Unfortunately, this is not representative of existing writing conditions employed in phase mask writing, where a plane wave illumination of the core from, for example, a frequency doubled $Ar^+$ (CW 244 nm) laser or from an exciplex laser such as ArF (193 nm).

Figure 4 shows the FDTD simulation of 193 nm TE-polarized light striking a fibre identical to that of Figure 1(a) from the side at two particular orientations [28]. The orientation at 0° has more uniform distribution of UV light within the core region; however, a close inspection of the peak intensities reveals that whilst much less uniform, the orientation at 30° has a very high-peak intensity at the back of the core, suggesting that there is additional lensing effects arising from the lattice itself, despite a greater amount of light scattered at this orientation. This is consistent with constructive and destructive interference of coherent light scattered by the lattice (our laser coherence is >600 $\mu$m), as alluded to in previous sections. A conjecture would be that for high-exponent processes the 30° orientation is preferred. On the other hand, for single-photon processes, such as those involved when a germanosilicate core is present, 0° is preferred.

More recently, FDTD simulation was extended to a more complex 12-ring photonic crystal fibre, shown in Figure 1(b), with a highly photosensitive and very high-NA

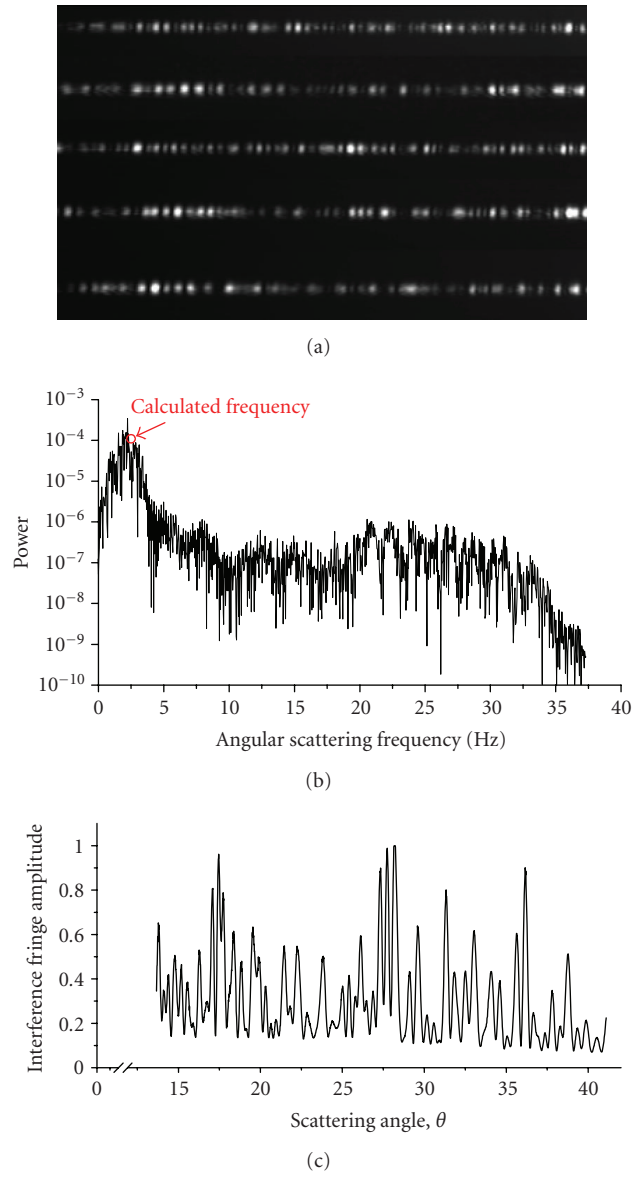


Figure 3: (a) Interference pattern images, (b) FFT of the scattered light at 543 nm, and (c) intensity plot at 543 nm [23].

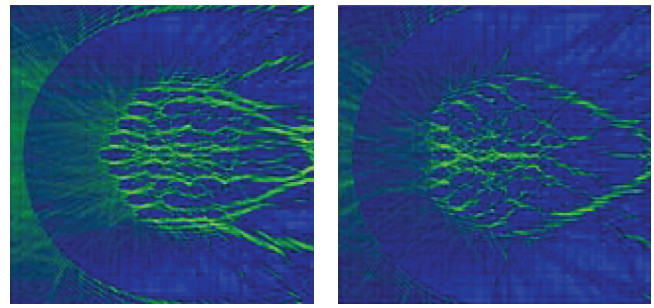


Figure 4: 193 nm light (TE) focussed and scattered within a 4-ring photonic crystal fibre (Figure 1(a)): (a) 0° (ΓM) and (b) 30° (ΓK) orientations [28].

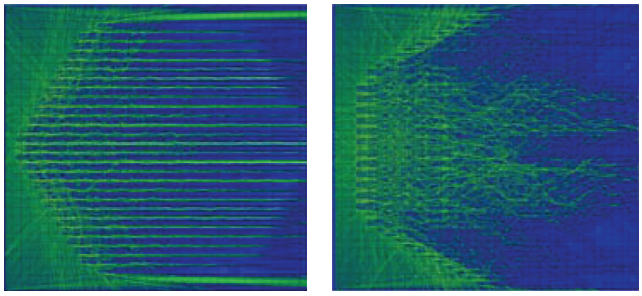

(a) (b)

Figure 5: 193 nm light (TE) focussed and scattered within a 12-ring photonic crystal fibre (Figure 1(b)): (a) 0° (ΓM) and (b) 30° (ΓK) orientations [30].

core designed for nonlinear work. The results are shown in Figure 5. Given restrictions on computational time, the full fibre structure, including the outer fibre diameter, was not simulated. A plane wavefront is used to excite the entire structure, approximately simulating the front expected within the Rayleigh range of a focusing lens. The effect of not considering the outer fibre diameter, and therefore wavefront curvature, results in the 0° orientation light seemingly zipping through the "wave guiding" regions between the holes. For this particular fibre this is especially important because the core is a triangular region defined by four defects (or four missing holes) in the center. Further, the central region of this core is composed of germanosilicate for added photosensitivity. However, it would appear based on this simulation that the transmitted light, whilst significant, actually bypasses the photosensitive region in the center. One could assume, therefore, that the preferred angle is 30°. Evidently, the expected results are highly sensitive not only to the lattice parameters, but also to the core structure and outer fibre diameter as well—different fibres may very well have unique solutions and, further, regular structured fibres are likely to be distinct to those with quasiperiodic structures including, for example, Fresnel fibres with chirped Bragg structures.

To investigate the particular case of the 12-ring fibre described above, grating writing into the fibre was carried out using motorized controlled rotation [30]. The particularly high concentration of germanium in the photosensitive region means this fibre permits ready formation of type IIa gratings [33, 34]. Therefore, information can be extracted in three ways: (1) average index shift from the Bragg wavelength shift, (2) index modulation from the grating strength, and (3) qualitative intensity variations based on the rollover from type I to type II a, which is known to be sensitive to writing intensity [35]. In order to calibrate the orientation, 244 nm light was used to directly excite germanium oxygen deficiency centers in the photosensitive core and blue luminescence monitored as a function of rotation angle. Although grating writing is carried out at 193 nm, the amount of blue luminescence generated by this wavelength is considerably less than that generated with 244 nm. Figure 6 shows an image of the end face of the

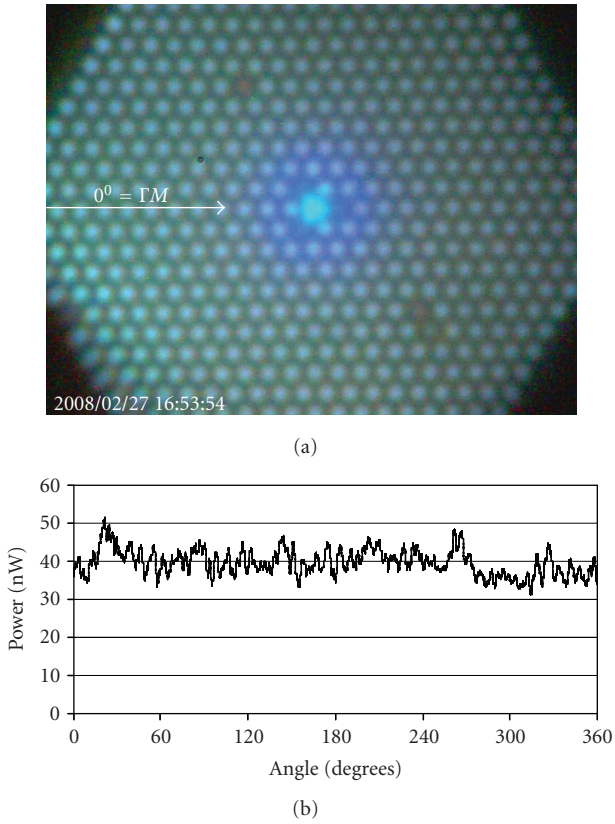


Figure 6: Blue luminescence propagating along the core of the 12-ring photonic crystal fibre is readily imaged. Also visible is the luminescence supported in the holes akin to whispering gallery modes of a hollow waveguide. The profile of the blue luminescence as a function of rotation angle is shown below [28–31].

fibre with the photosensitive region brightly illuminated and the monitored profile as a function of rotation. Based on these results, the optimum angle of excitation is found to be 21.5°. However, luminescence is reasonably strong elsewhere including for 0° and 30°, where it is identical. These two angles are important as these orientations are easily aligned visually—the sensitivity of 21.5° demands greater care in alignment. The observed variation in signal reaching the photosensitive core, including experimental error, is approaching 30% which is significant.

The experimental grating results at 0°, 21.5°, and at 30° are shown in Figure 7. As expected from the luminescence studies, the average index growth profiles, from positive to negative index change for a series of gratings are found to overlap exactly for 0° and 30°. The actual grating strengths varied in part because of the interference of the two modes of this fibre over the short length spliced between two standard single mode telecommunications fibres. It is observed that for all cases, the rollover from type I to type IIa (Type I*n*) grating occurs at the same cumulative fluence despite the fringe contrast variations also indicating that the same intensity is present for the two angles.

The results at 21.5° were found to have a larger average index, consistent with the luminescence studies—however,

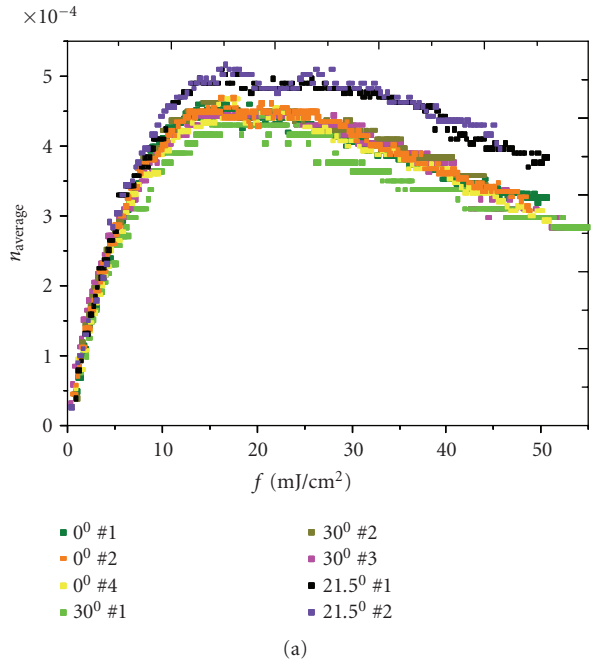


(a)

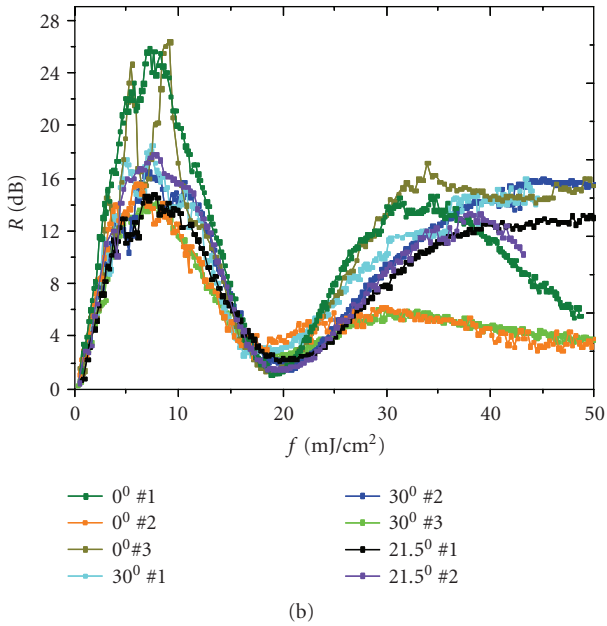


(b)

Figure 7: Type I and Type IIa evolution in a 12-ring photonic crystal fibre with germanosilicate core. (a) Average index (extracted from $\Delta\lambda$ shift) and (b) grating strength as a function of fluence [34].

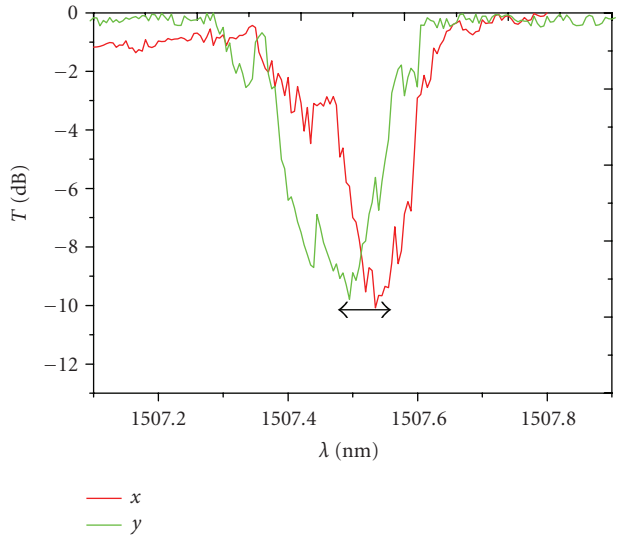


Figure 8: Grating induced into fibre core at 21.5° incident writing beam to the 0° axis. Large birefringence is observed ($\sim 1 \times 10^{-4}$).

the experimental variation over a series of runs at this angle was much more significant so the results in themselves were not conclusive at this stage. More interestingly, we observed that the asymmetric frame of reference of the structure with respect to the irradiating beam meant considerable asymmetry was introduced into the core and the grating had large birefringence ($\sim 1 \times 10^{-4}$) as shown in Figure 8 [34].

In both simulations described above, only the orthogonal incidence of a plane wave to the fibre has been considered. Whilst this has been sufficient for good qualitative agreement with experiments, in practice, the diffraction orders of a phase mask setup, or the angles of a two beam interference setup, have a vectorial component typically ~30–35° to the fibre axis for grating writing in the telecommunications window. The main impact of this, however, will be to affect the quality of the fringe pattern at the core rather than the total cumulative fluence provided care is taken with overall alignment. Any deviations, such as fibre tilt, will complicate results.

In summary, the general problem of scattering demands that attention is paid to the rotationally variant scattering properties of most structured optical fibres, including crystalline (photonic crystal) and quasicrystalline (Fresnel) and random structured fibres. The most obvious solution described above is rotational control of the fibre positioning during grating writing. Practical alignment of fibres can be achieved in several ways including monitoring of defect luminescence [28–30] or, for example, in other fibres such as $Er^{3+}$-doped fibres, rare earth emission during UV excitation [28, 29] with rotation. Alternatively, the more sophisticated and active approach using measurement of the transmitted wavefront across the fibre to feedback into wavefront phase adjuster as mentioned earlier can be adopted. This would depend on the availability of suitable phase adjusters such as liquid crystal arrays [32] or MEMs mirrors and may not be feasible for shorter UV wavelengths, but amenable to longer wavelengths including those used in multiphoton grating writing.

## 3. Reducing Scattering

We have discussed both type I and type IIa formation in photonic crystal fibres containing germanosilicate and in all respects the photosensitive properties are well established in conventional fibre grating writing, although the cumulative fluencies tend to be much higher as a result of the scattered

light away from the core. However, the structured optical fibre has demonstrated how an unconventional design can be used to obtain further spatial information to help improve the understanding of the physical origins associated with such gratings generally. Previous work using spatial characterization to help elucidate underlying mechanisms used the differences seen by a fundamental and a higher-order mode in a two-mode conventional optical fibre [36]. The results in Section 2 are consistent with that work.

It is clearly important to control rotational variance both in terms of reproducibility and in terms of grating writing efficiency. This is especially so for higher-exponent processes that require substantially more photons per unit area. An alternative approach to deal with this problem is to consider inserting material into the holes, that is, index matched to the silica so that the scattering is reduced or removed altogether. Whilst this is certainly a challenge for 193 nm grating writing, since there are few materials that transmit and do not ablate at such short wavelengths, this approach has been successfully used to improve grating writing at 248 nm [8].

A similar approach permitted the inscription of femtosecond-written damage gratings into structured optical fibre—by filling an air-clad fibre with a $Yb^{3+}$-doped germano-aluminosilicate step-index core (shown in Figure 1(d)) with index matching gel, a near IR (800 nm) femtosecond laser was able to access the core of the fibre and inscribe a high-temperature resistant damage grating [20]. A micrograph of two filaments induced on one side of the air-clad core is shown in Figure 9. Prior to this, the only gratings written directly into large diameter air-clad structured fibres, designed for high-power laser operation, were done so by using single photon excitation with either 244 nm or 193 nm [19]. This result was the first reported result of a grating written directly into the active medium of any large diameter fibre designed for high-power laser operation.

From here on we review the increasing interest in higher-exponent grating writing, including two-photon absorption with UV lasers and multiphoton absorption using femtosecond laser systems.

## 4. Hydrogen Loading

Another approach to reduce the impact of scattering in single-photon grating writing is to use hydrogen loading to maximize the photosensitivity available. However, the existence of the air holes surrounding the core poses a challenge for hydrogenation as it easily outdiffuses through the holes and escapes from the fibre by the end facets, which drastically reduces the photosensitivity. A practical solution is to seal the fibre end facets before hydrogen loading [37]. For the 12-ring photonic crystal fibre shown in Figure 1(b), this was done by fusion splicing the PCF length with lengths of standard SMF28 fibres on both sides. A number of problems are raised by splicing such different fibres, including (a) mismatch in fibre V parameter, (b) the existence of higher-order modes and intermodal interference fringes [38], and (c) splice integrity whilst minimizing losses.

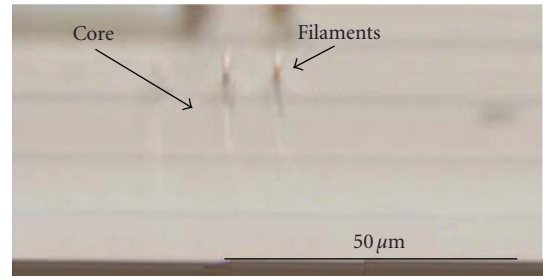


Figure 9: Femtosecond-induced filaments observed by optical microscope through the air cladding structure filled with index matching gel [20].

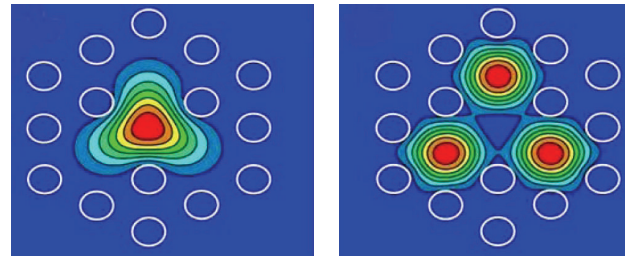


Figure 10: Calculated mode field profiles of the (a) fundamental mode and (b) the higher-order mode, which is made up of three nondegenerate but similar components, supported by the 12-ring photonic crystal fibre in Figure 1(b) [33, 34].

For the 12-ring fibre, insertion losses below 2 dB were obtained by monitoring coupling to the mode from the SMF28 to the fundamental mode of the structured fibre. This particular fibre has an effective higher-order mode that rests within the three lobes of the triangular core, as shown in Figure 10 and great care is required to avoid coupling into it. After splicing the samples, typical hydrogen loading conditions are 180 atm at 80°C for 5 to 7 days to ensure the holes are saturated in pressure and equilibrated to the pressure within the glass. Within this particular fibre, gratings >30 dB in strength were possible [8]. In all respects, the gratings are again identical to standard gratings written into conventional hydrogen-loaded germanosilicate fibres. Similar thermal annealing is observed (Figure 11) [39]. The estimated effective thermooptic coefficient is 12.3 pm/°C, which agrees well with values obtained on gratings written in high-concentration Ge-doped, conventional step-index silica fibre [40].

Hydrogen loading was also used to demonstrate the first femtosecond gratings in pure silica fibres using 266 nm femtosecond light [10]. In these experiments, the grating decay indicated they were relatively unstable and probably related to direct single-photon 266 nm hydride formation well below the damage threshold of the glass. Scattering, along with absorption by hydrogen species, prevented higher-exponent excitation below the band edge. Generally, below the damage threshold it has been shown that there is largely no difference between gratings written with UV femtosecond 244 nm

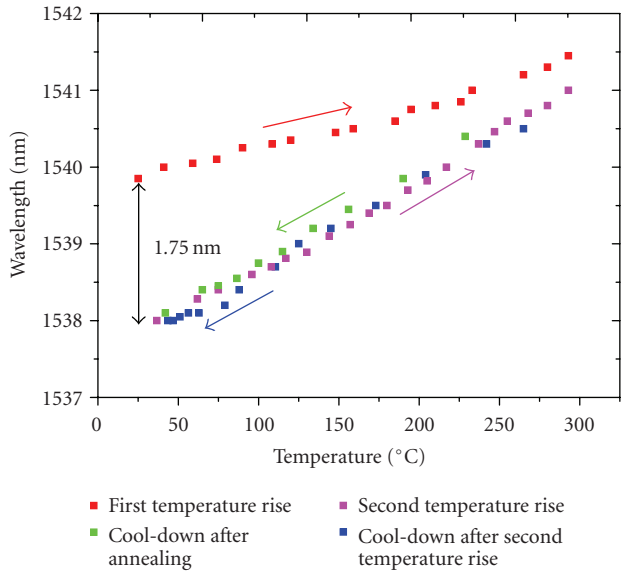


FIGURE 11: Temperature cycling of hydrogen-loaded 12-ring photonic crystal fibre grating (Figure 1(b)). The initial drop in Bragg wavelength arises from outdiffusion of the hydrogen, which raises the effective mode index by nearly $2 \times 10^{-3}$. Beyond this, the index change is stable after repeated cycling from room temperature to 300°C. There is no observed hysteresis [39].

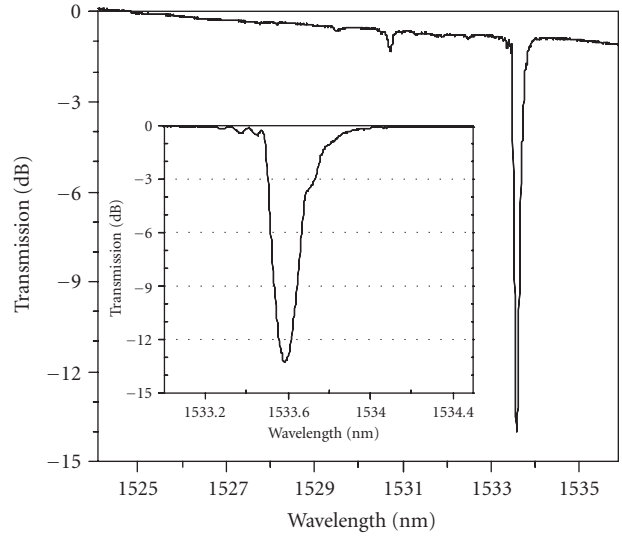


FIGURE 12: Grating in pure silica single-material photonic crystal fibre [14].

lasers and gratings written with CW 244 nm [41]. Thus no clear advantage has been established for the use of a femtosecond laser for writing of type I gratings.

## 5. Two Photon Grating Writing

Two photon absorption of UV light permits access below the band edge of glass to excite Si–O bonds, or other component in other glasses, that make up the glass network. Unlike single-photon excitation, defects are largely circumvented. Rather, softening and/or breaking of the oxide bonds of the network allow glass structural rearrangement, and therefore densification, to take place. The energy required for this process need not exceed the damage threshold, thereby avoiding cascaded ionization typical of femtosecond laser irradiation in addition to fracturing within the network associated with longer pulse excitation (type II gratings). Cumulative fluencies, therefore, tend to be large in comparison with other grating writing methods, particularly if the energy density is sufficient to soften the bonds and allows thermal relaxation into a different density glass, akin to thermal quenching of glass in a controlled fashion [42]. Consequently, this densification grating is usually of lower loss than damage gratings although within structured optical fibres this will give rise to surface corrugations within the air holes [43]. Generally speaking, the process becomes more efficient the deeper into the UV the excitation occurs and therefore 193 nm from the excited state complex (exciplex) of an ArF laser is significantly more efficient than, for example, 248 nm from a KrF laser. From the perspective of inscribing a periodic structure on dimensions approaching the nanoregime, this also leads to improved localization and fringe contrast. Going to shorter wavelengths, such as 157 nm generated from the excited state dimer (excimer) of an $F_2$ laser, poses practical challenges in terms of delivery optics and the need for a vacuum.

### 5.1. Densification Gratings in Single Material-Structured Fibres

Figure 12 shows the first transmission profile of a densification grating written into a 4-ring, single-material, silica-photonic crystal fibre similar to that in Figure 1(a) [14]. In such a fibre, the densification leads to corrugations within the air channels of the structured fibre, which was confirmed in studies involving the flow of ice formation inside water filled holes of such a grating [43]. Figure 13 shows the reflection spectrum of a similar grating written into the Fresnel fibre shown in Figure 1(c) [15]. The optical mode peaks in the center of the central hole. Nevertheless, sufficient light extends into the ring of silica around the hole to "see" a reasonably strong grating, a good example of how a bandgap fibre is modified to have a hybrid structure with air and glass. Of course, in all-solid bandgap structures this is unnecessary but the applications become somewhat restricted. This method of grating writing is based on well-established densification of silica glasses under UV irradiation which precedes germanosilicate grating writing by decades [44–47]. More recently, femtosecond lasers under strict control can operate just below the glass damage threshold to achieve similar results [48].

### 5.2. Densification Gratings in Nongermanosilicate Core Structured Fibres

Whilst two-photon absorption of UV light may require long cumulative fluencies for pure silica [14], when the glass

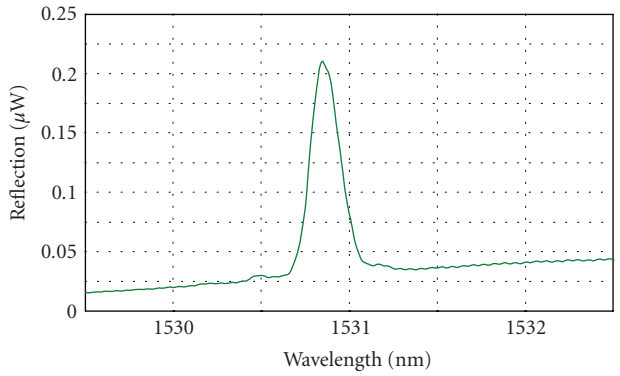


Figure 13: Reflection spectra of a 5 dB strong grating within the Fresnel fibre shown in Figure 12 [15]. The optical intensity of a propagating mode peaks in the core hole.

composition is mixed, the photosoftening threshold can be reduced and the writing processes enhanced and accelerated significantly. In the case of nongermanosilicate step-index core-structured fibres, competitive writing times with conventional grating writing have been demonstrated for the fabrication of $Er^{3+}$-doped aluminosilicate photonic crystal fibre distributed Bragg reflector (DBR) and distributed feedback (DFB) fibre lasers [16–18]. By way of example, the characteristic output of a DFB photonic crystal fibre laser fabricated in this fashion is shown in Figure 14. Writing times are now <20 minutes in such fibres depending on the device parameters sought. Given that much of this change occurs within the step-index region of the structured fibre core, corrugations are not so prominent. It is important to verify that the writing excitation process is two-photon even if the subsequent glass relaxation is unlikely to be directly correlated with the excitation.

Unfortunately, the small window for efficient two-photon induced index change just below the damage threshold, along with the error window found when dealing with scattering and other issues, has prevented to date a direct measure of the quadratic dependence with intensity of index change. Instead, as mentioned above, one approach is to infer the presence of densification itself from restrictions in ice flow that give rise to distortions in the grating profile and eventually fibre cracking [43]. This takes advantage of the fact that water freezing within small capillaries leads to a super-cooled liquid phase between the ice and the glass interface which "lubricates" flow of the ice as it expands from the liquid state. This super-cooled layer is small, and therefore the lubrication process is impeded in the presence of corrugations. However, for this fibre the changes occur within the step-index portion and may not translate to the surrounding silica walls of the air holes. A less direct approach is to repeat the experiments in a preform slice from which the doped core inserted into the structured optical fibre during fabrication is made [49, 50]. Direct depressions arising from densification can, therefore, be measured using atomic force microscopy (AFM), laser diffraction from periodic densified regions, and phase microscopy. Figure 15 shows the measured dependencies determined from such

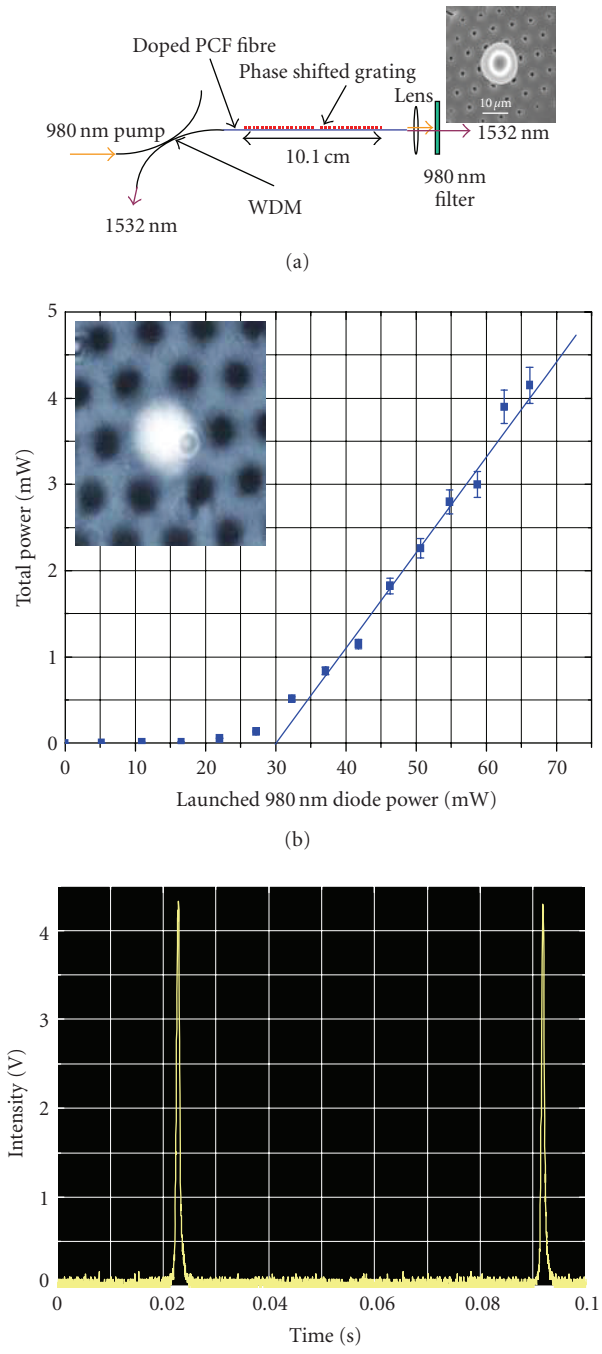


Figure 14: Characteristics of a DFB photonic crystal fire laser. The grating is written by a 2-photon process which avoids the need for hydrogen loading. The top shows a schematic of the setup and a profile of the measured laser output. Center is the characteristic power curve—inset shows the doped section illuminated with white light. Bottom shows the laser operates single polarization. The measured linewidth by self-heterodyne is <50 kHz [17].

techniques for both 193 nm single-photon excitation of a germanosilicate perform and what is thought to be a two-photon excitation of an $Er^{3+}$-doped aluminosilicate perform

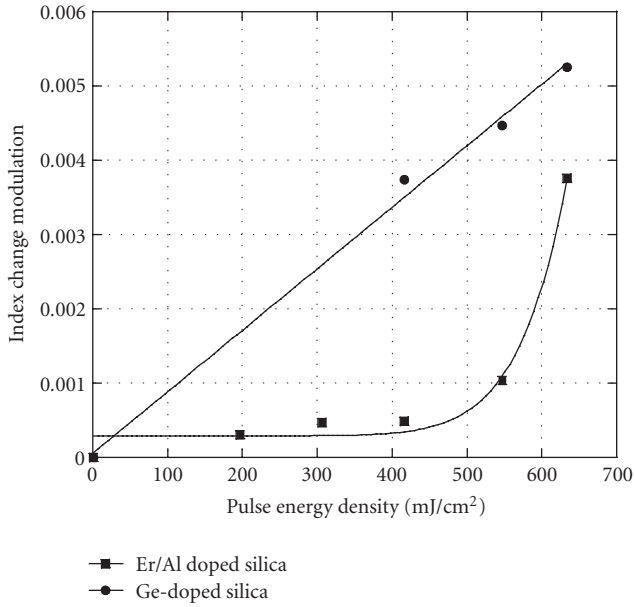


Figure 15: Index modulation as a function of pulse energy for a germanosilicate preform (linear) and an $Er^{3+}$-doped aluminosilicate preform (non-linear). The latter preform is a slice from that used to draw the fibre into which the DFB of Figure 12 was drawn [46, 47].

[46, 47]. Densification has been confirmed but further work is necessary to clarify the complex nonlinear behavior observed.

## 6. Femtosecond Laser Written Gratings

Multiphoton absorption with exponents >5 using ultrashort pulses (~100–600 femtoseconds typically) is an increasingly popular way of writing long period and Bragg gratings either into the ODC absorption band (type I gratings) or into the glass band edge directly (femtosecond type II gratings) into both conventional [51–58] and structured optical fibres [20, 21]. Although using long pulses with exciplex lasers can access multiphoton processes [59], the much shorter timescale of femtosecond excitation means that electronic avalanche ionization can be generated locally on a timescale much faster than any direct photon decoupling away from the excitation site. The large rapid local index change leads to filamentation in part arising from self-focusing effects by the generated plasma, which acts to prevent the collateral damage more familiar to long pulse lasers. Given that the spatial extent of these cylindrical filaments is commensurate or smaller than the probing wavelength within the VIS-NIR window, significant Mie scattering can be generated if not adjusted. These gratings, therefore, have significant diffractive scattering losses increasing toward shorter wavelengths [60, 61]. Despite these large scattering losses, these gratings have been used to successfully demonstrate a stable 100 W CW $Yb^{3+}$-doped fibre laser operating ~1 $\mu$m [62]. Since the pump wavelength is coupled into the inner cladding, the grating losses at the pump wavelength are minimized. This is a tremendous improvement over the failure of type I gratings to perform within a similar fibre laser operating at only 15 W [19, 63]. However, the extremely serious problem of very high-optical fields giving rise to large local temperatures within $Yb^{3+}$-doped optical fibres, a work horse of high-power fibre lasers up to the kW regime, has not been fully resolved. Femtosecond gratings are now known to self-erase within such lasers when operating as a Q-switched laser [64], a phenomenon of considerable scientific and practical interest. At very high powers, therefore, at this point in time it remains preferable to keep the gratings external to the active medium. This stringent limitation is almost certainly most serious for $Yb^{3+}$ which is known to have a high-thermal nonradiative component as well as unusual resonant excitation processes which may couple light directly into the band edge and consequently also leading to index change [65].

To summarize the processes briefly, it has been well established that the damage mechanism can be described in terms of multiphoton ionization of electrons, heating of free electrons, and a shock-like transfer of the energy to the lattice. This process is well known as ablation of a surface material—however, when localized within a material by these multiphoton processes, the shockwave leads to what has been called a microexplosion [66]. At sufficiently high intensity, this allows direct void formation to also be induced in the glass, an approach that appears to be aided by having a photosensitive dopant within the glass. One example is cerium-doped glass that has been used to make 3-D microfluidic channels [67]. Associated with this structural change is densification when the intensity is low [68]. The ionization mechanism underpinning femtosecond laser operation is therefore not dependent exclusively on the wavelength. Both 266 nm via two photons [69] and 522 nm via few photons have been used to achieve similar results [70].

### 6.1. Gratings in Single-Material Photonic Crystal Fibres

Femtosecond grating writing in single-material all-silica photonic crystal fibres has recently been reported for few ring structures [21]. The authors comment that scattering issues are the primary reason why this has not been extended beyond a few rings. Tapering of the fibres is one solution to help reduce this scattering, since the period of the hole spacing is now smaller than the wavelength, reducing scattering substantially.

### 6.2. Gratings in Air-Clad Structured Fibres

Earlier, we described grating writing through an air-clad fibre by using index matching gel to remove the Fresnel reflections from the hole air-silica interface. In this way, femtosecond gratings were inscribed into air-clad structured fibres, where only a single ring of air holes defined the inner cladding of a double-clad fibre with a central step-index core containing $Yb^{3+}$ ions for high-power fibre lasers [20]. Figure 1(d) shows the cross-section of such a fibre. This fibre was used using

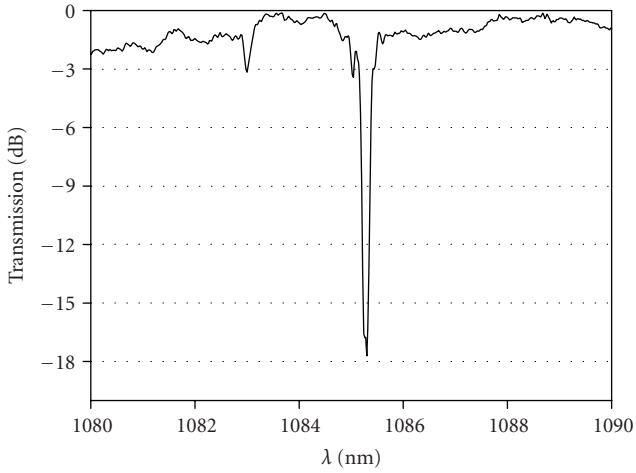


Figure 16: Transmission spectra of a femtosecond grating written into the $Yb^{3+}$-doped core of an air clad fibre 400 $\mu$m diameter [20]. A higher-order mode grating is also observed.

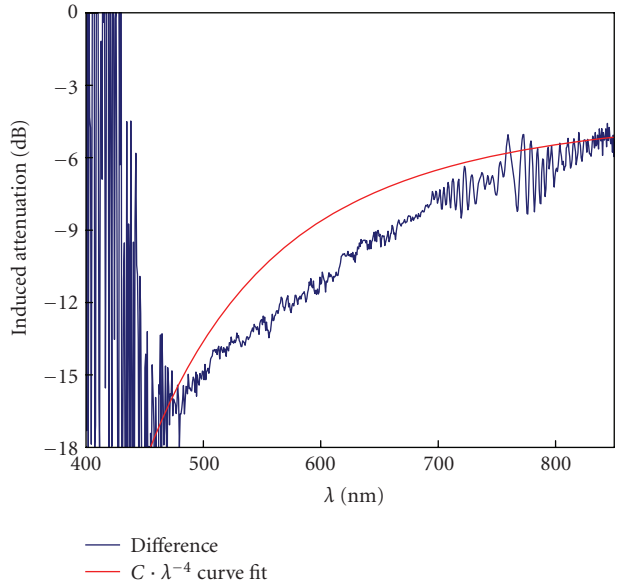


Figure 17: Induced short-wavelength loss of air-clad grating shown in Figure 14. An almost linear dependence is observed consistent with Mie scattering [20].

bulk mirrors and end face reflection to generate >100 W fibre laser power.

Bragg gratings were produced using a femtosecond laser (800 nm, 100 femtoseconds, 1 kHz) period by period as the beam is scanned over the fibre. A transmission spectrum with 16 dB rejection is shown in Figure 16. Similar laser performances to the 100 W fibre laser reported much later using femtosecond gratings in conventional double-clad fibres [62] can be expected. The use of a gel made it difficult to remove after grating writing to prevent high-power fibre laser operation. This could be improved using index-matched liquids rather than gel so that heating can be used to subsequently remove the liquid. Characteristic of such gratings is the observation of substantial diffractive scattering at short wavelengths shown in Figure 17 [20]. Such losses reduce the overall efficiency of high-power fibre lasers since the pump wavelength in particular experiences loss. A detailed and systematic study of this loss confirmed similar properties to conventional type II gratings [60, 61] despite the much more uniform nature of the processed regions. Although the structural nature arising from photoinduced ionization and melting may differ as a result of different excitation and local quenching rates, this is unsurprising given both are damage gratings written above the damage threshold of the glass. In fact, the uniformity leads to efficient side diffraction light travelling within such a fibre, which can be utilized to make an ideal component for a compact fibre spectrometer, suitable for a number of applications including sensing, monitoring, and external coupling of fibre laser light.

## 7. Properties and Applications

A key factor that separates structured fibre gratings from conventional gratings is the composite nature of the fibre. By controlling the hole distribution and size, mechanical properties are altered, including acoustic and pressure response, as well as even more basic properties such as strain optic coefficient. Inserting material gives greater scope for adjusting composite system properties such as the effective thermooptic coefficient discussed earlier. The flexibility in adjusting such parameters also offers new solutions to perennial problems including sensors perspective, separating strain, and thermal properties. Some of these properties are reviewed here.

### 7.1. Strain and Temperature Response

An important distinction between conventional step-index fibres and structured optical fibres, even those with a step-index core, is the striking differences in properties possible between the so-called fundamental mode and the higher-order modes. Depending on the design, losses and effective indices are comparable with a step-index fibre. In an ideal fibre, losses are almost entirely due to evanescent field penetration outside of the core (except in the special case, where the cladding may extend to infinity). This is not true for a structured optical fibre, where additional leakage loss between air holes or filled channels occurs. On the other hand, the high-index contrast between, for example, air and silica means the evanescent field peaks and is much more tightly localized to the interface, although losses can still be higher if the hole size is sufficiently small to allow coupling between one side and the other, perhaps through excitation of whispering gallery modes. These properties are formulated by the different effective fibre mode indices which are the index of the composite system. It may be expected that the properties of structured fibres will differ and vary to those of step-index fibres. Given that in the first instance the fundamental leaky mode of the structured fibre has a $k$ vector along the fibre axis and therefore the role of leakage

loss is somewhat suppressed, the fundamental mode may not be so distinctive in behavior to that of the step-index analog. This forms the justification for the step-index approximation of simple-structured fibres, where the cladding index is, on average, lower than the core index. On the other hand, tightly confining such a fibre will deliver noticeable and application worthy differences. By adjusting the crystal lattice parameters of a photonic crystal fibre appropriately, unique composite system properties can be displayed. A good example is the demonstration of dual dispersion compensation and Raman amplification [71].

In contrast, higher-order modes will be significantly affected by leakage loss and greater evanescent field penetration into the holes. The extreme example of this is the air-clad fibre shown in Figure 1(d), where diffractive scattering plays a critical role in ensuring mode mixing and overlap with the core is high [72, 73], an important advantage that permits air-clad high-power fibre lasers to retain symmetry. In practice, even the higher-order modes of an ordinary regular photonic crystal fibre are far more sensitive to the cladding structure and enable practical sensing to be developed [74]. Even over short lengths supposedly, single-mode photonic crystal fibre can support higher-order leaky modes that lead to analogous intermodal interference observed with short lengths of standard single-mode telecommunications fibre [75]. It is noted within the literature that many gratings written into single-mode structured fibres have an observable higher-order mode resonance [9, 14, 20].

It is this difference between the well-confined fundamental mode and the higher-order modes that allows a qualitative study of the properties of a structured optical fibre using Bragg gratings to determine both effective strain and thermooptic coefficients and compare with those obtained for standard optical fibres. In previous work, fiber Bragg gratings, written by two-photon excitation, within a two-mode solid core photonic crystal fiber, which has a cladding region defined by a silica layer containing a triangular lattice of air-channels, were used to obtain the strain and temperature dependence of the structured fibre. The core is composed of an inner, doped core, and one outer silica ring—the presence of $Er^{3+}$ plays no important role in the Bragg resonance dependence with strain [76]. The effective indices of the two modes give rise to two distinct grating peaks (Figure 1)—we note that this higher-order mode is made up of slightly nondegenerate components [18] but the resolution used was not able to separate these components. The modes are determined by the corresponding fractional powers ($\eta$) of each mode within the higher-index-doped region (0.002) and in the surrounding silica. Leakage phenomena play an important part in determining and defining the mode field radius and therefore the fractional distribution of light of the modes either in the doped core or in the silica. Therefore, those modes with large transverse vector components will be sensitive to changes in the hole shape and stress between the holes in the structure arising from, for example, tensile or compressive stress applied along the fiber.

But it is also clear that this sensitivity will very much depend on air fraction, the regularity of the lattice, the constituent materials, and the type of index guidance. For example, the Fresnel fibre described earlier has much less air fraction, no regularity, is single-material all-silica, and the mode is largely determined by diffractive guidance even for the fundamental mode rather than an average step-index-like effect. Therefore, a comparison of both temperature and strain effects of the fundamental mode within a single-material Fresnel fibre and a single-material photonic crystal fibre will further illustrate just how much flexibility in design exists by controlling structure alone.

### 7.1.1. Temperature Dependence

#### *(a) Fundamental versus Higher-Order Modes*

From Figure 18, the transmission spectrum of a 4-ring photonic crystal fiber with a fibre grating has two reflection bands corresponding with the two modes it is designed to support, one at longer wavelengths (1535.2 nm) for the fundamental mode, and the other ~4 nm at shorter wavelengths for the higher-order mode. By monitoring these peaks, it is possible to determine the observed shifts experienced by each mode with temperature or applied strain. Figure 19 shows the obtained temperature dependencies for each mode—both grating transmission bands are found to have a similar linear variation with temperature. These results are in accordance with the material properties of the fiber, since the thermal expansion coefficient, $\alpha_{SiO_2}$, of the fiber ($\alpha_{SiO2} \sim 0.55 \times 10^{-6}$ for silica) is an order of magnitude smaller than the thermooptic coefficient—for germanium-doped silica core fiber this is $(1/n_{\text{eff}})(\partial n_{\text{eff}}/\partial T) \sim 8.6 \times 10^{-6}$, which serves as a reference value [77]. From the grating response as a function of temperature, the fundamental mode wavelength dependence is $\partial\lambda_{B1}/\partial T = 19.72\,\text{pm}/^\circ\text{C}$, and for 1535.2 nm of $\partial\lambda_{B2}/\partial T = 20.14\,\text{pm}/^\circ\text{C}$. These correspond to $(1/n_{\text{eff1}})(\partial n_{\text{eff1}}/\partial T) = 12.9 \times 10^{-6\circ}\text{C}^{-1}$ and $(1/n_{\text{eff2}})(\partial n_{\text{eff2}}/\partial T) = 12.8 \times 10^{-6\circ}\text{C}^{-1}$ which are nearly double that of pure silica although similar to doped optical fibres. This larger value is due to the $Er^{3+}$-doped aluminosilicate core and it is not surprising that the higher-order mode, which sees more silica, has a slightly lower value. Therefore, the composite system behavior is expected on the basis of constituent component materials.

An alternative approach to cancel out the temperature dependence by filling the channels with a liquid that has a large negative refractive thermooptic coefficient, such as many organic liquids [78], was mentioned earlier. The primary advantage of this is within sensor applications the contribution to the observed grating shift from temperature is removed altogether leaving only the strain contribution to be measured. This is important for many strain and pressure sensors. It is also a very simple means of packaging a grating—a viscous fluid within the channels can also serve to dampen external noise parameters.

#### *(b) Fresnel versus Photonic Crystal Fibre*

Figure 20 shows the relative wavelength shift of a Bragg grating written by 2-photon excitation within a single-material

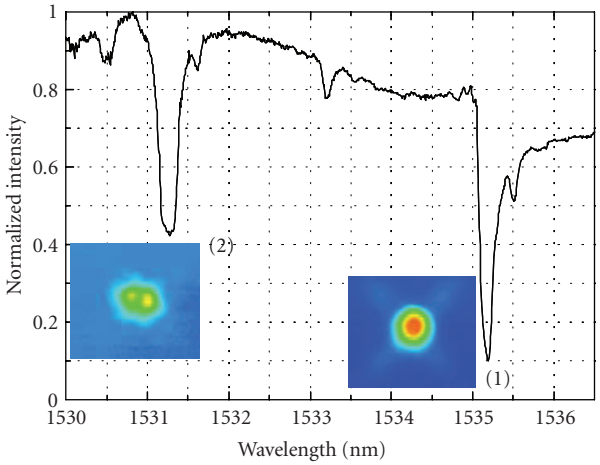


Figure 18: Transmission spectrum of a two-photon written Bragg gratings within a two-mode, 4-ring photonic crystal fibre. (1) fundamental mode; (2) higher order mode and the dip in the centre is some cross coupling between the two arises from some asymmetry in transverse profile of the induced index change [76].

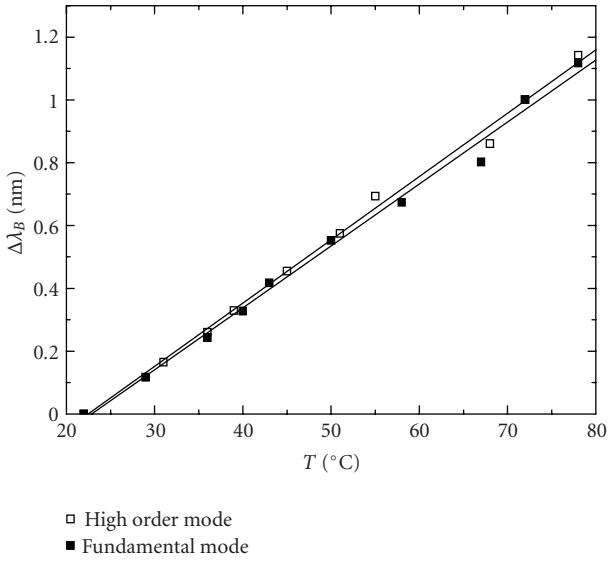


Figure 19: Temperature dependence of the two modes of the fibre described in Figure 18 [74, 76].

all-silica Fresnel fibre (Figure 1(c)) and a similar single-material, single-mode, all-silica 4-ring photonic crystal fibre (Figure 1(a)) as a function of temperature. Below 100°C the Fresnel fibre has a slightly higher temperature dependence, or effective thermooptic coefficient, $((1/n_{\text{eff1}})(\partial n_{\text{eff1}}/\partial T) = 7.8 \times 10^{-6}/°\text{C}^{-1}$ compared to the photonic crystal fibre of $6.5 \times 10^{-6}/°\text{C}$, although both are very close to that of pure silica $\sim 6 \times 10^{-6}/°\text{C}$ [79]. What is interesting to observe, is that unlike the previous results for the step-index $Er^{3+}$-doped aluminosilicate step-index core photonic crystal fibre, there is a quadratic dependence on this effective thermooptic coefficient, which is particularly pronounced for the Fresnel fibre. This is directly attributable to mode field confinement

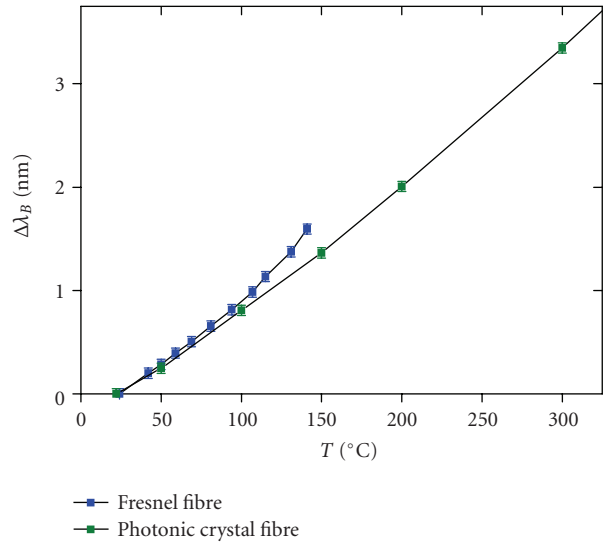


Figure 20: Temperature dependence of the fundamental mode within two types of structured optical fibre [15].

by the air holes as the index of the glass changes and, hence, great care must be taken when interpreting the temperature dependence of the structured optical fibres since this is not solely a material-dependent parameter as can be assumed in the case of conventional step-index fibres. The apparent observation of a sharp transition within the Fresnel fibre may characterize a cutoff condition for propagation which is especially sensitive in the Fresnel fibre given the larger dependence on diffractive propagation.

Clearly, the illustrated results reflect overall huge scope to adjust both the fibre design and fibre parameters and control properties such as the temperature dependence. This can be applied to enhance various configurations of thermally tunable devices using structured fibres, active or passive, and gratings, for example. For sensing applications, this control over the temperature dependence can be used to help separate the difficult corelationship between temperature and strain.

This example illustrates the flexibility in tailoring the properties of single-material fibres. Such fibres have other advantages—for example, given that the index contrast with air is sufficiently high, properties such as form birefringence can be readily introduced into these fibres. Form birefringence within a single-material fibre is free of the temperature problem associated with two materials of different thermal expansion coefficient—fibre that has a zero temperature dependence of birefringence from −20 to +800°C has been demonstrated [80]. These results were extended to a spun version of this fibre [81], which has important applications, amongst many, to electric field sensors and gyroscopes.

### 7.1.2. Strain Dependence

In contrast to the temperature dependencies, there is a difference between the fundamental mode and the higher-order mode of the previous $Er^{3+}$-doped aluminosilicate photonic

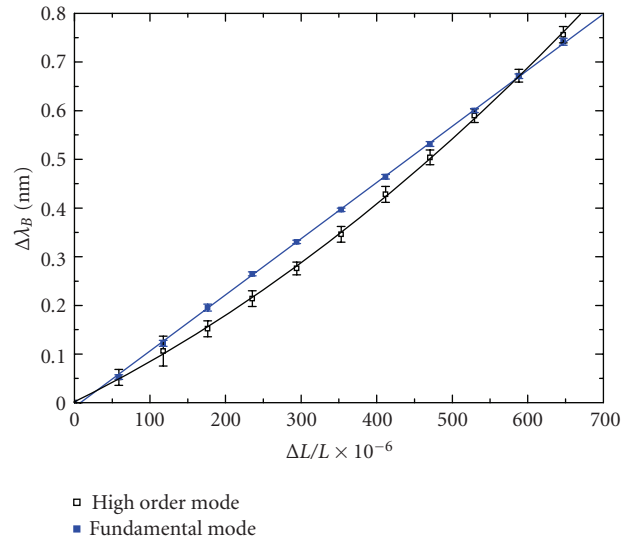


Figure 21: Wavelength shift versus applied longitudinal strain on the $Er^{3+}$ doped, aluminosilicate dual mode photonic crystal fibre fibre. A quadratic dependence is observed for the higher order mode [74, 76].

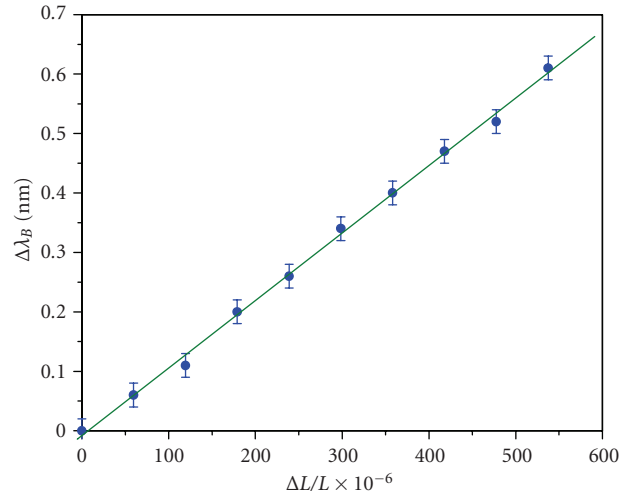


Figure 22: Wavelength shift versus applied longitudinal strain on the Fresnel fibre. No higher order mode is observed in this fibre [15].

crystal fibre. The observed shift with applied strain in the Bragg wavelength corresponding to the fundamental mode (Figure 21) has a linear behavior ($\partial\lambda_{B1}/\partial\varepsilon = 1.2\,\text{pm}/\mu\varepsilon$). However, the shorter Bragg wavelength, corresponding to the high-order mode, has nonlinear behavior described by a quadratic dependence. This arises from the compressive stress that is generated by the applied tensile strain (which can be estimated via Poisson's relations). Unlike conventional fibers, the higher-order leaky modes (in particular) of a photonic crystal fiber are sensitive to changes in stress between the holes and both the hole size and shape as well as the ratio of the hole diameter over the hole pitch, $d/\Lambda$ [82]. Since the holes are not centered, the compression of the first ring, in part arising as the solid core resists the compressive force, leads to an increase in $d/\Lambda$ with positive strain (applied tension). This problem is a well-known one that also contributes to hole deformation of the first ring during fiber fabrication if not addressed [83]. By increasing $d/\Lambda$, the modal confinement loss decreases [82], leading to improved confinement of the mode—this then alters the respective fractions of power, $\eta$, in the center core and in the silica ring and cladding. Since the effective refractive index is dependent on this fraction, there is an additional shift in the Bragg wavelength ($\lambda_B = 2n_{\text{eff}}d$) that deviates the curve from linearity. Given that the changes are based on circular confinement and therefore mode area, to first approximation a quadratic dependence ($\lambda \propto a\varepsilon + b\varepsilon^2$) is expected and observed [76]. The strainoptic coefficient, therefore, reduces to $\partial\lambda_{B1}/\partial\varepsilon = a + 2b\varepsilon$. Further, the grating strength is also dependent on this fraction [$\kappa = \tanh^2(\pi\Delta\nu L\eta/\lambda)$] and we expect to observe a change in grating strength as a function of strain. The air structure itself becomes integral to defining the material properties and in this context is indistinguishable from a composite material. Therefore, the whole medium can be considered a unique super-structured material (SSM) with properties that can be tailored by tailoring the refractive index in a way analogous to tailoring the atomic distribution of constituents and their fractions in composite systems.

In contrast to this fibre, and despite the large interaction of the sensitive fundamental diffractive mode with the structure given its reduced confinement and the absence of an insulating step-index core, the Fresnel fibre has only a linear dependence mode with strain, as shown in Figure 22 [15]. This is explained by the very low-air fraction and the irregular arrangement of holes that prevent a sponge-like structure susceptible to compressive effects.

The most obvious application of this work is to enable a simple distinction between strain and temperature from the perspective of controlling strain instead of temperature. The ability to remove, or unravel, the strain contribution is a key problem in fibre sensing with gratings generally and structured optical fibres offer a unique pathway to resolving this.

## 7.2. Dual-Mode Operation for Sensing

Above, we described the dual-mode operation of a structured fibre grating which effectively allows the fundamental mode to be the reference arm of a potential sensor based on such fibre whilst the higher-order mode is the probe arm. In this way, the temperature and strain can be separated out without additional fibre sensors being required. Recently, a much more sensitive version of such a device was demonstrated using a dual-mode DFB fibre laser inscribed directly into the same fibre [18].

## 7.3. Diffraction from a Photonic Crystal Fibre

We described above solid-core photonic crystal fibres by an analogous effective step-index fibre but noted that this

approximation, used by many authors (see, e.g., [2] and the references therein), is generally not valid for higher-order modes. In fact, the effective core and cladding of this step-index approximation can be highly sensitive to the extent of the modal field into the cladding. As a consequence of the high-core-cladding index contrast, the contribution to mode propagation from, for example, a periodic arrangement of holes is negligible when the wavelength of light is larger than the bridge thickness between the holes but smaller than the core diameter. On the other hand, for less confined modes or when the wavelength of light is commensurate or smaller than the interstitial hole spacing, as well as the core size itself, a periodic lattice provides phase conditions that allow coherent scattering of light and therefore diffractive confinement [84]. This resonant phenomenon has been observed in bending loss tests, where light leaks out from the core and is launched into the cladding, generating a short wavelength cutoff in the fibre transmission band [85]. This short wavelength cutoff is sensitive to the perturbations applied to the fibre as well as the index of the material within the hole. In fact, such regular coupling of light between the interstitial regions of a regular lattice-structured fibre plays a key role in high-bend loss characteristic of such fibres [86]. The best way to prevent this is, therefore, to remove the crystalline regularity of this lattice thereby spoiling the coupling—zero bend loss has been demonstrated using a chirped Fresnel fibre (or fractal fibre) [86] which in turn served as the basis for ideal tapered structured fibre for efficient metal free SNOM [87].

It has been proposed that these higher-order diffraction effects related to the lattice periodicity can even be used to advantage in novel sensors [25]. In fact, the corrugations associated with densification gratings produce the necessary coupling to the lattice through scattering. The condition for the wavelength dependence of this scattering will also be sensitive to what is in the air channels—in effect a refractive index diagnostic tool can be demonstrated. The refractive index of ice was measured this way, confirming how a simple Bragg condition suffices to describe the processes at short wavelengths. Therefore, the refractive index of the material within the holes, $n_h$, is given by [25]

$$n_h = \frac{n_{\text{core}} \cos\left[\sin^{-1}(\lambda m/2n\Lambda)\right] - x_{\text{SiO}_2} n_{\text{SiO}_2}}{x_h}, \qquad (2)$$

where $n_{\text{cladding}} = x_h n_h + x_{\text{SiO}_2} n_{\text{SiO}_2}$, $x_{\text{SiO}_2}$ and $x_h$ are the fractions of silica and holes that make up the cladding, $m$ is the grating order, $\Lambda$ is the lattice pitch, and $n_{\text{SiO}_2}$ the index of $SiO_2$. Figure 23 shows the calculated refractive index of water determined from the transmission band edge shift in the visible to longer wavelengths [25] as a function of temperature. Freezing is observed to occur at a lower temperature than zero, $\sim -3^\circ$C, consistent with very high pressures induced within the microchannel. To lower the m.p. of ice by such an amount requires a local pressure >30 Mpa [88], giving an indication of the high-effective pressures that can be generated within micro- and nanocapillaries of ice 1 hour, which has ~9% volume increase from the liquid state. This has important implications for micro- and nanofluidics. The calculated refractive index for the frozen ice is in agreement within error with that of ice 1 hour as expected.

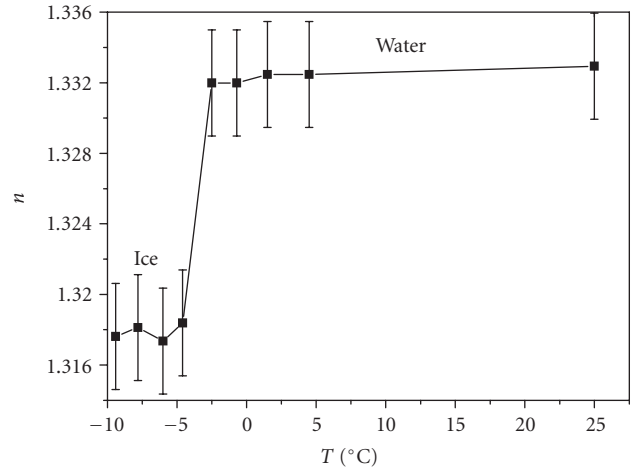


Figure 23: Refractive index measurement of the water and ice 1 H before, during, and after freezing [25].

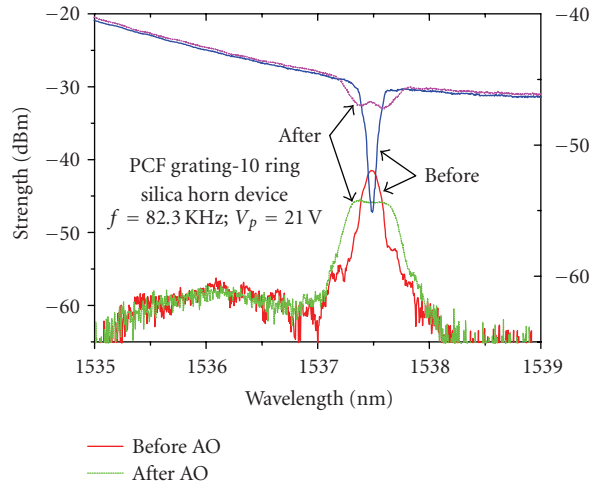


Figure 24: Transmission and reflection spectra of a uniform Bragg grating in a germanosilicate-doped core photonic crystal fibre with and without an applied acoustic wave with frequency ~82.3 kHz. At this frequency, a central phase shift is introduced and the band gap broadens. This change was sufficient to generate >10 dB signal contrast when switching a tuneable laser on and off [89].

## 7.4. Acoustic Tuning of PCF Gratings

Given the control over the cladding parameters, including the size and positioning of the holes, within a structured optical fibre another property which may be expected to differ is the generation and propagation of acoustic waves within the fibre. This has particular important applications within acoustic-based pressure and hydrophone sensors, including DFB fibre laser arrays in underwater detection of seismic waves, enemy submarine and naval craft, and more. It is, therefore, of note that the first recent reports of acoustic waves in photonic crystal fibre involved Bragg

gratings inscribed into the fibres for these applications [89–91]. A tuneable Moire grating was demonstrated for the first time [89] by having an acoustic standing wave established over the Bragg grating which leads to bandwidth broadening and a phase-shifted structure as shown in Figure 22. Further work is underway to explore the potential of structured fibres in enhancing and controlling these properties.

## 8. Conclusions

Considerable work has already been carried out in the inscription of Bragg gratings and other structures within structured optical fibres. Both positive and negative index gratings in Type I regime (below the damage threshold [22]) are easily demonstrated and unsurprising within structure fibres containing standard photosensitive cores. However, the control and refinement of this writing process is considerably more difficult as a result of the rotational variance of the optical fibre. Progress in this direction has led to a considerable improvement in the reliable inscription of gratings. More challenging, but in many ways far more important, has been the inscription of higher-exponent photon gratings, including densification and damage gratings, that do not rely on accessing defects so that much of the advantages of structured fibres, including single-material fibres with no temperature dependence arising from differences in expansion coefficients. Some of the distinct advantages of structured fibres have been argued from the perspective of the grating itself. Gratings act as both a critical diagnostic interferometer and as an important spectrally selective component to further extend these advantages in much the same way gratings have, and continue, to extend conventional optical fibre. Applications are liberal spanning from telecommunications, lasers, sensors, and diagnostics.

## Acknowledgments

The authors would like to acknowledge various students, staff, and colleagues, both local (Andrew Michie and Mattias Aslund from IPL, Sydney University, Graham Marshall, Nem Jovanovic et al. from Macquarie University; Shane Huntington et al. from Melbourne University) and overseas (Henrick Sorenson, Hans Deyerl, Martin Kristensen et al. from Research Centre COM, Danish Technical University; Matthieu Lancry and Bertrand Poumellec, Universide de Paris Sude, France), who have contributed over recent years to some aspects of the described work. Funding for this work came from the Australian Research Council and the Department of Education, Science and Training (DEST), Australia. Cicero Martelli acknowledges a CAPES, Brazil Student scholarship, and Somnath Bandyopadhyay acknowledges a Raman Research Fellowship of CSIR, India for his stay in Australia.

## References

[1] P. Kaiser and H. W. Astle, "Low-loss single-material fibers made from pure fused silica," *Bell System Technical Journal*, vol. 53, no. 6, pp. 1021–1039, 1974.

[2] A. Bjarklev, J. Broeng, and A. S. Bjarklev, *Photonic Crystal Fibres*, Kluwer Academic Publishers, Boston, Mass, USA, 2003.

[3] J. Canning, "Fresnel optics inside optical fibres," in *Photonics Research Developments*, chapter 4, Nova Science, Huntington, NY, USA, 2008.

[4] H. R. Sørensen, J. Canning, J. Lægsgaard, K. Hansen, and P. Varming, "Liquid filling of photonic crystal fibres for grating writing," *Optics Communications*, vol. 270, no. 2, pp. 207–210, 2007.

[5] J. Canning, S. K. Lim, T. K. Yip, and C. Martelli, "New device functionality within structured optical fibres by selective filling," in *Proceedings of the Joint Conference on Opto-Electronics and Communications Conference and the Australian Conference on Optical Fibre Technology (ACOFT/OECC '08)*, Sydney, Australia, July 2008.

[6] C. Martelli, J. Canning, J. R. Reimers, M. Sintic, D. Stocks, and M. J. Crossley, "Evanescent field spectroscopy using structured optical fibres: detection of charge-transfer at the porphyrin-silica interface," submitted to *Journal of the American Chemical Society*.

[7] B. J. Eggleton, P. S. Westbrook, R. S. Windeler, S. Spälter, and T. A. Strasser, "Grating resonances in air-silica microstructured optical fibers," *Optics Letters*, vol. 24, no. 21, pp. 1460–1462, 1999.

[8] H. R. Sørensen, J. Canning, J. Lægsgaard, K. Hansen, and P. Varming, "Liquid filling of photoniccrystal fibres for grating writing," *Optics Communications*, vol. 270, no. 2, pp. 207–210, 2007.

[9] V. Beugin, L. Bigot, P. Niay, et al., "Efficient Bragg gratings in phosphosilicate and germanosilicate photonic crystal fiber," *Applied Optics*, vol. 45, no. 32, pp. 8186–8193, 2006.

[10] L. B. Fu, G. D. Marshall, J. A. Bolger, et al., "Femtosecond laser writing Bragg gratings in pure silica photonic crystal fibres," *Electronics Letters*, vol. 41, no. 11, pp. 638–640, 2005.

[11] M. C. Phan Huy, G. Laffont, Y. Frignac, et al., "Fibre Bragg grating photowriting in microstructured optical fibres for refractive index measurement," *Measurement Science and Technology*, vol. 17, no. 5, pp. 992–997, 2006.

[12] G. Violakis and S. Pissadakis, "Improved efficiency Bragg grating inscription in a commercial solid core microstructured optical fiber," in *Proceedings of the 9th International Conference on Transparent Optical Networks (ICTON '07)*, vol. 2, pp. 217–220, Rome , Italy, July 2007.

[13] J. Albert, M. Fokine, and W. Margulis, "Grating formation in pure silica-core fibers," *Optics Letters*, vol. 27, no. 10, pp. 809–811, 2002.

[14] N. Groothoff, J. Canning, E. Buckley, K. Lyttikainen, and J. Zagari, "Bragg gratings in air-silica structured fibers," *Optics Letters*, vol. 28, no. 4, pp. 233–235, 2003.

[15] N. Groothoff, C. Martelli, J. Canning, and K. Lyytikainen, "Fibre Bragg grating in Fresnel fibre with temperature and strain characterisation," in *Proceedings of the 30th Australian Conference on Optical Fibre Technology (ACOFT '05)*, Sydney, Australia, July 2005.

[16] J. Canning, N. Groothoff, E. Buckley, T. Ryan, K. Lyytikainen, and J. Digweed, "All-fibre photonic crystal distributed Bragg reflector (PC-DBR) fibre laser," *Optics Express*, vol. 11, no. 17, pp. 1995–2000, 2003.

[17] N. Groothoff, J. Canning, T. Ryan, K. Lyytikainen, and H. Inglis, "Distributed feedback photonic crystal fibre (DFB-PCF) laser," *Optics Express*, vol. 13, no. 8, pp. 2924–2930, 2005.

[18] N. Groothoff, C. Martelli, and J. Canning, "A dual wavelength distributed-feedback fiber laser," *Journal of Applied Physics*, vol. 103, no. 1, Article ID 013101, 6 pages, 2008.

[19] J. Canning, S. D. Jackson, M. L. Åslund, N. Groothoff, B. Ashton, and K. Lyytikainen, "Air-clad fibre laser with internal Bragg grating," *Electronics Letters*, vol. 41, no. 20, pp. 1103–1104, 2005.

[20] N. Groothoff, J. Canning, N. Jovanovic, G. D. Marshall, and M. J. Whitford, "Gratings in large diameter air-clad optical fibre using a femtosecond laser," in *Proceedings of the OSA Topical Meeting: Bragg Gratings, Photosensitivity and Poling (BGPP '07)*, Quebec City, Canada, September 2007.

[21] S. J. Mihailov, D. Grobnic, H. Ding, C. W. Smelser, and J. Broeng, "Femtosecond IR laser fabrication of Bragg gratings in photonic crystal fibers and tapers," *IEEE Photonics Technology Letters*, vol. 18, no. 17, pp. 1837–1839, 2006.

[22] J. Canning, "Fibre gratings and devices," in *Lasers and Photonics Reviews*, John Wiley & Sons, New York, NY, USA, 2008.

[23] C. Martelli, J. Canning, B. Gibson, and S. Huntington, "Cryptography based on coherent scattering of light," in *Proceedings of the Joint International Conference on Optical Internet and the 32nd Australian Conference on Optical Fibre Technology (COIN-ACOFT '07)*, pp. 1–3, Melbourne, Australia, June 2007.

[24] R. C. Gauthier, "Photonic quasi-crystals: a review," in *Proceedings of the Progress in Electromagnetics Research Symposium (PIERS '08)*, p. 151, Hangzhou, China, March 2008.

[25] C. Martelli, J. Canning, M. Kristensen, and N. Groothoff, "Refractive index measurement within a photonic crystal fibre based on short wavelength diffraction," *Sensors*, vol. 7, no. 11, pp. 2492–2498, 2007.

[26] J. De Iuliis, "Modelling the angular dependence on Bragg grating writing in photonic crystal fibre," Student Practical Optical Design Report, University of Newcastle, 2006.

[27] G. D. Marshall, D. J. Kan, A. A. Asatryan, L. C. Botten, and M. J. Withford, "Transverse coupling to the core of a photonic crystal fiber: the photo-inscription of gratings," *Optics Express*, vol. 15, no. 12, pp. 7876–7887, 2007.

[28] J. Canning, "Gratings and grating devices in structured fibres using 193 nm from an ArF laser," in *Proceedings of the OSA Topical Meeting: Bragg Gratings, Photosensitivity and Poling (BGPP '07)*, Quebec City, Canada, September 2007.

[29] J. L. Holdsworth, J. Canning, and C. Dewhurst, "Rotational dependence of laser light accessing photonic crystal fibre cores from the side," in *Proceedings of the 19th International Conference on Optical Fibre Sensors*, D. Sampson, S. Collins, K. Oh, and R. Yamauchi, Eds., vol. 7004 of *Proceedings of SPIE*, pp. 1–4, Perth, Australia, April 2008.

[30] J. Holdsworth, S. Bandyopadhyay, J. Canning, M. Stevenson, and J. de Iuliis, "Transversely illuminating the core of photonic crystal fibres," in *Proceedings of the Joint Conference of the Opto-Electronics and Communications Conference and the Australian Conference on Optical Fibre Technology (OECC/ACOFT '08)*, Sydney, Australia, July 2008.

[31] J. Holdsworth, K. Cook, J. Canning, S. Bandyopadhyay, and M. Stevenson, "Rotationally variant grating writing in photonic crystal fibres," submitted to *Optics Express*.

[32] A. P. Mosk, "Focussing of light by disordered metamaterials," in *Proceedings of the Progress in Electromagnetics Research Symposium (PIERS '08)*, p. 741, Hangzhou, China, March 2008.

[33] K. Cook, A. Pohl, and J. Canning, "Positive and negative index gratings in 10-ring photonic crystal fibres with germanosilicate cores using 193 nm," in *Proceedings of the Joint Conference of the Opto-Electronics and Communications Conference and the Australian Conference on Optical Fibre Technology (OECC/ACOFT '08)*, Sydney, Australia, July 2008.

[34] K. Cook, A. Pohl, and J. Canning, "Type IIA gratings in hydrogen-free 10-ring photonic crystal fibre with germanosilicate core," submitted to *Optics Letters*.

[35] N. Groothoff and J. Canning, "Enhanced type IIA gratings for high-temperature operation," *Optics Letters*, vol. 29, no. 20, pp. 2360–2362, 2004.

[36] J. Canning, K. Sommer, M. Englund, and S. Huntington, "Direct evidence of two types of UV-induced glass changes in silicate-based optical fibers," *Advanced Materials*, vol. 13, no. 12-13, pp. 970–973, 2001.

[37] H. Sorensen, J. B. Jensen, F. Bruyere, and K. P. Hansen, "Practical hydrogen loading of air silica fibers," in *Bragg Gratings Photosensitivity and Poling in Glass Waveguides*, Trends in Optics and Photonics Series, Optical Society of America, Washington, DC, USA , 2005.

[38] D. Káčik, I. Turek, I. Martinček, J. Canning, N. A. Issa, and K. Lyytikäinen, "Intermodal interference in a photonic crystal fibre," *Optics Express*, vol. 12, no. 15, pp. 3465–3470, 2004.

[39] A. Pohl, K. Cook, and J. Canning, "Bragg grating writing in $H_2$-loaded many-layered PCF without liquid filling of the holes," in *Proceedings of the Joint Conference of the Opto-Electronics and Communications Conference and the Australian Conference on Optical Fibre Technology (OECC/ACOFT '08)*, Sydney, Australia, July 2008.

[40] M. Janos and J. Canning, "Permanent and transient resonances thermally induced in optical fibre Bragg gratings," *Electronics Letters*, vol. 31, no. 12, pp. 1007–1009, 1995.

[41] A. Canagasabey, J. Canning, J. Mills, D. P. Banks, and M. Ibsen, "Fibre Bragg grating fabrication in germanosilicate fibres with 244 nm femtosecond laser light," in *Proceedings of the 2nd Pacific International Conference on Applications of Lasers and Optics (PICALO '06)*, Melbourne, Australia, April 2006.

[42] A. Wootton, B. Thomas, and P. Harrowell, "Radiation-induced densification in amorphous silica: a computer simulation study," *Journal of Chemical Physics*, vol. 115, no. 7, pp. 3336–3341, 2001.

[43] C. Martelli, J. Canning, M. Kristensen, and N. Groothoff, "Impact of water and ice 1h formation in a photonic crystal fiber grating," *Optics Letters*, vol. 31, no. 6, pp. 706–708, 2006.

[44] W. Primak, L. H. Fuchs, and P. Day, "Radiation damage in insulators," *Physical Review*, vol. 92, no. 4, pp. 1064–1065, 1953.

[45] W. Primak and H. Szymanski, "Radiation damage in vitreous silica: annealing of the density changes," *Physical Review*, vol. 101, no. 4, pp. 1268–1271, 1956.

[46] W. Primak and R. Kampwirth, "The radiation compaction of vitreous silica," *Journal of Applied Physics*, vol. 39, no. 12, pp. 5651–5658, 1968.

[47] C. Fiori and R. A. B. Devine, "Evidence for a wide continuum of polymorphs in *a*-$SiO_2$," *Physical Review B*, vol. 33, no. 4, pp. 2972–2974, 1986.

[48] M. Lancry and B. Poumellec, "Multiphoton absorption processes & UV laser processing of silica-based materials," in *Proceedings of the 1st International Workshop on Multiphoton Processes in Glass and Glassy Materials*, J. Canning, Ed., Sydney, Australia, December 2006.

[49] N. Groothoff, M. Lancry, B. Poumellec, and J. Canning, "193 nm photolytic mechanism in Er/Al doped silica," in *Proceedings of the Joint Conference on Opto-Electronics and Communications Conference and the Australian Conference*

*on Optical Fibre Technology (ACOFT/OECC '08)*, Sydney, Australia, July 2008.

[50] M. Lancry, N. Groothoff, B. Poumellec, and J. Canning, "Two-photon grating writing in Er/Al doped preform plates using 193 nm laser light," In preparation.

[51] A. Dragomir, D. N. Nikogosyan, K. A. Zagorulko, P. G. Kryukov, and E. M. Dianov, "Inscription of fiber Bragg gratings by ultraviolet femtosecond radiation," *Optics Letters*, vol. 28, no. 22, pp. 2171–2173, 2003.

[52] S. J. Mihailov, C. W. Smelser, P. Lu, et al., "Fiber Bragg gratings made with a phase mask and 800-nm femtosecond radiation," *Optics Letters*, vol. 28, no. 12, pp. 995–997, 2003.

[53] K. A. Zagorulko, P. G. Kryukov, Yu. V. Larionov, et al., "Fabrication of fiber Bragg gratings with 267 nm femtosecond radiation," *Optics Express*, vol. 12, no. 24, pp. 5996–6001, 2004.

[54] A. Martinez, M. Dubov, I. Khrushchev, and I. Bennion, "Direct writing of fibre Bragg gratings by femtosecond laser," *Electronics Letters*, vol. 40, no. 19, pp. 1170–1172, 2004.

[55] C. W. Smelser, S. J. Mihailov, D. Grobnic, et al., "Multiple-beam interference patterns in optical fiber generated with ultrafast pulses and a phase mask," *Optics Letters*, vol. 29, no. 13, pp. 1458–1460, 2004.

[56] C. W. Smelser, S. J. Mihailov, and D. Grobnic, "Hydrogen loading for fiber grating writing with a femtosecond laser and a phase mask," *Optics Letters*, vol. 29, no. 18, pp. 2127–2129, 2004.

[57] C. W. Smelser, S. J. Mihailov, and D. Grobnic, "Formation of type I-IR and type II-IR gratings with an ultrafast IR laser and a phase mask," *Optics Express*, vol. 13, no. 14, pp. 5377–5386, 2005.

[58] in *Proceedings of the 1st International Workshop on Multiphoton Processes in Glass and Glassy Materials*, J. Canning, Ed., Sydney, Australia, December 2006.

[59] C. G. Askins, T.-E. Tsai, G. M. Williams, M. A. Putnam, M. Bashkansky, and E. J. Friebele, "Fiber Bragg reflectors prepared by a single excimer pulse," *Optics Letters*, vol. 17, no. 11, pp. 833–835, 1992.

[60] M. L. Åslund, N. Jovanovic, N. Groothoff, et al., "Large diffractive scattering losses in the visible region produced by femtosecond laser written Bragg gratings," in *Proceedings of the Australian Conference on Optical Fibre Technology & Opto-Electronics and Communications Conference (ACOFT/OECC '08)*, Sydney, Australia, July 2008.

[61] M. L. Åslund, N. Jovanovic, N. Groothoff, et al., "Optical loss mechanisms in femtosecond laser-written point-by-point fibre Bragg gratings," *Optics Express*, vol. 16, no. 18, pp. 14248–14254, 2008.

[62] N. Jovanovic, M. L. Åslund, A. Fuerbach, S. D. Jackson, G. D. Marshall, and M. J. Withford, "Narrow linewidth, 100 W cw $Yb^{3+}$-doped silica fiber laser with a point-by-point Bragg grating inscribed directly into the active core," *Optics Letters*, vol. 32, no. 19, pp. 2804–2806, 2007.

[63] M. L. Åslund, S. D. Jackson, J. Canning, N. Groothoff, B. Ashton, and K. Lyytikainen, "High power $Yb^{3+}$ doped air-clad fibre laser using a Bragg grating written into the active medium," in *Proceedings of the 7th Australian Conference on Optics, Lasers and Spectroscopy (ACOLS '05)*, Roturua, New Zealand, December 2005, paper WeA2.

[64] M. L. Åslund, private communication, unpublished work, 2007.

[65] J. Arkwright, G. Atkins, Z. Brodzeli, et al., "All optical switching in rare-earth doped fibers," in *Proceedings of the Pacific Rim Conference on Lasers and Electro-Optics (CLEO/Pacific Rim '97)*, p. 265, Chiba, Japan, July 1997, paper FH1.

[66] E. N. Glezer and E. Mazur, "Ultrafast-laser driven micro-explosions in transparent materials," *Applied Physics Letters*, vol. 71, no. 7, pp. 882–884, 1997.

[67] K. Sugioka, Y. Cheng, and K. Midorikawa, "Three-dimensional micromachining of glass using femtosecond laser for lab-on-a-chip device manufacture," *Applied Physics A*, vol. 81, no. 1, pp. 1–10, 2005.

[68] J. W. Chan, T. R. Huser, S. H. Risbud, and D. M. Krol, "Modification of the fused silica glass network associated with waveguide fabrication using femtosecond laser pulses," *Applied Physics A*, vol. 76, no. 3, pp. 367–372, 2003.

[69] S. A. Slattery, D. N. Nikogosyan, and G. Brambilla, "Fiber Bragg grating inscription by high-intensity femtosecond UV laser light: comparison with other existing methods of fabrication," *Journal of the Optical Society of America B*, vol. 22, no. 2, pp. 354–361, 2005.

[70] L. Shah, A. Arai, S. Eaton, and P. Herman, "Waveguide writing in fused silica with a femtosecond fiber laser at 522 nm and 1 MHz repetition rate," *Optics Express*, vol. 13, no. 6, pp. 1999–2006, 2005.

[71] K. Digweed-Lyytikainen, C. A. De Francisco, D. Spadoti, et al., "Photonic crystal optical fibers for dispersion compensation and Raman amplification: design and experiment," *Microwave and Optical Technology Letters*, vol. 49, no. 4, pp. 872–874, 2007.

[72] M. L. Åslund, J. Canning, S. D. Jackson, A. Teixeira, and K. Lyytikäinen, "Diffraction in air-clad fibres," *Optics Express*, vol. 13, no. 14, pp. 5227–5233, 2005.

[73] M. L. Åslund, S. D. Jackson, J. Canning, A. Teixeira, and K. Lyytikäinen-Digweed, "The influence of skew rays on angular losses in air-clad fibres," *Optics Communications*, vol. 262, no. 1, pp. 77–81, 2006.

[74] C. Martelli, J. Canning, N. Groothoff, and K. Lyytikainen, "Strain and temperature characterization of photonic crystal fiber Bragg gratings," *Optics Letters*, vol. 30, no. 14, pp. 1785–1787, 2005.

[75] D. Káčik, I. Turek, I. Martinček, J. Canning, N. A. Issa, and K. Lyytikäinen, "Intermodal interference in a photonic crystal fibre," *Optics Express*, vol. 12, no. 15, pp. 3465–3470, 2004.

[76] C. Martelli, J. Canning, N. Groothoff, and K. Lyttikainen, "Bragg gratings in photonic crystal fibers: strain and temperature chacterization," in *17th International Conference on Optical Fibre Sensors*, M. Voet, R. Willsch, W. Ecke, J. Jones, and B. Culshaw, Eds., vol. 5855 of *Proceedings of SPIE*, pp. 302–305, Bruges, Belgium, May 2005.

[77] M. Janos and J. Canning, "Permanent and transient resonances thermally induced in optical fibre Bragg gratings," *Electronics Letters*, vol. 31, no. 12, pp. 1007–1009, 1995.

[78] H. R. Sørensen, J. Canning, J. Lægsgaard, and K. Hansen, "Control of the wavelength dependent thermo-optic coefficients in structured fibres," *Optics Express*, vol. 14, no. 14, pp. 6428–6433, 2006.

[79] O. V. Mazurin, M. V. Streltsina, and T. P. Shvaiko-shvaikovskaya, Eds., *Handbook of Glass Data. Part A. Silica Glass and Binary Silicate Glasses*, Elsevier, Amsterdam, The Netherlands, 1983.

[80] A. Michie, J. Canning, K. Lyytikäinen, M. L. Åslund, and J. Digweed, "Temperature independent highly birefringent photonic crystal fibre," *Optics Express*, vol. 12, no. 21, pp. 5160–5165, 2004.

[81] A. Michie, J. Canning, I. Bassett, et al., "Spun elliptically birefringent photonic crystal fibre," *Optics Express*, vol. 15, no. 4, pp. 1811–1816, 2007.

[82] D. Ferrarini, L. Vincetti, M. Zoboli, A. Cucinotta, and S. Selleri, "Leakage properties of photonic crystal fibers," *Optics Express*, vol. 10, no. 23, pp. 1314–1319, 2002.

[83] K. Lyytikäinen, *Control of complex structural geometry in optical fibre drawing*, Ph.D. thesis, School of Physics and Interdisciplinary Photonics Laboratories, The University of Sydney, Sydney, Australia, 2004.

[84] J. Canning, "Diffraction-free mode generation and propagation in optical waveguides," *Optics Communications*, vol. 207, no. 1–6, pp. 35–39, 2002.

[85] D. Káčik, I. Turek, I. Martinček, J. Canning, and K. Lyytikainen, "The role of diffraction in influencing the short wavelength loss edge of photonic crystal fibres," in *Proceedings of the 30th Australian Conference on Optical Fibre Technology (ACOFT '05)*, Sydney, Australia, July 2005.

[86] C. Martelli, J. Canning, B. Gibson, and S. Huntington, "Bend loss in structured optical fibres," *Optics Express*, vol. 15, no. 26, pp. 17639–17644, 2007.

[87] C. M. Rollinson, S. M. Orbons, S. T. Huntington, et al., "Near field characterisation of a nano-structured metamaterial with a metal-free optical fiber probe," submitted to *Nano Letters*.

[88] V. F. Petrenko and R. W. Whitworth, *Physics of Ice*, Oxford University Press, New York, NY, USA, 2002.

[89] A. A. P. Pohl, R. A. Oliveira, K. Cook, and J. Canning, "Modulation of a photonic crystal fibre Bragg grating induced by acoustical waves," submitted to *Optics Express*.

[90] A. A. P. Pohl, P. T. Neves Jr., R. A. Oliveira, M. Stevenson, N. Groothoff, and J. Canning, "Technique for estimating the tuning speed of fiber Bragg gratings," in *19th International Conference on Optical Fibre Sensors*, vol. 7004 of *Proceedings of SPIE*, Perth, Australia, April 2008.

[91] R. A. Oliveira, P. de T. Neves Jr., J. M. Maia, A. de A. P. Pohl, and J. Canning, "Modulação da Refletividade de Redes de Bragg usando Interação Acusto-Óptica de Baixa Freqüência," in *Proceedings of the 13 SBMO Brazilian Symposium on Microwave and Optoelectronics and 8th CBMag Brazilian Congress of Eletromagnetismo (MOMAG '08)*, pp. 396–398, Florianpolis, Brazil, September 2008.

Hindawi Publishing Corporation
Laser Chemistry
Volume 2008, Article ID 416251, 20 pages
doi:10.1155/2008/416251

*Review Article*

# Induced Bragg Gratings in Optical Fibers and Waveguides Using an Ultrafast Infrared Laser and a Phase Mask

**Stephen J. Mihailov, Dan Grobnic, Christopher W. Smelser, Ping Lu, Robert B. Walker, and Huimin Ding**

*Optical Communications and Electrophotonics Group, Communications Research Centre Canada, 3701 Carling Avenue, Ottawa, Ontario, Canada K2H 8S2*

Correspondence should be addressed to Stephen J. Mihailov, stephen.mihailov@crc.ca

Received 26 March 2008; Accepted 22 April 2008

Recommended by Saulius Juodkazis

Since its development in 2003, the technique of Bragg grating inscription in optical fibers and waveguides with ultrafast infrared radiation and a phase mask has proven to be as simple as the standard UV-laser grating writing techniques but far more versatile. The ultrafast IR laser-based process allows for the creation of grating structures in glassy and crystalline materials that are not typically UV photosensitive. In this article, we will review the studies that have been performed at the Communications Research Centre Canada on the grating formation processes as well as applications of the ultrafast laser technique to fabricate gratings in various optical fibers and waveguides.



## 1. Introduction

High-power femtosecond (fs) lasers systems are being used extensively for laser-material processing of glassy materials in order to fabricate microfluidic and photonic devices. The ultrahigh peak power infrared (IR) radiation generated by many of these systems has been used to induce large index changes in bulk glasses for the fabrication of imbedded waveguides and surface structures [1, 2]. In glass optical fiber, femtosecond laser systems have been used to induce large index changes and fabricate long-period fiber grating structures in a step-and-repeat fashion [3, 4].

The process of induced index change in bulk glasses resulting from femtosecond-IR laser exposure is thought to result from a multiphoton absorption/ionization process resulting in material compaction and/or defect formation depending on the intensity of the exposure [1]. Above the ionization threshold intensity $I$th, multiphoton ionization (MPI) induced dielectric breakdown likely results in localized melting and material compaction causing an index change that is permanent up to the glass transition temperature $t_g$, of the material. The value of $I$th is material-dependent.

Below $I$th, another regime of induced index change has been observed that can be erased by annealing with temperatures below the material $t_g$ [5]. In this regime, multiphoton absorption likely results in defect formation similar to that seen for ultraviolet—(UV-) induced index changes in photosensitive germanium doped silica glasses.

Laser induced index change is the key feature of most fiber Bragg grating (FBG) manufacturing. Typically FBGs are made by side exposure of the UV-sensitive fiber core to a spatially modulated UV laser beam. The modulated UV beam is typically created by interfering two or more UV beams using either a bulk interferometer or a zero-order-nulled phase mask [6]. For femtosecond systems, interferometric setups for generating beam modulation are nontrivial to align since path lengths of the interfering beams need to be matched to within the spatial location of the femtosecond-pulse [2], which for a 120-femtosecond pulse would be $\sim 36\,\mu$m. The phase mask technique solves the alignment problem since the optical path lengths of the

generated beams are automatically matched for an incoming beam that is at normal incidence to the mask.

Femtosecond UV laser inscriptions of fiber gratings using silica phase masks have been performed by a number of research groups [7–10]. Typically, silica-based fibers are placed in close proximity to the mask, and large index changes have been generated in suitably UV photosensitive waveguides. A limitation of this technique however is that lower pulse intensities need to be employed since high nonlinear absorption and group velocity dispersion would otherwise occur within the mask. Such nonlinear absorption reduces the amount of light transmitted through the mask that is available to induce an index change in the fiber and simultaneously degrades the phase mask with time.

Combining the ultrafast IR laser and the phase mask approach, we successfully demonstrated the efficient fabrication of retroreflecting FBGs in standard telecom and pure silica core single mode fibers [11, 12]. The technique has proven to be as simple as the standard UV-laser writing technique but is far more versatile as grating inscription is not limited to materials that are traditionally UV-photosensitive such as Ge-doped silica. Using the femtosecond-IR laser and the phase mask, we have successfully inscribed high index-modulation grating structures in pure silica core fibers [12], borosilicate glass waveguides [13], reverse proton exchange $LiNb0_3$ waveguides [14], sapphire optical fiber [15, 16], fluoride glass fibers [17], actively doped silica fibers [18], phosphate glass fibers [19], and pure silica photonic crystal fibers and tapers [20]. In this paper, we will summarize our investigations into the processes of ultrafast IR laser-induced FBGs with a phase mask along with many of the applications that have arisen from the use of this technique, such as direct fabrication of gratings through protective fiber coatings, fabrication of fiber laser cavities, and the fabrication of high-temperature-stable grating sensors.

## 2. Phase Mask Design

The phase masks used in these studies are similar to standard all-silica phase masks used for UV laser FBG inscription however the etch depth is optimized for operation in the near IR (800 nm) as opposed to the UV. Standard UV masks used for fabrication of C-band FBGs typically have mask pitches $\Lambda_m$ of $\sim 1.07\,\mu$m with good zero-order transmission suppression. The majority of the transmitted energy then couples into the $\pm 1$ orders generated by the mask. Even when optimized for operation at 800 nm, a mask pitch of $1.07\,\mu$m has considerable coupling of the incident energy into the zero-order due to the proximity of the irradiating wavelength to $\Lambda_m$ [11, 12]. Nevertheless, high-quality gratings can be inscribed using standard mask pitches as will be described below.

In addition to standard mask pitches, phase masks were fabricated with $\Lambda_m$ values that would produce higher-order Bragg resonances $\lambda_B$. At $\lambda_B$, the grating pitch in the fiber, $\Lambda_G$, is defined by $m\lambda_B = n_{\text{eff}}\Lambda_G$ where $m$ is the order number and $n_{\text{eff}}$ is the effective index of the fiber. As the process for ultrafast IR laser-induced index change is a nonlinear one, it was thought to be likely that higher-order mask pitches would easily produce Bragg resonances in the telecom band. Four phase masks were then produced by e-beam lithography with different pitches such that higher-order Bragg resonances occurred at 1550 nm within standard telecom *Corning SMF-28* fiber, namely 4.284, 3.213, 2.142, and $1.071\,\mu$m. Gratings with high index modulations, $\Delta n$, were easily written with each phase mask. Gratings written with the higher-order pitch phase masks (i.e., $>1.07\,\mu$m) had the additional advantage of having grating structures that were directly observable under a standard optical microscope.

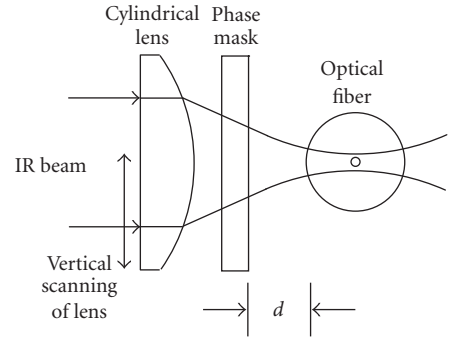


Figure 1: Schematic representation of lens-fiber-phase mask geometry for waveguide exposures.

## 3. Experimental Conditions

In these studies, Fourier transform limited 125 femtosecond duration laser pulses from a regeneratively amplified Ti: sapphire laser operating at 800 nm were used to illuminate optical fibers and waveguides by passing the irradiating beam through a cylindrical focusing lens and a phase mask as shown in Figure 1. Gaussian beam diameters incident on the focusing lens were typically 6.4 mm. Depending on the study that was being performed, pulse energies were varied between 0.2 and 2 mJ/pulse, repetition rates were varied from 1 to 1000 Hz, and various cylindrical focusing lenses were used ($f$ = 12 to 160 mm). When tight focusing geometries were used, it was found that vertical scanning of the irradiating beam across the waveguide normal to its axis eased alignment tolerances of the beam with respect to the waveguide core as well as allowed for the fabrication of many interesting grating structures. Typically, the incident beam was centered onto the fiber core and then scanned vertically over the fiber cross-section using a piezoactuated translation stage with a $\pm 10\,\mu$m travel and a 20-second period. The fiber-phase mask distance $d$ also proved to be a very important parameter as it would allow for the writing of pure two-beam interference gratings with a phase mask, even one possessing poor zero-order suppression. Grating spectra were typically measured using an $Er^+$ white light source and an optical spectrum analyzer or a tunable C-L band laser.

Annealing experiments of grating structures were typically performed in a Lindberg tube furnace equipped with an internal quartz tube of 2.54 cm diameter centered within the furnace tube. Gratings were loosely placed in the inner

tube so that no external stresses were applied to the grating. The experiments were performed in ambient air, and the heating rate was limited to 10°C/min. A swept tunable laser system was used to continually measure the grating spectral responses.

## 4. Ultrafast Laser-Induced Grating Processes

### 4.1. Phase Mask-Order Interference: Order Walk Off

Ultrafast laser pulses interact differently with phase masks as compared to nanoseconds pulses or continuous wave CW sources. The spatial localization of the ultrafast pulse envelope incident on the mask is small (~40 $\mu$m for a 125 femtosecond pulse). As the diffracted pulses produced by the mask propagate away from the mask surface, the propagation distance of each pulse, when projected onto the optical axis normal to the mask, appears different, as is shown in Figure 2(a). The diffracted pulse envelopes have different arrival times at a given distance $d$ normal to the mask. For sufficiently large $d$, the diffracted-order pairs (0, ±1, ±2, etc.) no longer overlap resulting in a diffracted-order walk-off effect (see Figure 2(b)). For a mask with $\Lambda_m = 3.213\,\mu$m and a 125 femtosecond pulse, the spatial separation of the ±1 order from the zero and ±2 orders would occur at fiber-mask distances $d > 1.3$ mm. As the induced index change using ultrafast IR radiation is highly nonlinear and highly localized within the target material, small $d$ values (i.e., near the mask) produce multiple-order complex interference field patterns within the waveguide [21]. For large $d$ values, the two-beam interference fringe patterns, caused by the diffracted-order walk-off effect, can be produced inside the waveguide with only the high-energy ±1 orders from the mask (see Figure 2(b)) [22]. A clear advantage of the walk-off effect is that for short pulses, the phase mask need not be zero-order suppressed to produce a two-beam interference pattern. Although not investigated here, it is likely that this remote writing process would also be advantageous for grating inscription with femtosecond UV sources. By using a tight focusing arrangement and a large displacement between the phase mask and fiber, the power densities and hence nonlinear absorption in the phase mask could be significantly reduced thus prolonging the life of the phase mask and allowing for higher power densities of UV light to interact with the fiber.

### 4.2. Type I-IR Versus Type II-IR

With the application of the order walk-off effect and vertical scanning of the beam across the waveguide axis, fabrication of gratings could be performed in a controlled way allowing for the study of grating formation processes below and above the ionization threshold $I$th. For femtosecond pulses interacting near the phase mask, the complex interference field resulting from multiple beam overlap, had high-peak intensities that would create gratings through an ionization process likely accentuated by self-focusing. This process

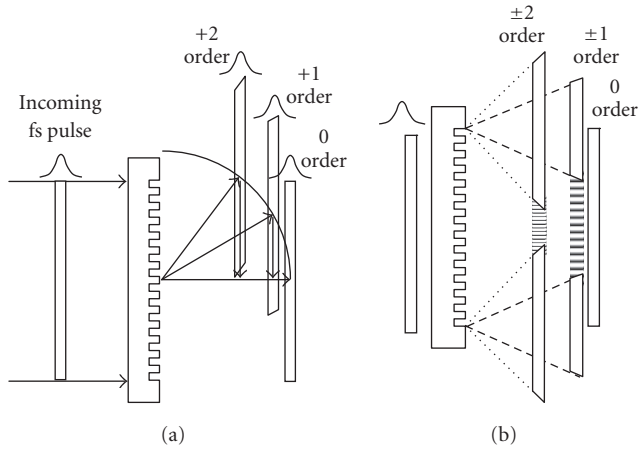


Figure 2: Schematic of diffractive order walk-off (a) pulse envelope projection normal to phase mask, (b) two-beam interference from each order pair.

produced gratings with the same pitch as the mask that were stable up to the glass transition temperature of the fiber. Sudrie et al. defined this intensity regime for index change in bulk silica glasses as type II [5]. In order to avoid confusion with type II UV-induced gratings, we defined this FBG formation regime as being type II-IR [23]. At greater distances from the mask, for the same pulse energy, the generated two-beam interference pattern had reduced peak intensities that did not traverse the threshold value for type II formation. Grating structures with high $\Delta n$'s were created after a more lengthy exposure that had a grating pitch that was half that of the mask.

To study the stability of the $\Delta n$ of the gratings written in the type I-IR and II-IR regimes, an isochronal annealing study was performed where the FBG temperature was increased in 100°C increments and held at each temperature for one hour. For comparison, a type I UV-induced FBG was inscribed in $H_2$-loaded *SMF-28* fiber (3000 psi, 85°C, 24 hours) using a frequency doubled argon-ion laser and a phase mask which produced a $\Delta n = 5 \times 10^{-4}$. The estimated initial $\Delta n$ for the femtosecond IR gratings was $1.5 \times 10^{-3}$. In Figure 3, the short-term performance of the UV and femtosecond IR FBGs with respect to temperature is presented where the initial $\Delta n$ of each of the FBGs is normalized to 1. With increasing temperature, the $\Delta n$ of the UV grating, denoted by the circles, decreases and completely disappears when the grating temperature approaches 1000°C. The annealing properties of the type I-IR FBG, denoted by black squares in Figure 3, are very similar to those of the type I UV gratings. For the fs type II-IR FBG, the reflectivity increased slightly up to 500°C and then remained stable. These annealing results suggest that the type I-IR gratings are due to a highly nonlinear defect formation process resulting from multiphoton absorption while the type II-IR gratings are "damage" gratings resulting from a multiphoton ionization process. The increase in the $\Delta n$ of the type II-IR grating with temperature is likely the result of annealing of less stable index change that occurs in the

less intense trough regions of the interference field. As the intensities in these regions are below $I$th, the index change is the result of a type I-IR process and is erased at elevated temperatures.

## 4.3. Type I-IR Scaling Behavior

Compared to techniques that measure femtosecond IR-induced index changes in bulk glasses, the technique of Bragg grating inscription in existing waveguides for measurement of index change is very sensitive thus allowing for the detection of index changes as small as $1 \times 10^{-6}$. A series of experiments were performed in Ge-doped *SMF-28* fiber using the setup shown in Figure 1 in order to determine the scaling behavior of the $\Delta n$ growth of a type I-IR grating as a function of the interference field intensity, where peak field intensity was directly related to the pulse energy [23]. The 6.4 mm diameter beam from the IR-laser was focused with a $f = 30$ mm focal length through the $\Lambda_m = 3.21\,\mu$m phase mask onto the fiber. The fiber was placed at distance $d = 5$ mm behind the mask to ensure two-beam interference. The pulse repetition rate of the laser was kept at 100 Hz. Several FBGs were then fabricated using the different pulse energies of 850, 900, 950, 1000, 1100, and 1200 $\mu$J. The transmission loss at $\lambda_B$ for each grating was continuously monitored. The spectra were then modeled using a commercial FBG software package.

The growth of $\Delta n$ as a function of exposure time and pulse energy is presented in Figure 4(a) as well as the scaling behavior as a function of energy, which is presented in Figure 4(b). Linear regression of the logarithm of the scaling behavior versus the logarithm of the pulse energy yields a slope of 5, meaning that the absorption process involved in the index growth scales with the fifth power of the peak intensity of the interference field $I^5$. A fifth power dependency on intensity suggests that the absorption process is a 5-photon one.

The 800 nm wavelength or 1.55 eV photon energy of the ultrafast IR source is far removed from the typical bandgap of Ge-doped silica, which is thought to be ~7.1 eV [24]. A 5-photon absorption process amounting to 7.75 eV has sufficient energy to bridge the 7.1 eV bandgap of the Ge-doped silica. Similar annealing behavior between the type I-IR and type I-UV gratings also suggests that a similar defect and/or compaction related mechanism of induced index change may be occurring in the type I-IR FBGs.

## 4.4. Hydrogen Loading

The possibility that a similar mechanism of induced index change was occurring in the Ge-doped fibers for both type I-UV and type I-IR FBGs suggested that fiber photosensitization processes used for UV exposures such as high Ge-core content of the waveguide or hydrogen loading [25] might also enhance type I-IR grating formation in Ge-doped fibers. As femtosecond-IR exposures of Ge-doped bulk silica generate GeE' and germanium-oxygen-deficient centers [1], FBG formation threshold intensity reduction with $H_2$-loading may result from a similar mechanism as seen in UV-induced

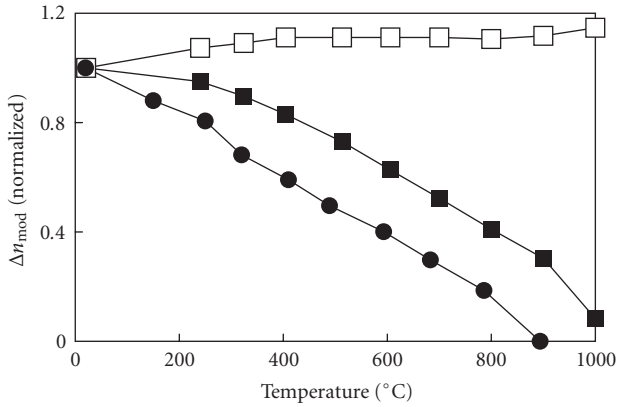


Figure 3: Short-term annealing of type II-IR (white square), type I-IR (black square), type I-UV (black cirlce), grating held at each temperature for 1 hour.

index changes. Increased UV-photosensitivity due to $H_2$-loading of Ge-doped silica is likely due to higher formation rates of GeE' centers through photoinduced reactions of $H_2$ with Ge-$SiO_2$ [26]. This may be the case in the femtosecond-IR regime as well. Another series of experiments were then performed to determine if there was a variation in the threshold pulse energies needed to induce a $\Delta n$ in standard telecom Ge-doped fibers when loaded with high-pressure hydrogen. For comparison, measurements of the threshold intensity for grating inscription in unloaded Ge-doped fibers as well as loaded and loaded pure silica core single mode fibers were also performed [27]. Fibers were $H_2$-loaded at 85°C, 3000 psi for 24 hours.

While no variation in the intensity threshold for grating formation was observed in either the $H_2$-loaded or unloaded all-silica core single mode fiber, the threshold intensity in the case of the *SMF-28* fiber was reduced by a factor of 3. For comparison, isochronal annealing studies were preformed on UV-induced and ultrafast-IR-induced FBGs written in $H_2$-loaded *SMF-28* fiber. Temperatures were increased in 100°C increments and allowed to stabilize for one hour. The annealing curves of low- and high-reflectivity gratings induced with either a frequency doubled UV $Ar^+$ laser or the femtosecond-IR laser show similar responses to temperature (see Figure 5). For the FBG's reported in [27], no broadband IR absorption due to the formation of Ge-OH defects had been observed. In subsequent experiments however that were not previously reported, the induction of high $\Delta n = 5 \times 10^{-3}$ in $H_2$-loaded *SMF-28* fibers did in fact result in the formation of the Ge-OH absorption band in the 1400 nm range suggesting that the photosensitivity enhancement due to hydrogen for ultrafast IR may have similar mechanisms as those that occur for UV exposures.

## 4.5. Modeling Nonlinear Index Change: the Rouard Method

Typically, the modeling of UV-induced gratings using coupled mode theory, the matrix method or Rouard's method

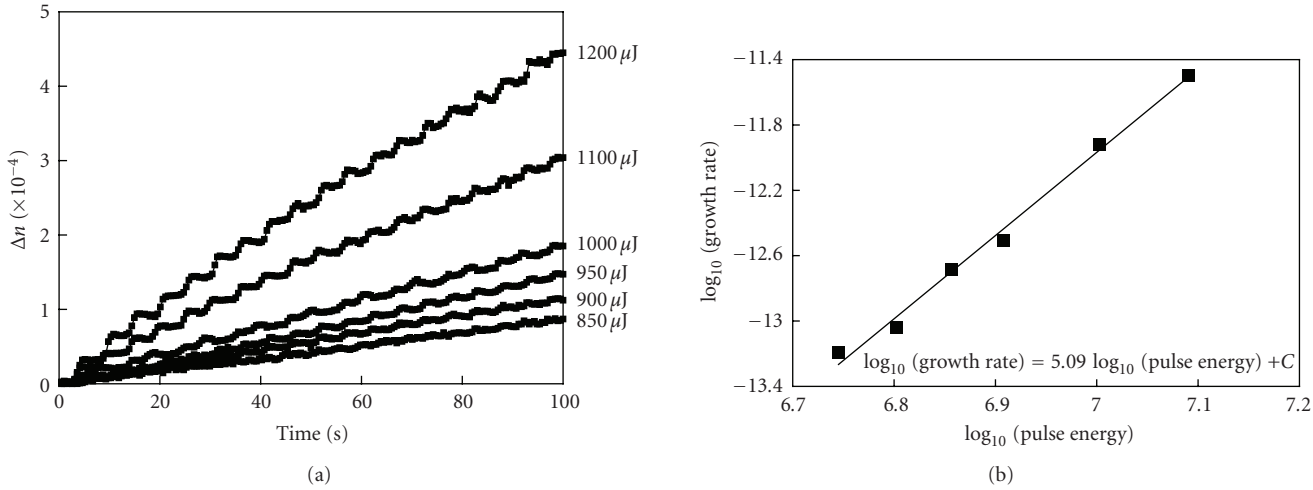


Figure 4: (a) Growth of the index modulation as a function of time and pulse energy. (b) Scaling behavior of the $\Delta n$ growth rate as function of energy.

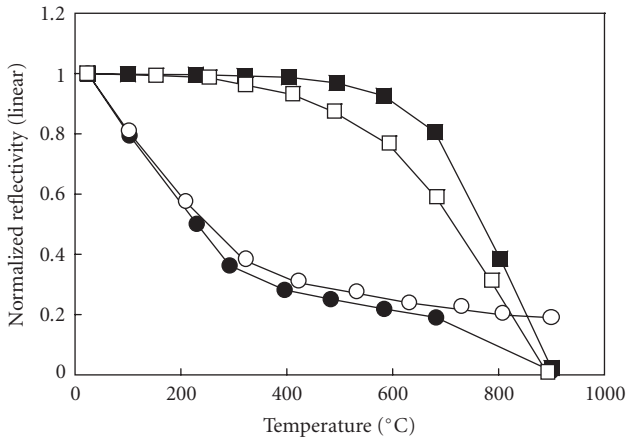


Figure 5: Isochronal annealing curves of low- (circles, $\Delta n \sim 10^{-5}$) and high- (squares, $\Delta n \sim 10^{-3}$) reflectivity FBGs written in $H_2$-loaded *SMF-28* fiber with CW UV laser light (white shape) or femtosecond-IR laser light (black shape).

assumes that the $\Delta n$ is sinusoidal in nature [28]. As the process for type I-IR-induced index change has been shown to be highly nonlinear, this assumption is no longer valid. In order to model the type I-IR FBG spectral responses the nonsinusoidal nature of the induced $\Delta n$ needs to be taken into account.

Rouard's method is an effective technique for modeling an arbitrary index profile [29–31] in a waveguide. By using Rouard's method to model ultrafast IR FBG grating responses, the nonsinusoidal nature of the type I-IR $\Delta n$ was taken into account by subdividing individual fringe planes into a series of Fresnel reflections [32]. This technique proved to be quite powerful as it automatically generated for example, higher-order Bragg resonances when a nonsinusoidal $\Delta n$ was considered. Such higher-order Bragg resonances occur when the $\Delta n$ deviates from a sinusoidal profile [33]. The model also provided subtle insight into variations of growth rates of $\Delta n$ as a function of incident intensity. For peak fringe intensities in *SMF-28* fiber that were above the threshold for grating formation but well below those that would produce a type II-IR grating, the spectral response was most accurately modeled using an $I^6$ scaling of the $\Delta n$ (see Figure 6) [32].

For fringe intensities that were approaching the type II-IR threshold, saturation in the growth rate of the $\Delta n$ is observed which results in a more "top-hat" like modulation profile. The spectral response was most accurately modeled using a saturation function for the normalized $\Delta n$ where

$$\Delta n_{\text{norm}} = \frac{I^6}{C + I^6}, \tag{1}$$

and $C$ is a constant equaling 0.05. Figure 7 presents the experimental result along with modeled response [32]. Limiting behavior and intensity clamping are common in highly nonlinear absorption processes and may be responsible for this observed saturation effect [34].

## 4.6. High-Order Spectral Response Characteristics

We have shown that the five-photon absorption process associated with the type I-IR gratings results in a $\Delta n$ profile that is nonsinusoidal. Unlike UV laser-induced gratings, which in the absence of saturation of the index change have only one Bragg resonance, the type I-IR gratings possess a number of higher-order Bragg resonances [35].

If the index modulation along the grating in the waveguide no longer follows a sinusoidal profile, $\Delta n(z)$ can be expanded as a Fourier series [33, 36]:

$$\Delta n(z) = \frac{\Delta n_0}{2} + \sum_{m=1}^{\infty} \Delta n_m \cos\left(\frac{2m\pi z}{N\Lambda_G}\right), \tag{2}$$

where $m$ is the order number, $N\Lambda_G$ is the grating periodicity in the waveguide that is an integer number $N$ multiplied by

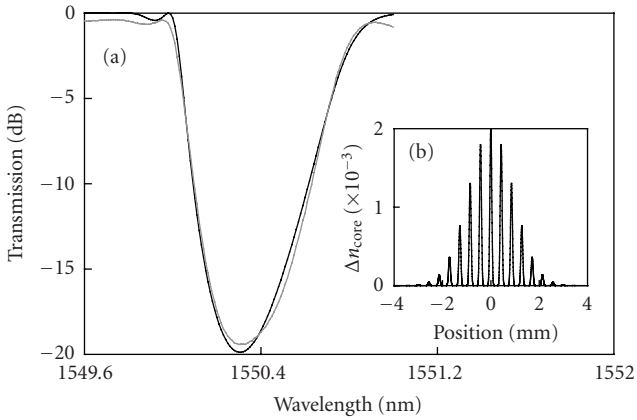


Figure 6: Comparison of modeled (black) and experimental (gray) spectra for an irradiation intensity below the type I-IR to type II-IR transition ($2.7 \times 10^{13}$ W/cm$^2$). Inset is the $\Delta n$ profile used to model the spectrum; fringe spacing is not to scale in figure.

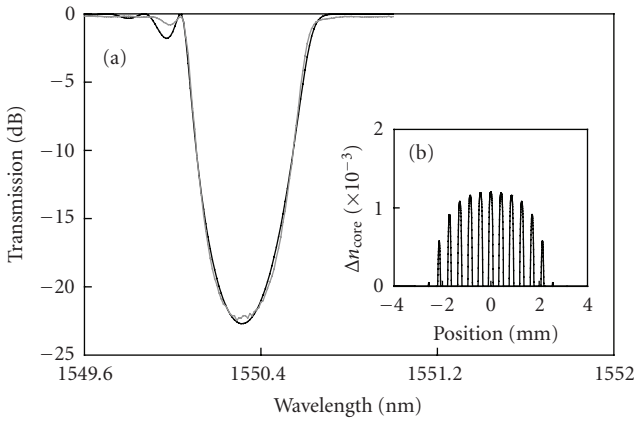


Figure 7: Comparison of experimental (black) and modeled (gray) spectra for an irradiation intensity approaching the type I-IR to type II-IR transition ($4 \times 10^{13}$ W/cm$^2$). Inset is the index modulation profile used to model the spectrum; fringe spacing is not to scale in figure.

the first-order grating pitch. $\Lambda_G$ and $\Delta n_m$ are the Fourier coefficients of order $m$. $\Delta n_0$ is the index change averaged over the length of the grating and is often associated with the wavelength shift of the Bragg resonance $\lambda_B$.

In [36], the evaluation of the Fourier components associated with each grating mask was determined for the order resonance that occurred in the 1550 nm wavelength range for both unloaded and $H_2$-loaded *SMF-28* telecommunication fiber, for example the 1550 nm resonance of a grating made with the 4.28 $\mu$m phase mask using the two-beam interference technique corresponds to the $\Delta n_4$ Fourier component. By monitoring the wavelength shift that occurred while inscribing gratings of a specific reflectivity with each of the phase masks pitched 1.071, 2.142, 3.213, and 4.284 $\mu$m, respectively, the relative amplitudes for the Fourier coefficients were determined (see Figure 8).

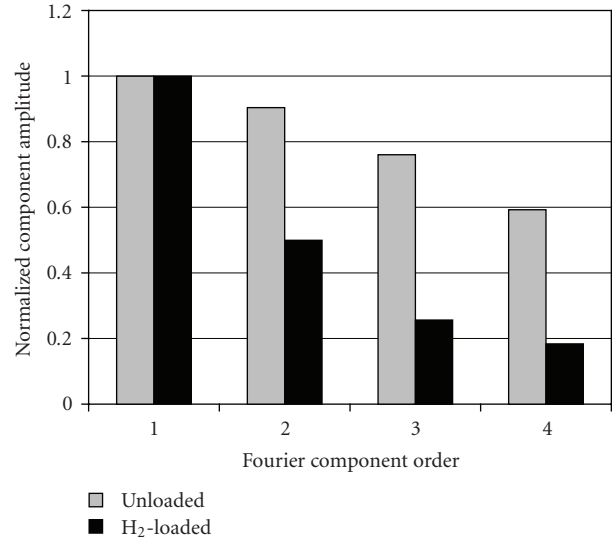


Figure 8: Comparison of the Fourier components for the pristine and hydrogen-loaded *SMF-28* fiber. The magnitude of the first-order component has been set to 1.

Using pulse intensities that were below the threshold for grating formation in unloaded fiber, the Fourier components of gratings written in $H_2$-loaded *SMF-28* fiber are consistent with those that would be achieved through a 5-photon distortion of the sinusoidal modulation. For gratings in unloaded fiber written with intensities mid-way between the type I-IR threshold and the type II-IR threshold, the Fourier components are consistent with a modulation profile that is squarer.

For gratings written in the type II-IR regime, the induced index change is no longer the result of a multiphoton absorption process but a multiphoton ionization process resulting in localized damage. Using a *Corning 980* Flexcore-fiber with a cutoff wavelength of 980 nm, and the 4.28 $\mu$m pitched phase mask, the induced type II-IR grating generates a large number of higher-order Bragg resonances in the 1000–1800 nm range, many with almost equal coupling; see Figure 9. This suggests that in the type II-IR regime the induced index modulation has a much more square profile than does the 5-photon absorption related profile.

## 5. Applications of Ultrafast Induced Bragg Gratings in Optical Fiber and Aaveguides

### 5.1. Cladding Mode Suppression

An important application of FBG technology is for high reflectivity narrowband reflectors in wavelength-division multiplexing (WDM) systems of optical networks. Such FBGs typically suffer from an out-of-band loss on the short wavelength side of the Bragg resonance which is due to strong coupling from the forward propagating core mode ($LP_{01}$) into discrete backward-propagating cladding modes [37]. Cladding mode coupling is caused by a mismatch in the overlap between the $LP_{01}$ mode and the fiber core in

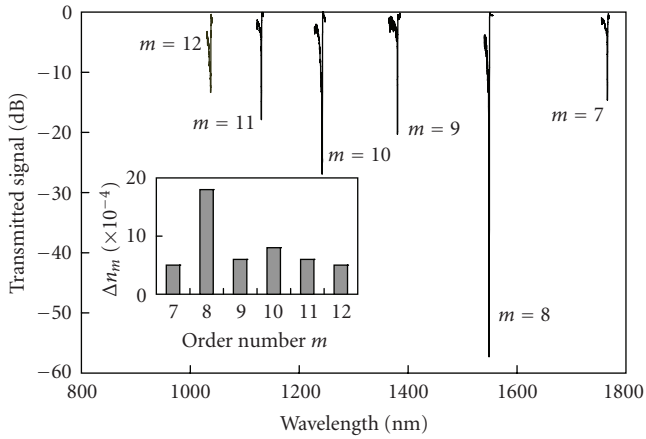


Figure 9: Transmission spectrum of a type II-IR grating written in 980 nm cutoff single mode fiber with the 4.28 $\mu$m pitched phase mask. Inset depicts the calculated index modulations of each of the diffracted orders assuming that they were the fundamental resonance.

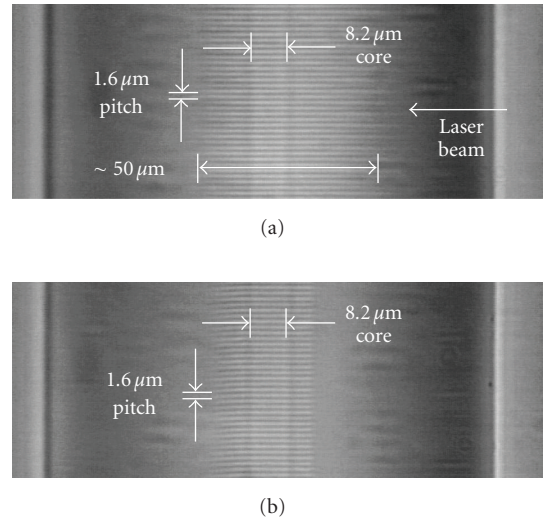


Figure 10: Microscope images of photoinduced index modulation in *SMF-28*; (see Figure 10(a)). The fiber is imaged near the core and is viewed normal to the beam axis. In Figure 10(b) the fiber is rotated 90° and is viewed along the beam axis.

which the FBG is inscribed. To suppress cladding mode coupling, specialty fibers were developed which possessed UV-sensitive cladding as well as core regions. When the FBG was inscribed uniformly across both photosensitive regions of the fiber-cross section where the $LP_{01}$ mode had nonzero power, coupling to cladding modes was eliminated [38]. The major drawback of this technique was that these specialty fibers are costly to produce, and fiber photosensitivity also needed to be enhanced by $H_2$-loading.

Initial FBG inscriptions with the femtosecond-IR laser and the phase mask showed that structures could be written with almost equal ease in either all-silica core or Ge-doped silica core fibers without $H_2$-loading [12]. By implementing the order-walk effect and beam scanning, high-quality gratings were inscribed in both the core and cladding region of standard *SMF-28* fiber in such a way that the $LP_{01}$ mode was completely subtended by grating structure in the core and cladding (see Figure 10). This resulted in an almost complete suppression of the coupling into cladding modes as shown in Figure 11 [39]. In [39], a third-order grating with $\Lambda_G = 1.6\,\mu$m was used in order to observe the structure directly under an optical microscope. Similar FBGs written at the fundamental grating pitch of $\Lambda_G = 0.535\,\mu$m also demonstrated excellent cladding mode suppression but the structure could not be directly observed under the optical microscope as in Figure 10.

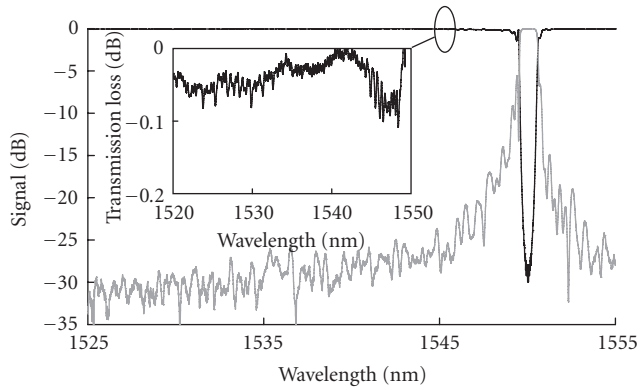


Figure 11: Transmission of cladding mode suppressed grating in *SMF-28* shown in Figure 10. Inset figure shows the cladding mode loss expressed as difference between the transmission spectrum and 1-R reflection spectrum.

## 5.2. Writing through the Fiber Jacket

Standard UV-laser inscription processes of FBGs typically require the removal of the protective polymer coating prior to exposure as these coatings usually are highly absorbing in the UV. Coating removal and replacement are time-consuming processes that threaten the mechanical integrity of the fiber and are therefore undesirable from a manufacturing viewpoint.

Recently, FBG inscription through the standard polymer coating of a fiber was reported using femtosecond-IR radiation and the point-by-point method [40] where the tight focusing geometry was able to produce a large intensity differential between the fiber coating and the fiber core. Substantial $\Delta n$ values were induced in the core without damaging the coating ($\Delta n = 3 \times 10^{-4}$).

Using the femtosecond-IR laser and the phase mask technique, FBGs were successfully inscribed through the acrylate coating of standard *SMF-28* fiber, when the fiber had been loaded with hydrogen [41]. A tight focusing lens was used with a focal length $f = 12$ mm, but with the fiber placed at distance $d = 1$ mm behind the 1.071 $\mu$m phase mask which resulted in a fundamental period grating in the fiber of 0.5355 $\mu$m when irradiated with 400 $\mu J$ and

125 femtoseconds pulses. The resultant FBG had a $\Delta n = 3.5 \times 10^{-4}$.

Under identical exposure conditions (100 Hz, 20 seconds cycle of $\pm 10\,\mu$m beam sweep and pulse energies of $220\,\mu$J), grating growth as a function of time was compared for gratings written through the acrylate coating of the $H_2$-loaded *SMF-28* with growth rates obtained when the loaded *SMF-28* fiber had been chemically stripped. In Figure 12(a), significant grating growth is initially observed for FBGs written through the jacket. However after ~5 minutes exposure, no further increase in $\Delta n$ was observed. For the stripped fiber, the grating growth continues even after a 90-minute exposure (see Figure 12(b)). Observation of the exposed region of the polymer jacket under the microscope revealed some damage to the jacket surface. Several femtosecond IR laser-based ablation studies of polymeric materials have shown that the threshold for induced index change and polymer ablation decreases with the number of incident pulses [42, 43]. It is likely that the first several hundred pulses incident on the acrylate polymer coating are creating "incubation sites" that eventually reduce the transmission of the IR radiation through the jacket thus limiting the $\Delta n$ growth. Using an optical fiber pull tester (Vytran PTR-100), the breakage strength was compared to pristine *SMF-28* fiber. For the 5 devices that were tested, the breakage strength was $4.5 \pm 0.5$ GPa ($690 \pm 80$ kpsi) as compared to $5.3 \pm 0.3$ GPa ($770 \pm 40$ kpsi) for the pristine fiber.

In another set of experiments, FBGs were inscribed through the acrylate coatings of high-Ge content high NA *SM1500(4.2/125)* fibers from *FiberCore*. Using exposure conditions similar to those used with the *SMF-28* fibers, but with pulse energies up to $440\,\mu$J/pulse, high index modulations were induced through the jacket of this high-NA fiber both with and without $H_2$-loading [44]. Figure 13 displays the growth rate of the $\Delta n$ as a function of exposure for $H_2$-loaded fiber. Index modulation values approaching $10^{-2}$ are realized with the jacket removed. As with standard SMF fiber, saturation in the induced index change through the jacket is observed. The inset image of Figure 13 displays the transmission spectra of gratings written through the acrylate jacket with and without hydrogen loading producing $\Delta n$ of $1.4 \times 10^{-3}$ and $7 \times 10^{-4}$, respectively.

For downhole monitoring applications in the oil and gas industry, FBG sensors are written into optical fibers coated with polyimide, which is thermally stable up to 300°C. For standard UV grating inscription, the polyimide coating needs to be removed, as it is strongly absorbing in the UV. Polyimide is resistant to chemical attack. Coating removal is then a nontrivial exercise requiring immersion of the fiber in a hot sulfuric acid bath. Using the femtosecond-IR laser phase mask technique, we were able to directly inscribe gratings through the polyimide jacket of commercially available high-NA fibers from *OFS-Fitel* (*ClearLite CL-POLY-1310-21*) after the fiber was $H_2$-loaded.

For unloaded *OFS* fiber, the maximum FBG reflectivity achievable was 1%. A reflection spectrum of the device is shown in Figure 14(a). The Bragg resonance of the FBG, $\lambda_B$, is 1555.24 nm, which corresponds to an effective core mode index $n_{\text{eff}} = 1.452$. Similar FBGs written in *SMF-28*

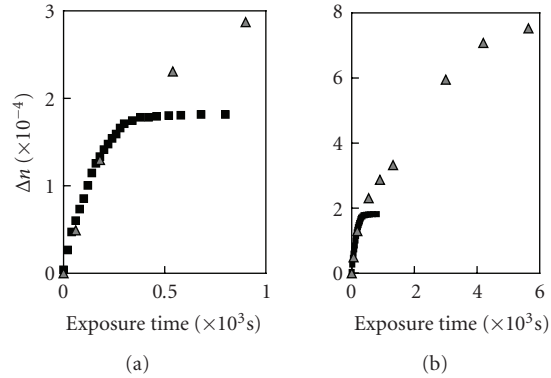


Figure 12: (a) Increase in $\Delta n$ as a function of exposure time for gratings written through the polymer coating with $250\,\mu$J pulses and a $f = 19$ mm cylindrical lens (black squares) and gratings written on stripped *SMF-28* fibre (gray triangles); (b) Long-term continued grating growth on stripped *SMF-28* fiber.

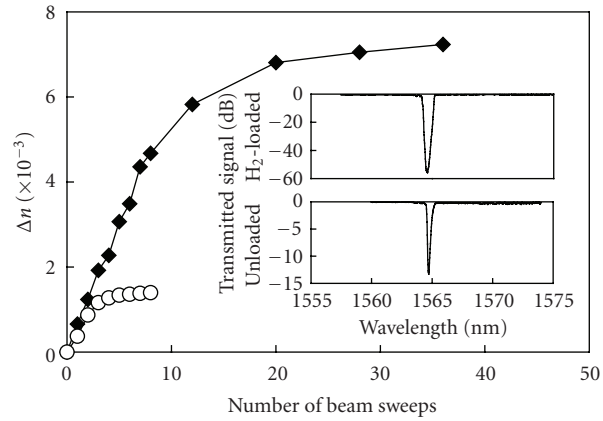


Figure 13: Grating growth in $H_2$-loaded *FiberCore* fiber through the jacket (white circles) and with jacket removed (black diamonds). Inset image is of transmission spectra of gratings written through thejacket with (top) and without (bottom) $H_2$-loading.

result in a $n_{\text{eff}} = 1.447$, implying that there is a higher Ge-dopant concentration in the high-NA fiber. The transmission spectrum of an FBG written in $H_2$-loaded *OFS* fiber with pulse energies of $180\,\mu$J is presented in Figure 14(b). The total exposure time for the hydrogen loaded grating inscription was 5 minutes, after which no further grating growth was observed. For both the loaded and unloaded *OFS* fibers, the induced-index change for the gratings occurred in type I-IR regime. Using the Rouard method, the transmission spectrum of the grating was modeled assuming a Gaussian index profile 6.4 mm in length and a 5-photon process. The modeled response is shown as the dotted line in Figure 14(b). From the model, the maximum index modulation in the core corresponding to the experimental data is $\Delta n = 4.8 \times 10^{-4}$. For the unloaded case, the reflectivity of 1% corresponds to a $\Delta n = 3 \times 10^{-5}$.

Observation of the exposed region of the polymer jacket under an optical microscope revealed some damage to the

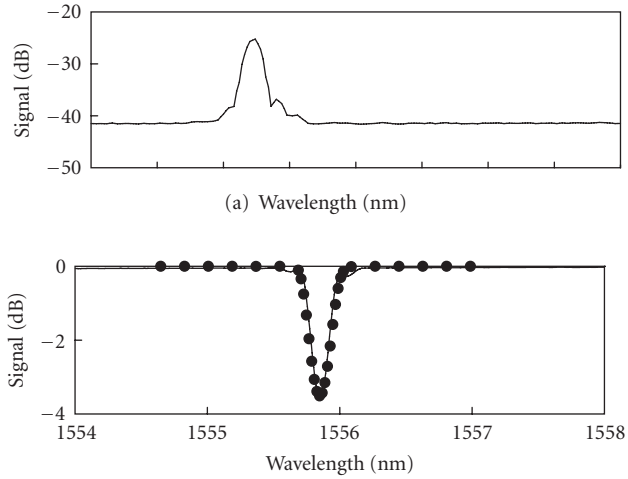


Figure 14: (a) Reflection spectrum of an FBG written through the polyimide jacket of the *OFS* fiber without $H_2$-loading; (b) transmission spectrum of an FBG written through the polyimide jacket of $H_2$-loaded OFS fibre. Overlaid modeled spectrum shown with black dots.

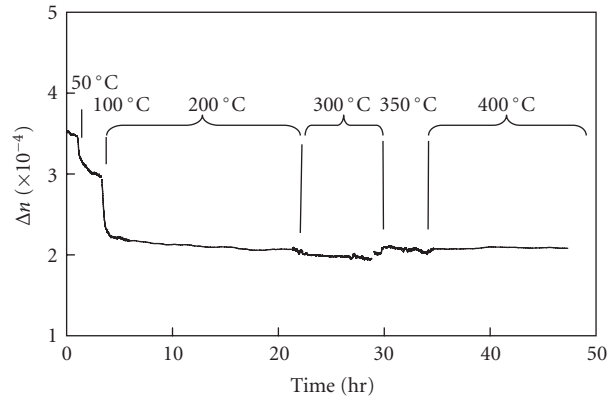


Figure 15: Isochronal annealing study of an FBG in the polyimide coated OFS fiber.

jacket surface after the 5-minute exposure. Femtosecond-IR laser machining studies of polyimide have shown that the ablation threshold for polyimide decreases with the number of incident pulses [43]. It is likely that the first several hundred pulses are inducing "incubation sites" in the polyimide polymer coating that eventually reduces the transmission of the IR radiation through the jacket thus limiting the $\Delta n$ growth.

To study the FBG temperature stability, isochronal annealing studies were performed on the gratings at elevated temperatures. In Figure 15, the reduction of $\Delta n$ at various elevated temperatures is shown for a grating with an initial $\Delta n$ of $3.6 \times 10^{-4}$. A portion of the $\Delta n$ is rapidly annealed out at 200°C but the remaining $\Delta n$ is relatively stable with increasing temperature up to 400°C. After 16 hours at 400°C, the grating had a $\Delta n$ of $2 \times 10^{-4}$ with no visible erasure. As the rated operating temperature of the fiber coating is 300°C, it is likely that the grating reflectivity will remain stable within the operating temperature of the coating. When the fiber temperature was increased in 100°C increments and annealed for 1 hour at each temperature, grating erasure was observed with complete grating erasure occurring at 800°C. In a separate experiment, another device was annealed at 360°C for 140 hours after being preannealed at 75°C for 36 hours in order to out-gas any remaining hydrogen (see Figure 16). After 140 hours, a $\Delta n \gg 2.2 \times 10^{-4}$ remained.

## 5.3. Gratings in Active Fibers for Fiber Lasers

Fiber lasers have become essential components for telecom and sensing applications because of their high efficiency, gain, and good beam quality. Writing Bragg gratings reflectors directly into the core of active single mode optical fibers is a convenient way to create compact, fiber compatible, and low-loss laser resonator cavities. Traditional UV laser inscription of fiber Bragg gratings (FBGs) however is not appropriate for short cavity fiber lasers where high levels of Erbium–Ytterbium doping ($Er^{3+}$ and $Yb^{3+}$) are required [45]. Germanium (Ge) codoping of the fiber core, needed to enhance UV photosensitivity, causes ion clustering of $Er^{3+}$ and $Yb^{3+}$ core dopants resulting in low laser efficiency [46]. Glass substrates other than silica, for example fluoride or phosphate glass, are more desirable host materials for active dopants as higher concentrations of $Er^{3+}$ and $Yb^{3+}$ can be realized. Dissimilarity with silica however makes coupling of these fibers to external resonator mirrors difficult. Direct inscription of FBG resonators in these fibers would be preferable.

Recently, femtosecond-IR lasers were used to inscribe grating reflectors directly into conventional, nonphotosensitive, silica-based Er:Yb-codoped fiber by the point-by-point [47], or phase mask techniques [48] for the manufacturing of fiber lasers. These gratings successfully resulted in lasing of the fiber laser cavities. In our laboratories, short strong gratings were induced in heavily doped Er-Yb phosphate glass fiber producing resonator cavity reflectivities above 99.99% for a 6-mm-long grating corresponding to $\Delta n > 1.5 \times 10^{-3}$ [15]. Femtosecond IR laser-induced gratings have also been fabricated in undoped [17] and doped fluoride fibers [49].

The impact, however, of high active doping levels on femtosecond-IR laser inscription of FBGs was unclear. In order to develop recipes for laser cavity grating inscription, investigations to determine optimal exposure conditions and active doping levels in silica-based fibers were performed [18]. High $\Delta n$ FBGs were written in commercially available fibers with different concentrations of $Er^{3+}$ and/or $Yb^{3+}$ in order to study the magnitude of FBG reflectivity and spectral quality as a function of active doping levels. For each fiber that was studied, the saturation in induced $\Delta n$, the spectral quality and out-of-band loss were evaluated and compared with gratings made in pure silica core single mode fibers.

Various active fibers with different levels of doping were tested. Since $Er^{3+}$ and $Yb^{3+}$ dopant concentration values were unavailable, it was assumed that they were

Table 1: Active fibers evaluated.

| Fiber | Dopant | Loss (dB/m) at $\lambda$ nm | | Core size | $\lambda_{\text{cut off}}$ | NA |
|---|---|---|---|---|---|---|
| | | 1532 | 980 | ($\mu$m) | (nm) | |
| INO EY302 | Er:Yb | 29 | 227 | $4 \times 6$ | 1145 | 0.14 |
| INO EY305 | Er:Yb | 22 | 477 | 6 | 1200 | 0.18 |
| INO EY550 | Er:Yb | 11.2 | 593 | $2.5 \times 9$ | 900 | 0.17 |
| *Coractive EY18-06* | Er:Yb | 58 | 400 | 6 | na | 0.18 |
| INO Yb214 | Y | 0 | 612 | 6.2 | 900 | 0.12 |
| INO Er406 | Er | 37 | 18 | 3.4 | 860 | 0.2 |
| Corguide | Er | 25 | 10 | 6 | na | na |
| Brown University | Er | 12 | 4 | 8 | na | na |

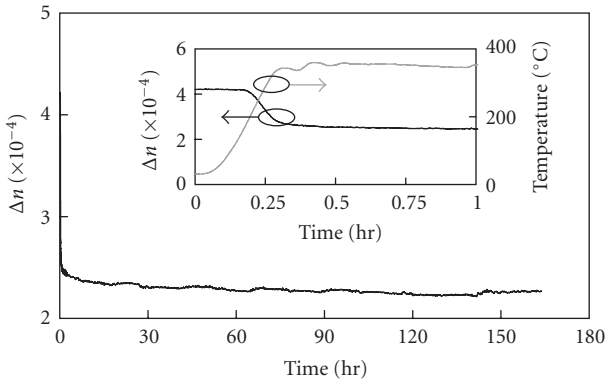


Figure 16: Long-term annealing study at 360°C of an FBG in *OFS* fiber. Inset is an expanded view of the initial annealing with $\Delta n$ and temperature denoted by black and gray traces, respectively.

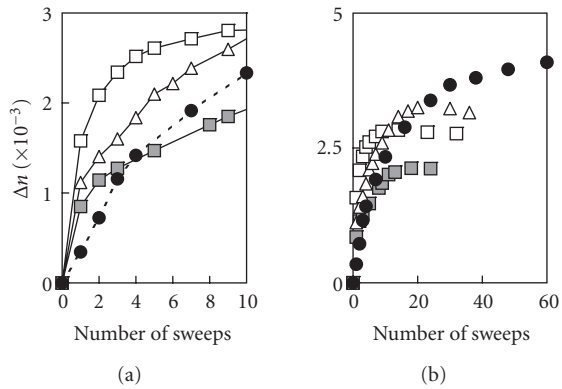


Figure 17: (a) Initial growth and saturated growth (b) of $\Delta n$ versus IR exposures for different active fibers and for pure silica core fiber (black dots). White triangles denote *EY302*, white squares denote *EY305*, and gray squares denote *Er406*.

proportional to the losses given at telecommunication and pump wavelengths, respectively, as specified in Table 1. The FBGs were written using a first-order 1.07 $\mu$m pitched phase mask positioned 1 mm away from the fibers. All exposures were made using 1.2 mJ pulses of IR radiation with laser repetition rates set at 100 Hz.

Grating growth was very rapid, producing Bragg resonances of –40 dB after only a few seconds of exposure. All FBGs made in the doped active fibers listed in Table 1 share two characteristics: the initial FBG growth rate exceeds that of pure silica core fibers (see Figure 17(a)) and the growth of the $\Delta n$ in *all* the FBGs made in active fibers saturate well below the pure silica core fiber levels of $4 \times 10^{-3}$. For FBGs in active fiber, the saturated $\Delta n$ was estimated to be 2 to $3.5 \times 10^{-3}$ (see Figure 17(b)).

The plot of the saturated $\Delta n$ versus the absorption at 1532 nm and 980 nm for the gratings was highly scattered (see Figure 18). Error bars denote the average values of three gratings written in the fiber. A weak negative correlation between saturated $\Delta n$'s and increasing Er and Yb content of the active fibers was observed. The large scatter of the saturated $\Delta n$'s may be due to the different glass composition between the fibers that were studied. With all the doped fibers tested, spectral quality and out-of-band insertion losses were similar to the cladding mode suppressed gratings in standard fiber presented in Figure 11.

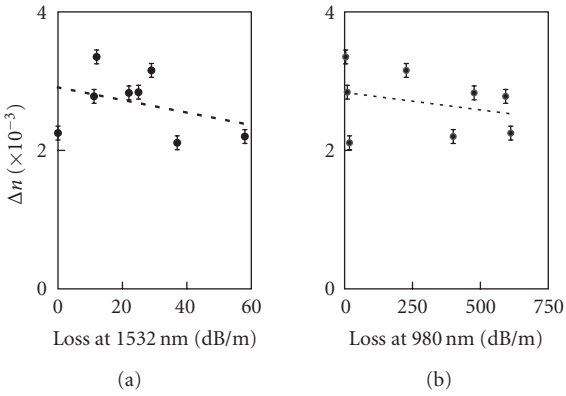


Figure 18: Saturation levels of the active fibers $\Delta n$'s as a function of (a) loss at 1550 nm and (b) loss at 980 nm. Error bars denote the averaging of the values obtained from the three sequential exposures of the fiber. Dotted lines denote the linear regression through the data points.

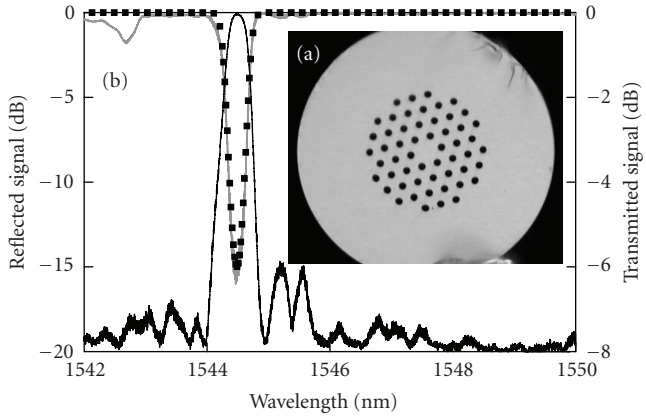


FIGURE 19: (a) Cross section of *ESM-12-01* fiber. (b) Transmission (gray), reflection (black), and modeled (dotted) spectra of a grating written in *ESM-12-01* fiber with 1200 $\mu$J pulse energy 200 Hz. Total exposure time 5 minutes.

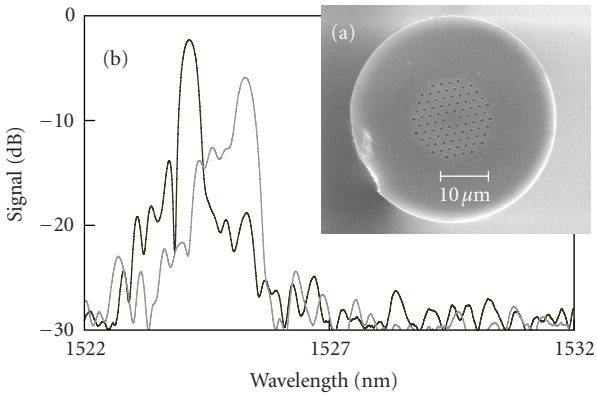


FIGURE 20: (a) Scanning electron microscope image of 45 $\mu$m diameter *LMA-15* taper, (b) reflection spectra of grating in 45 $\mu$m *LMA-15* fiber taper for two orthogonal polarizations.

## 5.4. Gratings in Photonic Crystal Fibers

Inscription of FBG structures in photonic crystal fibers (PCFs) enhances the flexibility of the PCF for telecommunication as well as microfluidic sensing related applications. Direct inscription of FBGs in pure silica PCF has been achieved using ArF excimer laser irradiation as well as femtosecond UV irradiation producing $\Delta n \sim 2 \times 10^{-4}$ after a 3.8-hour write time and $\sim 1 \times 10^{-4}$ after a one hour exposure time [9, 50].

Using the femtosecond-IR laser-phase mask approach, FBGs were written in pure silica PCF and fiber tapers [20]. Scattering of the writing beam by the PCF cladding holes can be reduced by selecting fiber geometries with smaller number of cladding holes between the fiber surface and the core. With such a PCF, for example the *ESM-12-01* fiber from *Blaze Photonics*/*Crystal Fibre*, which has 3 rows of air holes surrounding the silica core, a $\Delta n$ value of $\sim 4 \times 10^{-4}$ was obtained after a 5-minute exposure with a $\Lambda_m = 3.12\,\mu$m mask, tight focusing ($f = 30$ mm), and high pulse energy (1200 $\mu$J/pulse at 200 Hz). The spectral response of the grating in the *ESM-12-01* fiber is shown in Figure 19. For other PCF with larger number of air holes, scattering of the incident IR light did not result in any grating fabrication in the core, even at pulse energies that resulted in damage to the fiber. By tapering such PCF in a $H_2/O_2$ flame, the fiber diameter could be reduced causing the bandgap generated by the cladding holes as seen by the transversal IR beam to shift to a wavelength that was not resonant with the IR source. The resultant narrower hole diameter and spacing in the tapered PCF allowed partial transmission of the IR radiation into the core resulting in FBGs in the tapered regions of the PCF with $\Delta n \sim 3 \times 10^{-4}$ after an 80-second exposure. Alternatively, the holes of the PCF could be collapsed altogether. Gratings inscribed in the collapsed region across the entire cross section of the taper diameter produced multimode transmission/reflection responses.

The tapering of the PCF by the $H_2/O_2$ flame such that the air holes was not collapsed but still produced a high level of birefringence in the tapered region [51]. *LMA-15* PCF from *Crystal Fibre A/S* was tapered from its initial 230 $\mu$m outer diameter to a taper waist diameter of 45 $\mu$m and 10 mm length. The fiber taper still guided the fundamental mode without any loss. By inscribing a weak grating in the PCF core of the taper region, the birefringence of the PCF taper was quantified. In Figure 20, the grating was probed with polarized light from a tunable laser source and the spectral characteristics of the gratings made in the tapered PCF show a strong dependence on the signal polarization. When the polarization of the signal was rotated using an inline fiber polarizer, it was possible to switch the main reflection spectrum from the Bragg resonance wavelength at 1525.2 nm to a lower wavelength of 1524.1 nm. For a birefringent Bragg grating, the wavelength shift between the two orthogonal polarizations $\Delta\lambda_B$ will be related to the difference between the $n_{\text{eff}}$ of the two modes $\Delta n_{\text{eff}}$ by: $\Delta\lambda_B/\lambda_B = \Delta n_{\text{eff}}/n_{\text{eff}}$ which results in a $\Delta n_{\text{eff}}$ or birefringence value of $1.05 \times 10^{-3}$.

## 5.5. Induction of High Birefringence

For some applications, a given amount of birefringence in an optical device or system is desirable, among the most important being the single polarization fiber lasers [52] and Bragg grating sensing [53]. Typically, highly birefringent fibers of complex design are used in these specialized applications. The birefringence, however, could be introduced locally by processing the optical substrate with high-energy laser pulses. Small amounts of birefringence ($4 \times 10^{-5}$) can be created with UV exposure of Ge-doped fibers [54] by controlling the polarization of the UV-writing source so that it was normal to the optical fiber axis.

Similarly, type I-IR FBGs induced with a phase mask uniformly about the core have been shown to produce similar levels of birefringence when the polarization of the IR beam was also polarized normal to the fiber axis ($\sim 10^{-5}$) [55]. In the type II-IR regime, FBGs written uniformly about the fiber core produced levels of birefringence approaching $10^{-4}$, an order of magnitude higher than the birefringence

resulting from the type I-IR exposure. Although the type II-IR gratings potentially produce enough birefringence for most applications, one draw back of these structures is that there is typically increased insertion loss for gratings with stronger $\Delta n$'s. For applications such as short cavity single polarization lasers, the increased loss associated with the birefringent laser resonator mirror would reduce the laser performance.

In our laboratories, we have shown that if a type II-IR grating structure is made in the cladding close to but not overlapping the core, such that there is no retroreflectance from the structure, a large amount of birefringence is locally induced in the core region without generating excess loss [56]. Birefringence values as high as $\sim 8 \times 10^{-4}$ were obtained in the core of *SMF-28* fiber when type II-IR grating structures were inscribed in the cladding of the fiber on both sides of the core in close proximity to the core/cladding interface. The splitting of the reflection spectrum of a weak probe grating written in the core is shown in Figure 21 along with a schematic of the exposure which produced the high birefringence result and a photomicrograph of the grating induced in the cladding. The birefringence is likely due to induced stress rather than direct asymmetric refractive index modification.

When a strong type I-IR grating (~95% reflectivity) is present in the core, the type II-IR cladding exposures resulted not only in increased birefringence of the effective core mode, as measured by the induced polarization dependent wavelength shift, but also resulted in a large grating strength difference between orthogonal polarization axes ($\Delta$Tr) for the Bragg resonance. As can be seen in Figure 22, the ordinary polarization corresponds to a 15 dB strong grating while the extraordinary polarization results in a secondary resonance of 5 dB located 540 pm away from the main resonance ($\sim 5 \times 10^{-4}$ birefringence) resulting in $\Delta$Tr = 10 dB. The difference in the $\Delta n$ with polarization based on the evaluation of the refractive index modulation of the two gratings resulted in a value of $\sim 2 \times 10^{-4}$ assuming the approximation of a fundamental (first-order) grating. Since the spectrum of the original grating measured before the cladding exposure did not display a large $\Delta$Tr at the Bragg resonance, it can be assumed that the initial $\Delta n$ was similar for the two principle states of polarization and the change in $\Delta$Tr was a result of the cladding exposure.

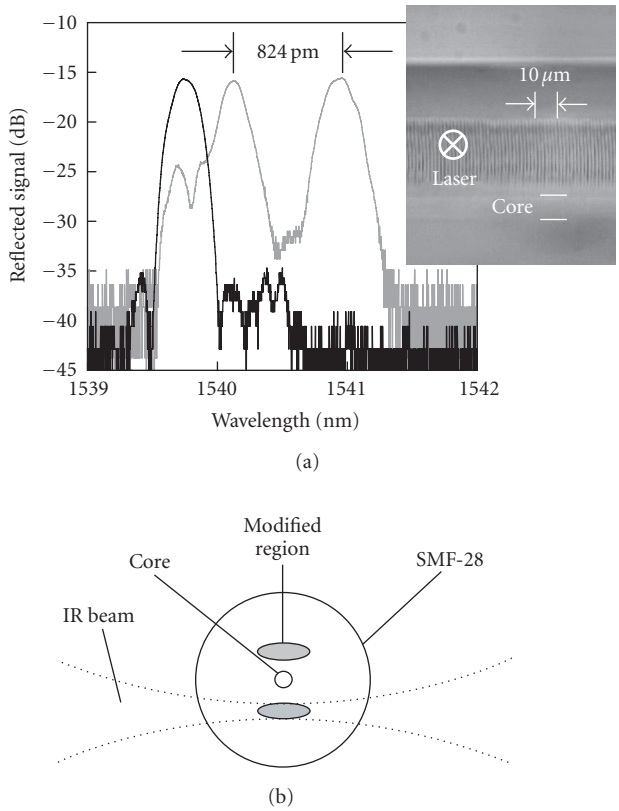


Figure 21: The spectra of the probe grating before and after the cladding exposure are denoted by black and grey traces, respectively. Inset photomicrograph shows a type II-IR exposure in *SMF-28* fiber in the cladding proximate to the core. Image taken along the exposure beam axis (b) shows a schematic representation of the exposure conditions that produced the high birefringent spectral result.

## 5.6. High-Temperature Stable Sensor Gratings

A very important application of FBG technology is its usage as sensing elements. FBGs are capable of monitoring both temperature and strain through variations in the spectral response of the grating, which can be directly correlated to strain and temperature imposed on the grating structure [57]. The applicability of traditional UV laser-induced FBGs is restricted to lower temperatures (<600°C) because of the instability of the UV generated grating structure at higher temperatures. High-temperature grating stability is especially important for sensing applications such as monitoring furnaces, combustion situations, and so forth.

Femtosecond IR laser-induced gratings in standard *SMF-28* and all silica core single mode fiber have displayed high long-term thermal stability at 1000°C when the FBGs were inscribed in the type II-IR regime [12]. Above 1000°C, the silica substrate itself is susceptible to structural transformations that limit the functionality of the fiber [58]. For temperatures >1000°C, fiber substrates other than silica need to be considered. The most successful optical fiber used for high-temperature sensor applications is the single crystal sapphire fiber that has a glass transition temperature $t_g$ of ~2030°C. Unlike conventional silica-based single mode optical fibers, sapphire fibers are made in the form of rods absent a cladding layer. With fiber diameters commercially available, beam propagation within the fiber is highly multimode at the 1550 nm telecommunication wavelengths. Present sapphire fiber sensors are mostly based on Fabry-Perot structures within the fiber producing a broadband interferometric signal that varies with temperature [59].

Femtosecond IR-laser induced gratings in sapphire fiber show no degradation of the grating strength at high temperatures up to 1500°C [15, 16]. The sapphire FBGs (SFBG) have definite advantages over other sapphire fiber sensors

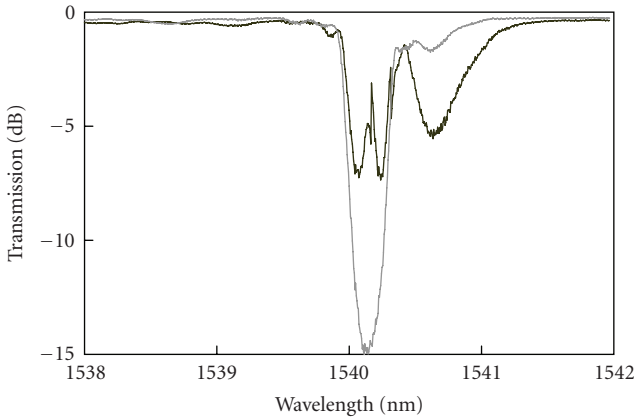


FIGURE 22: Large birefringence of the refractive-index modulation induced by a symmetric cladding exposure of a strong type I-IR core grating. The two orthogonal polarization states are denoted by the gray and black traces, respectively.

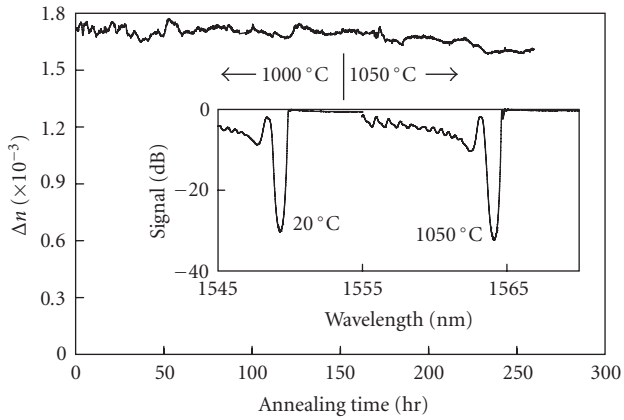


FIGURE 23: Long-term annealing at 1000 and 1050°C of a femtosecond IR FBG. Inset displays the initial room temperature transmission spectrum and the final spectrum at 1050°C for 100 hours.

that rely on Fabry-Perot etalons at the fiber tip. Unlike Fabry-Perot sapphire sensors, SFBG sensors with their discrete resonant wavelength could potentially be used as distributed optical sensor arrays up to 2000°C. The SFBGs that are inscribed in sapphire fiber using femtosecond-IR lasers and a phase mask are naturally multimode devices. The multimode reflection spectrum observed with the retroreflective SFBGs is characterized by a large bandwidth having a complicated structure that consists of a superposition of different modes reflected by the grating. Although the SFBG sensor can be used in the multimode regime, propagation of a single mode is preferable due to stability and the detection advantages that a narrowband single mode reflection response offers. To produce a single mode response, the multimode SFBGs were probed using tapered single mode fibers. Single and low-order mode reflection/transmission responses are produced when the mode field of the launched single mode is matched with the fundamental mode supported by the sapphire fiber. For a 150 $\mu$m diameter sapphire fiber, this would correspond to an $LP_{01}$ mode field ~150 $\mu$m in diameter. When single mode optical fiber is tapered such that the normalized frequency or $V$ number of the core is <1, the fundamental $LP_{01}$ mode is no longer core guided but is guided by the cladding-air interface resulting in a mode field with the same diameter as the tapered fiber. Matching taper and sapphire fiber outer diameters may excite only a single mode of the sapphire fiber. The evanescent tapers were made from fibers with different cutoff wavelengths $\lambda_{cut}$.

Although, theoretically less efficient for mode matching, the expanded fundamental mode of a single mode fiber can also be used to reduce the number of modes excited by the probing signal. As in the case of tapers, the single mode probe signal from a fiber collimator can be launched from a single mode 1550 nm optical circulator into the SFBG, and the reflected signal can be detected at the third port of the circulator instead of using the less efficient fiber couplers. A configuration made of an input single mode tapered fiber and multimode silica fiber used for output coupling was also tested and has delivered a filtered multimode transmission spectrum. The tapered coupling improved the spectral resolution of the sapphire FBG as compared to its multimode responses. Such improvements facilitate the utilization of the sapphire FBG as a high-temperature sensor.

### 5.6.1. Thermally Stable FBGs in $SIO_2$ Based Fibers

FBGs written with ultrafast IR radiation exhibit different thermal stability characteristics depending upon the pulse duration and energy. Above a low-intensity threshold for grating formation (type I-IR) [23], $\Delta n$ values with similar thermal stability to UV-induced gratings can be generated as was shown in Figure 3. At higher power levels that are consistent with white light generation in the fibers, thermally ultra-stable defects/damage sites could be produced (type II-IR).

A long-term study of type II-IR grating stability was performed by inscribing large $\Delta n$ type II-IR FBGs in *SMF-28* fiber which were then heated to 1000°C in steps of 100°C for 1 hour at each temperature [58]. Once 1000°C was reached, the grating was then kept at constant temperature for 150, hours and the grating reflectivity and resonant wavelength were monitored (see Figure 23). There was no noticeable degradation of the increased grating strength for the duration of the test and the grating maintained $\Delta n = 1.7 \times 10^{-3}$. The initial increase in the femtoseconds grating $\Delta n$, shown in Figure 3 previously, is likely a result of the two kinds of index change being written simultaneously. The peaks of the complex interference pattern are sufficiently intense to ultimately ionize the glass in the fiber producing an index change that is durable with temperature. In the valleys of the interference pattern, the intensity is below the type II-IR threshold, however some type I-IR index change is generated. As the device is annealed, the permanent type II-IR index change remains while the annealable type I-IR index change is erased resulting in a higher $\Delta n$. The

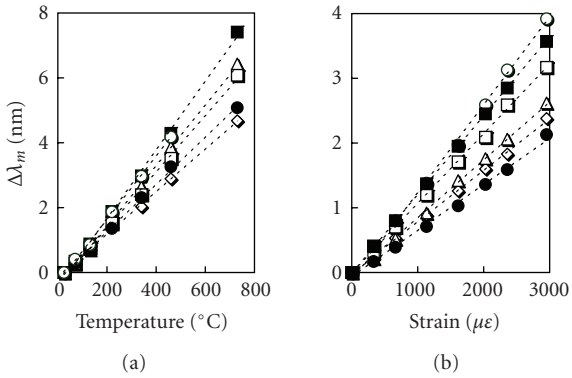


FIGURE 24: (a) Bragg-order wavelength variation as a function of temperature for the grating shown in Figure 9, (b) Bragg-order wavelength variation as a function of strain. Orders $m = 7, 8, 9, 10, 11$, and 12 are denoted by white circles, black squares, white squares, triangles, diamonds, and black circles, respectively.

temperature of the femtoseconds grating was subsequently increased and kept at 1050°C for 100 hours (see Figure 23). The $\Delta n$ of the femtoseconds grating decreased slightly from $1.7 \times 10^{-3}$ to $1.6 \times 10^{-3}$ during 100 hours at 1050°C. A drift of the Bragg resonance to longer wavelengths of 0.2 nm was detected at the end of experiment. Spectra taken initially at room temperature and after 100 hours at 1050°C are shown in inset of Figure 23.

### 5.6.2. High-Temperature Multiparameter Sensor in $SIO_2$

As presented in Section 4.6 above, the type II-IR FBG written in *Corning 980 Flexcore* fiber with a cutoff wavelength of 980 nm and the 4.28 $\mu$m pitched phase mask has many Fourier components in its spectral response that produces Bragg resonances at various wavelengths (see Figure 9). The large number of spectral resonances generated by a single grating structure is available to be used for multiparameter sensing. Aside from strain and temperature, other parameters like bending, pressure, and so forth could be simultaneously measured using only one grating. The availability of supplementary spectral characteristics could also be used to improve the accuracy of the strain-temperature discrimination.

Wavelength shifts of the various diffracted orders as a function of the temperature in the absence of strain are shown in Figure 24(a). The temperature was changed from ~20°C to ~800°C. The room temperature 1550 nm Bragg resonance wavelength was monitored in order to confirm that the thermal equilibrium was reached after ~30 minutes at each temperature. After the thermal equilibrium was reached, all the resonances of the Bragg grating were measured at constant temperature. At room temperature, the gratings were subjected to controlled stress in a specially designed jig. The strain was applied incrementally from 0 to 3000 $\mu\varepsilon$. After each strain increment, the wavelength shift was monitored in the 1550 nm range until the measurement confirmed that the Bragg wavelength was stable, as measured by an optical spectrum analyzer. The Bragg wavelength of each diffraction order was then evaluated by scanning a 10 nm spectral range around each high-order resonance. Wavelength shifts of the various diffracted orders as a function of strain are shown in Figure 24(b).

Under the application of strain and temperature and of another arbitrary parameter $P$, the grating spectrum of order $m$ will undergo a wavelength shift:

$$\Delta\lambda_m(\varepsilon, T, P) = K_{\varepsilon m}\Delta\varepsilon + K_{Tm}\Delta T + K_{Pm}\Delta P, \qquad (3)$$

where $\Delta\lambda_m$ are the wavelength shifts when the ambient parameters; stress ($\varepsilon$), temperature ($T$), and a generic general parameter ($P$) are changing by the amount of $\Delta\varepsilon$, $\Delta T$, and $\Delta P$. Considering temperature and strain, the variations in $\Delta\lambda_m$ differ from order to order as shown in Figures 24(a) and 24(b). Assuming that the resonance shifts are linear and independent of each other, the slopes or $K$ values of the $\Delta\lambda_m$ versus $T$ or $\varepsilon$ curves can be used to setup a $2 \times 2$ **K** matrix which will allow for the discrimination between temperature and strain using a single Bragg grating [60]. By employing more than two resonances, the problem becomes one that is over defined, potentially resulting in reduced measurement error. Alternatively, other parameters in addition to temperature and strain could also be monitored.

### 5.6.3. High-Temperature Stable FBGs in Sapphire Fiber: Multimode Response

FBGs were fabricated in crystalline sapphire fiber with diameters of 60, 100, 120, 150, and 180 $\mu$m by exposing the fibers to the 125 femtoseconds pulsed-IR radiation. The tests were made using the 4.28 $\mu$m period phase mask that resulted in a 5th-order Bragg resonance in the sapphire fiber at 1490 nm. Alternatively, a 1.747 $\mu$m period phase mask was used that gives a second-order Bragg resonance in sapphire fiber at 1523 nm. The first phase-mask, although producing lower reflectivity high-order resonances, has the advantage of producing grating structures in sapphire fiber that are easily observed under an optical microscope. The shorter pitched phase mask was specially designed to generate a low-order resonance in the sapphire fiber in the telecom wavelength range. In this way, the grating growth could be conveniently monitored with an erbium white light source and a spectrum analyzer.

The sapphire FBGs (SFBGs) were fabricated using the setup shown in Figure 1. The femtosecond-IR pulses were focused with a 25-mm-focal length lens through the phase mask and onto the sapphire fiber. Since the sapphire fibers have a hexagonal cross-section, they were placed in a rotation jig that would allow the fiber to be turned along its axis in order to optimize the exposure. The femtosecond-IR beam was focused inside the fiber and then scanned normal to the fiber using a precision vertical stage in order to expose the whole cross section of the sapphire fiber to the laser beam. As the sapphire fiber is essentially a sapphire rod absent a cladding layer, the spectral response from an inscribed grating is highly multimode. To measure the multimode

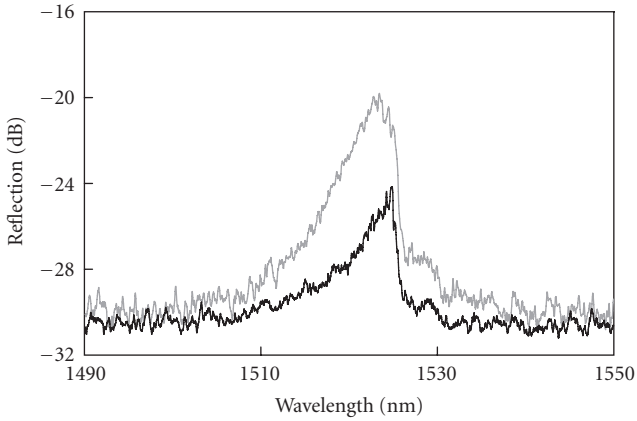


Figure 25: Multimode reflection spectra of the gratings written in the 150 $\mu$m core diameter sapphire fiber measured from the short side (gray line) and from the long side (black line) of a 120 cm-long sapphire fiber.

response from the SFBG, an S-C band tunable laser was passed through a 3-dB-multimode coupler made in-house with 105/125 $\mu$m core/clad silica fiber. The output port of the coupler was mounted on 5-axis precision stages and butt-coupled to the sapphire fiber with index matching oil having a refractive index of 1.46. The reflected response was measured using a fast detector.

SFBGs were fabricated in 150 $\mu$m diameter fibers with both the 4.28 and 1.747 $\mu$m phase masks producing maximum reflectivities of 8%. There is a limitation on the maximum reflectivity of a multimode fiber grating due to the large number of modes that the fiber will support. In 105 $\mu$m core multimode silica fiber, using standard writing conditions, the maximum reflectivity obtained using a first-order phase mask was 30%, which corresponded to a $\Delta n \sim 3 \times 10^{-3}$. This reflectivity was not reached in gratings made in sapphire with similar diameters of 100 $\mu$m or even in the case of smaller diameters of 70 and 60 $\mu$m. It is possible that the lower reflectivity obtained in sapphire fibers as compared to silica is the result of a lower saturation level of the $\Delta n$ that can be induced in sapphire fiber using the method of ultrafast radiation and the phase mask.

The magnitude of the SFBG reflectivity also depends on the position of the grating along the sapphire fiber length. The multimode response of an SFBG written in a 120-cm-long sapphire fiber with 150 $\mu$m core at ~20 cm from one end of the fiber is presented in the Figure 25. In the figure, the multimode reflection spectrum measured from the short end is presented together with the spectral response of the same grating measured from the long side of the sapphire fiber. There is systematic 4–6 dB difference in the strength of the reflected signal when it propagates through 1 meter of the sapphire fiber. This loss is likely related to the propagation of the mode as well as mode conversion within the fiber. In addition to the reflectivity, the bandwidth of the grating response is also reduced which implies that higher-order modes are lost as the signal propagates along the length of the fiber.

### 5.6.4. High-Temperature Stable FBGs in Sapphire Fiber: Single Mode Response

Multimode responses from FBG sensors are not as desirable as single mode responses since the spectral bandwidth is broad and the dynamic range of the reflection signal is low. In order to achieve a quasi-single mode response from the SFBG, it was necessary to investigate other approaches to probe the grating aside from the multimode coupler. The maximization of single mode coupling to the multimode sapphire fiber can be achieved by the generation of a large mode field diameter (MFD) single mode by for example, a fiber taper [16].

For single mode fibers, the normalized frequency or $V$ number is given by

$$V = \frac{2\pi r}{\lambda}\sqrt{(n_{\text{co}}^2 - n_{\text{cl}}^2)}, \tag{4}$$

where $r$ is the core radius, $\lambda$ is the wavelength, and $n_i$ is the refractive index of the core or cladding. For single mode operation, $V \leq 2.405$. When a fiber is tapered, the ratio of cladding/core radii remains constant however $V$ decreases. The transition of the fundamental $LP_{01}$ mode from a core-cladding guided into a cladding-air guided mode occurs when [61]

$$V < V_{\text{cc}} \cong \sqrt{\frac{2}{\ln S}}\left\{1 + \frac{0.26}{\ln S}\right\}^{-1/2}, \tag{5}$$

where $S$ is the ratio of the cladding to core diameters.

Once condition (5) is met, the fundamental mode expands into the cladding resulting in a large area mode that can be better coupled into the sapphire fiber. As the expanded mode field is limited by the outer diameter of the taper, maximization of the single mode coupling occurs when the difference between the taper and the sapphire fiber diameters is minimized. Fiber tapers were fabricated using *Corning Puremode HI 780* single mode fiber with an outer diameter $\phi = 125\,\mu$m and a cutoff wavelength $\lambda_{\text{cut}} < 720$ nm using a swept hydrogen flame while the fiber was pulled on precision translation stages. When pulled to taper diameters $\leq 70\,\mu$m, the fundamental mode was completely guided by the cladding air interface as shown schematically in Figure 26. Commercially available 50 $\mu$m and 60 $\mu$m diameter fiber collimators were also used for testing.

In order to obtain a single mode response from the sapphire grating, a probe signal from the swept tunable laser system was passed through a 1550-nm-range optical circulator and into the tapered fiber/fiber collimator. The output of the collimator and the tapers were mounted on 5-axis precision stages and butt-coupled to the sapphire fiber with index matching oil having a refractive index of 1.46.

The same SFBG that produced the multimode response shown in Figure 25 was also probed with a 60 $\mu$m diameter taper (see Figure 27). The reflection spectrum measured with the 60 $\mu$m taper has a 3 dB bandwidth of 0.33 nm similar to that of an FBG in single mode fiber, which is compared to the multimode spectrum that has a 3 dB bandwidth of 6 nm.

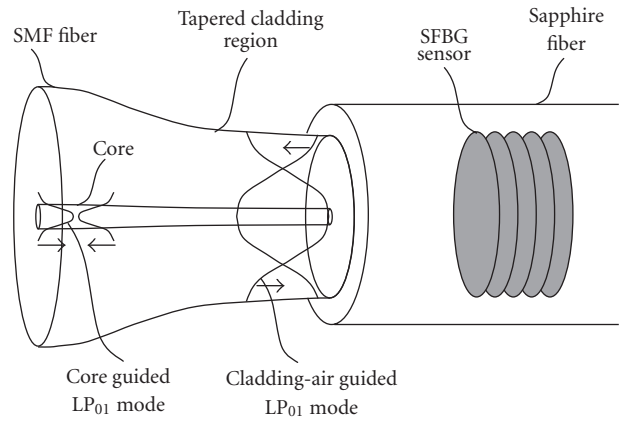


FIGURE 26: Schematic of the $LP_{01}$ mode field expansion resulting from fiber tapering and coupling of the taper into the sapphire fiber.

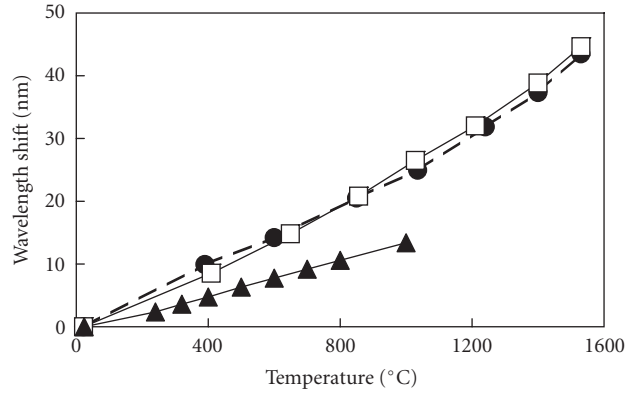


FIGURE 28: Variation of single mode (white squares) and the multimode SFBG wavelength response (black circles,) with temperature. Wavelength variation of the Bragg resonance of a type II-IR FBG written in *SMF-28* fiber is also shown (black triangle).

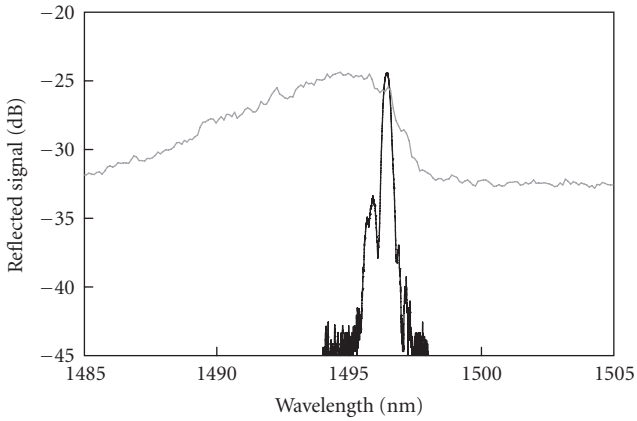


FIGURE 27: Reflection spectra of SFBG with a 100-$\mu$m-silica core multimode fibre (dotted line) and a 60-$\mu$m-taper (black line) as the input couplers.

Compared to the multimode response, there is also a 10 dB improvement in the signal-to-noise ratio of the 60 $\mu$m taper response. The loss at the taper/sapphire splice is 4.5 dB per pass. This loss may be due to the mismatch of excited modes generated by and collected by the tapers.

To measure the response of the SFBG to temperature, the portion of the sapphire fiber that contained the Bragg grating was inserted into a high-temperature ceramic microfurnace (NTT model CMH-7022). In order to position the Bragg grating within the microfurnace, an He-Ne laser was connected to the input port of the multimode coupler. The red light scattered by the Bragg grating was then used to position the grating accurately within the center of the furnace where the temperature distribution was at its maximum. The microfurnace temperature was monitored at its center using a platinum-rhodium thermocouple with a measurement range up 1700°C. A gradient with a 20% decrease in the temperature from the center to edge of the 20-mm-long microfurnace was observed. The wavelength shift of the SFBG as a function of temperature for both the single and multimode spectral responses is presented in Figure 28. Both the single and multimode responses are similar. For comparison, the wavelength shift at 1550 nm of the high-temperature stable type II-IR grating written in *SMF-28* is also shown. Up to 1000°C, the Bragg resonances of both the sapphire and Ge-doped silica fibers vary linearly with temperature, 26 pm/°C and 14 pm/°C, respectively.

## 5.7. Gratings in Other Crystalline Materials

### 5.7.1. Bragg Gratings in Lithium Niobate Waveguides

Along with sapphire, the femtosecond-IR laser grating inscription technique has also been demonstrated in other crystalline waveguides and fibers. Lithium niobate ($LiNbO_3$), because of its ferroelectric nature, is an attractive material for fabrication of active integrated optical devices. The versatility of the waveguides made in this material can be enhanced through the creation of efficient permanent grating structures. Due to the electro-optic properties of the substrate, the lithium niobate Bragg gratings have the potential to satisfy the rapid tuning requirements needed by telecommunication components, such as tunable add/drop filters (ROADMs), tunable dispersion compensators, switches, and so forth that are used for dynamic control of the signal in the network nodes of agile all-optical communication networks.

In our laboratory, gratings were fabricated in 40 mm long reverse proton exchange (RPE) $LiNbO_3$ channel waveguides using the femtosecond-IR laser-phase mask approach [14]. Using the setup shown in Figure 1 with an $f$ = 30 mm focusing lens and the 4.28 $\mu$m pitched phase mask in the two-beam interference regime and 600 $\mu$J pulse energies, grating responses up to -3.5 dB in transmission for exposures at 100 Hz for 1 minute were achieved. The peak field intensity corresponding to the pulse energies used was 2.0 to 2.5 $\times$ $10^{13}$ W/cm$^2$, which is of the same order of magnitude as previously established IR ultrafast laser ablation thresholds of $LiNbO_3$ [62]. The spectral responses of the grating are shown

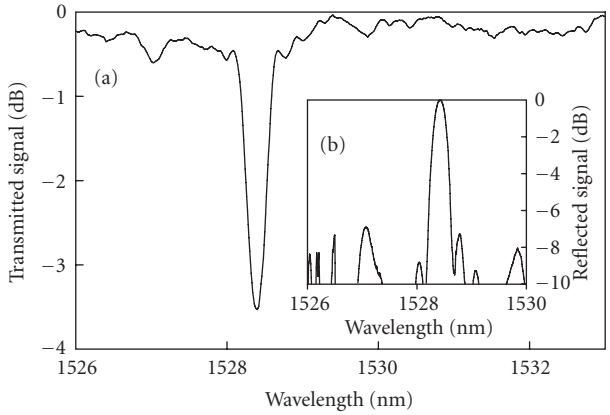


Figure 29: (a) Transmitted spectral response of a lithium niobate grating made with femtosecond IR-radiation. (b) Reflected spectral response.

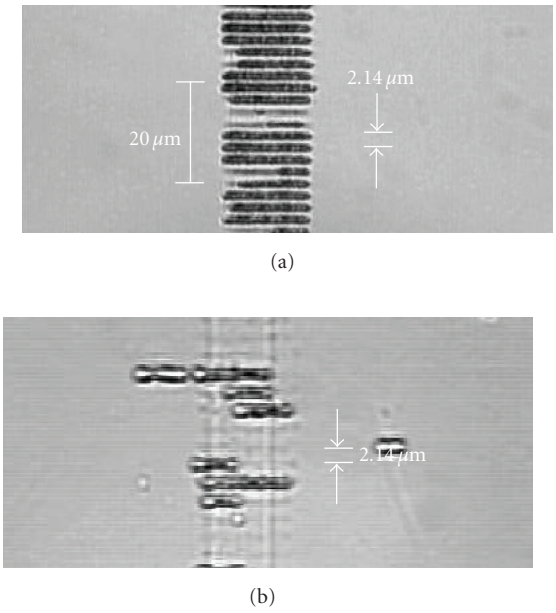


Figure 30: Optical microscope image of the grating induced (a) on the surface and (b) below the surface of the lithium niobate waveguide.

in Figures 29(a) and 29(b). The measured Bragg reflection corresponds to a sixth-order resonance for an effective index of the propagation mode through the waveguide of 2.135.

Bragg gratings made in the $LiNbO_3$ waveguide corresponding to the spectral responses presented in Figure 29 were inspected visually with an optical microscope. As can be seen in Figure 30(a), a surface relief corrugated grating has formed on the waveguide that is a typical ablation effect. Measurement of the surface relief grating with an atomic force microscope revealed a 300 nm corrugation depth.

In the regions were the ablation process is incomplete, a secondary grating could be seen a few microns below the crystal surface displaying a different physical structure as compared to that of the surface grating (Figure 30(b)). The surface and subsurface gratings are in phase suggesting that they are being created by the same laser exposure. The surface ablation threshold is less than that of the damage threshold to the subsurface material. The core of the waveguide is positioned near the surface and within the Rayleigh range of the 30 mm focal length lens (~20 $\mu$m). It is expected therefore that the surface and subsurface regions see the same threshold intensity. The subsurface refractive index change does not have the morphology of catastrophic damage. The surface and subsurface gratings develop simultaneously. Surface grating development ultimately arrests the evolution of the subsurface grating due to scattering of the femtosecond-IR radiation by the surface layer.

### 5.7.2. YAG Fiber Bragg Grating

The femtosecond-IR laser phase mask technique was used to inscribe Bragg gratings into 100 $\mu$m diameter yttrium aluminium garnet (YAG) fiber rod manufactured by *Micro-Materials Inc.* Using a 4.28-$\mu$m-pitch phase mask and 900 $\mu$J pulse energies and an $f = 30$ mm focal length cylindrical lens, a grating structure was observed under the optical microscope as shown in Figure 31.

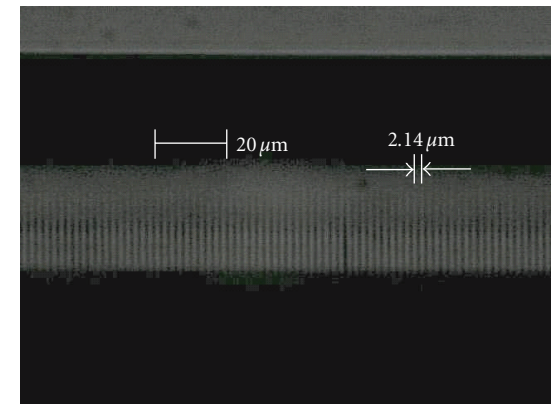


Figure 31: Optical microscope image of the grating induced in 100 $\mu$m diameter YAG fiber.

## 6. Conclusions

In this paper, we have summarized our work on femtosecond laser inscription of Bragg gratings in various materials. The use of high-peak-power femtosecond infrared radiation and a phase mask for the inscription of Bragg gratings in optical fiber and waveguides has been shown to be as easy to implement as standard ultraviolet laser grating inscription techniques. The true advantage of the femtosecond technique over the ultraviolet laser approach is that Bragg gratings can be inscribed in many more optical materials that need not be sensitive to ultraviolet radiation. In fact, to date, we have successfully inscribed grating structures in any solid material that is transparent to the infrared radiation. As a result, not only traditional Bragg grating sensor and telecommunication applications can be realized using our approach but also

applications where grating inscription was formerly not possible. Some of these applications include grating inscription in exotic waveguide structures such as crystalline sapphire optical fiber and lithium niobate waveguides, glasses such as pure silica, borosilicate, actively doped silica, fluoride, phosphate glasses, and photonic crystal fibers. Depending on the intensity regime used, high spectral quality gratings can be easily manufactured for telecommunication type applications such as dense wavelength division multiplexing or fiber laser cavity mirrors. High reliability gratings can be easily fabricated by direct writing through the standard protective coatings of fibers, removing extra processing steps in grating manufacturing. With higher intensities, high spectral quality gratings can be written that are thermally stable up to the glass transition temperature of the material into which they are written. Such gratings show potential for high temperature sensing applications (1000°C). Gratings in sapphire fiber could conceivably be used in high-temperature sensor applications up to 2000°C.

## References


[1] K. M. Davis, K. Miura, N. Sugimoto, and K. Hirao, "Writing waveguides in glass with a femtosecond laser," *Optics Letters*, vol. 21, no. 21, pp. 1729–1731, 1996.

[2] K.-I. Kawamura, N. Sarukura, M. Hirano, and H. Hosono, "Holographic encoding of fine-pitched micrograting structures in amorphous $SiO_2$ thin films on silicon by a single femtosecond laser pulse," *Applied Physics Letters*, vol. 78, no. 8, pp. 1038–1040, 2001.

[3] E. Fertein, C. Przygodzki, H. Delbarre, A. Hidayat, M. Douay, and P. Niay, "Refractive-index changes of standard telecommunication fiber through exposure to femto-second laser pulses at 810 cm," *Applied Optics*, vol. 40, no. 21, pp. 3506–3508, 2001.

[4] Y. Kondo, K. Nouchi, T. Mitsuyu, M. Watanabe, P. G. Kazansky, and K. Hirao, "Fabrication of long-period fiber gratings by focused irradiation of infrared femtosecond laser pulses," *Optics Letters*, vol. 24, no. 10, pp. 646–648, 1999.

[5] L. Sudrie, M. Franco, B. Prade, and A. Mysyrowicz, "Study of damage in fused silica induced by ultra-short IR laser pulses," *Optics Communications*, vol. 191, no. 3–6, pp. 333–339, 2001.

[6] K. O. Hill and G. Meltz, "Fiber Bragg grating technology fundamentals and overview," *Journal of Lightwave Technology*, vol. 15, no. 8, pp. 1263–1276, 1997.

[7] A. Dragomir, D. N. Nikogosyan, K. A. Zagorulko, P. G. Kryukov, and E. M. Dianov, "Inscription of fiber Bragg gratings by ultraviolet femtosecond radiation," *Optics Letters*, vol. 28, no. 22, pp. 2171–2173, 2003.

[8] K. A. Zagorulko, P. G. Kryukov, Y. V. Larionov, et al., "Fabrication of fiber Bragg gratings with 267 nm femtosecond radiation," *Optics Express*, vol. 12, no. 24, pp. 5996–6001, 2004.

[9] L. B. Fu, G. D. Marshall, J. A. Bolger, et al., "Femtosecond laser writing Bragg gratings in pure silica photonic crystal fibres," *Electronics Letters*, vol. 41, no. 11, pp. 638–640, 2005.

[10] G. Violakis, M. Konstantaki, and S. Pissadakis, "Accelerated recording of negative index gratings in Ge-doped optical fibers using 248-nm 500-fs laser radiation," *IEEE Photonics Technology Letters*, vol. 18, no. 10, pp. 1182–1184, 2006.

[11] S. J. Mihailov, C. W. Smelser, P. Lu, et al., "Fiber Bragg gratings made with a phase mask and 800-nm femtosecond radiation," *Optics Letters*, vol. 28, no. 12, pp. 995–997, 2003.

[12] S. J. Mihailov, C. W. Smelser, D. Grobnic, et al., "Bragg gratings written in all-$SiO_2$ and Ge-doped core fibers with 800-nm femtosecond radiation and a phase mask," *Journal of Lightwave Technology*, vol. 22, no. 1, pp. 94–100, 2004.

[13] D. Grobnic, S. J. Mihailov, C. W. Smelser, M. Becker, and M. W. Rothhardt, "Femtosecond laser fabrication of Bragg gratings in borosilicate ion-exchange waveguides," *IEEE Photonics Technology Letters*, vol. 18, no. 13, pp. 1403–1405, 2006.

[14] D. Grobnic, S. J. Mihailov, C. W. Smelser, F. Genereux, G. Baldenberger, and R. Vallee, "Bragg gratings made in reverse proton exchange lithium niobate waveguides with a femtosecond IR laser and a phase mask," *IEEE Photonics Technology Letters*, vol. 17, no. 7, pp. 1453–1455, 2005.

[15] D. Grobnic, S. J. Mihailov, C. W. Smelser, and H. Ding, "Sapphire fiber Bragg grating sensor made using femtosecond laser radiation for ultrahigh temperature applications," *IEEE Photonics Technology Letters*, vol. 16, no. 11, pp. 2505–2507, 2004.

[16] D. Grobnic, S. J. Mihailov, H. Ding, F. Bilodeau, and C. W. Smelser, "Single and low order mode interrogation of a multimode sapphire fibre Bragg grating sensor with tapered fibres," *Measurement Science and Technology*, vol. 17, no. 5, pp. 980–984, 2006.

[17] D. Grobnic, S. J. Mihailov, and C. W. Smelser, "Femtosecond IR laser inscription of Bragg gratings in single- and multimode fluoride fibers," *IEEE Photonics Technology Letters*, vol. 18, no. 24, pp. 2686–2688, 2006.

[18] D. Grobnic, S. J. Mihailov, R. B. Walker, and C. W. Smelser, "Characteristics of strong Bragg gratings made with femtosecond IR radiation in heavily doped $Er^{3+}$ and $Yb^{3+}$ silica fibers," in *Bragg Gratings, Photosensitivity and Poling in Glass Waveguides (BGPP '07)*, Quebec City, Canada, September 2007, paper BTuC4.

[19] D. Grobnic, S. J. Mihailov, R. B. Walker, C. W. Smelser, C. Lafond, and A. Croteau, "Bragg gratings made with a femtosecond laser in heavily doped Er-Yb phosphate glass fiber," *IEEE Photonics Technology Letters*, vol. 19, no. 12, pp. 943–945, 2007.

[20] S. J. Mihailov, D. Grobnic, H. Ding, C. W. Smelser, and J. Broeng, "Femtosecond IR laser fabrication of Bragg gratings in photonic crystal fibers and tapers," *IEEE Photonics Technology Letters*, vol. 18, no. 17, pp. 1837–1839, 2006.

[21] C. W. Smelser, S. J. Mihailov, D. Grobnic, et al., "Multiple-beam interference patterns in optical fiber generated with ultrafast pulses and a phase mask," *Optics Letters*, vol. 29, no. 13, pp. 1458–1460, 2004.

[22] C. W. Smelser, D. Grobnic, and S. J. Mihailov, "Generation of pure two-beam interference grating structures in an optical fiber with a femtosecond infrared source and a phase mask," *Optics Letters*, vol. 29, no. 15, pp. 1730–1732, 2004.

[23] C. W. Smelser, S. J. Mihailov, and D. Grobnic, "Formation of type I-IR and type II-IR gratings with an ultrafast IR laser and a phase mask," *Optics Express*, vol. 13, no. 14, pp. 5377–5386, 2005.

[24] J. Nishii, N. Kitamura, H. Yamanaka, H. Hosono, and H. Kawazoe, "Ultraviolet-raditationinduced chemical reactions through one- and two- photon absorption processes in $GeO_2$-$SiO_2$ glasses," *Optics Letters*, vol. 20, no. 10, pp. 1184–1186, 1995.

[25] P. J. Lemaire, R. M. Atkins, V. Mizrahi, and W. A. Reed, "High pressure $H_2$ loading as a technique for achieving ultrahigh UV photosensitivity and thermal sensitivity in $GeO_2$ doped optical fibres," *Electronics Letters*, vol. 29, no. 13, pp. 1191–1193, 1993.

[26] T.-E. Tsai, G. M. Williams, and E. J. Friebele, "Index structure of fiber Bragg gratings in Ge-$SiO_2$ fibers," *Optics Letters*, vol. 22, no. 4, pp. 224–226, 1997.

[27] C. W. Smelser, S. J. Mihailov, and D. Grobnic, "Hydrogen loading for fiber grating writing with a femtosecond laser and a phase mask," *Optics Letters*, vol. 29, no. 18, pp. 2127–2129, 2004.

[28] R. Kashyap, *Fiber Bragg Gratings*, Academic Press, New York, NY, USA, 1999.

[29] L. A. Weller-Brophy and D. G. Hall, "Analysis of waveguide gratings: application of Rouard's method," *Journal of the Optical Society of America A*, vol. 2, no. 6, pp. 863–871, 1985.

[30] L. A. Weller-Brophy and D. G. Hall, "Analysis of waveguide gratings: a comparison of the results of Rouard's method and coupled-mode theory," *Journal of the Optical Society of America A*, vol. 4, no. 1, pp. 60–65, 1987.

[31] Z. H. Wang, G.-D. Peng, and P. L. Chu, "Improved Rouard's method for fiber and waveguide gratings," *Optics Communications*, vol. 177, no. 1–6, pp. 245–250, 2000.

[32] C. W. Smelser, S. J. Mihailov, and D. Grobnic, "Rouard's method modeling of type I-IR fiber Bragg gratings made using an ultrafast IR laser and a phase mask," *Journal of the Optical Society of America B*, vol. 23, no. 10, pp. 2011–2017, 2006.

[33] W. X. Xie, M. Douay, P. Bernage, P. Niay, J. F. Bayon, and T. Georges, "Second order diffraction efficiency of Bragg gratings written within germanosilicate fibres," *Optics Communications*, vol. 101, no. 1-2, pp. 85–91, 1993.

[34] D. M. Rayner, A. Naumov, and P. B. Corkum, "Ultrashort pulse non-linear optical absorption in transparent media," *Optics Express*, vol. 13, no. 9, pp. 3208–3217, 2005.

[35] D. Grobnic, S. J. Mihailov, and C. W. Smelser, "High order spectral response characteristics of fiber Bragg gratings made with ultrafast IR radiation and phase mask," in *Proceedings of Bragg Gratings, Poling & Photosensitivity/ 30th Australian Conference on Optical Fibre Technology (BGPP/ACOFT '05)*, pp. 463–464, Sydney, Australia, July 2005.

[36] C. W. Smelser, S. J. Mihailov, and D. Grobnic, "Characterization of Fourier components in type I infrared ultrafast laser induced fiber Bragg gratings," *Optics Letters*, vol. 32, no. 11, pp. 1453–1455, 2007.

[37] T. Erdogan, "Fiber grating spectra," *Journal of Lightwave Technology*, vol. 15, no. 8, pp. 1277–1294, 1997.

[38] L. Dong, G. Qi, M. Marro, et al., "Suppression of cladding mode coupling loss in fiber Bragg gratings," *Journal of Lightwave Technology*, vol. 18, no. 11, pp. 1583–1590, 2000.

[39] D. Grobnic, C. W. Smelser, S. J. Mihailov, R. B. Walker, and P. Lu, "Fiber Bragg gratings with suppressed cladding modes made in *SMF-28* with a femtosecond IR laser and a phase mask," *IEEE Photonics Technology Letters*, vol. 16, no. 8, pp. 1864–1866, 2004.

[40] A. Martinez, I. Y. Khrushchev, and I. Bennion, "Direct inscription of Bragg gratings in coated fibers by an infrared femtosecond laser," *Optics Letters*, vol. 31, no. 11, pp. 1603–1605, 2006.

[41] S. J. Mihailov, D. Grobnic, and C. W. Smelser, "Efficient grating writing through fibre coating with femtosecond IR radiation and phase mask," *Electronics Letters*, vol. 43, no. 8, pp. 442–443, 2007.

[42] S. Martin, J. Krüger, A. Hertwig, A. Fiedler, and W. Kautek, "Femtosecond laser interaction with protection materials," *Applied Surface Science*, vol. 208-209, pp. 333–339, 2003.

[43] S. Baudach, J. Bonse, and W. Kautek, "Ablation experiments on polyimide with femtosecond laser pulses," *Applied Physics A*, vol. 69, no. 7, pp. S395–S398, 1999.

[44] D. Grobnic, S. J. Mihailov, C. W. Smelser, and R. T. Ramos, "Ultrafast IR laser writing of strong Bragg gratings through the coating of high Ge-doped optical fibers," *IEEE Photonics Technology Letters*, vol. 20, no. 12, pp. 973–975, 2008.

[45] W. H. Loh, B. N. Samson, L. Dong, G. J. Cowle, and K. Hsu, "High performance single frequency fiber grating-based erbium/ytterbium-codoped fiber lasers," *Journal of Lightwave Technology*, vol. 16, no. 1, pp. 114–118, 1998.

[46] L. Dong, W. H. Loh, J. E. Caplen, J. D. Minelly, K. Hsu, and L. Reekie, "Efficient single-frequency fiber lasers with novel photosensitive Er/Yb optical fibers," *Optics Letters*, vol. 22, no. 10, pp. 694–696, 1997.

[47] Y. Lai, A. Martinez, I. Khrushchev, and I. Bennion, "Distributed Bragg reflector fiber laser fabricated by femtosecond laser inscription," *Optics Letters*, vol. 31, no. 11, pp. 1672–1674, 2006.

[48] E. Wikszak, J. Thomas, J. Burghoff, et al., "Erbium fiber laser based on intracore femtosecond-written fiber Bragg grating," *Optics Letters*, vol. 31, no. 16, pp. 2390–2392, 2006.

[49] M. Bernier, D. Faucher, R. Vallée, et al., "Bragg gratings photoinduced in ZBLAN fibers by femtosecond pulses at 800 nm," *Optics Letters*, vol. 32, no. 5, pp. 454–456, 2007.

[50] N. Groothoff, J. Canning, E. Buckley, K. Lyttikainen, and J. Zagari, "Bragg gratings in air-silica structured fibers," *Optics Letters*, vol. 28, no. 4, pp. 233–235, 2003.

[51] D. Grobnic, H. Ding, S. J. Mihailov, C. W. Smelser, and J. Broeng, "High birefringence fibre Bragg gratings written in tapered photonic crystal fibre with femtosecond IR radiation," *Electronics Letters*, vol. 43, no. 1, pp. 16–18, 2007.

[52] V. Mizrahi, D. J. DiGiovanni, R. M. Atkins, S. G. Grubb, Y.-K. Park, and J.-M. P. Delavaux, "Stable single-mode erbium fiber-grating laser for digital communication," *Journal of Lightwave Technology*, vol. 11, no. 12, pp. 2021–2025, 1993.

[53] S. Kreger, S. Calvert, and E. Udd, "High pressure sensing using fiber Bragg gratings written in birefringent side hole fiber," in *Proceedings of the 15th Optical Fiber Sensors Conference Technical Digest (OFS '02)*, vol. 1, pp. 355–358, Portland, Ore, USA, May 2002.

[54] T. Erdogan and V. Mizrahi, "Characterization of UV-induced birefringence in photosensitive Ge-doped silica optical fibers," *Journal of the Optical Society of America B*, vol. 11, no. 10, pp. 2100–2105, 1994.

[55] P. Lu, D. Grobnic, and S. J. Mihailov, "Characterization of the birefringence in fiber Bragg gratings fabricated with an ultrafast-infrared laser," *Journal of Lightwave Technology*, vol. 25, no. 3, pp. 779–786, 2007.

[56] D. Grobnic, S. J. Mihailov, and C. W. Smelser, "Localized high birefringence induced in *SMF-28* fiber by femtosecond IR laser exposure of the cladding," *Journal of Lightwave Technology*, vol. 25, no. 8, pp. 1996–2001, 2007.

[57] A. D. Kersey, M. A. Davis, H. J. Patrick, et al., "Fiber grating sensors," *Journal of Lightwave Technology*, vol. 15, no. 8, pp. 1442–1463, 1997.

[58] D. Grobnic, C. W. Smelser, S. J. Mihailov, and R. B. Walker, "Long-term thermal stability tests at 100°C of silica fibre Bragg gratings made with ultrafast laser radiation," *Measurement Science and Technology*, vol. 17, no. 5, pp. 1009–1013, 2006.

[59] A. Wang, S. Gollapudi, R. G. May, K. A. Murphy, and R. O. Claus, "Sapphire optical fiber-based interferometer for high

temperature environmental applications," *Smart Materials and Structures*, vol. 4, no. 2, pp. 147–151, 1995.

[60] M. G. Xu, J.-L. Archambault, L. Reekie, and J. P. Dakin, "Discrimination between strain and temperature effects using dual-wavelength fibre grating sensors," *Electronics Letters*, vol. 30, no. 13, pp. 1085–1087, 1994.

[61] J. D. Love, W. M. Henry, W. J. Stewart, R. J. Black, S. Lacroix, and F. Gonthier, "Tapered single-mode fibres and devices. I. Adiabaticity criteria," *IEE Proceedings in Optoelectronics*, vol. 138, no. 5, pp. 343–354, 1991.

[62] E. A. Stach, V. Radmilovic, D. Deshpande, A. Malshe, D. Alexander, and D. Doerr, "Nanoscale surface and subsurface defects induced in lithium niobate by a femtosecond laser," *Applied Physics Letters*, vol. 83, no. 21, pp. 4420–4422, 2003.

Hindawi Publishing Corporation
Laser Chemistry
Volume 2008, Article ID 170632, 13 pages
doi:10.1155/2008/170632

*Research Article*

# Laser-Induced Backside Wet Etching of Transparent Materials with Organic and Metallic Absorbers

**K. Zimmer and R. Böhme**

*Leibniz-Institut für Oberflächenmodifizierung, Permoserstraße 15, 04318 Leipzig, Germany*

Correspondence should be addressed to K. Zimmer, klaus.zimmer@iom-leipzig.de

Received 24 July 2008; Accepted 27 August 2008

Recommended by Jacques Albert

Laser-induced backside wet etching (LIBWE) allows the high-quality etching of transparent materials for micro- and nanopatterning. Recent own results of LIBWE with hydrocarbon and metallic absorbers (H- and M-LIBWE) are summarized and compared with selected results of other groups regarding the etching process and the etched surface. Significant results on the impact of the liquid absorber, the material and the wavelength, and the pulse length of the laser to the etching are selected for this comparison. The etching of submicron-sized periodic structures in sapphire and fused silica with interference techniques and the selection of the preferred method in dependence on the material and the processing goal discussed. The experimental results are discussed on a thermal model considering both interface and volume absorption of the laser beam. These results have the conclusion that the etching at M-LIBWE is mainly due to material melting and evaporation whereas at H-LIBWE, a modified near-surface region with a very high absorption is ablated.



## 1. Introduction

The high-quality, precise, low-damage processing of transparent dielectrics by lasers with respect to high-quality micro- and nanopatterning of these materials is still a challenge [1–3]. Therefore, the lateral and vertical resolution of the patterning process should be reduced and the surface quality, that is roughness, waviness, and processing-induced near-surface material modification, must be improved.

In addition to traditionally used nanosecond lasers that allow ablation of such materials, for example, fused silica, at high laser fluences [4, 5], nowadays ultrashort pulse or VUV lasers are exploited increasingly [6–9]. These lasers cause material ablation after multiphoton and single-photon excitation and enable material processing at low laser fluences with lower ablation rates which can result in improved surface qualities. In consequence, one key for high-quality materials processing is a high absorption of the laser beam by the material, in particular the surface. This results in near-surface energy deposition, high energy densities, and fast phase transitions and prevents excessive melting of the material already at low laser fluences.

With the aim of absorption enhancement of transparent materials, two beam laser ablation techniques have been developed. Principally, a first low-fluence high-photon-energy laser is used for the generation of free electrons and temporary defects whereas a second high-fluence (UV) laser is employed for ablation after photon absorption by the laser-induced transient absorption centres [10, 11]. Such temporary modifications for surface absorption enhancement were applied also to backside ablation. Zhang etal. introduced laser-induced plasma-assisted ablation (LIPAA) that makes use of laser-induced plasma from metal plate placed behind the transparent sample. The laser plasma modifies the backside of the transparent sample and the enhanced laser absorption resulting in backside ablation [12–16].

Nowadays a number of indirect laser processing methods is in development that aims also to a near-surface absorption of the laser energy at the backside of transparent samples. However, the enhanced surface/interface absorption is

Table 1: Main characteristics of the backside etching techniques with nanosecond laser pulses in comparison to laser ablation.

| Characteristic | Technique | | |
|---|---|---|---|
| | H-LIBWE | M-LIBWE | Ablation |
| Threshold fluence | Low | High | High |
| Laser wavelength | UV/vis | UV-IR | UV (IR) |
| Etch rate | Average | High | High |
| Incubation effects | Distinct | No | Noticeable |
| Etching quality | Very good | Good | Average |

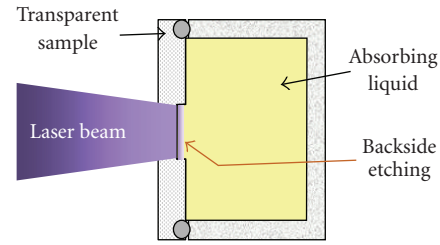


Figure 1: Basic experimental set-up for LIBWE.

achieved at these methods by additional materials. Depending on the additive to enhance the energy deposition near the transparent solid surface, different techniques can be distinguished.

The laser etching by surface-adsorbed layer (LESAL) technique uses hydrocarbon layers adsorbed at the backside of the sample to enhance the laser beam absorption [17–20]. Recently, the so-called laser-induced backside dry etching (LIBDE) was demonstrated by Hopp etal. using a thin metal film for laser energy deposition [21]. Laser-induced backside wet etching (LIBWE) developed by Niino's group makes use of the high absorption of organic liquids (H-LIBWE—hydrocarbon LIBWE) for excimer laser wavelengths [22–24]. Previously Shafeev performed material processing at the interface to liquids with a similar set-up but uses much higher laser fluences of a high repetition rate copper vapour laser [25, 26]. Zimmer et al. applied liquid metals (M-LIBWE—liquid metal LIBWE) instead of the initially exploited organic solutions for backside wet etching [27–29].

To ensure a sufficiently high absorption of the organic liquids, UV excimer lasers (XeF, XeCl, KrF, ArF) have to be used for H-LIBWE. Higher harmonics of high repetition rate Nd:YAG lasers (530 nm, 266 nm) were applied for etching, too [30, 31]. However, the utilization of visible wavelengths requires special dyes for absorption and in addition higher laser fluences [30]. For very high repetition rates, the bubble lifetime can exceed the pulse interval whereby the etching process is influenced and lower etch rates were found [30, 31]. A wide range of liquids were investigated for H-LIBWE comprising mainly solutions of dyes in organic solvents [22, 32], solutions of inorganic and organic absorbers in water [25, 26, 33, 34], and liquid metals [27, 35]. Only some experiments on LIBWE with ultrashort pulse lasers are known [36, 37].

The most studies aim at the effects of specific material processing conditions (liquid, wavelength, etc.) on the etching process and the properties of the etched surface. The effect of H-LIBWE to the properties of the processed surface was investigated in [38, 39] and gave evidence for a strong surface modification and incubation. Some studies aim at the comparison of experimental LIBWE results with (numerical) model calculations [32, 40]. In [32], it was found that the interface temperature at H-LIBWE is below the melting temperature of the fused silica for the laser fluences at the etch threshold; however, in this work interface modifications were neglected. In Table 1, the most important characteristics of patterning processes for transparent materials are listed for H- and M-LIBWE in comparison to laser ablation.

All the mentioned backside etching techniques have been used for micro- and nanopatterning of different transparent glass and crystals [22, 23, 41–43]. Examples are the etching of submicron and nanometer gratings in fused silica [44–46] and sapphire [47], the submicron patterning on-the-fly with one laser pulse [48], the etching of micro-optical elements [18, 39, 42, 49–53], and the fabrication of arrays for biomedical purposes [30, 54].

## 2. Experimental

The basic configuration of the experimental set-up for LIBWE is shown in Figure 1. The etching chamber holds the substrates and contains the liquid absorber. The chamber assembly is often incorporated into a laser workstation or a similar installation for precise processing and full parameter control as has been described elsewhere [30, 55]. In summary, the laser beam goes trough the transparent sample and is absorbed at its backside by the liquid.

Mainly the following laser parameters were varied with one set-up: the spot size, the laser fluence, the pulse number. Depending on the laser source and the beam quality, the laser beam is directly focussed or used for mask projection. In consequence, the intensity distribution of the laser spot is either Gaussian-like for solid state lasers (e.g., Nd:YAG) or uniform with an average deviation in the range of ±5% for excimer lasers. The wavelength, the pulse length, and the temporal pulse shape are also characteristics of the used laser source: nanosecond (UV: XeF, KrF, ArF excimer lasers and IR: Nd:YAG laser; $tp \sim 20, \ldots, 30$ nanoseconds) as well as picosecond laser pulses (4th Nd:YAG laser, $tp$ = 150 picoseconds) were applied. Usually low repetition rates (<10 Hz) were used in the basic experiments. To achieve high spatial resolution down to the submicron range, interference techniques such as phase mask projection [44] and interferometer set-ups [47] were applied.

### 2.1. Samples

For backside etching, double-side polished high-quality substrates were used. The material of choice in most of the experiments was optical-grade fused silica (FS). Further,

crystalline materials such as quartz, sapphire, and fluorides ($CaF_2$, $MgF_2$) with a thickness of some mm were utilized. To allow high-resolution mask projection, thin samples (<1 mm) were used. The surface roughness was always in the range of 1nm rms or even lower; the fused silica samples regularly have a roughness of about 0.2 to 0.3 nm rms. The samples were used as received without further cleaning.

## 2.2. Liquids

Two classes of liquids are used: (i) *hydrocarbon liquids* that are solutions of pyrene in toluene (py:toluene), acetone, tetrachloroethylene, and so forth, at concentrations of usually 0.5 M (M = mol/L) and (ii) *liquid metals* such as gallium (Ga) and mercury (Hg).

## 2.3. Processing Procedure

After mounting the samples to the chamber, the etching was performed. For large area processing, for example, writing of arrays or micro-optical patterns, a circulating pump assembly might be used [30]. This allows the continuous exhaust, the filtering, and the cooling down of the used solution. After processing the samples were cleaned from the liquid absorber either by washing in organic solvents (acetone, ethanol, etc.) or by etching in suitable acids (e.g., nitric acid); ultrasonic can be applied, in addition. Subsequently, the samples were washed in water and dried in a dry nitrogen stream. For removing adherent carbon contaminations a soft oxygen-plasma cleaning procedure was applied, too [37].

## 2.4. Analytic of Etched Surfaces

The topography over the full range of spatial frequencies, laser-induced modifications, and the near-surface material properties (composition, absorption structure, etc.) of the etched samples were investigated by the following analytical techniques: Scanning electron microscope (SEM, either a JEOL JSM 6600 or a Zeiss CARL ZEISS Ultra 55) was employed for taking top-view or cross-section images of the etched samples. White-light interference microscopy (e.g., Micromap 512) was frequently performed to measure the etch depth, the topography, the waviness, and the roughness ($\mu$m-range) of the etched surfaces with an accuracy down to 1 nm in depth. High-resolution investigations of the topography and the roughness are performed by AFM measurements using a Nanoscop III instrument. The transmission of irradiated sample regions was measured utilizing a scanning UV/VIS spectrometer (Shimadzu UV-2101PC UV/VIS scanning spectrophotometer, $\lambda = 200$–$800$ nm). For determining structural defects in solid material and near-surface contaminations channeling/RBS- (Rutherford Back Scattering) measurements with a 2MeV-$He^{2+}$ beam of about 1.5 mm diameter were performed.

# 3. Experimental Results for Laser Etching of Transparent Materials

As already mentioned the most principal task of the rear side liquid is the absorption of the laser radiation near the solid backside surface. Therefore can be expected a better the material etching for laser beam absorption closer to the surface. Two basic classes of liquid absorbers must be considered:

(i) hydrocarbon liquids or solutions (H-LIBWE),

(ii) liquid metals (M-LIBWE).

The classical H-LIBWE requires nanosecond-pulsed UV or VIS laser to match the absorption of the liquid. Nevertheless, typical laser penetration depths of organic liquids are some microns. The liquid metal LIBWE permits the utilization of IR laser pulses for etching since metal absorbs efficiently over the whole range of the spectrum with a short penetration depths ($\alpha^{-1} \ll 100$ nm).

Typical images of the etched fused silica surfaces are shown in Figure 2 for H-LIBWE with py:toluene in (a) and M-LIBWE with gallium in (b). The size and the shape of the edges and the etched bottom show a very good quality in both cases. Although the microroughness is low for both techniques, M-LIBWE shows a higher waviness of the etched surface that looks like frozen waves. These features together with the high etch rates let us suggest that the material etching for M-LIBWE involves a molten phase that resolidifies after material ejection.

## 3.1. Etch Rate of Fused Silica

The most accessible and informative experimental result is the etch rate of the material depending on the laser fluence and the pulse number. The etch rate of fused silica for 248 nm excimer laser pulses depending on the laser fluence and the pulses number is shown in comparison for H-LIBWE with a 0.5 mol/L pyrene/toluene solution (0.5 M py:toluene) and M-LIBWE with gallium in Figure 3, respectively.

At least three etching characteristics are different for both approaches: (i) M-LIBWE offers much higher etch rates than H-LIBWE but (ii) requires much higher laser threshold fluences for etching. In addition, (iii) strong incubation effects were detected at H-LIBWE whereas M-LIBWE features almost no incubation effects [27, 56]. The higher threshold fluences at M-LIBWE can be explained in parts by the higher reflectivity of the interface and the higher thermal conductivity of the liquid metal absorber, respectively [28, 35]. Because all other experimental parameters are similar, the incubation must be linked to the used liquid that should cause an additional laser irradiation-induced change of the interface region in order to enhance the laser absorption either in the liquid or in the near-solid region. The negligible incubation effect at M-LIBWE can be explained by the high absorption coefficient and the high stability of the liquid metals. On the other hand, the organic liquids and solutions used at H-LIBWE suffer from photothermal and/or

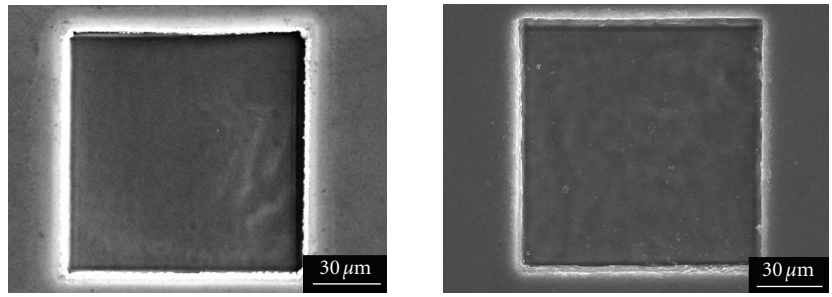


(a) (b)

Figure 2: SEM images of etched square patterns in fused silica with $100 \times 100\,\mu m^2$ by 248 nm excimer laser: (a) H-LIBWE with py:toluene (300 pulses at $1.4\,J/cm^2$) and (b) M-LIBWE with Ga (30 pulses at $3.4\,J/cm^2$).

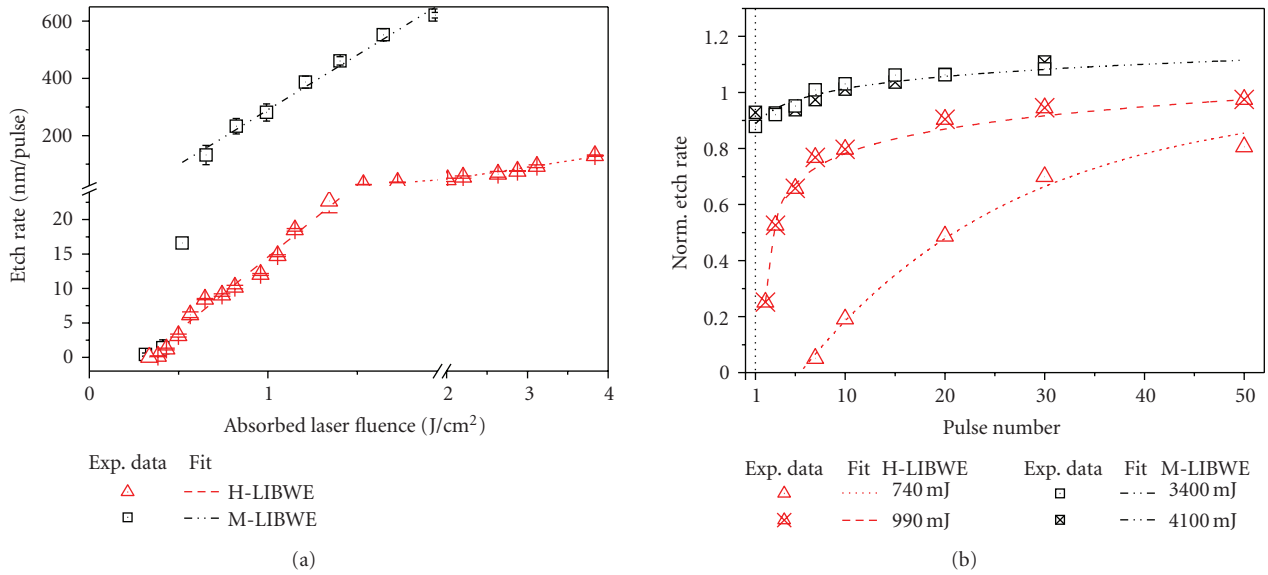


(a) (b)

Figure 3: Etch rate of fused silica with 248 nm excimer laser pulses and a spot with size of $100 \times 100\,\mu m^2$. Comparison of H-LIBWE with a 0.5 M py:toluene and M-LIBWE with gallium. (a) Etch rate depending on the laser fluence. (b) Normalized etch rate depending on the pulse number.

photochemical decomposition under intense pulsed UV laser irradiation [57].

The analysis of hydrocarbon solutions showed among a lot of soot a number of decomposition products at HPLC-MS due to laser exposure. However, the composition of the liquid is not altered in this extent to explain a much higher (local) absorption coefficient of the liquid [58]. The decomposition of hydrocarbon liquids under UV laser irradiation can result in conjunction with high temperatures to the formation of excited atoms or radicals. This can be of interest when halogenated hydrocarbons are used that might form chemical radicals that are able to etch solid materials directly [59].

### 3.2. Etch Characteristics for Different Materials and Absorbing Liquids

The etch characteristics, for example etch rate and surface morphology, depend on the used liquid for both classes of liquid absorbers: hydrocarbon solutions and liquid metals. The etch rates of fused silica are shown in Figure 4 for two different absorbers in each case—gallium and mercury and py:toluene and py:halogenated benzenes. In both cases, the threshold fluence and the etch rate dependency are affected by the used liquid. The comparison for M-LIBWE in Figure 4(b) shows that mercury has a less etch threshold (Hg: $0.76\,J/cm^2$; Ga: $1.3/2.1\,J/cm^2$) and a slightly lower etch rate than gallium. However, in both cases a linear rise of the etch rate, no incubation effects, and similar etch pits with well-defined edges and flat bottoms have been observed [27, 29]. The lower threshold of mercury can be explained by the twofold lower thermal diffusion length (Hg: $0.66\,\mu m$; Ga: $1.24\,\mu m$ at $tp = 25$ nanoseconds). The lower slope of the etch rate raise for mercury can be discussed also by the different material properties of mercury.

The etch rate dependencies achieved for H-LIBWE of fused silica using either pyrene-doped toluene or mono-halogenated benzenes (0.5 M) are rather dissimilar; however,

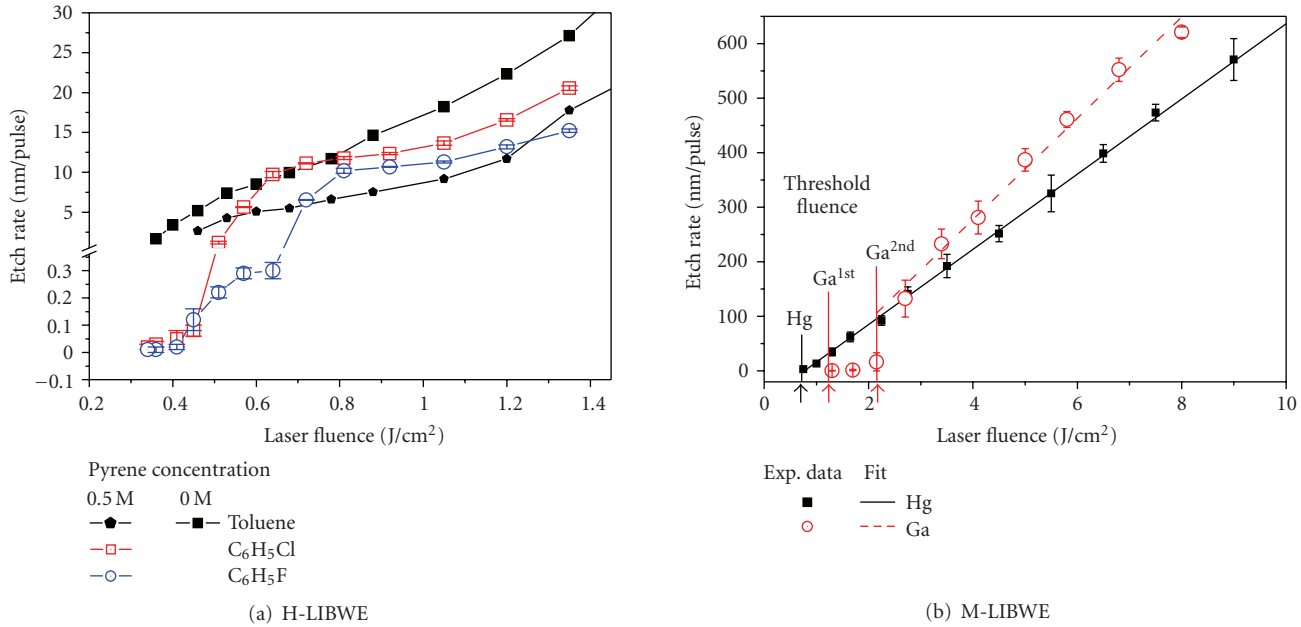


FIGURE 4: Etch rates of fused silica for different liquids at 248 nm laser pulse irradiation. (a) Etch rate of fused silica for toluene with and without solved pyrene and for halogenated benzenes (fluorine and chlorine benzene) at 300 pulses. (b) Etch rate for fused silica at 30 pulses using gallium and mercury as liquid metals.

above a certain laser fluence of about 0.7 J/cm$^2$, similar etch rates and a linear rise can be observed. Especially at low fluences, a much lower rate and a higher slope of the rate were measured for the halogenated solvent although the absorption coefficient was similar due to the high pyrene concentration. It should be noted that the threshold fluence for the pyrene-doped solutions is similar (~0.33 J/cm$^2$) but significantly less than the threshold for pure toluene (0.45 J/cm$^2$). The etch rate with pure toluene also increases almost linearly but is only a bit less than that achievable with pyrene. Though the threshold depends on the liquid absorption, there is no linear correlation as the pyrene doping causes a sevenfold increase of the absorption but the threshold is reduced only little.

The laser-induced decomposition of halogenated hydrocarbons, however, can result in halogen radicals [57, 58, 60, 61] and can, therefore, contribute to the etching [58, 62]. However, this does not explain the lower etch rate if at halogenated organics the same processes occur. Therefore, the halogen radicals may also affect the overall processes of the etching, for example, in the liquid, vapour, bubble, and so forth, where different chemical reactions and physical processes might occur.

Similar to the liquid absorber, the properties of the material etched by LIBWE affect the etch result. The SEM images in Figure 5 depicting etch pits in sapphire, calcium fluoride ($CaF_2$), and fused silica show this clearly. In contrast to the flat bottom and the well-defined edges of the fused silica, the etched patterns of both sapphire and $CaF_2$ feature an uneven, grainy surface and an irregular edge.

The main differences of the materials that can account for the morphological changes are the thermal properties and the mechanical and chemical resistance of the materials. For instance, the thermal conductivity $k$ of the crystals (sapphire: 40 and $CaF_2$: 9.7 W·(m·K)$^{-1}$) is much higher than that of fused silica (1.4 W·(m·K)$^{-1}$). Therefore, the higher heat diffusion length forces the heat dissipation and does not allow as high heating rates and high temperatures as for fused silica. With these arguments, the surface morphology of sapphire and $CaF_2$ can be interpreted by melting, melt ejection, and resolidification of a near-surface layer. The formation of microcracks in these brittle materials must be taken into account in addition.

### 3.3. Modification of the Etched Surface at H-LIBWE

The surfaces of etched fused silica and quartz samples were investigated with different analytical techniques such as XPS, Raman spectroscopy, and RBS to study the process-induced near-surface chemical and structural modifications [23, 39, 62, 63]. The kind and the amount of the modification depend on the applied laser fluence and the pulse number [58]. In general, with increasing laser fluence, the mainly found carbon contaminations at low fluences reduce whereas the depth of structural transformations increases.

To study the impact of the near-surface material modifications on the etching process, optical transmission measurements were performed. The inset of Figure 6 shows the transmission of an etched fused silica sample (0.76 J/ccm$^2$) depending on the wavelength (200 nm to 800 nm). In general, a reduced transmission in the UV is obvious and can also be observed for other fluences and pulse numbers.

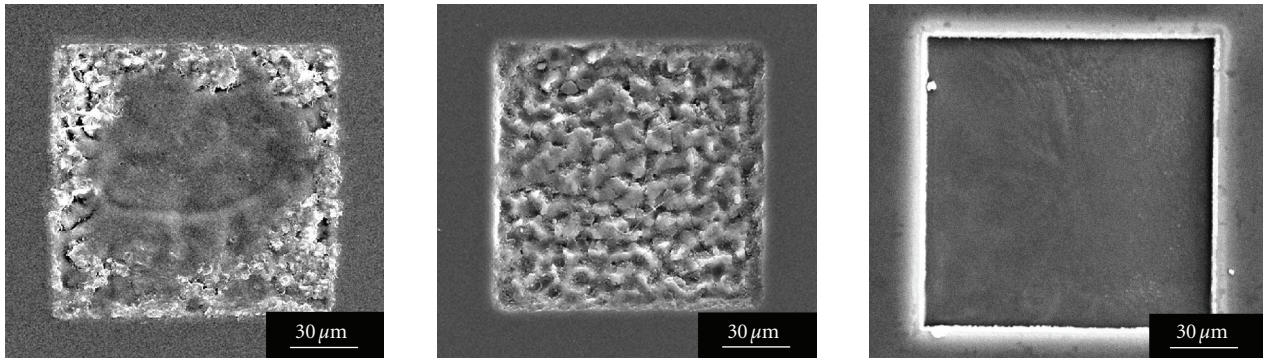


(a) (b) (c)

Figure 5: Surface morphology of H-LIBWE etched sapphire (a) and $CaF_2$ (b) in comparison to the standard material fused silica (c).

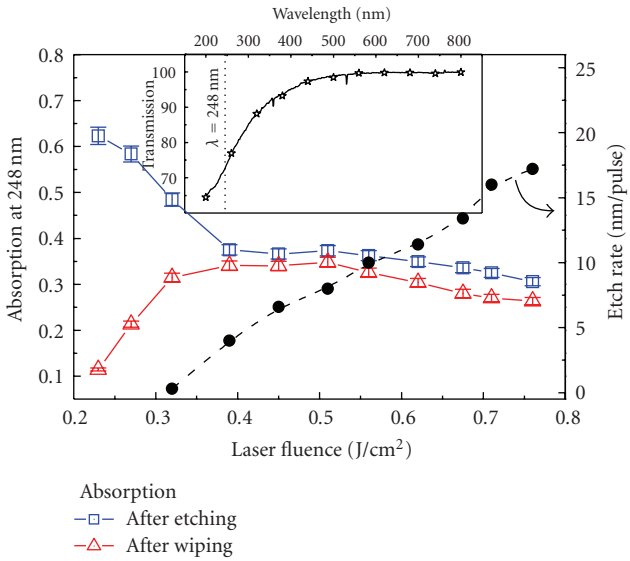


Figure 6: Absorption of etched fused silica surface depending on the laser fluence. The inset shows spectra of an etched fused silica sample (F = 0.76 J/cm$^2$) with a reduced transmission in the UV.

According to [58], the spectrum can be interpreted as a superposition of the spectra from carbon and defect-enriched fused silica. Thus, the observed changes of the spectra taken at different etch conditions also refer to alterations of the surface modification. The change of the absorption at $\lambda = 248$ nm with the applied laser fluence for etched and wiped samples is shown in Figure 6, too. It should be noted that surface modifications occur below the threshold and the modifications can be divided in loosely adherent—that can be whipped away—and incorporated modifications. Together with the XPS and Raman spectroscopy results, the loosely adherent modifications are mainly carbon or carbon products from the decomposition of the organic absorber [58]. The near-surface fused silica modifications can be removed completely by ion beam sputtering of about 50 nm [58, 64]. This depth is similar to the depth of structural defects found in quartz [63].

The remarkable high absorption of a thin (<50 nm) near-surface region of about 30 to 40% is due to structural modifications of the fused silica and a chemical modification of the surface or by a carbon-containing film.

## 3.4. Etching of Submicron Patterns in Transparent Materials

From the basic results, it is clear that micropatterning of fused silica can be easily achieved with different liquids and laser sources. A lot of examples are known for different technical fields. However, with the reduction of the feature size, the requirements for the etching process are enhanced concerning the resolution of the etching process, the homogeneity of the etching, and the smoothness of the surface.

### 3.4.1. Submicron Grating Etching in Fused Silica

These requirements for etching of submicron patterns are fulfilled for fused silica for both H- and M-LIBWE. The first experiments on etching high-resolution 1 D gratings with a period of ~750 nm are presented in [44]. Depending on the average fluence and the pulse number, grating depths of up to 180 nm with a nearly sinusoidal profile were achieved. This profile mainly results from the sine interference pattern together with the linear etch rate rise. However, additional to the gratings an overall etching, that is, etching in the fringes minima at $F \sim 0$, was observed especially at higher laser fluences and pulse numbers. Further experiments on overetching of already prepatterned substrates showed that the modulation depth of submicron patterns reduces at overetching with a homogeneous laser beam [65]. The effect was discussed by the better heating of topographic peaks by heat transport from the liquid but the effect seems to be too strong to be completely explained therewith.

Results on high-resolution etching of surface relief line gratings in fused silica down to 104 nm periods presented in [45, 46] show a reduction of the grating depth with the

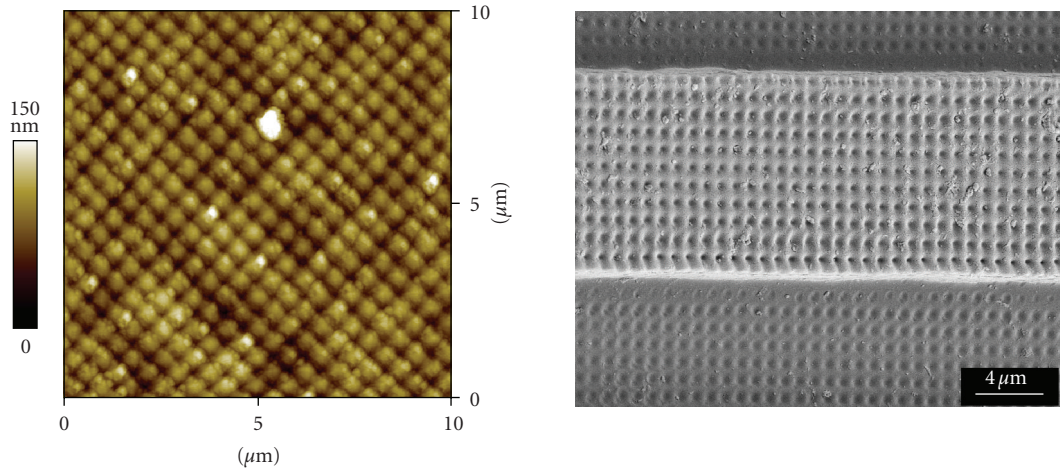


(a) (b)

Figure 7: Submicron 2 D gratings with periods $p \sim 550$ nm and 780 nm etched in fused silica, respectively. (a) Grating obtained by H-LIBWE with a py:acetone solution and (b) grating etched on a prepatterned substrate (line width $\sim 7.5\,\mu$m, prepattern depth $\sim 3\mu$m) using mercury as absorber.

reduction of the period. This finding can be discussed by the reduction of the modulation of the interface temperature because of the thermal diffusion length of the material given by $L_T = 2 \cdot \sqrt{D_T \cdot t}$ with $D_T = k/\rho \cdot c_p$. The thermal diffusion lengths $L_T$ for fused silica and organic solvents are in the order of 0.18 and 0.09 $\mu$m for the used 8-nanosecond 266 nm laser pulses [45, 46] and about 0.3 $\mu$m and 0.15 $\mu$m for pulse lengths of 25 nanoseconds, respectively. For pattern periods $p$ of similar or smaller than thermal diffusion length (e.g., $\sim$100 nm), the heat transport smears interference patterns and only shallow gratings are etched whereas $\sim 0.5\,\mu$m gratings can be etched proper. This means that high-resolution patterns with high modulation depths can be hardly obtained for materials—either the solid and the liquid or both—with high $L_T$.

In Figure 7, 2 D gratings in FS with periods of about 550 nm and 780 nm are shown for H- and M-LIBWE in comparison. The maximal achieved grating depth of $\sim$160 to 180 nm is similar in both cases and is achieved near the threshold of grating etching. However, with M-LIBWE gratings with a depth of 60 nm can be etched with one laser pulse and can enable submicron patterning "on-the-fly" [48]. The thermal diffusion length of $\sim 0.6\,\mu$m can result in a strong overetching effect especially at rising laser fluence that can occur than already with the first laser pulse.

### 3.4.2. Submicron Grating Etching by Ultrashort Laser Pulses

To overcome the problem and enable high-quality etching of highly conductive materials by LIBWE, shorter laser pulses must be applied. For 150-picosecond pulse duration, for example, of the fourth harmonic (266 nm) of an EKSPLA Nd:YAG-laser system, the thermal diffusion length is reduced by a factor greater than 10 and results in thermal diffusion lengths of less than 200 nm for application-relevant highly conductive materials. For sapphire with a rather high thermal diffusivity $D$ of $1.63 \times 10^{-5}$ m$^2$/s, a length of 70 nm can be calculated.

Surface relief gratings were inscribed in sapphire and in fused silica as well as in different fluorides using H-LIBWE with 266 nm, 150-picosecond laser pulses by applying different interference techniques, for example, phase mask placed in contact to the front surface of the sample. As shown in Figure 8, the quality of surface relief gratings with an average depth of $\sim$50 nm etched in sapphire is similar to that achieved for fused silica. However, the threshold laser fluence for etching of gratings is in parts higher for sapphire due to the higher melting and evaporation temperature and due to the, of course, higher thermal conductivity. Details for sapphire grating etching are given in [47].

Therefore, H-LIBWE with ultrashort laser pulses is favourable for etching patterns in several dielectrics with periods shorter than 500 nm due to the combination of the advantages of ultrashort processing and backside etching [37]. The etching of well-developed 100 nm patterns with ultrashort laser pulse H-LIBWE in fused silica was shown recently [66].

## 4. Mechanism of Laser Etching

### 4.1. Processes at Laser Backside Etching

The irradiation of the solid-liquid interface by pulsed laser results in a number of processes in both materials, for instance fast heating, transient pressure, shock waves, melting and boiling, bubble formation and collapse, and modification or decomposition of the materials. These processes are linked together in a complex manner and finally cause materials erosion. However, it is generally accepted that laser absorption and heating of the near-interface regions of both materials is the main process for backside etching.

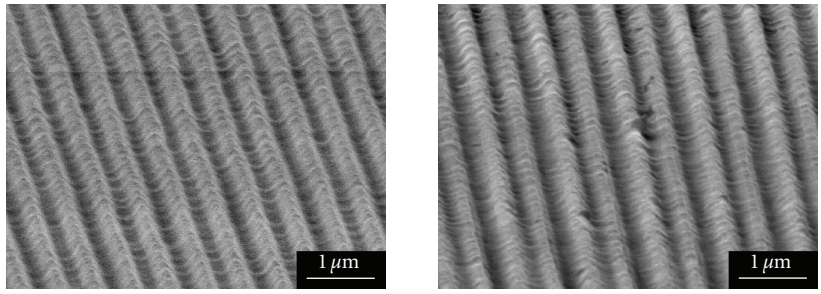


(a) (b)

Figure 8: H-LIBWE etched line gratings with a period of ~530 nm in fused silica (a) and sapphire (b). The SEM images show a similar quality of the inscribed gratings.

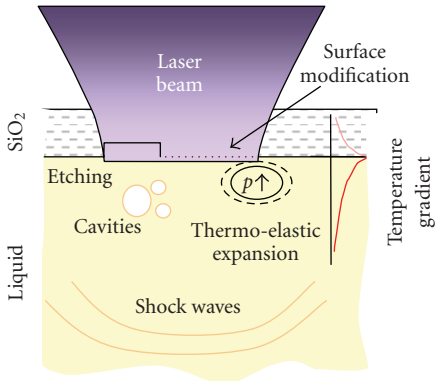


Figure 9: Sketch of the main processes at LIBWE. These processes, however, contribute to etching for both LIBWE versions in a different manner.

Figure 9 shows a sketch of the processes in discussion that are involved in the etching mechanism.

In consequence of the laser heating during LIBWE, the softening and the material [23] or phase transitions [32, 40, 50, 64] are discussed with regards to materials erosion. The softened, destabilized, weakened, or even melted material region near the surface might be expelled by mechanical forces resulting from the fast heating, shockwaves, or bubble formation [23]. The complete modeling of all processes is extremely complex as thermal, mechanical, chemical, and transport processes interacting each other within a very short time have to be considered.

## 4.2. Modeling of Thermal Processes at Laser Backside Etching

Thermal processes are very important for backside etching processes with nanosecond lasers but cannot be neglected for even shorter pulses. A correct solution for the temperature field is very complex because a number of processes are simultaneously coupled to the diffusive heat transfer. Therefore, usually the simple models considering only heat diffusion are used.

In Figure 10, the laser absorption and the temperature profiles are sketched together with the characteristic lengths ($L_T$, $L_O = \alpha^{-1}$) for H- and M-LIBWE. In addition, the laser intensity $I_L$ and the laser pulse energy accounting for interface heating $E_P^{(I)}$ are shown. From Figure 10, it is clear that the absorbed laser radiation is utilized in a different manner for heating at both LIBWE approaches. Whereas at M-LIBWE ($L_O^L \ll L_T^L$), the high thermal flux determines the temperature evolution at H-LIBWE ($L_O^L \gg L_T^L$), the laser energy absorption in the liquid mainly affects the temperature distribution and only minor heat energy dissipates from the interface region to the liquid. Therefore, the highest temperature occurs at H- and M-LIBWE in the liquid and at the interface, respectively. It is also seen, that the temperature profiles at different times ($t1 < tp$ and $tp$) reflect the different processes.

Although the primary laser-matter interaction upon ultrashort laser irradiation is often different due to the additional processes induced by the short pulses, for example, multiphoton absorption and other nonlinear phenomena, the absorbed energy finally is transformed into heat and can induce similar processes as with nanosecond lasers.

## 4.3. Thermal Calculations for LIBWE

For the rough estimation of the influence of experimental parameters on the etching process, simple thermal models have been developed. As only thermal processes are considered—this does not include the processes of material etching itself—they are only suitable to estimate specific values, for example, the threshold fluence $Fth$ or a critical interface temperature. In such models, regularly constant material parameters and no phase transitions are presumed.

Analytical solutions of the heat equation for surfaces are known for the approximations of fixed coefficients, a constant laser power, and neglecting phase transitions [2, 67]. Further, Carslow/Jaeger gives a solution for heating of an internal interface for interface absorption that can be well applied for M-LIBWE considering the reflectivity and the absorption of the interface [67].

This solution is not valid for H-LIBWE because the absorption coefficient at H-LIBWE is much less, a remarkable interface absorption was measured, and $(\alpha^L)^{-1} \gg L_T^L$.

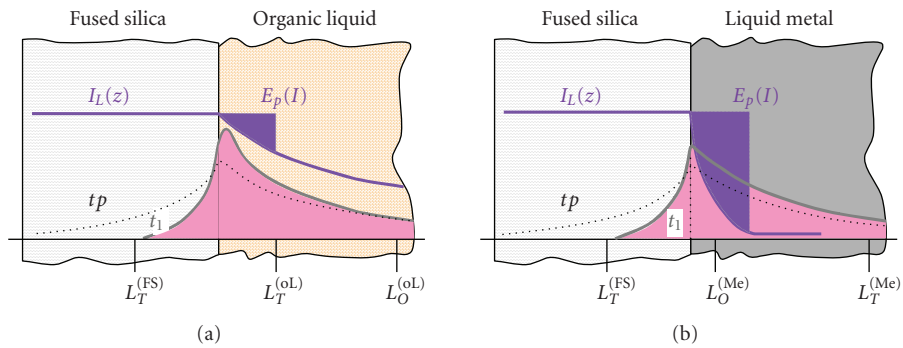


FIGURE 10: Sketches of the temperature profiles, the laser intensity, and the absorbed laser energy together with the characteristic lengths are shown for H- and M-LIBWE. $E_p$ is the laser pulse energy causing the heating of the interface.

However, an approximation for calculating the interface temperature $T_I$ at H-LIBWE is given in [64]. This approximation combines the analytical solution for the interface absorption with a caloric approach accounting for the absorption in the liquid.

An analytical solution for $T_1$ for LIBWE for the heating by the laser pulse with a duration $\tau_p$ ($0 \le t \le \tau_p$) considering both volume and interface absorption is given in [68] to be

$$T_I = \frac{\sqrt{D_L}}{k_{\mathrm{FS}} \cdot \sqrt{D_L} + k_L \cdot \sqrt{D_{\mathrm{FS}}}} \cdot \left\{ I_V^L \cdot \frac{\alpha_L}{4} \cdot L_T^L \cdot L_{\mathrm{T}}^{\mathrm{FS}} + I_{\mathrm{I}}^{\mathrm{FS}} \cdot \frac{L_{\mathrm{T}}^{\mathrm{FS}}}{\sqrt{\pi}} \right\}, \tag{1}$$

whereas $D$, $k$, and $L_T$ denote the thermal diffusivity, the thermal conductivity, and the heat diffusion length, respectively. $I_I$ and $I_V$ represent the absorbed laser power at the interface and into the liquid volume and $\alpha$ stands for the absorption coefficient. The superscripts FS and $L$ indicate the fused silica and the liquid that can be either a metal or a hydrocarbon solution, respectively.

The most important outcomes from the models are that higher absorption coefficients of the liquid and/or an elevated absorption of the interface result in higher interface temperatures. A low thermal conductivity and short pulses are additional opportunities to get higher temperatures. Calculated laser-induced temperatures across a solid-liquid interface at H-LIBWE are shown in Figure 11. In the left side (a) shows analytically and numerically calculated temperatures of the fused silica/py:toluene interface with and without interface absorption in comparison and demonstrates the large effect of an additional interface absorption. For example, due to 10% interface absorption, the temperature rises more then twice and exceeds the boiling temperature of fused silica. Although the temperature gets higher—resulting from the additional interface absorption raise—also for sapphire samples (dashed lines in Figure 11), the effect is much less for sapphire than for fused silica due to the significant higher thermal conductivity ($k_{\mathrm{FS}} \sim 1.4$ and $k_{\mathrm{Sp}} \sim 40\,\mathrm{W/m \cdot K}$) and does not result in temperatures exceeding the critical temperature for etching, for example, the boiling temperature. Therefore, the low surface quality observed for dielectrics with a high thermal conductivity can be explained by the temperatures field. However, with shorter pulses and a sufficient interface absorption, the melting and boiling of the sapphire surface can be easily achieved as shown in Figure 11(b) in addition.

Combining the experimental found interface absorption values with the experimental applied laser exposure parameters, the interface temperature for H-LIBWE at the multipulse threshold fluence for laser etching of fused silica with a 0.5 M py:toluene absorber was calculated using the mentioned models. Temperatures of more than 4000 K were calculated at Fth = $0.32\,\mathrm{J/cm^2}$ mainly due to the interface absorption of ~35% [62]. These extremely high temperatures already at the threshold cause highly dynamic processes of phase transitions and material etching. Furthermore, as the peak power of the (excimer) laser pulse is at the beginning of the pulse and much higher than the average pulse ($F/tp$) used for the calculations, it is expected that the etching (material removing) occurs within the pulse length. The high temperatures and the expected fast (explosive) processes resemble laser ablation of polymers. However, in the case of H-LIBWE, the ablation-like processes are limited to the near-surface volume that is modified having a very high absorbance. Therefore, the etch rate at H-LIBWE is not predetermined by the thermal diffusion into the fused silica but is given by the amount and the depth of the surface modification.

The comparison of the experimental found etch thresholds at M-LIBWE (Ga, FS, $\lambda = 248\,\mathrm{nm}$) provides a basically different result [27–29]. Here the first threshold fluence correlates with the melting temperature of fused silica whereas at the second threshold the boiling temperature is exceeded. Some other characteristics of Ga-LIBWE, such as the high etch rates and the smooth, wavelike etched surface with rim-like borders indication melting and resolidification, point at a different etch mechanism. A more evaporation-like mechanism can be suggested from the comparison of the etching efficiency with the only three times larger volumetric energy density for fused silica evaporation.

## 4.4. Mechanism of Backside Etching

The discussion of the experimental results with respect to thermal models shows that basically at least two mechanisms

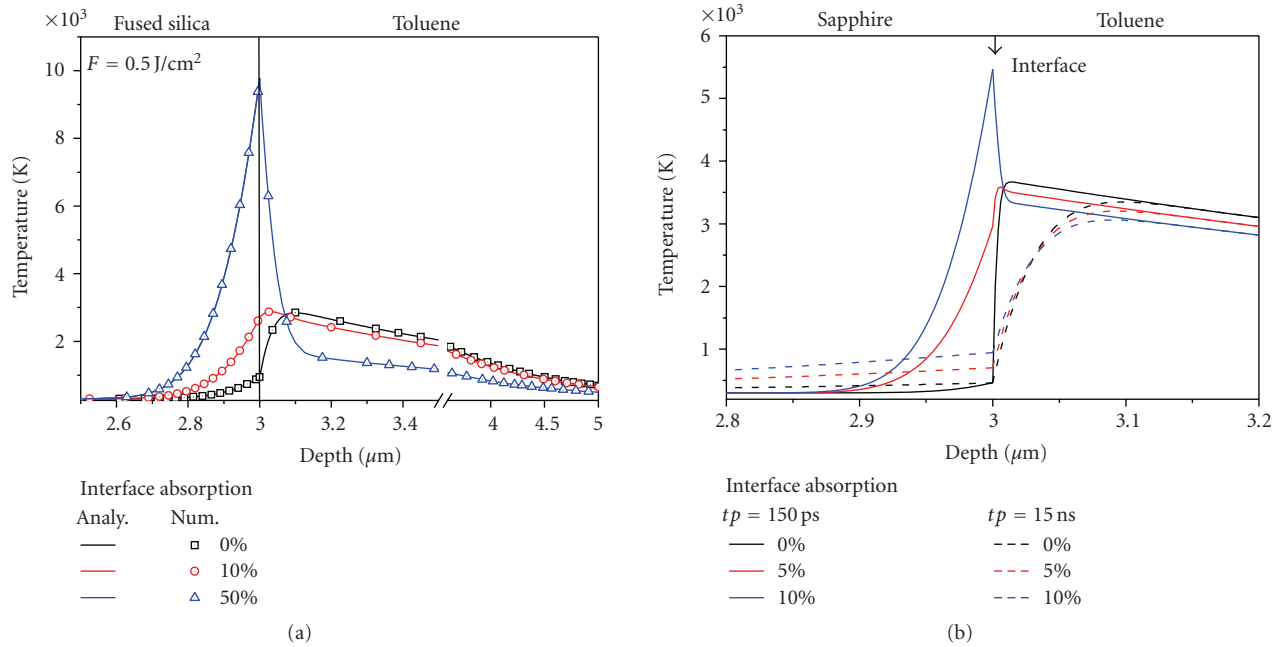


FIGURE 11: Calculated temperature profiles across the solid/liquid interface for H-LIBWE (248 nm, py:toluene: (a) analytically and numerically calculated temperatures for fused silica samples of different interface absorption values of 0, 10, and 50% and (b) sapphire sample for two laser pulse lengths of 15 nanoseconds and 150 picoseconds and different interface absorptions.

of LIBWE have to be distinguished. The first model bases on the heating by a highly absorbing material without significant modification of the solid due to primary or secondary processes at etching, that is, M-LIBWE, and the second mechanism is heavily affected by surface modifications due to secondary processes in combination with fast thermal processes at the solid-liquid interface, that is, H-LIBWE. Additionally, other process characteristics, for example, the confinement of the secondary processes by the absorber, may strongly influence the mechanism at all as the comparison of backside ablation in water/air confinement has been shown [69]. Therefore, the interaction strength of secondary processes, for example, shock waves, liquid decomposition and material deposition, laser-induced plasma and rapid melting and resolidification, with the solid surface depends also on material characteristics of the absorber (liquid), the possible and most likely paths of excitation and relaxation, and the interaction time; all effects are influenced by the confinement.

The sketch shown in Figure 12 gives an overview on the mechanism and the near-surface processes essential for hydrocarbon laser-induced backside wet etching. Here the main focus is on the surface whereas the other processes already mentioned and shown in the figure are also going on.

At the first laser pulse with a fluence above the etching threshold Fth($\infty$), the laser radiation is absorbed by the organic liquid and heats it up to temperatures below the melting temperature of the solid. However, the organic solution vaporizes and decomposes due to photothermal and photochemical processes so that the formation of bubbles is forced. Due to heating, decomposition, and bubble formation, the surface is modified increasingly with the pulse number by liquid decomposition products, for example, carbon, resulting in a thin highly absorbing film on top of the solid. Due to this, the solid surface temperature increases with the pulse number and exceeds a critical temperature $T_c$ at $N_{\text{inc}}$. At this state, the transparent solid material is etched [58]. However, as has been shown, the temperatures that can be achieved at etching are very high so that ablation-like processes occur at the solid surface that is confined by the liquid. This confinement may enhance the interaction of secondary processes with the solid and results in a modified near-surface region of the solid with a high absorption as shown in the figure. This modified near-surface solid region highly absorbs the UV laser radiation and results in an efficient interface heating. At this point the process of surface modification is self-maintaining but needs the absorbing liquid. This general view is more or less changed by the experimental conditions used.

With this extended model considering process-induced surface modifications, some experimental findings can be explained. So the threshold fluence correlates at different UV wavelengths not with the absorption coefficients of the liquid but with the measured absorption in the modified layer according to the extended mechanism. Probably in the same manner the neglectable change of the etching threshold with the absorption coefficient of the liquid absorber (due to dye, e.g., pyrene, admixture) can be explained because the threshold is mainly given by the enhancement of the absorption by carbon-film surface modification from decomposition processes that also appear without dyes.

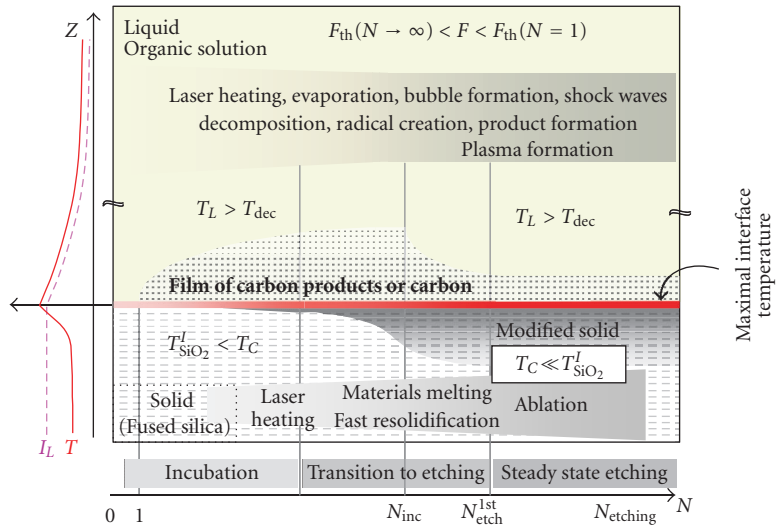


FIGURE 12: Schematic sketch of the processes at H-LIBWE. In particular, the changes of the surface modification at prolonged laser irradiation are shown and probably explain the observed incubation effects at H-LIBWE. The gray level is a measure of the strength.

The concrete processes of solid modifications depend, of course, on the composition of the organic liquid absorber whereby the different thresholds can be explained, for instance.

## 5. Summary

High quality etching of transparent materials with pulsed laser radiation can be achieved by two different LIBWE approaches using hydrocarbon or metallic liquid absorbers. The processing parameters, the achievable patterns, and the surface morphology depend on the used absorber. Hence, the processing parameters such as wavelength, liquid absorber, laser fluence, and so forth must be well chosen with respect to the solid material and the processing goal. The thermal modeling of H-LIBWE shows that the highly absorbing surface modification will cause extreme high temperatures of the modified solid surface that probably results in ablation-like material erosion processes. Submicron gratings can be etched by LIBWE not only in thermal low conducting materials such as fused silica using organic or metallic absorbers but also in crystalline materials, for example, sapphire, applying well-chosen parameters to meet the preconditions for surface modification and high-modulation surface heating of the transparent sample.

## Acknowledgments

The authors gratefully acknowledge the financial support of the Deutsche Forschungsgemeinschaft (DFG ZI 660/5-2 and DFG ZI660/3), the EU within the Research Infrastructures activities of FP6 (Project: Laserlab-Europe; Contract no. RII3-CT-2003-506350), and the Deutscher Akademischer Austausch Dienst (DAAD D/06/05877). The authors are deeply indebted to S. Pissadakis and B. Hopp for their help and interest in the work and the fruitful discussions. The authors acknowledge M. Erhardt, Ph. Hadrava, D. Hirsch, R. Fechner, P. Hertel, and E. Salamatin for their diligence in contributing to the experimental work and for the careful reading of the manuscript.

## References

[1] S. Sinzinger and J. Jahns, *Microoptics*, Wiley-VCH, Berlin, Germany, 2003.

[2] D. Bäuerle, *Laser Processing and Chemistry*, Springer, Berlin, Germany, 3rd edition, 2000.

[3] B. Lan, M.-H. Hong, K.-D. Ye, Z.-B. Wang, S.-X. Cheng, and T.-C. Chong, "Laser precision engineering of glass substrates," *Japanese Journal of Applied Physics*, vol. 43, no. 10, pp. 7102–7106, 2004.

[4] J. Ihlemann and B. Wolff-Rottke, "Excimer laser micro machining of inorganic dielectrics," *Applied Surface Science*, vol. 106, pp. 282–286, 1996.

[5] J. Ihlemann, B. Wolff, and P. Simon, "Nanosecond and femtosecond excimer laser ablation of fused silica," *Applied Physics A*, vol. 54, no. 4, pp. 363–368, 1992.

[6] M. Lenzner, J. Krüger, W. Kautek, and F. Krausz, "Incubation of laser ablation in fused silica with 5-fs pulses," *Applied Physics A*, vol. 69, no. 4, pp. 465–466, 1999.

[7] W. Kautek, J. Krüger, M. Lenzner, S. Sartania, C. Spielmann, and F. Krausz, "Laser ablation of dielectrics with pulse durations between 20 fs and 3 ps," *Applied Physics Letters*, vol. 69, no. 21, pp. 3146–3148, 1996.

[8] D. Schäfer, J. Ihlemann, G. Marowsky, and P. R. Herman, "F2-laser ablation patterning of dielectric layers," *Applied Physics A*, vol. 72, no. 3, pp. 377–379, 2001.

[9] P. R. Herman, R. S. Marjoribanks, A. Oettl, K. Chen, I. Konovalov, and S. Ness, "Laser shaping of photonic materials: deep-ultraviolet and ultrafast lasers," *Applied Surface Science*, vol. 154, pp. 577–586, 2000.

[10] K. Sugioka, S. Wada, H. Tashiro, K. Toyoda, Y. Ohnuma, and A. Nakamura, "Multiwavelength excitation by vacuum-ultraviolet beams coupled with fourth harmonics of a Q-switched Nd:YAG laser for high-quality ablation of fused

quartz," *Applied Physics Letters*, vol. 67, no. 19, pp. 2789–2791, 1995.

[11] K. Sugioka, J. Zhang, S. Wada, H. Tashiro, and K. Toyoda, "Novel ablation of wide band-gap materials by multiwavelength excitation using a VUV-UV laser system," *Nanotechnology*, vol. 9, no. 2, pp. 99–103, 1998.

[12] J. Zhang, K. Sugioka, and K. Midorikawa, "High-quality and high-efficiency machining of glass materials by laser-induced plasma-assisted ablation using conventional nanosecond UV, visible, and infrared lasers," *Applied Physics A*, vol. 69, no. 7, pp. S879–S882, 1999.

[13] J. Zhang, K. Sugioka, and K. Midorikawa, "Laser-induced plasma-assisted ablation of fused quartz using the fourth harmonic of a $Nd^+$:YAG laser," *Applied Physics A*, vol. 67, no. 5, pp. 545–549, 1998.

[14] J. Zhang, K. Sugioka, and K. Midorikawa, "Direct fabrication of micrograting in fused quartz by laser-induced plasma-assisted ablation with a KrF excimer laser," *Optics Letters*, vol. 23, no. 18, pp. 1486–1488, 1998.

[15] K. Sugioka, K. Obata, K. Midorikawa, et al., "Advanced materials processing based on interaction of laser beam and a medium," *Journal of Photochemistry and Photobiology A*, vol. 158, no. 2-3, pp. 171–178, 2003.

[16] K. Sugioka, K. Obata, M. H. Hong, et al., "Hybrid laser processing for microfabrication of glass," *Applied Physics A*, vol. 77, no. 2, pp. 251–257, 2003.

[17] R. Böhme and K. Zimmer, "Low roughness laser etching of fused silica using an adsorbed layer," *Applied Surface Science*, vol. 239, no. 1, pp. 109–116, 2004.

[18] R. Böhme, K. Zimmer, D. Ruthe, and B. Rauschenbach, "Backside etching at the interface to diluted medium with nanometer etch rates," *Journal of Laser Micro/Nanoengineering*, vol. 1, no. 3, pp. 190–194, 2006.

[19] K. Zimmer, R. Böhme, and B. Rauschenbach, "Laser etching of fused silica using an adsorbed toluene layer," *Applied Physics A*, vol. 79, no. 8, pp. 1883–1885, 2004.

[20] K. Zimmer, R. Böhme, and B. Rauschenbach, "Adsorbed layer etching of fused silica by excimer laser with nanometer depth precision," *Microelectronic Engineering*, vol. 78-79, no. 1–4, pp. 324–330, 2005.

[21] T. Smausz, T. Csizmadia, N. Kresz, C. Vass, Z. Márton, and B. Hopp, "Influence on the laser induced backside dry etching of thickness and material of the absorber, laser spot size and multipulse irradiation," *Applied Surface Science*, vol. 254, no. 4, pp. 1091–1095, 2007.

[22] J. Wang, H. Niino, and A. Yabe, "Micromachining of quartz crystal with excimer lasers by laser-induced backside wet etching," *Applied Physics A*, vol. 69, no. 7, pp. S271–S273, 1999.

[23] J. Wang, H. Niino, and A. Yabe, "One-step microfabrication of fused silica by laser ablation of an organic solution," *Applied Physics A*, vol. 68, no. 1, pp. 111–113, 1999.

[24] J. Wang, H. Niino, and A. Yabe, "Micromachining of transparent materials with super-heated liquid generated by multiphotonic absorption of organic molecule," *Applied Surface Science*, vol. 154, pp. 571–576, 2000.

[25] S. I. Dolgaev, A. A. Lyalin, A. V. Simakin, V. V. Voronov, and G. A. Shafeev, "Fast etching and metallization of via-holes in sapphire with the help of radiation by a copper vapor laser," *Applied Surface Science*, vol. 109-110, pp. 201–205, 1997.

[26] S. I. Dolgaev, A. A. Lyalin, A. V. Simakin, and G. A. Shafeev, "Fast etching of sapphire by a visible range quasi-cw laser radiation," *Applied Surface Science*, vol. 96–98, pp. 491–495, 1996.

[27] K. Zimmer, R. Böhme, D. Ruthe, and B. Rauschenbach, "Backside laser etching of fused silica using liquid gallium," *Applied Physics A*, vol. 84, no. 4, pp. 455–458, 2006.

[28] K. Zimmer, R. Böhme, and B. Rauschenbach, "Using IR laser radiation for backside etching of fused silica," *Applied Physics A*, vol. 86, no. 3, pp. 409–414, 2007.

[29] K. Zimmer, R. Böhme, D. Hirsch, and B. Rauschenbach, "Backside etching of fused silica with UV laser pulses using mercury," *Journal of Physics D*, vol. 39, no. 21, pp. 4651–4655, 2006.

[30] J.-Y. Cheng, M.-H. Yen, C.-W. Wei, Y.-C. Chuang, and T.-H. Young, "Crack-free direct-writing on glass using a low-power UV laser in the manufacture of a microfluidic chip," *Journal of Micromechanics and Microengineering*, vol. 15, no. 6, pp. 1147–1156, 2005.

[31] H. Niino, Y. Kawaguchi, T. Sato, A. Narazaki, T. Gumpenberger, and R. Kurosaki, "Surface micro-structuring of silica glass by laser-induced backside wet etching with ns-pulsed laser at high repetition rate," *Journal of Laser Micro/Nanoengineering*, vol. 1, no. 1, pp. 39–43, 2006.

[32] C. Vass, T. Smausz, and B. Hopp, "Wet etching of fused silica: a multiplex study," *Journal of Physics D*, vol. 37, no. 17, pp. 2449–2454, 2004.

[33] X. Ding, Y. Kawaguchi, H. Niino, and A. Yabe, "Laser-induced high-quality etching of fused silica using a novel aqueous medium," *Applied Physics A*, vol. 75, no. 6, pp. 641–645, 2002.

[34] X. Ding, Y. Yasui, Y. Kawaguchi, H. Niino, and A. Yabe, "Laser-induced back-side wet etching of fused silica with an aqueous solution containing organic molecules," *Applied Physics A*, vol. 75, no. 3, pp. 437–440, 2002.

[35] R. Böhme and K. Zimmer, "Indirect laser etching of fused silica: towards high etching rate processing," *Applied Surface Science*, vol. 253, no. 19, pp. 8091–8096, 2007.

[36] C. Vass, D. Sebök, and B. Hopp, "Comparing study of subpicosecond and nanosecond wet etching of fused silica," *Applied Surface Science*, vol. 252, no. 13, pp. 4768–4772, 2006.

[37] R. Böhme, S. Pissadakis, M. Ehrhardt, D. Ruthe, and K. Zimmer, "Ultra-short laser processing of transparent material at the interface to liquid," *Journal of Physics D*, vol. 39, no. 7, pp. 1398–1404, 2006.

[38] R. Böhme, D. Spemann, and K. Zimmer, "Surface characterization of backside-etched transparent dielectrics," *Thin Solid Films*, vol. 453-454, pp. 127–132, 2004.

[39] G. Kopitkovas, T. Lippert, C. David, S. Canulescu, A. Wokaun, and J. Gobrecht, "Fabrication of beam homogenizers in quartz by laser micromachining," *Journal of Photochemistry and Photobiology A*, vol. 166, no. 1–3, pp. 135–140, 2004.

[40] C. Vass, B. Hopp, T. Smausz, and F. Ignácz, "Experiments and numerical calculations for the interpretation of the backside wet etching of fused silica," *Thin Solid Films*, vol. 453-454, pp. 121–126, 2004.

[41] K. Zimmer, A. Braun, and R. Böhme, "Etching of fused silica and glass with excimer laser at 351 nm," *Applied Surface Science*, vol. 208-209, no. 1, pp. 199–204, 2003.

[42] G. Kopitkovas, T. Lippert, C. David, A. Wokaun, and J. Gobrecht, "Surface micromachining of UV transparent materials," *Thin Solid Films*, vol. 453-454, pp. 31–35, 2004.

[43] X. Ding, T. Sato, Y. Kawaguchi, and H. Niino, "Laser-induced backside wet etching of sapphire," *Japanese Journal of Applied Physics*, vol. 42, no. 2B, pp. L176–L178, 2003.

[44] K. Zimmer, R. Böhme, A. Braun, B. Rauschenbach, and F. Bigl, "Excimer laser-induced etching of sub-micron surface relief

gratings in fused silica using phase grating projection," *Applied Physics A*, vol. 74, no. 4, pp. 453–456, 2002.

[45] C. Vass, K. Osvay, and B. Hopp, "Fabrication of 150 nm period grating in fused silica by two-beam interferometric laser induced backside wet etching method," *Optics Express*, vol. 14, no. 18, pp. 8354–8359, 2006.

[46] C. Vass, K. Osvay, B. Hopp, and Z. Bor, "104 nm period grating fabrication in fused silica by immersion two-beam interferometric laser induced backside wet etching technique," *Applied Physics A*, vol. 87, no. 4, pp. 611–613, 2007.

[47] S. Pissadakis, R. Böhme, and K. Zimmer, "Sub-micron periodic structuring of sapphire by laser induced backside wet etching technique," *Optics Express*, vol. 15, no. 4, pp. 1428–1433, 2007.

[48] R. Böhme and K. Zimmer, "Laser-induced writing of submicron surface relief gratings in fused silica on the fly," *Journal of Laser Micro/Nanoengineering*, vol. 2, no. 3, pp. 178–182, 2007.

[49] G. Kopitkovas, T. Lippert, N. Murazawa, et al., "Laser processing of micro-optical components in quartz," *Applied Surface Science*, vol. 254, no. 4, pp. 1073–1078, 2007.

[50] G. Kopitkovas, T. Lippert, C. David, A. Wokaun, and J. Gobrecht, "Fabrication of micro-optical elements in quartz by laser induced backside wet etching," *Microelectronic Engineering*, vol. 67-68, pp. 438–444, 2003.

[51] K. Zimmer and R. Böhme, "Precise etching of fused silica for refractive and diffractive micro-optical applications," *Optics and Lasers in Engineering*, vol. 43, no. 12, pp. 1349–1360, 2005.

[52] K. Zimmer and R. Böhme, "Precise etching of fused silica for micro-optical applications," *Applied Surface Science*, vol. 243, no. 1–4, pp. 415–420, 2005.

[53] R. Böhme, K. Zimmer, and B. Rauschenbach, "Direct laser etching of transparent materials: writing of high-quality micro- and submicron-structures enables surface features for optical applications," in *Proceedings of the 7th International Conference on Correlation Optics*, vol. 6254 of *Proceedings of SPIE*, pp. 1–9, Chernivtsi, Ukraine, September 2006.

[54] T. Gumpenberger, T. Sato, R. Kurosaki, A. Narazaki, Y. Kawaguchi, and H. Niino, "Fabrication of a novel microfluidic device incorporating 2-D array of microbeads," *Chemistry Letters*, vol. 35, no. 2, pp. 218–219, 2006.

[55] K. Zimmer and A. Braun, "Excimer laser machining for 3D-surface structuring," in *Photo-Excited Processes, Diagnostics and Applications*, A. Peled, Ed., pp. 301–335, Kluwer Academic Publishers, Boston, Mass, USA, 2003.

[56] K. Zimmer, R. Böhme, D. Hirsch, and B. Rauschenbach, "Backside etching of fused silica with UV laser pulses using mercury," *Journal of Physics D*, vol. 39, no. 21, pp. 4651–4655, 2006.

[57] Y. Tsuboi, K. Hatanaka, H. Fukumura, and H. Masuhara, "The 248 nm excimer laser ablation of liquid benzene derivatives: a relation between ablation threshold and molecular photochemical reactivity," *Journal of Physical Chemistry*, vol. 98, no. 44, pp. 11237–11241, 1994.

[58] R. Böhme, *Laser-induced backside wet etching of glasses and crystals*, Ph.D. thesis, Zentrum für Ingenieurwissenschaften, Martin-Luther-Universität, Halle-Wittenberg, Halle, Germany, 2007.

[59] R. Böhme and K. Zimmer, "Effects of halogenated organic solvents on laser-induced backside wet etching of fused silica," *Applied Physics A*, vol. 83, no. 1, pp. 9–12, 2006.

[60] K. Hatanaka, M. Kawao, Y. Tsuboi, H. Fukumura, and H. Masuhara, "Switching from photochemical to photothermal mechanism in laser ablation of benzene solutions," *Journal of Applied Physics*, vol. 82, no. 11, pp. 5799–5806, 1997.

[61] Y. Tsuboi, K. Hatanaka, H. Fukumura, and H. Masuhara, "The 248-nm excimer-laser-ablation mechanism of liquid benzene derivatives: photochemical formation of benzyl radical leads to ablation," *Journal of Physical Chemistry A*, vol. 102, no. 10, pp. 1661–1665, 1998.

[62] R. Böhme, *Laser-Based Etching Technique for Micro/Nano Patterning of Transparent Materials*, VDM, Saarbrücken, Germany, 2007.

[63] R. Böhme, A. Braun, and K. Zimmer, "Backside etching of UV-transparent materials at the interface to liquids," *Applied Surface Science*, vol. 186, no. 1–4, pp. 276–281, 2002.

[64] K. Zimmer, R. Böhme, D. Ruthe, and B. Rauschenbach, "The influence of laser-induced surface modifications on the backside etching process," *Applied Surface Science*, vol. 253, no. 15, pp. 6588–6594, 2007.

[65] R. Böhme, J. Zajadacz, K. Zimmer, and B. Rauschenbach, "Topography and roughness evolution of microstructured surfaces at laser-induced backside wet etching," *Applied Physics A*, vol. 80, no. 2, pp. 433–438, 2005.

[66] R. Böhme, C. Vass, B. Hopp, and K. Zimmer, "Sub-wavelength ripples in fused silica after the irradiation the solid/liquid interface with ultrashort laser pulses," to appear in *Nanotechnologies*.

[67] H. S. Carslaw and J. C. Jaeger, *Conduction of Heat in Solids*, Oxford University Press, Oxford, UK, 1959.

[68] K. Zimmer, "Analytical solution of the laser-induced temperature distribution across internal material interfaces," *International Journal of Heat and Mass Transfer*. In press.

[69] R. Böhme, K. Zimmer, and B. Rauschenbach, "Laser backside etching of fused silica due to carbon layer ablation," *Applied Physics A*, vol. 82, no. 2, pp. 325–328, 2006.

Hindawi Publishing Corporation
Laser Chemistry
Volume 2008, Article ID 534951, 9 pages
doi:10.1155/2008/534951

*Review Article*

# Ultrafast Four-Wave Optical Parametric Amplification in Transparent Condensed Bulk Media

**Audrius Dubietis, Gintaras Tamošauskas, Gintaras Valiulis, and Algis Piskarskas**

*Department of Quantum Electronics, Vilnius University, Saulėtekio Avenue 9, Building 3, 10222 Vilnius, Lithuania*

Correspondence should be addressed to Audrius Dubietis, audrius.dubietis@ff.vu.lt

Received 28 March 2008; Accepted 15 May 2008

Recommended by Saulius Juodkazis

We present a short overview of recent advances in ultrashort pulse four-wave optical parametric amplification in transparent condensed bulk media with Kerr nonlinearity. Highly efficient (10% to 15% pump-to-signal energy conversion) four-wave optical parametric amplification in water and fused silica is experimentally demonstrated. The amplification process highly benefits from 1-dimensional spatial soliton propagation regime, which sets in under proper combination of cylindrical beam focusing and noncollinear phase matching geometry with millijoule pumping. Under these operating conditions, strong four-wave coupling quenches catastrophic beam break-up and filamentation, and the setup operates reasonably below the damage threshold of the nonlinear medium. The proposed methodology offers a number of advantages as compared to guided-wave configurations in gaseous media.



## 1. Introduction

Four-wave mixing in transparent isotropic media with instantaneous nonlinear response (Kerr nonlinearity) is widely used in many fields of modern photonics: wide band telecommunications, imaging, metrology, and nonlinear optics [1]. In the ultrashort pulse regime, four-wave mixing manifests itself through generation of a broadband radiation, often termed white-light continuum, which can be produced in any media regardless of its physical state (e.g., solids, liquids, and gases) [2]. Generation of the white-light continuum is associated with four-wave mixing, and, more precisely, with four-wave parametric amplification of the quantum noise, where multicolor radiation emerges at certain directions predefined by the phase-matching condition in bulk dispersive media. Far from frequency resonances, the nonlinear third-order susceptibility is rather low and therefore substantially high laser field intensity is required to induce an appreciable nonlinear response of the medium. On the other hand, high intensity gives rise to a manifold of competing nonlinear optical effects: stimulated Raman scattering, self- and cross-phase-modulation, and self-focusing, simultaneously occurring almost at the same intensity threshold [3]. In extended, wide-aperture bulk media, four-wave mixing is univocally linked to femtosecond filamentation phenomena, which represent an ultimate medium response to high optical intensity, and which recently experience a boost of interest associated with femtosecond pulse nonlinear optics [4, 5].

The discovery of the four-wave-mixing-driven optical parametric amplification dates back to the dawn of nonlinear optics [6]. However, real progress in the field by employing bulk transparent amplifying media has made a sensible breakthrough only recently. In 1997, Durfee et al. proposed a scheme for the four-wave parametric amplification in the ultrashort pulse regime, which exploits self-guided propagation of intense pump beam in noble gas-filled capillary waveguide [7]. The proposed technique successfully combined all the essential prerequisites for efficient energy exchange between the interacting waves through cubic response of the nonlinear medium: almost collinear phase-matching, high pump intensity, and long interaction length. Moreover, use of low dispersion gaseous media allowed to achieve broad amplification bandwidth [8, 9]. More recently, four-wave optical parametric amplification

was demonstrated in the filamentation regime, where the signal was amplified along the intense femtosecond filament in noble gas or air [10, 11] and has led to amplification of optical pulses with duration down to few optical-cycles [12].

In condensed bulk media, the conditions for efficient four-wave optical parametric amplification are much less favored [13]. Due to high material dispersion, nondegenerate four-wave parametric interactions could be phase matched only noncollinearly. This severely reduces useful beam overlap length in tight focusing geometry and implies using of short samples of the nonlinear media. On the other hand, applicable pump intensity is much limited by the occurrence of competing nonlinear effects: self-focusing, self- and cross-phase modulation, stimulated Raman scattering, and eventually, optical damage, which come into play almost at the same intensity threshold. So far, typical energy of the pulses amplified via parametric four-wave processes in bulk solid state media was in the order of $\sim 1\,\mu$J in the visible spectral range [14] and few hundreds of nJ in the midinfrared spectral range [15]. A new route in practical implementation of efficient four-wave optical parametric amplification in water by means of cylindrical focusing and accessing 1-dimensional spatial soliton propagation regime, which benefits from extended beam overlap distance in the noncollinear phase-matching geometry, has been proposed [16].

In this paper, with an example of water as the nonlinear medium, we briefly overview the underlying principles that lead to efficient four-wave optical parametric amplification in bulk condensed media with Kerr nonlinearity. We demonstrate that the proposed methodology might be successfully applied to isotropic solid-state media (fused silica, in particular) to achieve the amplification of high-energy and broadband optical pulses. We also discuss further directions in development of the four-wave optical parametric amplifiers (FWOPAs) operating in the ultrashort pulse regime.

## 2. Phase-Matching Geometry and Experimental Setup

In isotropic medium, the cubic nonlinearity couples together four frequency components of the optical field through the induced nonlinear polarization. In the most general case, the nonlinear polarization might oscillate at positive 22 different frequencies and the observed process is termed four-wave mixing [17]. Confining ourselves to the particular case of interaction: four-wave parametric amplification with $\omega_i = \omega_p + \omega_p - \omega_s$ (here subscripts $p, s, i$ stand for pump, signal, and idler waves), we will obtain a set of four equations describing the complex amplitude behavior versus propagation distance $z$ for the signal, idler, and two pump waves. For simplicity, if we assume that the two pump waves are identical, the interaction is fully described by the set of three coupled equations:

$$\begin{aligned}
\frac{\partial A_s}{\partial z} + L_s(A_s) &= -i\sigma_s A_p^2 A_i^* e^{-i(\Delta k z)} - i\sigma_s |A_s|^2 A_s \\
&\quad - i\sigma_s \left(2|A_i|^2 + 2|A_p|^2\right) A_s, \\
\frac{\partial A_i}{\partial z} + L_i(A_i) &= -i\sigma_i A_p^2 A_s^* e^{-i(\Delta k z)} - i\sigma_i |A_i|^2 A_i \\
&\quad - i\sigma_i \left(2|A_s|^2 + 2|A_p|^2\right) A_i, \\
\frac{\partial A_p}{\partial z} + L_p(A_p) &= -i\sigma_p A_s A_i A_p^* e^{i(\Delta k z)} - i\sigma_p |A_p|^2 A_p \\
&\quad - i\sigma_p \left(2|A_i|^2 + 2|A_s|^2\right) A_p,
\end{aligned} \tag{1}$$

where $A_j$ is the complex amplitude with $j = p, s, i$ referring to pump, signal, and idler waves. $\sigma_j$ is the nonlinear coupling coefficient expressed through third-order nonlinear material susceptibility $\chi^{(3)}$:

$$\sigma_j = \frac{3}{8}\frac{\omega_j}{c n_j}\chi^{(3)}, \tag{2}$$

and $L_j$ is the linear propagation operator, which describes pulse propagation with the group velocity $u_j = \partial\omega_j/k_j$ and accounts for the group velocity dispersion, lateral walk-off, and diffraction:

$$L_j = \frac{1}{u_j}\frac{\partial}{\partial t} - \frac{i}{2}g_j\frac{\partial^2}{\partial t^2} + \beta_j\frac{\partial}{\partial x} + \frac{i}{2k_j}\nabla_\perp, \tag{3}$$

where $u_j$ is the pulse group velocity, $g_j$ is the group velocity dispersion coefficient, $\beta_j$ is the propagation angle with respect to the pump beam axis (in small-angle approximation it takes values of $\theta$ for the signal, $\phi$ for the idler, and 0 for the pump waves), $k_j = n_j\omega_j/c$ is the wave number, and $\nabla_\perp$ is the Laplace operator. The first term on the right-hand side of (1) describes the four-wave parametric amplification, while the second and third terms describe the effects of self-focusing and cross-phase modulation, respectively. For the pump beam, cross-phase modulation term is weak and can be neglected, whereas it plays a relevant role in spatial reshaping of the signal and idler waves. By contrast, self-focusing term is essential for the pump beam due to its high intensity, and may not be accounted in the equations describing propagation of the signal and idler waves. For what concerns the parametric amplification (first term on the right-hand side), the strength of induced nonlinear polarization, oscillating at frequency $\omega_i$, crucially depends on the phase mismatch of the interacting waves, which is expressed as $\Delta k = 2k_p - k_s - k_i$. Assuming normal group velocity dispersion, in collinear configuration $k_p + k_p$ is always smaller than $k_s + k_i$, therefore the condition of perfect phase matching $\Delta k = 0$ is achievable in noncollinear geometry only. The wave-vector matching diagram for the four-wave parametric amplification is depicted in Figure 1. It considers an intense pump beam, represented by the sum of two collinear wave-vectors $\mathbf{k}_p$, signal ($\mathbf{k}_s$), and idler ($\mathbf{k}_i$) beams propagating at some angles $\theta$ and $\phi$ with respect to the pump beam propagation axis. The phase-matching condition is described by a vector equation: $2\mathbf{k}_p = \mathbf{k}_s + \mathbf{k}_i$, which, projected in the transverse and longitudinal directions with respect to the pump beam axis, reads as

$$\begin{aligned}
2k_p &= k_s\cos\theta + k_i\cos\phi, \\
k_s\sin\theta &= k_i\sin\phi.
\end{aligned} \tag{4}$$

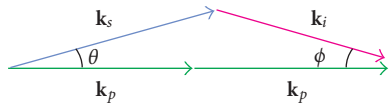


FIGURE 1: Wave-vector diagram describing the noncollinear four-wave parametric amplification. Color notation is for illustration of frequencies: $\omega_s > \omega_p > \omega_i$; note that the pump wave is composed of two photons of $\omega_p$.

After simple algebra, phase-matching angle $\theta$ between the pump and signal beams is expressed as

$$\cos\theta = \frac{2k_p^2 + k_s^2 - k_i^2}{4k_s k_p}, \tag{5}$$

and which may be found with account for particular wavelengths and dispersion relation of the nonlinear medium used.

In the experiments, we used a commercial Nd:glass laser system (Twinkle, Light Conversion Ltd., Vilnius, Lithuania) which delivered 1-picosecond pulses at 1054 nm with energy up to 6 mJ at 10 Hz repetition rate. A fraction of either fundamental or second laser harmonics served as the pump beam for the FWOPA. The seed signal was delivered by a broadly (320–2600 nm) tunable, second-harmonic pumped optical parametric generator/amplifier system (Topas, Light Conversion Ltd.). Energy of the pump beam was adjusted by means of a half-wave plate and a thin-film polarizer, whereas energy of the seed signal was varied using a variable neutral density filter. Both pump and signal beams,parallel to each other, had linear polarization. The beam size of both pump and seed signal was aligned using suitable telescopes, and the temporal delay was matched using motorized mechanical delay lines. The beams were loosely focused onto the input face of a thick nonlinear medium by means of a cylindrical lens. The complete geometrical arrangement is illustrated in Figure 2, providing top and side views of the interaction. The focusing was performed in the vertical ($y$) plane, while the beams were crossed in the horizontal ($x$) plane, thus ensuring a good spatial overlap along entire sample length. Note that the input face of the nonlinear medium is placed exactly at the geometrical focus of the lens, and further 1-dimensional beam contraction along $y$-axis inside the medium is due to self-focusing effect. The beam crossing angle was calculated according to (5), with accounts for dispersive properties of the particular nonlinear medium and wavelengths used.

## 3. Four-Wave Parametric Amplification in Water: Stable 1-Dimensional Spatial Solitons versus Multiple Filamentation

The first set of experiments was performed using water as the nonlinear amplifying medium, which was contained within a variable-length cuvette with 1-mm-thick fused silica windows. The construction of the cuvette allowed to vary its length and therefore to precisely monitor beam propagation dynamics inside the nonlinear medium. Second

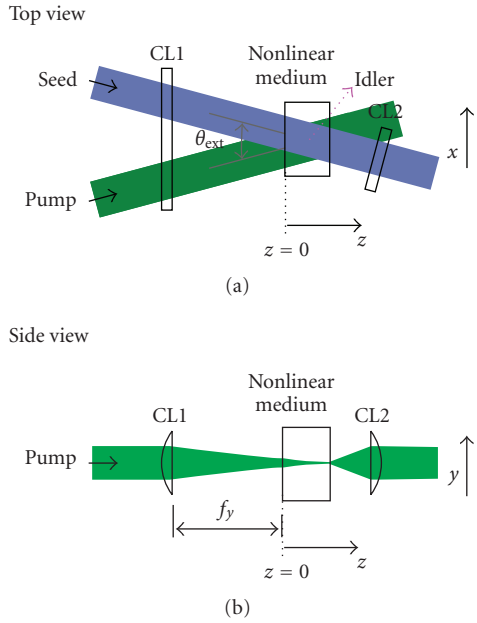


FIGURE 2: Geometrical beam arrangement in the FWOPA using cylindrical beam focusing. $\theta_{\text{ext}}$ is the external phase matching angle, $\theta_{\text{ext}} \approx n\theta$. CL1 and CL2 are cylindrical lenses for beam focusing and restoring, respectively.

harmonic of the laser served as the pump beam ($\lambda_p$ = 527 nm) and cylindrical focusing with $f_y$ = +500 mm, $f_x$ = $\infty$ lens, yielded almost identical pump and seed signal beam dimensions of 1.2 mm × 130 $\mu$m at the input face of the water cuvette, as depicted in Figure 3(a). Energy of the pump beam was set to $E_p$ = 75 $\mu$J, that is ~65 $P_{\text{cr}}$ in terms of critical power for self-focusing, where $P_{\text{cr}} = 3.77\lambda_p^2/(8\pi n_0 n_2)$ = 1.15 MW, with $n_0$ = 1.33 and $n_2$ = $2.7 \times 10^{-16}$ cm/W being linear and nonlinear refractive indexes of water, respectively. In the absence of the seed signal, highly elliptic pump beam undergoes gradual contraction in the $y$-plane, and after passing the nonlinear focus located at $z$ = 25 mm, it breaks up into an array of almost equally spaced multiple filaments, as shown in Figure 3(b). This break-up pattern is universal, and has been observed under different operating conditions and in a variety of nonlinear media [18–21]. Interestingly, further propagation of periodic multifilamentary structures in water gives rise to phase-matched stokes and antistokes emission at large angles mediated by the stimulated Raman scattering [22].

Injection of a weak signal beam ($\lambda_s$ = 490 nm) at the phase-matching angle ($\theta_{\text{ext}}$ = 1.0 deg) immediately quenches the beam break-up and filament formation. In this case, pump beam still contracts along its short ($y$-axis) direction and transforms into a uniform light stripe with 24 $\mu$m FWHM diameter (Figure 3(c)). This structure propagates over a considerable distance without apparent diffraction (Figure 3(d)) inside the nonlinear medium, as measured by imaging the output face of the variable water cuvette onto a 10-bit dynamic range CCD camera (COHU-6612 linked to Spiricon LBA-400PC frame grabber). The diffraction-free

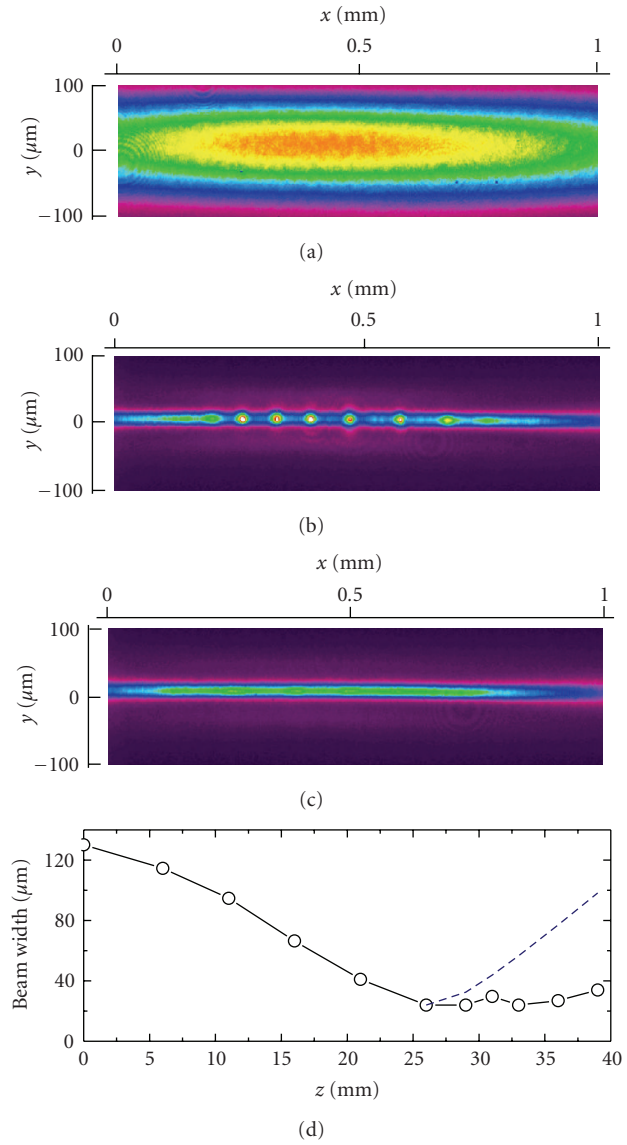


FIGURE 3: Near-field intensity profiles of the pump beam: (a) at the input and at the output of 40-mm-long water cell; (b) in the absence; (c) in the presence of the seed signal launched at the phase-matching angle; (d) measured FWHM diameter of the pump beam (circles and solid curve) versus propagation distance $z$ within the nonlinear medium and calculated diffraction spreading of the Gaussian beam of the same diameter (dashed curve).

propagation regime of the pump beam extends over a distance of 15 mm, that is almost 4.5 times larger than the diffraction length for a Gaussian beam of the same diameter ($z_R \approx 3.3$ mm). As a consequence, the pump beam preserves its high intensity and remains optimally overlapped with the noncollinear seed, thus providing an ideal condition for efficient four-wave parametric amplification to take place. The amplified signal ($\lambda_s = 490$ nm) and idler ($\lambda_i = 570$ nm) beams exhibit high spatial quality and diffraction-free propagation as well, with their propagation being driven by spatial cross-phase modulation imposed by the intense pump beam. The overall observation suggests formation of stable 1-dimensional multicolor parametric solitons due to strong four-wave coupling. Here, off-axis propagating signal and idler waves act as a damping mechanism that efficiently suppresses any local spike that forms in the pump beam as a result of modulational instability. In our experiment, the soliton regime is sustained within a wide range of input parameters, with pump energy as high as 90 $\mu J$ and seed signal energy as low as 10 nJ.

Figure 4 illustrates some of the autocorrelation measurements of the pump and signal pulses performed by a scanning autocorrelator, which also employs beam imaging. It is worth mentioning that in the absence of the seed signal, the pump breaks up not only in the spatial domain, but also in the temporal domain, resulting in pulse splitting within each individual filament (the result is presented elsewhere [23]). The split pulses further undergo complex propagation, similar to that observed in a single filament propagation dynamics [24]. However, the spatial as well as the temporal break-ups of the pump are quenched after injection of the seed pulse. The only observed slight deterioration of the pump pulse temporal profile (Figure 4(b)) occurs due to significant pump energy depletion. Under these settings, the amplified signal retains a clean Gaussian intensity profile as shown in Figure 4(d) and exhibits some slight pulsewidth narrowing from 0.7 picosecond to 0.5 picosecond as a result of parametric gain.

Summarizing the above observations, we conclude that noncollinear four-wave coupling is a highly efficient mechanism of the removal of space-time instabilities of 1-dimensional spatial solitons in bulk nonlinear medium in the ultrashort pulse regime. It is worth mentioning that the stability problem of 1-dimensional spatial solitons in bulk media attracts a great attention from the fundamental and applied research (see [25] and references therein for an overview on the related topics) and stable 1-dimensional spatial solitons in the ultrashort pulse regime were never observed before.

## 4. Energy Scaling

Water FWOPA provides extremely high energy conversion efficiency from pump to parametric waves with a figure as high as 25% in the gain saturation regime with $E_p = 60\,\mu$J. The obtained result suggests a signal gain factor of ~100, with almost 15% pump-to-signal energy conversion. A distinct property of water FWOPA, operating at signal and idler wavelengths close to those of the pump, concerns a strong cascading effect, which manifests itself as an emergence of a series of frequency upshifted and downshifted components at the output, as shown in Figure 5.

The cascaded frequency components are generated through the multistep four-wave mixing processes $\mathbf{k_{s1}} = 2\mathbf{k_s} - \mathbf{k_p}$, $\mathbf{k_{s2}} = 2\mathbf{k_{s1}} - \mathbf{k_s}$, and so forth [14]. Here, genuine signal and idler waves and their cascaded counterparts, indicated by subscript numbering, serve as a new pump in the particular four-wave mixing process. The unequal number and uneven energy distribution between the generated frequency components can be explained by a particular

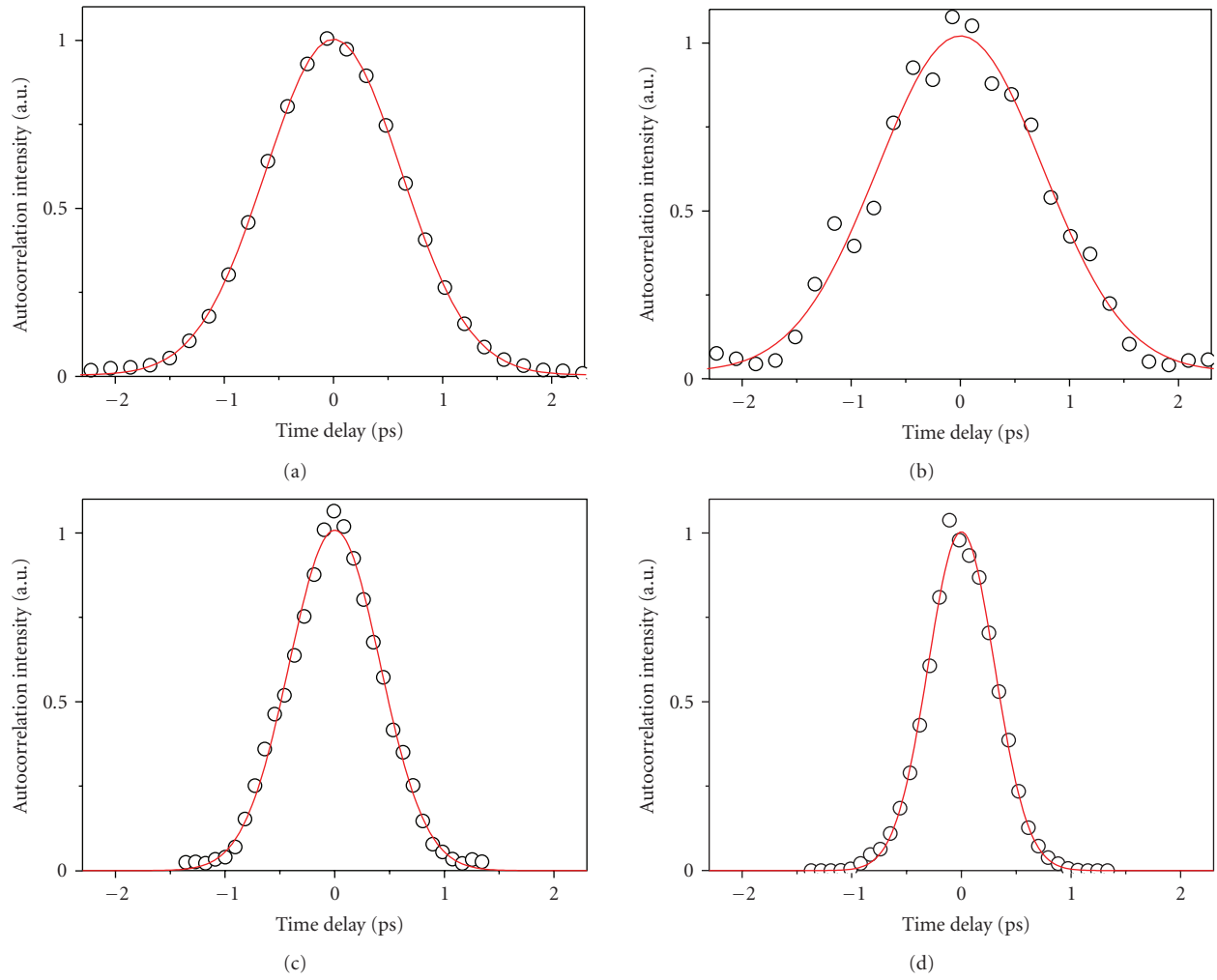


FIGURE 4: Normalized autocorrelation functions of (a) input pump pulse, (b) depleted pump pulse at the FWOPA output, (c) input seed signal, and (d) output amplified signal. Red curves represent a corresponding Gaussian fit. Output pulses were measured after propagation in 40-mm-long water cuvette, with $E_p = 60\,\mu J$ and pump-to-signal conversion of 15%.

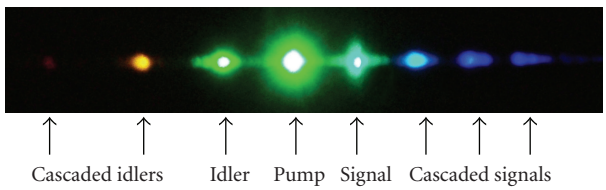


FIGURE 5: FWOPA output imaged on the screen after the wavefront restoring cylindrical lens. The intense green spot in the center is the pump, the closest cyan and green spots are the signal and idler waves, respectively, while the remaining colorful spots are additional frequency components generated by the cascading.

phase-mismatch, which is established under predefined propagation angles and nontrivial impact of increasing linear absorption of water towards lower frequencies. The impact of these processes is investigated in more detail in [16, 23]. Here we just mention that under present operating conditions, the cascaded components comprise only up to 20% of the total output energy and contribute with less than 5% of the overall energy conversion. The number as well as energy of the cascaded components can be suppressed by tuning wavelength of the seed signal farther from that of the pump. The amplified signal energy is $10\,\mu$J, that compares to the signal energy obtained via four-wave mixing in noble gases and air under millijoule-pulse pumping [9–11]. Being different from guided-wave schemes, the pump beam size in 1-dimensional spatial soliton regime is not limited along one of the transverse dimensions (along $x$-axis), so present setup offers an excellent possibility of easy beam-size and energy scaling.

In order to demonstrate energy scaling capabilities of the FWOPA, we performed a second experiment on the four-wave optical parametric amplification in 12-mm-long fused silica (UV-grade, type KU-1) sample with pumping at fundamental laser frequency $\lambda_p = 1054$ nm and seeding with $\lambda_p = 730$ nm. General settings in the interaction scheme are very similar as those depicted in Figure 2. The initial beam sizes of the pump and seed signal were expanded

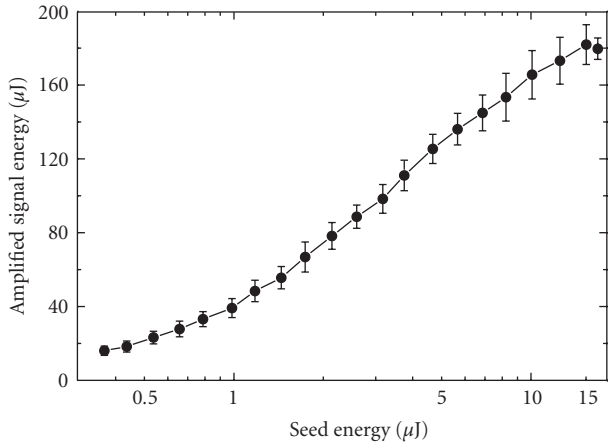


Figure 6: Amplified signal energy versus seed pulse energy measured at $E_p = 1.8$ mJ in 12-mm-long fused silica sample.

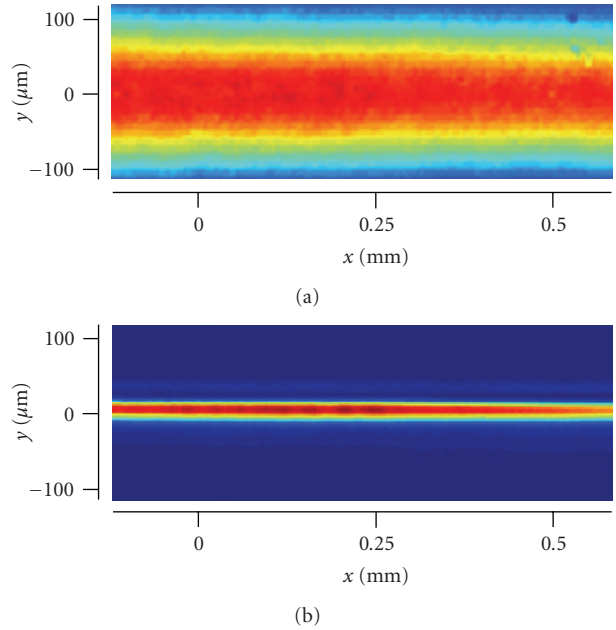


Figure 7: Near-field intensity profiles of (a) seed signal and (b) amplified signal at the fused silica FWOPA input and output, respectively.

by suitable telescopes, focused with $f_y = +750$ mm, $f_x = \infty$ lens, yielding beam FWHM dimensions at the input face of the fused silica sample of 3.7 mm × 195 $\mu$m and 2.8 mm × 135 $\mu$m, respectively, and crossed at $\theta_{\text{ext}} = 1.59°$ so as to ensure perfect phase matching.

The operational characteristics of the fused silica FWOPA at high energy pumping ($E_p = 1.8$ mJ) are depicted in Figure 6. By varying energy of the seed pulse from 0.3 $\mu$J to 16 $\mu$J, we access the complete coverage of the amplification regimes: from the small signal gain up to the gain saturation. The highest small signal gain of ~80 is measured within seed energy interval of 0.3–1.5 $\mu$J. The gain factor gradually drops with increasing seed signal energy and saturates at ~10 with 15 $\mu$J seed. In this condition, the largest amplified signal energy of 180 $\mu$J is achieved, pointing to an appreciable pump-to-signal energy conversion efficiency of 9.2%. As compared to previous results of water-based FWOPA, the present configuration is able to support high-energy amplification regime in condensed medium, and what is to the best of our knowledge the first demonstration of four-wave parametric amplification in transparent bulk medium with millijoule pumping. We also underline that such an impressive amplified signal energy extracted from the present scheme outreaches those produced so far in gaseous media by almost 20 times [7–12].

Figure 7 illustrates the central portion of the intensity profiles of input (seed) and output (amplified) signals, demonstrating how it reshapes into a smooth light stripe having ~17 $\mu$m FWHM diameter imposed by the propagation dynamics of the intense pump beam, which experiences 1-dimensional self-focusing. The pump beam, as measured at the output face of the fused silica sample, contracts along the $y$-axis to a dimension of ~25 $\mu$m, whereas its wider ($x$-axis) dimension remains almost the same. The details of its spatial dynamics inside the sample were not captured due to fixed sample length, however, the observation of the spatial profile at the sample output suggests that no break-up into multiple filaments and no optical damage neither inside the sample nor on its output face there occurs at energies as high as 1.9 mJ. We have evaluated the pump beam intensity of 210 GW/cm$^2$ and 1.7 TW/cm$^2$ assuming Gaussian spatial and temporal profiles at the input and output faces of the fused silica sample, respectively. The latter converts to a maximum fluence of 1.8 J/cm$^2$ without an account of possible multiphoton absorption and energy conversion into the parametric waves. We note that the damage fluence for fused silica is 2.5 J/cm$^2$ for 1-picosecond pulses [26], so our operating conditions are safely below the optical damage threshold.

## 5. Broadband Four-Wave Optical Parametric Amplification

One of the most important characteristics of any optical parametric amplifier is the gain bandwidth, which essentially determines its ability to amplify ultrashort light pulses. In the framework of the ultrashort pulse propagation, the amplification bandwidth is defined by the group-velocity ($v_g = \partial\omega/\partial k$) differences between the signal and idler waves that convert to a wave-vector mismatch in the first-order approximation [27]:

$$\Delta k = \left(\frac{1}{v_{gi}} - \frac{1}{v_{gs}}\right)\Delta\omega. \tag{6}$$

In conventional three-wave optical parametric amplifiers, the broadband phase-matching is achieved by setting an appropriate angle between the pump and signal beams so as to match their wave-vector projections along the signal propagation direction: $v_{gs} = v_{gi}\cos\Theta$ [28], assuming that $v_{gs} < v_{gi}$ (that is the case of normal group-velocity dispersion) and where $\Theta$ denotes the angle between the

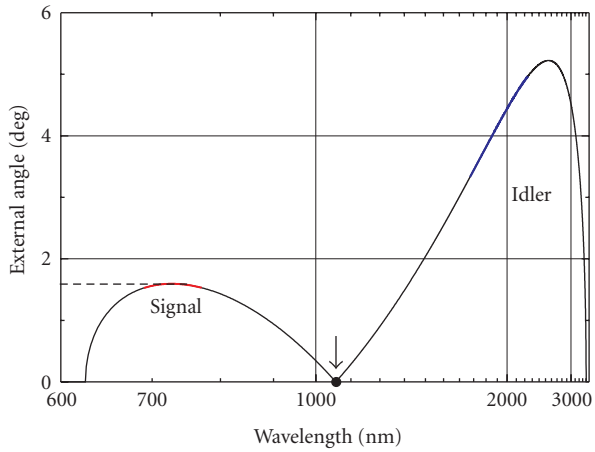


Figure 8: Phase-matching curve for the four-wave optical parametric amplification in fused silica. Wave-vectors of the pump with $\lambda_p = 1054$ nm lie on the propagation axis and are indicated by an arrow. Expected broadband amplification range for the signal is highlighted by the red curve, whereas the blue curve marks the corresponding idler wavelength range.

signal and corresponding idler frequency components. If the propagation direction of the signal is fixed, the angle $\Theta$ depends solely on its wavelength. The same considerations hold also for the four-wave optical parametric amplification. Figure 8 shows the phase matching curve in fused silica pumped by the fundamental harmonic of the Nd:glass laser ($\lambda_p = 1054$ nm). The character of the curve prompts that for signal wavelengths around 730 nm, there exists an optimum beam crossing angle of $\theta_{\text{ext}} = 1.59^\circ$, which keeps nearly constant over considerable signal wavelength range (indicated by a bold red curve). The corresponding idler waves (with wavelength from 1675 nm to 2240 nm) fan out within a wide range of angles (3.5°–5°, bold blue curve) when tuning the signal from 770 nm to 690 nm.

Experimentally, in the first approach, we have scanned the amplification bandwidth of the FWOPA by launching a tunable narrow-band (3 nm FWHM) seed signal from the parametric generator/amplifier system Topas, maintaining a constant delay between the pump and seed signal pulses and fixed crossing angle. Wavelength of the seed signal was varied in 5 nm step from 680 nm to 820 nm. The result is plotted in Figure 9, where the amplification bandwidth was measured in the small-signal ($E_s = 1\,\mu$J) amplification regime and in the gain saturation regime with $E_s = 8\,\mu$J. Both scanned spectral gain profiles are quite similar, indicating FWHM amplification bandwidth of ~75 nm.

And finally, we have seeded the 12-mm-long fused silica FWOPA with a broadband white-light continuum signal with central wavelength at 740 nm, which was generated by self-focusing of a pulsed Bessel beam. The broadband seed signal was produced as follows. The Gaussian output pulse of 1-picosecond duration at $\lambda = 740$ nm from the commercial optical parametric generator/amplifier system was directed to a BK7-glass axicon with apex angle of 175.4°, which produced a Bessel beam of the same pulsewidth, with

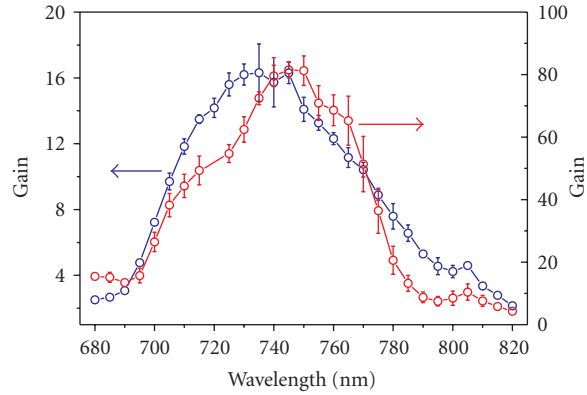


Figure 9: Scanning of the FWOPA amplification bandwidth with a narrow-band seed signal in the small signal amplification regime (red curve) and in the gain saturation regime (blue curve).

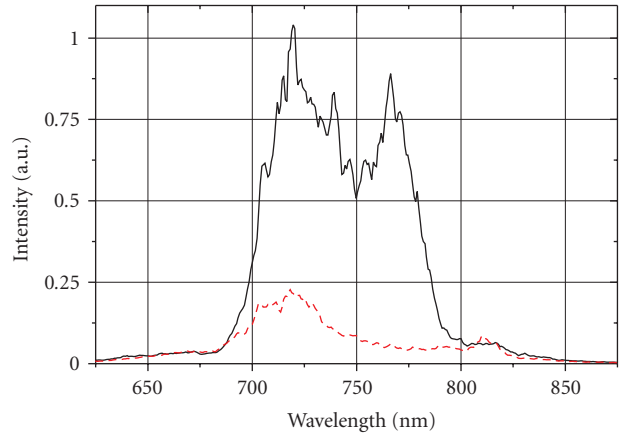


Figure 10: Amplified spectrum of the white-light continuum signal. Dashed curve indicates the input spectrum of broadband radiation.

diameter of the central core of ~10 $\mu$m. The ultrashort-pulsed Bessel with energy of ~50 $\mu$J was made to propagate in 20-mm-long fused silica sample, where it generated a narrow axial beam of high spatial quality with white-light spectral extent [29]. Here we note that the broadband axial radiation is easily separable from the intense spectral component of the pump Bessel beam by placing an iris aperture outside the Bessel zone. The spectral envelope of the white-light continuum radiation averaged over 100 laser shots is depicted by a dashed curve in Figure 10, and has a width of 170 nm estimated at $1/e^2$ level. Spatial dimensions of the white-light continuum beam were matched to those of the pump in a similar manner as described in the previous experiments. The energy of the broadband seed signal at the FWOPA input was 0.75 $\mu$J.

The experimental conditions (focusing geometry and the input beam sizes) were identical to the previous experiment, and the beam crossing angle was kept at $\theta_{\text{ext}} = 1.59^\circ$ so as to ensure broadband phase matching. Under these settings, the seed signal was amplified up to 11.5 $\mu$J energy with 1.8 mJ pump. We note here that the amplified signal energy could

be considerably increased optimizing the seed pulse energy as demonstrated with a narrow-band seed experiment; see the results depicted in Figure 6. The spectrum of the amplified signal is shown in Figure 10. Its estimated FWHM bandwidth is 73 nm, that is almost identical to that obtained with narrow-band signal scanning.

The pulse compression experiments with precise measurements of the pulse duration are in progress; we note, however, that the amplified spectrum width corresponds to a transform-limited pulse of ~10 fs duration.

## 6. Conclusions and Outlook

To summarize the results presented above, we have demonstrated an operating condition and methodology for highly efficient four-wave optical parametric amplification in isotropic transparent condensed media with Kerr nonlinearity. Our approach is based on cylindrical focusing geometry and utilization of 1-dimensional spatial soliton propagation regime, which comprise a complex solution for the problems generally encountered in the four-wave optical parametric amplification in bulk media so far as follows.

(i) Cylindrical focusing enables exact fulfillment of the noncollinear phase matching condition without reduction of the interaction length and allows high conversion efficiency to be achieved.

(ii) Stable 1-dimensional spatial soliton propagation regime ensures high beam quality and suppresses self-action effects in the space-time domain that lead to beam break-up, filamentation, and pulse splitting. In what follows, the setup operates reasonably below the damage threshold.

(iii) Being different from guided-wave configurations (hollow fibers and light filaments), 1-dimensional spatial solitons are not limited in aperture and therefore can be made to carry a large amount of energy, which can be easily scaled by increasing one (wider) transverse dimension without altering the propagation dynamics.

(iv) There is a great flexibility in achieving broad gain bandwidth in the four-wave parametric amplification process. It can be set either by making use of natural flattening of the noncollinear phase-matching curve or suitable signal pulse-front tilting (so-called achromatic phase matching) or eventually combining both possibilities altogether.

(v) Methodology of the four-wave optical parametric amplification is highly flexible in terms of wavelength range and therefore laser sources are to be used, and can be easily adapted to broad wavelength range from the UV up to mid-IR.

(vi) Condensed isotropic media have several advantages over gaseous media concerning their smaller dimensions and higher third-order nonlinearity. This property is essential for designing compact and high power four-wave optical parametric amplifiers.

The proposed four-wave optical parametric amplification methodology could be adapted to virtually all transparent media: solids, liquids, and gases and throughout a variety of wavelengths, especially those where conventional phase-matching techniques based on material birefringence are of limited use or not applicable at all. Using second-harmonic pump pulses from Nd:glass or Ti:sapphire laser systems, four-wave optical parametric amplification in transparent bulk isotropic media may be readily shifted into the UV spectral region, where conventional phase matching techniques based on material birefringence suffer from many serious constraints. Employing achromatic phase matching technique [30] (that is imposing angular dispersion on the seed signal such that individual spectral components that comprise the broadband pulse are made to propagate at different angles to fulfill the phase-matching condition), it is possible to further extend the gain bandwidth and/or achieve tunability of the amplified signal. Taking an advantage of energy scaling capabilities, the proposed methodology might foresee the amplification of few-optical cycle pulses to millijoule energy. And finally, our finding of quenching the spontaneous nature of beam break-up and filamentation by means of launching a weak seed signal opens a new route towards controllable propagation of intense laser beams.

## Acknowledgments

Authors acknowledge the financial support from the Lithuanian State Science and Studies Foundation (Project FORTAS, no. B-29/2008).

## References

[1] R. R. Alfano, "The ultimate white light," *Scientific American*, vol. 295, no. 6, pp. 86–93, 2006.

[2] R. R. Alfano, *The Supercontinuum Laser Source*, Springer, New York, NY, USA, 2006.

[3] A. L. Gaeta, "Collapsing light really shines," *Science*, vol. 301, no. 5629, pp. 54–55, 2003.

[4] A. Couairon and A. Mysyrowicz, "Femtosecond filamentation in transparent media," *Physics Reports*, vol. 441, no. 2–4, pp. 47–189, 2007.

[5] L. Bergé, S. Skupin, R. Nuter, J. Kasparian, and J.-P. Wolf, "Ultrashort filaments of light in weakly ionized, optically transparent media," *Reports on Progress in Physics*, vol. 70, no. 10, pp. 1633–1713, 2007.

[6] R. L. Carman, R. Y. Chiao, and P. L. Kelley, "Observation of degenerate stimulated four-photon interaction and four-wave parametric amplification," *Physical Review Letters*, vol. 17, no. 26, pp. 1281–1283, 1966.

[7] C. G. Durfee III, S. Backus, M. M. Murnane, and H. C. Kapteyn, "Ultrabroadband phase-matched optical parametric generation in the ultraviolet by use of guided waves," *Optics Letters*, vol. 22, no. 20, pp. 1565–1567, 1997.

[8] C. G. Durfee III, S. Backus, H. C. Kapteyn, and M. M. Murnane, "Intense 8-fs pulse generation in the deep ultraviolet," *Optics Letters*, vol. 24, no. 10, pp. 697–699, 1999.

[9] A. E. Jailaubekov and S. E. Bradforth, "Tunable 30-femtosecond pulses across the deep ultraviolet," *Applied Physics Letters*, vol. 87, no. 2, Article ID 021107, 3 pages, 2005.

[10] F. Théberge, N. Aközbek, W. Liu, A. Becker, and S. L. Chin, "Tunable ultrashort laser pulses generated through filamentation in gases," *Physical Review Letters*, vol. 97, no. 2, Article ID 023904, 4 pages, 2006.

[11] T. Fuji, T. Horio, and T. Suzuki, "Generation of 12 fs deep-ultraviolet pulses by four-wave mixing through filamentation in neon gas," *Optics Letters*, vol. 32, no. 17, pp. 2481–2483, 2007.

[12] T. Fuji and T. Suzuki, "Generation of sub-two-cycle mid-infrared pulses by four-wave mixing through filamentation in air," *Optics Letters*, vol. 32, no. 22, pp. 3330–3332, 2007.

[13] A. Penzkofer and H. J. Lehmeier, "Theoretical investigation of noncollinear phase-matched parametric four-photon amplification of ultrashort light pulses in isotropic media," *Optical and Quantum Electronics*, vol. 25, no. 11, pp. 815–844, 1993.

[14] H. Crespo, J. T. Mendonça, and A. Dos Santos, "Cascaded highly nondegenerate four-wave-mixing phenomenon in transparent isotropic condensed media," *Optics Letters*, vol. 25, no. 11, pp. 829–831, 2000.

[15] H.-K. Nienhuys, P. C. M. Planken, R. A. van Santen, and H. J. Bakker, "Generation of mid-infrared pulses by $X^{(3)}$ difference frequency generation in $CaF_2$ and $BaF_2$," *Optics Letters*, vol. 26, no. 17, pp. 1350–1352, 2001.

[16] A. Dubietis, G. Tamošauskas, P. Polesana, et al., "Highly efficient four-wave parametric amplification in transparent bulk Kerr medium," *Optics Express*, vol. 15, no. 18, pp. 11126–11132, 2007.

[17] R. W. Boyd, *Nonlinear Optics*, Academic Press, San Diego, Calif, USA, 2003.

[18] H. Schroeder and S. L. Chin, "Visualization of the evolution of multiple filaments in methanol," *Optics Communications*, vol. 234, no. 1–6, pp. 399–406, 2004.

[19] T. D. Grow and A. L. Gaeta, "Dependence of multiple filamentation on beam ellipticity," *Optics Express*, vol. 13, no. 12, pp. 4594–4599, 2005.

[20] M. Centurion, Y. Pu, and D. Psaltis, "Self-organization of spatial solitons," *Optics Express*, vol. 13, no. 16, pp. 6202–6211, 2005.

[21] A. Dubietis, E. Kučinskas, and G. Tamošauskas, "Formation of periodic multifilamentary structures by use of highly elliptical light beams," *Lithuanian Journal of Physics*, vol. 47, pp. 27–30, 2007.

[22] D. Faccio, A. Dubietis, G. Tamošauskas, et al., "Phase- and group-matched nonlinear interactions mediated by multiple filamentation in Kerr media," *Physical Review A*, vol. 76, no. 5, Article ID 055802, 4 pages, 2007.

[23] H. Valtna, A. Dubietis, G. Tamošauskas, et al., "Efficient four-wave parametric amplification and spatial soliton generation in transparent isotropic medium with Kerr nonlinearity," *Lithuanian Journal of Physics*, vol. 47, pp. 403–410, 2007.

[24] A. Matijosius, J. Trull, P. Di Trapani, et al., "Nonlinear space-time dynamics of ultrashort wave packets in water," *Optics Letters*, vol. 29, no. 10, pp. 1123–1125, 2004.

[25] C. Anastassiou, M. Soljačić, M. Segev, et al., "Eliminating the transverse instabilities of Kerr solitons," *Physical Review Letters*, vol. 85, no. 23, pp. 4888–4891, 2000.

[26] B. C. Stuart, M. D. Feit, A. M. Rubenchik, B. W. Shore, and M. D. Perry, "Laser-induced damage in dielectrics with nanosecond to subpicosecond pulses," *Physical Review Letters*, vol. 74, no. 12, pp. 2248–2251, 1995.

[27] G. Cerullo and S. De Silvestri, "Ultrafast optical parametric amplifiers," *Review of Scientific Instruments*, vol. 74, no. 1, pp. 1–18, 2003.

[28] T. Wilhelm, J. Piel, and E. Riedle, "Sub-20-fs pulses tunable across the visible from a blue-pumped single-pass non-collinear parametric converter," *Optics Letters*, vol. 22, no. 19, pp. 1494–1496, 1997.

[29] A. Dubietis, P. Polesana, G. Valiulis, A. Stabinis, P. Di Trapani, and A. Piskarskas, "Axial emission and spectral broadening in self-focusing of femtosecond Bessel beams," *Optics Express*, vol. 15, no. 7, pp. 4168–4175, 2007.

[30] O. E. Martinez, "Achromatic phase matching for second harmonic generation of femtosecond pulses," *IEEE Journal of Quantum Electronics*, vol. 25, no. 12, pp. 2464–2468, 1989.

Hindawi Publishing Corporation
Laser Chemistry
Volume 2008, Article ID 656490, 6 pages
doi:10.1155/2008/656490

*Research Article*

# Physical and Spectroscopic Properties of $Yb^{3+}$-Doped Fluorophosphate Laser Glasses

**Shujiang Liu[1] and Anxian Lu[2]**

[1] *Glass and Ceramic Key Laboratory, Shandong Institute of Light Industry, Jinan 250353, China*
[2] *School of Materials Science and Engineering, Central South University, Changsha 410083, China*

Correspondence should be addressed to Shujiang Liu, lsj_24@126.com

Received 24 April 2008; Accepted 4 August 2008

Recommended by Saulius Juodkazis

The physical properties including refractive index, Abbe number, nonlinear refractive index, microhardness and thermal expansion coefficient, and spectroscopic properties of $Yb^{3+}$-doped fluorophosphate laser glasses were investigated. The results show that due to the addition of fluoride, mechanical and thermal properties are promoted, emission cross-section $\sigma_{emi}$ is also greatly enhanced. The largest gain coefficient $\sigma_{emi} \cdot \tau_m$ ($0.824\,pm^2 \cdot ms$) can be obtained with the minimum pump intensity $I_{min}$ ($1.112\,kw/cm^2$). This kind of $Yb^{3+}$-doped fluorophosphate glass is an excellent candidate material for $Yb^{3+}$-doped host for high-power generation.



## 1. Introduction

With the rapid development of laser diode (LD) recently, $Yb^{3+}$ doped laser materials as the gain medium in high-energy solid-state laser systems have obtained much attention [1–3]. There are only two manifolds in the $Yb^{3+}$ energy level scheme, namely, the $^2F_{7/2}$ ground state and the $^2F_{5/2}$ excited state, and the absorption band is located at about 970 nm, with a large cross-section, which enables efficient pumping by high-power III–V diode lasers that are commercially available. The $Yb^{3+}$ ions are also of interest not only as high-power lasers for nuclear fusion but also as energy transfer sensitizers for infrared lasers and up conversion lasers [4, 5]. The main obstacle is mechanical and thermal problems in the development of high-average powder solid-laser materials because more than half of pumping energy precipitate in gain medium, though effective semiconductor diode is used as pumping source, which results in various problems such as thermal load, mechanical stress. Therefore, in addition to high optical and spectroscopic properties, excellent thermal and mechanical properties are necessary, to improve the repetition rate of the laser glass.

For a long term, $Yb^{3+}$ doped phosphate glasses have been regarded as ideal host matrix for high-power laser due to larger absorption and emission cross-section, less nonlinear refractive index [6–8]. However, the line-like network of phosphate glass results in higher thermal expansion coefficient (TEC), inferior physical properties such as mechanical and chemical durability [9, 10]. Furthermore, the hygroscopic tendency of phosphor lowers the fluorescence lifetime of $Yb^{3+}$ ions. Some early researches [11, 12] have shown that formation of P–O–B(4) bonds in borophosphate glass could greatly improve physical properties along with broad emission bandwidth. However, the photo energy of B–O bond ($\sim 1400\,cm^{-1}$) is larger, so that the fluorescence lifetime of borate glass is less as compared to other glass. In order to improve the water resistance of phosphate glass, fluorophosphate glass is available because fluorophosphate glass has *m* advantages such as long fluorescene life time, low nonlinear refractive index [13, 14].

To obtain excellent physical and spectroscopic properties of $Yb^{3+}$-doped laser glass, we investigated the relationship between composition and mechanical, thermal and spectroscopic properties of fluorophosphate glasses.

## 2. Experimental

Two series of fluorophosphate glasses were chosen, and the glass compositions (mol%) listed in Table 1 were prepared by melting 100 g batches using analytical grade $(NH_4)_2HPO_4$,

Table 1: Chemical composition of $Yb^{3+}$-doped fluorophosphate glasses.

| | A0 | A1 | A2 | A3 | A4 | B1 | B2 | B3 | B4 |
|---|---|---|---|---|---|---|---|---|---|
| $P_2O_5$ | 63 | 63 | 63 | 63 | 63 | 44 | 44 | 44 | 44 |
| $Al_2O_3$ | 7 | 7 | 7 | 7 | 7 | 7 | 7 | 7 | 7 |
| $Nb_2O_5$ | 1 | 1 | 1 | 1 | 1 | 4 | 4 | 4 | 4 |
| $Li_2O$ | 10 | 7.5 | 5 | 2.5 | — | — | — | — | — |
| BaO | 18 | 13.5 | 9 | 4.5 | — | — | — | — | — |
| LiF | — | 2.5 | 5 | 7.5 | 10 | 10 | 10 | 10 | — |
| NaF | — | — | — | — | — | 10 | 10 | — | 10 |
| $MgF_2$ | — | — | — | — | — | 24 | — | 20 | 20 |
| $CaF_2$ | — | 4.5 | 9 | 13.5 | 18 | — | 24 | 14 | 14 |
| $Yb_2O_3$ | 1 | 1 | 1 | 1 | 1 | 1 | 1 | 1 | 1 |

Table 2: Physical properties of $Yb^{3+}$-doped fluorophosphate glasses.

| | A0 | A1 | A2 | A3 | A4 | B1 | B2 | B3 | B4 |
|---|---|---|---|---|---|---|---|---|---|
| Refractive index $n_D$ | 1.556 | 1.551 | 1.548 | 1.543 | 1.540 | 1.509 | 1.510 | 1.510 | 1.510 |
| Abbe number $\nu$ | 62.23 | 66.86 | 67.90 | 67.32 | 64.32 | 63.07 | 62.72 | 64.20 | 63.94 |
| Nonlinear refractive index $n_2(\times 10^{-13}$ esu) | 1.36 | 1.20 | 1.16 | 1.15 | 1.23 | 1.15 | 1.16 | 1.12 | 1.13 |
| Microhardness (GPa) | 3.68 | 3.75 | 3.89 | 3.95 | 4.10 | 4.40 | 4.16 | 4.20 | 4.11 |
| Thermal expansion coefficient $\alpha(\times 10^{-7}/\mathrm{K})$ | 105.92 | 91.41 | 82.61 | 78.86 | 75.24 | 71.98 | 89.18 | 63.71 | 88.14 |

$Al_2O_3$, carbonate, Fluoride, $Nb_2O_5$, and $Yb_2O_3$ with a purity of above 99.99%. When each batch was slowly heated from room temperature up to 1000°C in a $Al_2O_3$ crucible, the crucible was covered to minimize the volatilization of phosphor, then the batch was melted at 1300~1320°C depending on the glass composition. Melts were quenched in stainless steel moulds and properly annealed. The final compositions of the glasses were checked by chemical analysis and found to be within ±1%.

The refractive index ($n_D$, $n_F$, and $n_C$) was measured on an Abbe refractometer (WZS-S) at room temperature at the wavelength of 589.3, 486.1, and 656.3 nm, respectively.

The microhardness of the investigated samples was measured using Vickers's microhardness indentor (MET-4). The eyepiece on the microscope of the apparatus allows measurements with an estimated accuracy of ±0.5 $\mu$m for the indentation diagonal. Grinding and well polishing were necessary to obtain polished and flat parallel surfaces glass samples before indentation testing. At least five indentation readings were made and measured for each sample. Testing was conducted with a load of 30 g and loading time 15 seconds. The measurements were carried out under normal atmospheric condition.

Thermal expansion coefficient of the investigated glass was carried out on 2.0 cm long rods using AS-100 automatic recording multiplier dilatometer with heating rate of 5°C/min. The uncertainty of linear thermal expansion from room temperature to 300°C is $\pm 5 \times 10^{-7}$/°C.

The samples for measurement of spectroscopic properties were cut to a size of 20 mm × 20 mm × 2 mm with two larger sides polished. Absorption spectra were recorded with Perkin-Elmer (Lambda 900) UV/VIS/NIR spectrophotometer, at room temperature, in the range of 870–1150 nm. Emission spectra were measured with Triax 550 spectrophotometer through exciting the samples with a diode laser operating around 940 nm. The emission from the sample was focused to a monochrometer and detected by the Ge detector. The signal was intensified with a lock in amplifier and processed by a computer. Fluorescence lifetimes were measured by exciting the samples with a Xenon lamp and detected by an S-1 photomultiplier tube. The fluorescence decay curves were recorded and averaged with a computer-controlled transient digitizer.

## 3. Results

### 3.1. Physical Properties

Table 2 summarizes the data of measured refractive index, Abbe number, nonlinear refractive index, microhardness, and thermal expansion coefficient for fluorophosphate glass samples.

The knowledge of low nonlinear refractive index $n_2$ is required for laser applications to prevent spatial intensity fluctuations in the wavefront and self-focusing which lead to damage of optical components. $n_2$ can be calculated using the formula [15]:

$$n_2 = \frac{\left[68(n_D - 1)\left(n_D^2 + 2\right)^2\right] \times 10^{-13}}{\nu\left[1.517 + \left(n_D^2 + 2\right)(n_D + 1)\nu/6n_D\right]^{1/2}} \text{esu}, \quad (1)$$

where $\nu$ is Abbe number, $\nu = (n_D - 1)/(n_F - n_C)$. $n_D$ is refractive index. It is clear that $n_D$ constantly decreases in series A with increasing content of LiF and $CaF_2$ at the expense of $Li_2O$ and BaO. It could mainly correlate with the difference of the polarizability of $F^-$ and $O^{2-}$, furthermore,

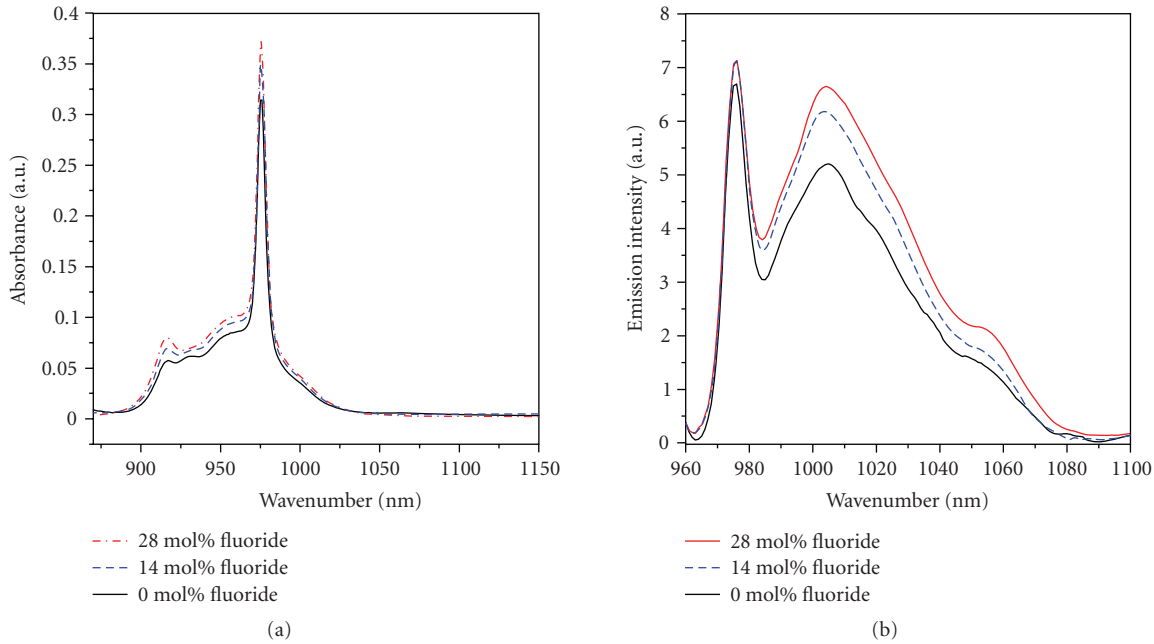


Figure 1: Absorption and emission spectra of $Yb^{3+}$ in A0, A2, and A4 glasses.

introduction of $Ca^{2+}$ with higher polarizing power than $Ba^{2+}$ promotes this refractive index behavior. $n_2$ is minimized at A3. In the samples of series B, $n_2$ is only related to $\nu$, since the values of $n_D$ are nearly same, as shown in Table 2. Furthermore, $n_2$ appear inverse to $\nu$ according to (1), such B3 glass has the minimum $n_2$ due to its largest $\nu$.

As shown in Table 1, with increasing fluoride content in the samples of series A, the microhardness increases gradually along with a decrease of thermal expansion coefficient. In series B, B1, and B3 glasses exhibit high microhardness and low-thermal expansion coefficient when compared to B2 and B4 on the same condition.

## 3.2. Spectroscopic Properties

The spectroscopic properties of $Yb^{3+}$ ions in glasses are determined by transition between the four subenergy levels of $^2F_{7/2}$ and three subenergy levels of $^2F_{5/2}$, and the emission cross-section is associated with integral absorption cross-section $\sum_{abs}$ which can be obtained by (2) [16]:

$$\sum_{abs} = \int \sigma_{abs}(\lambda)d\lambda, \tag{2}$$

$$\sigma_{abs}(\lambda) = \left(\frac{2.303\log(I_0/I)}{Nl}\right), \tag{3}$$

where $\sigma_{abs}$ is absorption cross-section, $N$ is the $Yb^{3+}$ ion concentration (ions/cm$^3$), and $l$ is the thickness of the sample, $\log(I_0/I)$ is absorbance. The reciprocity method was used to calculate the emission cross-section of $Yb^{3+}$ ions [17]:

$$\sigma_{emi}(\lambda) = \sigma_{abs}(\lambda)\frac{z_l}{z_\mu}\exp\left(\frac{E_{zl} - hc\lambda^{-1}}{kT}\right), \tag{4}$$

where $Z_l/Z_u$ is the partition function; $T$ is the absolute temperature; $E_{zl}$ is the zero line energy, which is defined as the energy separation between the lowest components of the upper ($^2F_{5/2}$) and lower states ($^2F_{5/2}$); $k$, $h$, and $c$ are Boltzman's constant, the Plank constant, and the velocity of light, respectively.

Spontaneous emission probability $A_{rad}$ is calculated as follows [18]:

$$A_{rad} = \frac{1}{\tau_{rad}} = \frac{8\pi cn^2}{\lambda_p^4}\frac{2J'+1}{2J+1}\sum_{abs}, \tag{5}$$

where $\lambda_p$ is the peak wavelength of absorption band, $n$ is the refractive index at the peak wavelength, which is obtained from Cauchy's equation $n(\lambda) = A + B/\lambda^2$ according to the measured $n_D$, $n_C$, or $n_F$. $J$ and $J'$ are the total momentums for the upper and lower levels.

Figure 1 shows the absorption and emission spectra of the samples of series A. The line shape of absorption spectra is similar except intensity in all samples, the main absorption peak is around 975 nm (as shown in Figure 1(a)), which corresponds to the energy transition of the lowest subenergy level of $^2F_{5/2}$ and $^2F_{7/2}$. The absorption spectra is characterized by broader line widths due to out-of-order glass structure in which $Yb^{3+}$ ions are localized in different coordination site and some portion of stark splitting energy overlap. As seen in Figure 1(b), the main emission peak of all samples is around 975 nm, and subemission peak is around 1006 nm which is mostly concerned. Other spectroscopic properties have been shown in Table 3.

In the Table 3, emission cross-section $\sigma_{emi}$ and fluorescence lifetime $\tau_m$ gradually increase as the fluoride content increases from 0 to 28 mol% in series A glasses. Series B glasses shows larger integral absorption cross-section $\sum_{abs}$

Table 3: Spectroscopic properties of $Yb^{3+}$-doped fluorophosphate glasses.

| | A0 | A1 | A2 | A3 | A4 | B1 | B2 | B3 | B4 |
|---|---|---|---|---|---|---|---|---|---|
| Concentration ($10^{20}$ ions/cm$^3$) | 2.753 | 2.745 | 2.740 | 2.746 | 2.744 | 3.127 | 3.120 | 3.075 | 3.027 |
| $\Sigma_{abs}$($10^4$ pm$^3$) | 3.93 | 3.86 | 3.54 | 3.65 | 3.73 | 4.76 | 4.84 | 5.49 | 5.51 |
| $\sigma_{emi}$(pm$^2$) | 0.598 | 0.601 | 0.608 | 0.649 | 0.653 | 0.915 | 0.947 | 1.065 | 1.032 |
| $A_{rad}$(s$^{-1}$) | 982 | 1018 | 921 | 951 | 968 | 1188 | 1208 | 1371 | 1376 |
| $\tau_m$(ms) | 0.84 | 0.87 | 0.98 | 1.03 | 1.08 | 0.89 | 0.87 | 0.73 | 0.75 |

and emission cross-section $\sigma_{emi}$, but less fluorescence lifetime $\tau_m$ compared to series A glasses.

## 4. Discussion

### 4.1. Effect of Fluoride on Mechanical and Thermal Properties

Excellent mechanical and thermal properties are indispensable to the laser driver for inertial confinement fusion (ICF), especially low-thermal expansion coefficient can reduce the thermal load of laser glasses, enhancing thermal shock toughness. As seen in Table 2, the microhardness increases and thermal expansion coefficient decreases when fluoride content gradually increases, moreover, the mechanical and thermal properties of series B glasses with higher fluoride content are superior to those of series A glasses. This anomalous behavior should be due to the structural change caused by the fluorides. It is clear from the glass composition as shown in Table 1 that the A0 glass without fluoride content mainly consists of metaphosphate ($\Sigma MO$: $P_2O_5$ = 1) group. Addition of fluorides leads to rupturing of long metaphosphate chains, $(PO_3^-)_n$ and the formation of short structural fragments of $P_2(O,F)_7$ and $P(O,F)_4$. However, these smaller fragments are linked up to a greater extent by the $Al(O,F)_6$ polyhedra [19], which leads to strengthening of the glass network. In particular, $Nb^{5+}$ with higher field strength also promotes the linkage of smaller fragments in series B glasses. In addition, the fact that B1 and B3 glasses display better mechanical and thermal properties is also explained by the high cation field strength for $Mg^{2+}$ and $Li^+$ ions.

### 4.2. Effect of Fluoride on Spectroscopic Properties

The emission cross-section $\sigma_{emi}$ has an important effect on laser properties of $Yb^{3+}$ ions because a larger $\sigma_{emi}$ indicates higher laser gain [20]. From (4), it can be seen that the value of emission cross-section is only determined by the absorption cross-section, which removes the errors of reabsorption in the experiment of fluorescence spectrum. As seen in Table 3, the $\sigma_{emi}$ increases with increase in fluoride content, and the increase of $\sigma_{emi}$ depends on the change of structure of fluorophosphate glasses. Addition of fluoride leads to the reduction of P–O–P linkages due to a gradual transformation of $(PO_3^-)_n$ to $P_2(O,F)_7$ and $P(O,F)_4$, which decreases the connectivity of the glass network. This behavior is strengthened by the concentration of $F^-$ ions. Moreover, the surrounding coordination $Yb^{3+}$ ions are also changed due to present mixed anions, fluorine, and oxygen. In particular, the series B glasses with higher $Nb_2O_5$ and fluoride content contain different types of structural units such as $P_2(O,F)_7$, $P(O,F)_4$, $Al(O,F)_6$, and $Nb(O,F)_6$ in the framework of fluorophosphate glass, which increases asymmetry of the $Yb^{3+}$ site environments and results in larger absorption and emission cross-section as shown in Table 3.

Generally, the decay rate for an excited state population, $\Gamma_m = 1/\tau_m$, is comprised of three processes: the radiative decay rate ($\Gamma_r$), the nonradiative decay rate ($\Gamma_{nr}$), and the additional nonradiative loss decay rate ($\Gamma_q$). The total decay rate is thus [21]:

$$\Gamma_m = \Gamma_r + \Gamma_{nr} + \Gamma_q = \frac{1}{\tau_r} + \frac{1}{\tau_{nr}} + \frac{1}{\tau_q}, \quad (6)$$

where $\tau_r$, $\tau_{nr}$, and $\tau_q$ are radiative decay, nonradiative decay, and additional nonradiative decay lifetime correspondingly. The radiative decay rate ($\Gamma_r$) is influenced by variations of the local crystal field symmetry at the rare-earth site. These variations are determined by the host matrix into which the ions are placed. Thus, $\tau_r$ depends on the ingredients around the $Yb^{3+}$ ions and structure of host matrix. Since $Yb^{3+}(^2F_{5/2} \rightarrow {}^2F_{7/2})$ possesses the simple electronic energy level structure and nonradiative decay does not exist, the second process ($\Gamma_{nr}$) is negligible (i.e., $\Gamma_{nr} = 0$). The third process, $\Gamma_q$, represents an additional nonradiative loss mechanism which involves impurity or $OH^-$ group [22]. For our glass samples starting with high purity materials, the effect of impurities can be little, so $\tau_q$ is dependent mostly on $OH^-$ groups. Based on that, the total lifetime $\tau_m$ is influenced mostly by radiative decay and additional nonradiative loss by $OH^-$ groups. $OH^-$ groups decrease, $\Gamma_q$ also decreases, then $\tau_q$ and $\tau_m$ increase correspondingly. As shown in Table 3, the $\tau_m$ increase with increase in fluoride content in series A glasses. This can be explained as follows: the hydroxyl and fluorine ions are isoelectronic with a similar ionic size, so that hydroxyl ions can be easily replaced by fluorine during melting, which decreases the traps of $OH^-$ and prolongs the measured fluorescence lifetime. Whereas series B glasses exhibit shorter $\tau_m$ compared to series A glasses, this could be related to the difference of local environment around the $Yb^{3+}$ ions in two host matrixes.

Table 4: Lasering properties of $Yb^{3+}$-doped fluorophosphate glasses.

| | A0 | A1 | A2 | A3 | A4 | B1 | B2 | B3 | B4 |
|---|---|---|---|---|---|---|---|---|---|
| $\sigma_{emi}\cdot\tau_m$(pm$^2$·millisecond) | 0.502 | 0.523 | 0.596 | 0.668 | 0.705 | 0.814 | 0.824 | 0.777 | 0.774 |
| $I_{min}$(kw/cm$^2$) | 1.761 | 1.68 | 1.516 | 1.615 | 1.27 | 1.073 | 1.112 | 1.176 | 1.172 |

### 4.3. Effect of Fluoride on Laser Parameters

The minimum pump intensity $I_{min}$ is a measure for the ease of pumping the laser material to get laser action. It is a very important parameter to evaluate the potential laser property. The lower the minimum pump intensity, the higher the pump efficiency, then the better laser property. $I_{min}$ describes the minimum absorbed pump intensity that is required for transparency to be achieved at the extraction wavelength. $I_{min}$ is calculated by the following equation [23]:

$$I_{min} = \beta_{min}\cdot I_{sat}, \tag{7}$$

where

$$\beta_{min} = \frac{\sigma_{abs}(\lambda_{laser})}{\sigma_{abs}(\lambda_{laser}) + \sigma_{emi}(\lambda_{laser})} = \left\{1 + \frac{Z_l}{Z_u}\exp\left(\frac{E_{zl} - hc\lambda_{laser}^{-1}}{kT}\right)\right\}, \tag{8}$$

$$I_{sat} = \frac{hc}{\lambda_{pump}\sigma_{abs}(\lambda_{pump})\tau_m},$$

where $\beta_{min}$ is defined as the minimum fraction of $Yb^{3+}$ ions that should be excited to balance the gain exactly with the ground state absorption at the laser wavelength. $I_{sat}$ is the pumping saturation intensity that characterizes the pumping dynamics. Minimum values of $\beta_{min}$, $I_{sat}$, and $I_{min}$ are apparently preferred in terms of laser properties. $I_{min}$ is mainly determined by $\sigma_{emi}$ and $\tau_m$ according to (7). The figure of merit of the $Yb^{3+}$-doped laser materials is given by the $I_{min}$ and $\sigma_{emi}$, and it turns out to be given by the emission cross-section $\sigma_{emi}$ and fluorescence lifetime $\tau_m$. Therefore, the combination of higher $\sigma_{emi}$, longer lifetime $\tau_m$, and lower minimum pump intensity $I_{min}$ give a better $Yb^{3+}$-doped laser material. The parameters such as laser gain coefficient $\sigma_{emi}\cdot\tau_m$ and minimum pump intensity $I_{min}$ are given in Table 4.

The $\sigma_{emi}\cdot\tau_m$ increases with increasing fluoride content in series A glasses, since addition of fluorine promotes emission cross-section $\sigma_{emi}$ and fluorescence lifetime $\tau_m$. In spite of shorter $\tau_m$, series B glasses exhibit higher values of $\sigma_{emi}\cdot\tau_m$ and $I_{min}$ due to higher $\sigma_{emi}$ and the $I_{min}$ of series B glasses is superior to the known QX/Yb glass [24]. Therefore, we believe that the fluorophosphate glasses are promising laser glasses for high-peak power and high-average power.

## 5. Conclusion

$Yb^{3+}$-doped fluorophosphate laser glasses have successfully been developed. A systematic investigation of physical properties including refractive index, Abbe number, nonlinear refractive index, microhardness, and thermal expansion coefficient has been performed as a function of fluoride content. With the increase of fluoride content, the microhardness increases gradually along with the decrease of thermal expansion coefficient. The structure around $Yb^{3+}$ is simultaneously changed which greatly influences the spectroscopic properties and laser parameters. The best laser performance is found in $44P_2O_5$-$7Al_2O_3$-$4Nb_2O_5$-10LiF-$20MgF_2$-$14CaF_2$-$1Yb_2O_3$ glass system with the gain coefficient $\sigma_{emi}\cdot\tau_m$(0.824 pm$^2$·ms) and minimum pump intensity $I_{min}$(1.112 kw/cm$^2$). The favorable combination of outstanding physical, spectroscopic properties and laser parameters indicates that current $Yb^{3+}$-doped fluorophosphate glass is an excellent candidate material for $Yb^{3+}$-doped host for high-power generation.

## Acknowledgment

This work is financially supported by the Chinese National Defense New Materials Project (MKPT-05-240).

## References

[1] S.-X. Dai, L.-L. Hu, Z.-H. Jiang, G.-S. Huang, W. Chen, and P.-Z. Deng, "Study of ytterbium-doped phosphate and borate laser glasses," *Chinese Journal of Lasers*, vol. 29, no. 1, pp. 82–86, 2002 (Chinese).

[2] G. Karlsson, V. Pasiskevicius, A. Fragemann, J. Hellstom, and F. Laurell, "Generation of 100 kW-level pulses at 1.53 $\mu$m in the diode-pumped Er-Yb:glass laser-PPKTP optical parametric amplifier system," in *International Conference on Lasers, Applications, and Technologies 2002: Advanced Lasers and Systems*, vol. 5137 of *Proceedings of SPIE*, pp. 37–42, Moscow, Russia, June 2002.

[3] S. Blaize, L. Bastard, C. Cassagnètes, and J. E. Broquin, "Multiwavelengths DFB waveguide laser arrays in Yb-Er codoped phosphate glass substrate," *IEEE Photonics Technology Letters*, vol. 15, no. 4, pp. 516–518, 2003.

[4] L. Zhang and H. Hu, "Evaluation of spectroscopic properties of $Yb^{3+}$ in tetraphosphate glass," *Journal of Non-Crystalline Solids*, vol. 292, no. 1–3, pp. 108–114, 2001.

[5] B. Peng and T. Izumitani, "Next generation laser glass for nuclear fusion," *The Review of Laser Engineering*, vol. 21, no. 12, pp. 1234–1244, 1993.

[6] J. H. Campbell, "Modeling platinum-inclusion dissolution in phosphate laser glasses," *Glass Science and Technology*, vol. 68, no. 3, pp. 96–101, 1995.

[7] C. Jiang, H. Liu, Q. Zeng, X. Tang, and F. Gan, "Yb: phosphate laser glass with high emission cross-section," *Journal of Physics and Chemistry of Solids*, vol. 61, no. 8, pp. 1217–1223, 2000.

[8] P. R. Ehrmann and J. H. Campbell, "Nonradiative energy losses and radiation trapping in neodymium-doped phosphate laser glasses," *Journal of the American Ceramic Society*, vol. 85, no. 5, pp. 1061–1069, 2002.

[9] S. Toyoda, S. Fujino, and K. Morinaga, "Density, viscosity and surface tension of 50RO-50$P_2O_5$ (R: Mg, Ca, Sr, Ba, and Zn) glass melts," *Journal of Non-Crystalline Solids*, vol. 321, no. 3, pp. 169–174, 2003.

[10] P. Y. Shih, S. W. Yung, and T. S. Chin, "FTIR and XPS studies of $P_2O_5$-$Na_2O$-CuO glasses," *Journal of Non-Crystalline Solids*, vol. 244, no. 2-3, pp. 211–222, 1999.

[11] P. A. Bingham, R. J. Hand, and S. D. Forder, "Doping of iron phosphate glasses with $Al_2O_3$, $SiO_2$ or $B_2O_3$ for improved thermal stability," *Materials Research Bulletin*, vol. 41, no. 9, pp. 1622–1630, 2006.

[12] H. Takebe, T. Harada, and M. Kuwabara, "Effect of $B_2O_3$ addition on the thermal properties and density of barium phosphate glasses," *Journal of Non-Crystalline Solids*, vol. 352, no. 6-7, pp. 709–713, 2006.

[13] L. Zhang, H. Sun, H. Wu, J. Wang, L. Hu, and J. Zhang, "Effects of $PbF_2$ on the spectroscopic, lasing and structural properties of $Yb^{3+}$-doped fluorophosphate glass," *Solid State Communications*, vol. 135, no. 1-2, pp. 150–154, 2005.

[14] J. H. Choi, A. Margaryan, A. Margaryan, and F. G. Shi, "Optical transition properties of $Yb^{3+}$ in new fluorophosphate glasses with high gain coefficient," *Journal of Alloys and Compounds*, vol. 396, no. 1-2, pp. 79–85, 2005.

[15] J. H. Campbell and T. I. Suratwala, "Nd-doped phosphate glasses for high-energy/high-peak-power lasers," *Journal of Non-Crystalline Solids*, vol. 263-264, pp. 318–341, 2000.

[16] H. Takebe, T. Murata, and K. Morinaga, "Compositional dependence of absorption and fluorescence of $Yb^{3+}$ in oxide glasses," *Journal of the American Ceramic Society*, vol. 79, no. 3, pp. 681–687, 1996.

[17] L. D. DeLoach, S. A. Payne, L. L. Chase, L. K. Smith, W. L. Kway, and W. F. Krupke, "Evaluation of absorption and emission properties of $Yb^{3+}$ doped crystals for laser applications," *IEEE Journal of Quantum Electronics*, vol. 29, no. 4, pp. 1179–1191, 1993.

[18] D. C. Yeh, W. A. Sibley, M. Suscavage, and M. G. Drexhage, "Radiation effects and optical transitions in $Yb^{3+}$ doped barium-thorium fluoride glass," *Journal of Non-Crystalline Solids*, vol. 88, no. 1, pp. 66–82, 1986.

[19] B. Karmakar, P. Kundu, and R. N. Dwivedi, "IR spectra and their application for evaluating physical properties of fluorophosphate glasses," *Journal of Non-Crystalline Solids*, vol. 289, no. 1–3, pp. 155–162, 2001.

[20] X. Zou and H. Toratani, "Evaluation of spectroscopic properties of $Yb^{3+}$ -doped glasses," *Physical Review B*, vol. 52, no. 22, pp. 15889–15897, 1995.

[21] T. Miyakawa and D. L. Dexter, "Phonon sidebands, multiphonon relaxation of excited states, and phonon-assisted energy transfer between ions in solids," *Physical Review B*, vol. 1, no. 7, pp. 2961–2969, 1970.

[22] L. Zhang, H. Hu, C. Qi, and F. Lin, "Spectroscopic properties and energy transfer in $Yb^{3+}/Er^{3+}$-doped phosphate glasses," *Optical Materials*, vol. 17, no. 3, pp. 371–377, 2001.

[23] L. D. DeLoach, S. A. Payne, L. K. Smith, W. L. Kway, and W. F. Krupke, "Laser and spectroscopic properties of $Sr_5(PO_4)_3F$:Yb," *Journal of the Optical Society of America B*, vol. 11, no. 2, pp. 269–276, 1994.

[24] U. Griebner, R. L. Koch, H. Schonnagel, et al., "Laser performance of a new ytterbium doped phosphate laser glass," in *Proceedings of the OSA Topical Meeting on Advanced Solid-State Lasers (ASSL '96)*, S. A. Payne and C. R. Pollock, Eds., vol. 1, pp. 26–29, OSA, San Francisco, Calif, USA, January-February 1996.

Hindawi Publishing Corporation
Laser Chemistry
Volume 2008, Article ID 623872, 6 pages
doi:10.1155/2008/623872

*Research Article*

# Processing of Dielectric Optical Coatings by Nanosecond and Femtosecond UV Laser Ablation

**J. Ihlemann, J. Békési, J.-H. Klein-Wiele, and P. Simon**

*Laser-Laboratorium Göttingen e.V., Hans-Adolf-Krebs-Weg 1, 37077 Göttingen, Germany*

Correspondence should be addressed to J. Ihlemann, juergen.ihlemann@llg-ev.de

Received 31 May 2008; Accepted 2 September 2008

Recommended by Jacques Albert

Microprocessing of dielectric optical coatings by UV laser ablation is demonstrated. Excimer laser ablation at deep UV wavelengths (248 nm, 193 nm) is used for the patterning of thin oxide films or layer stacks. The layer removal over extended areas as well as sub-$\mu$m-structuring is possible. The ablation of $SiO_2$, $Al_2O_3$, $HfO_2$, and $Ta_2O_5$ layers and layer systems has been investigated. Due to their optical, chemical, and thermal stability, these inorganic film materials are well suited for optical applications, even if UV-transparency is required. Transparent patterned films of $SiO_2$ are produced by patterning a UV-absorbing precursor $SiO_x$ suboxide layer and oxidizing it afterwards to $SiO_2$. In contrast to laser ablation of bulk material, in the case of thin films, the layer-layer or layer-substrate boundaries act as predetermined end points, so that precise depth control and a very smooth surface can be achieved. For large area ablation, nanosecond lasers are well suited; for patterning with submicron resolution, femtosecond excimer lasers are applied. Thus the fabrication of optical elements like dielectric masks, pixelated diffractive elements, and gratings can be accomplished.



## 1. Introduction

Optical coatings have a variety of applications. Especially design, fabrication, and applications of dielectric optical interference coatings are subject of numerous studies [1]. For the classical use as mirror, beam splitter, or antireflection coating, extended areas have to be homogeneously coated. Therefore, the production of dielectric coatings has been optimized to obtain such high quality coatings nearly without defects on large substrates. But there are other applications, where the coating is needed in locally well-defined areas, for example, masks or waveguides. Coating technology is not well developed in this direction. Deposition through stencil masks is possible but not with high spatial resolution. In this case, the coatings have to be processed following the deposition process in order to generate spatially well-defined patterns. Usually lithographic processes are applied, but they have limited applicability, because the required etching processes are complicated and not sufficiently developed for all used materials.

Laser ablation is a versatile and widespread method for microprocessing of materials. Nearly any kind of technical materials like polymers, metals, glass, ceramics, and composite materials has been investigated with respect to its response to intense pulsed laser irradiation [2, 3]. In the field of high-precision microfabrication, especially (UV-) excimer lasers are used due to their inherent capability of producing high spatial resolution. Various applications like drilling of micro holes or nozzles, marking of eye glasses, or stripping of wires have been developed and transferred into industrial processes.

But laser ablation is not only good for the treatment of bulk material, it can be utilized for the patterning of thin films as well, for example, optical coatings. In contrast to the treatment of bulk materials, where many laser pulses are required to, for example, drill a material to a certain depth, in the case of thin layers very few or even a single pulse is sufficient to generate the desired ablation pattern. Regarding the capability of simultaneous processing of large areas by mask projection, which is enabled by the flat top beam profile of excimer lasers, there seems to be a huge potential of patterning thin films by this method.

Because under certain conditions the layer-layer or layer-substrate boundaries act as predetermined breaking points,

the ablated depth profile is not directly correlated with the (sometimes inhomogeneous) beam profile. Whereas in the case of bulk material ablation, spatial variations of the beam intensity will lead to a correspondingly irregular surface profile, this will not necessarily be the case for layer ablation, because there is a certain process window concerning the fluence for complete layer ablation [4]. Thus even with some spatial variations of the irradiation fluence, a very flat surface can be achieved.

Patterning of optical layers is useful for the fabrication of optical components like waveguides, coupling gratings, refractive, reflective, or diffractive structures. In most cases, transparent films with high transmission in the operation wavelength range have to be used. For applications in the visible or infrared spectral ranges, often polymeric materials can be applied, though their mechanical and thermal stability is limited. For example, the laser patterning of layers for fabricating (diffractive) optical elements has already been performed with polyimide films [5]. For UV applications, the control of processing UV-transparent materials, especially inorganic oxide materials, is necessary. Within the broad range of methods for the microfabrication of optical elements, this paper treats the structuring of (UV-) transparent inorganic oxide layers and layer stacks by laser ablation. Special attention is paid to a combined process, where an absorbing suboxide (SiO) layer is patterned and afterwards oxidized into a transparent oxide ($SiO_2$).

## 2. Methods and Materials

### 2.1. Laser Systems

Excimer lasers are optimally suited for a number of tasks concerning ablation of optical coatings. The emitted UV-light is readily absorbed by most of the relevant coating materials. However, due to the specific band edge of each material, different laser wavelengths are required. $TiO_2$, for example, s already absorbed in the near UV (308 nm). Efficient absorption of $Ta_2O_5$ is obtained at 248 nm, and for $HfO_2$ an even shorter wavelength of 193 nm is required. Excimer lasers emit powerful pulses with a flat top beam profile enabling large area processing, for example, by mask projection. Even the pulse duration of 10 or 20 nanosecond seems to be quite optimal for the ablation of optical layers. The thermal diffusion length L of around 50 to 500 nm which is related to the laser pulse length $\tau$ by $L \sim \tau^{1/2}$ and characterizes the heat-affected zone (HAZ) is short enough to minimize lateral damage, but sufficiently long to provide heat flow within the typical layer thickness, which promotes the liftoff of a complete layer with a single pulse [6, 7]. However, when structure details in the submicron range have to be fabricated, for example, gratings with a period of several 100 nm, this thermal diffusion length is too large, so that shorter laser pulses are required. To combine the capability of high optical resolution with that of a small heat-affected zone, a UV ultrafast laser system is applied. This comprises a Ti:Sa front-end laser, a frequency tripling unit to convert the wavelength of the ultrashort pulses into the UV spectral range, and a specially designed KrF amplifier to boost up the energy of the pulses to the several mJ range. The current laser arrangement (Figure 1) uses a commercial Ti:Sa front-end system delivering pulses of 150 femtoseconds duration at a wavelength of 745 nm. After frequency tripling, seed pulses are obtained for the KrF amplifier module which is the key component of the system. This module is a modified version of a Lambda Physik *NovaLine* laser. In a three-pass amplification scheme, the pulses are amplified up to an energy of 30 mJ at repetition rates exceeding 350 Hz, resulting in an average power of 10 W at 248 nm [8]. The results on UV-femtosecond laser processing shown in Section 3 have been obtained using a predecessor system with 500 femtoseconds pulse duration.

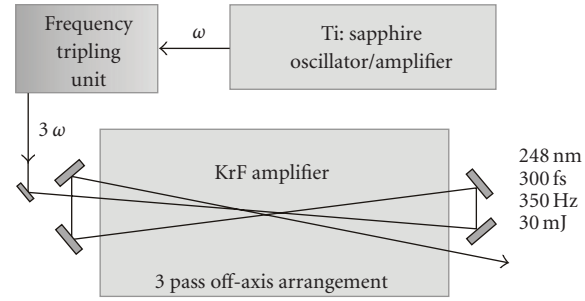


Figure 1: Layout of the UV femtosecond hybrid laser system.

### 2.2. Beam Delivery

Excimer laser processing is usually carried out in a mask projection configuration. A mask consisting of transparent and opaque (or reflective) areas is illuminated by the flat top laser beam. Using a lens or a complex imaging system, the mask is projected on the surface of the work piece, so that the pattern of the mask is reproduced (usually demagnified) in this plane leading to material ablation in the irradiated regions at sufficiently high fluence.

Mask projection is known to be a well-suited irradiation strategy for simultaneous treatment of extended sample areas. On the other hand, multiple beam interference has shown to be very effective in creating a great variety of periodic nanostructures [9–11]. But also a combination of these two techniques allows the fabrication of well-defined, versatile periodic nanostructures over large sample areas [12, 13]. To create a linear grating pattern, for example, a transmission grating is placed in the mask position, and this mask plane is imaged onto the sample surface using a lens or a microscope objective. By using a suitable arrangement of apertures, distinct diffraction orders can be transmitted while others are blocked. This way the simplest case of two beam interference can be realized, even with laser beams of limited spatial and temporal coherence.

### 2.3. Irradiation Configurations

In principle, there are two different methods to induce ablative removal of a film from a substrate. Either the beam is directed head-on towards the film leading to "front-side

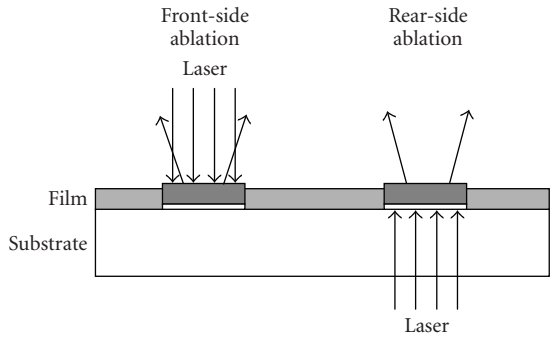


Figure 2: Front-side and rear-side laser ablation of coatings.

ablation," or the beam hits the film from the other side after passing through the substrate "rear-side ablation" (Figure 2). Rear-side ablation is possible, if the substrate is sufficiently transparent at the laser wavelength. For standard excimer laser wavelengths, this is the case, for example, for UV-grade fused silica.

In the case of front-side ablation, depending on laser fluence, film thickness, and absorption properties of film and substrate, the whole film or part of it can be ablated. If the film consists of a layer stack, it is even possible to ablate layer after layer by successive laser pulses [14]. In the case of rear-side irradiation with sufficient fluence, the whole film or layer stack is ablated with a single-laser pulse. The advantage of this method is that due to the forward transfer of the material in the direction of the laser beam, there is no possibility for the interaction of the laser radiation with already ablated fragments. In the case of front-side ablation, this interaction can lead to considerable debris formation around the ablated area, if no countermeasures are applied. Furthermore the required laser fluence for complete ablation is much higher and the edge quality is lower for front-side ablation.

## 2.4. Materials and Material Transformation

The materials of the coatings studied are mainly transparent metal oxides like $Al_2O_3$, $HfO_2$, $Ta_2O_5$, $Nb_2O_5$ with absorption edges somewhere in the UV. As a sufficiently high absorption is a prerequisite for precise ablation, special care has to be taken when selecting the laser wavelength. The applied laser wavelength should be below the absorption edge of the material. $Ta_2O_5$, $Nb_2O_5$ are transparent above about 300 nm, therefore, for ablation, a shorter wavelength, for example, 248 nm is required. $HfO_2$ is transparent down to about 220 nm, so that 193 nm should be used for ablation. $Al_2O_3$ and $SiO_2$ are transparent even at 193 nm, so the use of a 157 nm radiation is necessary. An alternative approach is the following: instead of an $SiO_2$-coating, a silicon monoxide (SiO) or at least a substoichiometric silicon oxide ($SiO_x$, $x < 2$) is deposited. These materials are UV-absorbing and can therefore be easily processed using 193 nm or 248 nm excimer lasers. After patterning, the remaining $SiO_x$ is oxidised to $SiO_2$ by heating it in air to obtain the desired functionality of the patterned coating (Figure 3). The ability

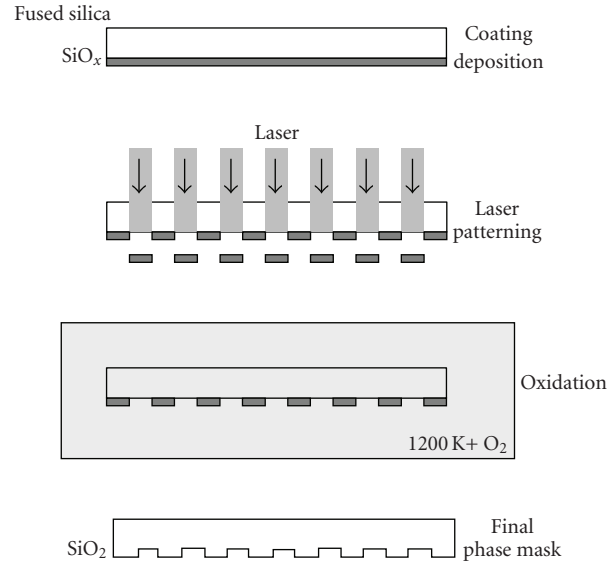


Figure 3: Processing scheme for patterning of SiO-coating with subsequent oxidation to $SiO_2$.

of UV laser radiation at 248 nm to cause ablation of $SiO_x$ films has already been demonstrated long time ago [15].

## 3. Results and Discussion

### 3.1. Single Layer Coatings

Figure 4 shows the results of rear-side ablation of a single silicon monoxide layer. Clean ablation with sharp edges and nearly without redeposition of debris is observed. The ablation depth as a function of the laser fluence for a 285 nm thick SiO-layer on fused silica is displayed in Figure 5. Within a fluence range of about 200 to 600 mJ/cm$^2$ the complete layer is ablated with a single-laser pulse (the ablation depth is constant and corresponds to the film thickness). Above this process window, at about 1 J/cm$^2$ the fused silica substrate is ablated, too. These observations can be explained by treating the layer-substrate boundary as predetermined end points, so that precise depth control and a very smooth surface can be achieved, even if the laser beam is somewhat inhomogeneous within the limits given by the process window. This behavior is similar to that observed in early work on ablating thin metal films with an excimer laser [16], which showed good potential resolution with liftoff through heat flow to the interface.

### 3.2. Diffractive Phase Elements

As an example for the patterning of a transparent film on a transparent substrate, the fabrication of a binary diffractive phase element (DPE) is demonstrated. DPEs are very attractive for beam shaping because of their basically lossless operation. They can be implemented by a (pixelated) surface profile on a transparent optical material and can be applied for beam homogenization, beam splitting or efficient

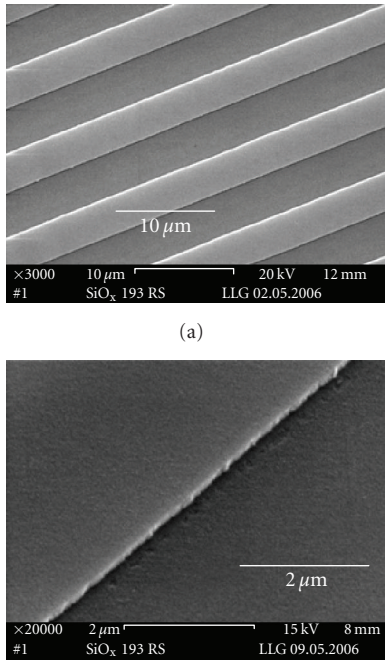


Figure 4: 175 nm SiO on fused silica, rear-side ablation, 193 nm, 20 nanoseconds, 540 mJ/cm$^2$, 1 pulse.

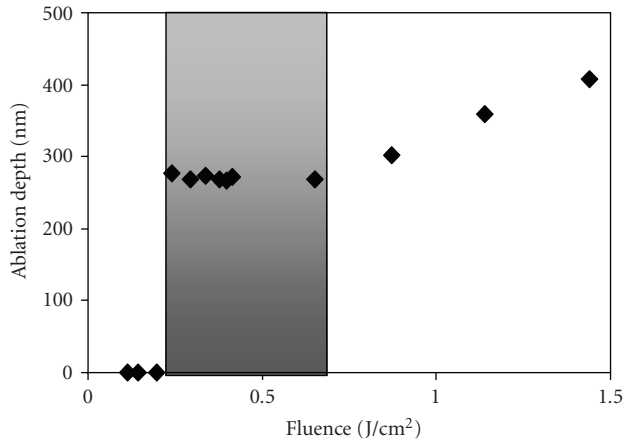


Figure 5: Ablation depth versus fluence of 193 nm-single pulse rear side ablation of a 285 nm thick SiO layer on fused silica. In the range from 200 to 600 mJ/cm$^2$ (marked grey), the complete layer is ablated; at fluences above 600 mJ/cm$^2$, in addition material from the substrate is ablated.

mask illumination. A binary phase element for operation at a UV-wavelength $\lambda$ can be made by ablation patterning a UV-transparent oxide film with a refractive index $n$ and a thickness of $D = \lambda/[2(n-1)]$. Pixel sizes of about $10 \times 10\,\mu m^2$ are convenient for fabrication and application. The ablation process can be performed pixel by pixel according to thecalculated DPE design or by creating the whole structure at the same time using a mask. For applications of the DPE in the near UV, $Ta_2O_5$ is an adequate material. $Ta_2O_5$ absorbs

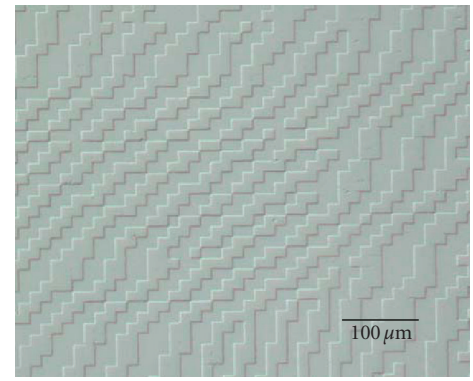


Figure 6: $SiO_2$-diffractive phase element made by single-pulse rear-side ablation of SiO at 248 nm, 25 nanoseconds, 350 mJ/cm$^2$, and subsequent oxidation.

at 248 nm sufficiently, to be patterned by ablation, but is transparent at 308 nm. This means that a DPE for use at 308 nm can be fabricated using 248 nm [17].

For fabricating a phase element to operate in the deep UV, for example, at 193 nm, a film material that is transparent at this wavelength is necessary, for example, $SiO_2$. In this case, the above mentioned two-step process is applied [18]. First, an absorbing SiO layer is patterned by laser ablation, then the patterned film is oxidised to UV-transparent $SiO_2$. Figure 6 shows a DPE made by this method.

## 3.3. Multilayer Coatings

A typical application for the patterning of multilayers for optical applications is the fabrication of dielectric optical masks. Such multilayer stacks, for example, of alternating $HfO_2$- (high refractive index) and $SiO_2$-layers (low refractive index) can be ablated by an ArF-excimer laser, because $HfO_2$ is absorbing at 193 nm. Although the thickness of the film is more than 1 $\mu$m, under certain conditions sub-$\mu$m edge definition is achieved in the case of rear side ablation.

If both materials of the dielectric layer stack are transparent at 193 nm, the ablation of these systems has to be performed either at even shorter wavelengths (Vacuum-UV) [19], or with an absorbing subsidiary layer. Thus dielectric mirrors with high reflectivity at 193 nm consisting of a stack of alternating $SiO_2$- and $Al_2O_3$-layers were patterned by depositing a 193 nm absorbing $HfO_2$- or SiO-layer between substrate and HR-stack and ablating in a rear side configuration (Figure 7) [20].

Dielectric masks fabricated by this method can be applied for high intensity laser applications, where metal masks (Cr on quartz) would be easily damaged. It is even possible to fabricate grey-level masks by ablating only a defined number of single layers instead of the whole stack [14]. As this process works only by front-side ablation, the edge definition of the ablated structures is limited. To achieve high-precision edges even in the case of front-side ablation, the UV-femtosecond laser system was applied. Figure 8 shows such an ablation

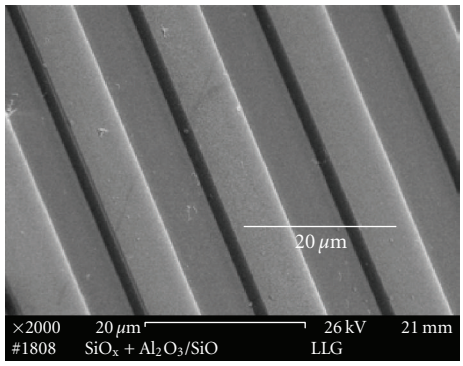


Figure 7: $Al_2O_3/SiO_2$-multilayer stack with underlying SiO-absorber layer on fused silica, rear side ablation, 193 nm, 20 nanoseconds, 500 mJ/cm$^2$, 1 pulse.

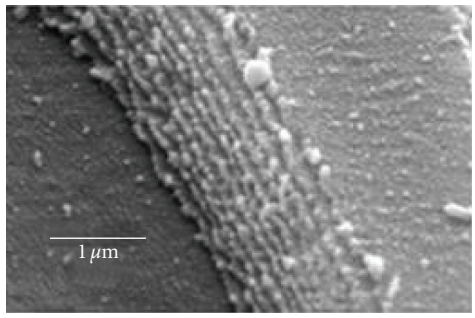


Figure 8: $HfO_2/SiO_2$-multilayer stack on fused silica, front-side ablation, 248 nm, 500 femtoseconds, multipulse irradiation.

edge, where the multilayer structure of the stack can be clearly resolved.

### 3.4. High-Resolution Patterning

Patterning a thin film with high (sub-$\mu$m) resolution is desirable, for instance, for the fabrication of optical gratings. To achieve the required optical resolution at high-fluence levels, a mask projection setup using a reflective objective is suitable. The laser pulse duration has to be limited, so that thermal diffusion of the energy coupled into the film does not lead to blurring of the submicron pattern. For metal films, pulse durations as short as 50 ps already lead to diminished structure resolution [21]. For polymer films with their low-thermal diffusivity, comparatively long nanosecond pulses can be applied, but metal oxide films exhibit rather high-thermal diffusivities, so that short pulses are required. Then it is possible to adjust the depth of the pattern in the film by the number of pulses, so that the film can be ablated partly or completely down to the substrate (front side ablation). Figure 9 shows a grating with 500 nm period made in a $Ta_2O_5$-film with the described ultrashort pulse excimer laser. Such gratings may by applied for coupling light into planar waveguide, or for the so-called *grating waveguide structures*, which are used, for example, for biosensors based on fluorescence detection [22–24]. Also SiO

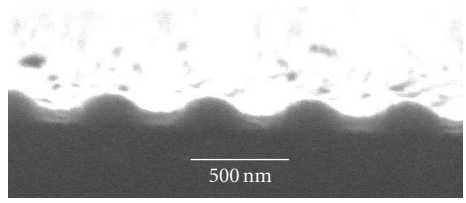


Figure 9: 150 nm $Ta_2O_5$ on glass, front side ablation, 248 nm, 500 femtoseconds, 300 mJ/cm$^2$, 2 pulses.

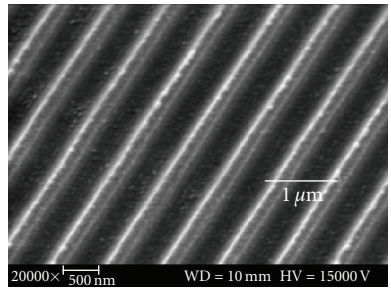


(a)

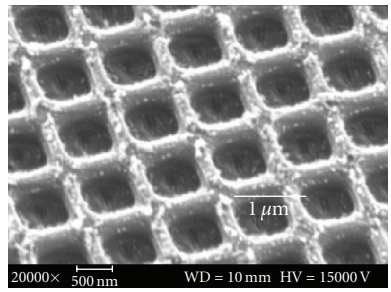


(b)

Figure 10: 175 nm SiO on fused silica, front side ablation at 248 nm, 500 femtoseconds.

layers can be patterned with high resolution using this UV-fs laser system (Figure 10).

## 4. Summary

UV-transparent inorganic oxide layers are patterned with excimer laser radiation with high precision. Complete layer stacks or only parts of them are ablated depending on fluence and irradiation conditions. To achieve high spatial resolution, a UV-fs-laser system is applied. Nonabsorbing layers are patterned by laser processing of an absorbing sub-stoichiometric "precursor" layer and subsequent oxidation. Thus, dielectric masks, pixelated diffractive phase elements, and submicron gratings are micro fabricated.

## Acknowledgment

The financial support from the BMWi of Germany (grant no. 16IN0395) is gratefully acknowledged.

## References


[1] N. Kaiser and H. K. Pulker, Eds., *Optical Interference Coatings*, Springer, Berlin, Germany, 2003.

[2] D. Basting and G. Marowsky, Eds., *Excimer Laser Technology*, Springer, Berlin, Germany, 2005.

[3] D. Bäuerle, *Laser Processing and Chemistry*, Springer, Berlin, Germany, 3rd edition, 2000.

[4] J. Ihlemann and K. Rubahn, "Excimer laser micro machining: fabrication and applications of dielectric masks," *Applied Surface Science*, vol. 154-155, pp. 587–592, 2000.

[5] G. P. Behrmann and M. T. Duignan, "Excimer laser micromachining for rapid fabrication of diffractive optical elements," *Applied Optics*, vol. 36, no. 20, pp. 4666–4674, 1997.

[6] E. Matthias, M. Reichling, J. Siegel, et al., "The influence of thermal diffusion on laser ablation of metal films," *Applied Physics A*, vol. 58, no. 2, pp. 129–136, 1994.

[7] J. Ihlemann and B. Wolff-Rottke, "Excimer laser ablation patterning of dielectric layers," *Applied Surface Science*, vol. 86, no. 1–4, pp. 228–233, 1995.

[8] J. Békési, S. Szatmári, P. Simon, and G. Marowsky, "Table-top KrF amplifier delivering 270 fs output pulses with over 9 W average power at 300 Hz," *Applied Physics B*, vol. 75, no. 4-5, pp. 521–524, 2002.

[9] H. M. Phillips and R. A. Sauerbrey, "Excimer-laser-produced nanostructures in polymers," *Optical Engineering*, vol. 32, no. 10, pp. 2424–2436, 1993.

[10] S. Pissadakis, L. Reekie, M. Hempstead, M. N. Zervas, and J. S. Wilkinson, "Ablated gratings on borosilicate glass by 193-nm excimer laser radiation," *Applied Physics A*, vol. 69, no. 7, pp. S739–S741, 1999.

[11] T. Kondo, S. Matsuo, S. Juodkazis, V. Mizeikis, and H. Misawa, "Multiphoton fabrication of periodic structures by multibeam interference of femtosecond pulses," *Applied Physics Letters*, vol. 82, no. 17, pp. 2758–2760, 2003.

[12] J.-H. Klein-Wiele and P. Simon, "Fabrication of periodic nanostructures by phase-controlled multiple-beam interference," *Applied Physics Letters*, vol. 83, no. 23, pp. 4707–4709, 2003.

[13] J.-H. Klein-Wiele, J. Békési, J. Ihlemann, and P. Simon, "High speed fabrication of periodic nanostructures," in *Proceedings of the 3rd International WLT-Conference Lasers in Manufacturing (LIM '05)*, p. 477, Munich, Germany, June 2005.

[14] K. Rubahn and J. Ihlemann, "Graded transmission dielectric optical masks by laser ablation," *Applied Surface Science*, vol. 127–129, pp. 881–884, 1998.

[15] C. Fiori and R. A. B. Devine, "High resolution ultraviolet photoablation of $SiO_x$ films," *Applied Physics Letters*, vol. 47, no. 4, pp. 361–362, 1985.

[16] J. E. Andrew, P. E. Dyer, R. D. Greenough, and P. H. Key, "Metal film removal and patterning using a XeCl laser," *Applied Physics Letters*, vol. 43, no. 11, pp. 1076–1078, 1983.

[17] J. Ihlemann and D. Schäfer, "Fabrication of diffractive phase elements for the UV-range by laser ablation patterning of dielectric layers," *Applied Surface Science*, vol. 197-198, pp. 856–861, 2002.

[18] M. Schulz-Ruhtenberg, J. Ihlemann, and J. Heber, "Laser patterning of $SiO_x$-layers for the fabrication of UV diffractive phase elements," *Applied Surface Science*, vol. 248, no. 1–4, pp. 190–195, 2005.

[19] D. Schäfer, J. Ihlemann, G. Marowsky, and P. R. Herman, "F2-laser ablation patterning of dielectric layers," *Applied Physics A*, vol. 72, no. 3, pp. 377–379, 2001.

[20] J. Ihlemann, K. Rubahn, and R. Thielsch, "Laser ablation patterning of dielectric layer stacks for 193-nm mask fabrication," in *Second International Symposium on Laser Precision Microfabrication*, vol. 4426 of *Proceedings of SPIE*, pp. 437–440, Singapore, May 2002.

[21] P. Simon and J. Ihlemann, "Machining of submicron structures on metals and semiconductors by ultrashort UV-laser pulses," *Applied Physics A*, vol. 63, no. 5, pp. 505–508, 1996.

[22] F. Beinhorn, J. Ihlemann, P. Simon, et al., "Sub-micron grating formation in $Ta_2O_5$-waveguides by femtosecond UV-laser ablation," *Applied Surface Science*, vol. 138-139, no. 1–4, pp. 107–110, 1999.

[23] S. Pissadakis, M. N. Zervas, L. Reekie, and J. S. Wilkinson, "High-reflectivity Bragg gratings fabricated by 248-nm excimer laser holographic ablation in thin $Ta_2O_5$ films overlaid on glass waveguides," *Applied Physics A*, vol. 79, no. 4–6, pp. 1093–1096, 2004.

[24] C. Kappel, A. Selle, T. Fricke-Begemann, M. A. Bader, and G. Marowsky, "Giant enhancement of two-photon fluorescence induced by resonant double grating waveguide structures," *Applied Physics B*, vol. 79, no. 5, pp. 531–534, 2004.

Hindawi Publishing Corporation
Laser Chemistry
Volume 2008, Article ID 892721, 4 pages
doi:10.1155/2008/892721

*Research Article*

# Three-Dimensional Residue-Free Volume Removal inside Sapphire by High-Temperature Etching after Irradiation of Femtosecond Laser Pulses

**Shigeki Matsuo, Kensuke Tokumi, Takuro Tomita, and Shuichi Hashimoto**

*Department of Ecosystem Engineering, The University of Tokushima, 2-1 Minamijosanjimacho, Tokushima 770-8506, Japan*

Correspondence should be addressed to Shigeki Matsuo, matsuos@eco.tokushima-u.ac.jp

Received 4 June 2008; Accepted 29 August 2008

Recommended by Stavros Pissadakis

We applied the femtosecond laser-assisted etching technique, that is, irradiation of focused femtosecond laser pulses followed by selective chemical etching, to volume removal inside sapphire. At room temperature, volume etching only slightly advanced while residue remained inside the volume. By increasing the etching temperature, complete volume etching without residue was achieved. Complete etching was, however, accompanied by undesirable phenomena of surface pits or cracks, which are expected to be excluded through further improvement of processing.



## 1. Introduction

Despite recent progress in micro/nanotechnology, material processing with three-dimensional (3D) shape flexibility remains a challenging task in the micrometer domain. Sacrificial layer etching [1] is an established technique in the field of microelectromechanical systems (MEMSs) for fabricating suspended structures. Nevertheless, it requires large-scale semiconductor equipment. Femtosecond (fs) laser processing of photopolymers [2, 3] is a widely used technique for 3D submicrometer processing, but the target materials of that technique are limited to polymers. For that reason, the technique is inapplicable to solid materials.

Femtosecond laser-assisted etching offers the possibility of removal processing with 3D flexibility in the micrometer domain. The technique consists of two steps: irradiation of focused femtosecond pulses along a predesigned pattern and subsequent chemical etching. The modified region will be etched out selectively; a 3D empty space is fabricated if the irradiated region is more soluble to the etchant. In fact, 3D microstructuring by femtosecond laser-assisted etching was first reported in 1999 with a photosensitive glass [4]. Subsequently, similar 3D microstructuring was reported with a nonphotosensitive material, silica glass [5], and other materials [6–9].

Sapphire ($Al_2O_3$ crystal) is a hard and inert material that plays important roles in optics and electronics. For example, it is used as a substrate material of a GaN light-emitting diode. Several techniques have been reported for micropatterning of sapphire and Ti:sapphire, such as a combination of ion implantation and wet chemical etching [10], reactive ion etching [11], and argon ion-beam etching [12]. Especially, a combination of ion implantation and wet chemical etching [10] enabled us to underetch the surface layer, but this technique requires very large and expensive equipment. Femtosecond laser-assisted etching is a promising technique for 3D microstructuring of sapphire; microchannels were fabricated by this technique [8, 13]. However, we have reported that complete removal of the volume region is difficult. Mesh-like residue remains after etching [14]. Volume etching is necessary for applications that require a complete hollow space, such as embedded optical components [15, 16], nanoaquariums for dynamic observation of living cells [17], and fluid mixing by optical rotators [18]. A new technique is necessary to achieve volume etching for sapphire. In all previous reports of femtosecond laser-assisted etching, wet etching was carried out at room

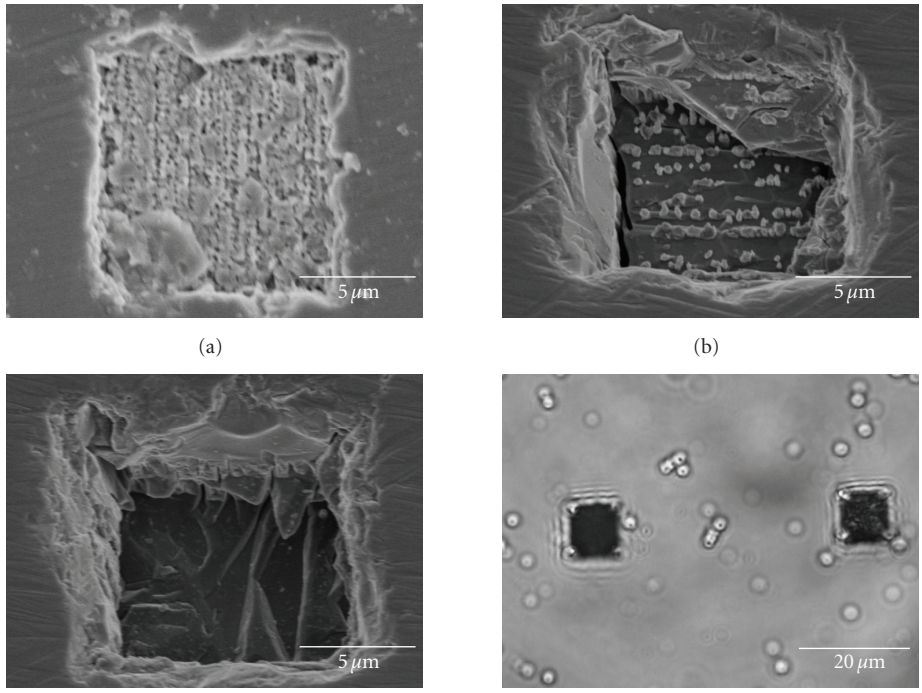


(a) (b) (c) (d)

Figure 1: (a)–(c) SEM micrographs inside sapphire with a laser irradiation condition of $p_x = 0.2\,\mu$m and $p_z = 2.0\,\mu$m, and after etching (a) at room temperature for 72 hours, (b) at 100°C for 24 hours, and (c) at 120°C for 24 hours. (d) Optical micrograph of sapphire after etching at 120°C for 48 hours. In this micrograph, both the surface and subsurface are visible.

temperature. In the present study, we carried out etching at high temperatures aiming at complete residue-free removal of the volume region inside sapphire.

## 2. Experimental

The sample used was sapphire (0001) substrate (Shinkosha Co., Ltd., Yokohama, Japan) grown using the Kyropoulos method. The typical FWHM of its X-ray rocking curve is 4 seconds. The sample was set on an inverted microscope (IX-70; Olympus Corp., Tokyo, Japan), and femtosecond laser pulses (800 nm, 130 femtoseconds) were focused by an objective lens (UPlanApo100; Olympus Corp.) and irradiated to the sample. Irradiation of a single femtosecond pulse with a typical pulse energy of about 40 nJ produced a micrometer-scale modified spot (amorphous region surrounded by a strain field [8]) inside the sapphire without cracking. Hereinafter, this spot is referred to as voxel.

The whole modified region is a square cuboid $10\,\mu$m below the surface, with four paths which connect the square cuboid and the surface. The size of the square cuboid was $x \times y \times z = 10 \times 10 \times 10\,\mu\text{m}^3$, where the $z$-axis is the direction perpendicular to the substrate surface. In the square cuboid region, voxels are arranged in a simple tetragonal lattice. The period on the $x$-axis and $y$-axis, $p_x$, was typically $0.2\,\mu$m. The period on the $z$-axis, $p_z$, was 1–4 $\mu$m; here the results with $p_z = 1\,\mu$m and $2\,\mu$m are reported. After irradiation, the sample was observed using optical microscopy.

The etchant was a 10% aqueous solution of hydrofluoric acid. Etching was carried out in a teflon-coated high-pressure cell. The cell, containing etchant and sample, was put in an electric oven at 80–150°C. After etching, the sample was inspected using optical microscopy and scanning electron microscopy (SEM). SEM observation was carried out on the surface and the subsurface irradiated region. For SEM observation of the subsurface irradiated region, the sample was mechanically polished so that the region was observable directly. The direct SEM observation of the irradiated region is important because nondestructive optical observation alone might be insufficient to reveal the residue [14].

## 3. Results and Discussion

Through these experiments, we discovered that both irradiation and etching conditions can improve removal capability, although each has its own disadvantages.

First, the results with $p_z = 2\,\mu$m are described. Figure 1(a) depicts an SEM micrograph inside after etching at room temperature for 72 hours. Volume etching only slightly advanced; a mesh-like residue was observed. Figure 1(b) presents an SEM micrograph of the interior after etching at an elevated temperature of 100°C for 24 hours. Volume etching was somewhat improved. A single layer was removed, but further advances in depth (in the $z$ direction) did not take place. When etching temperatures were further elevated to 120°C, much advance took place in volume etching; residue was lost and complete removal was achieved, as

shown in Figure 1(c). However, another problem appeared. Figure 1(d) shows an optical micrograph of sapphire after etching. In addition to the subsurface etched regions (dark squares), surface pits (small bright spots) can be seen. The pits were absent before etching but they appeared after etching for a long period. Reportedly, pits are generated on the surface of sapphire during high-temperature etching; the origin of the pits is related to dislocations [19]. The pits observed here have a hexagonal shape and are aligned to the same direction, which suggests that the shape is related to the crystalline nature of sapphire. In the present experiments, the generation of surface pits became a problem when the etching temperature was elevated. The pits on the surface scatter light to unintended directions. For that reason, they are undesirable for optical applications. We have performed examination with several etching temperatures and etching periods, but we were unable to find a temperature-period window in which complete volume etching can be achieved without surface pits. The surface pits can probably be removed by polishing subsequent to the etching, but it is a time-consuming process. A complete etching method that leaves no surface pits is desired. It is noteworthy that the roughness of the surface in the pit-free region did not deteriorate by etching ($R_a \lesssim 1$ nm; $R_a$ is the average of the roughness profile, as evaluated using atomic force microscopy).

For $p_z = 1.0\,\mu$m, etching advanced better than in the case of $p_z = 2.0\,\mu$m. Figure 2(a) depicts an SEM micrograph inside after etching at 100°C for 24 hours. From comparison with Figure 1(b), volume etching appears to be much more advanced with $p_z = 1.0\,\mu$m. However, another problem, cracking, appeared with $p_z = 1.0\,\mu$m. Figure 2(b) portrays optical micrographs inside sapphire after laser irradiation with $p_x = 0.2\,\mu$m and $p_z = 1.0\,\mu$m before and after etching. As shown there, cracks are visible from the corner of the square cuboid to the outside before etching (b1). After etching (b2), the laser-irradiated region darkened; the cracks are still observable. Cracks reduce the precision of fabrication and enable fluid to penetrate to unexpected regions. For that reason, generation of cracks should be avoided.

As described above, cracks did not appear by irradiation of a single femtosecond pulse with the present irradiation condition. After irradiation of the cuboid region with a small $p_z$ of $1.0\,\mu$m, cracks appeared at the outside of the corner of the cuboid region. These results suggest that cracks are generated by superposition of stress of multiple voxels. Consequently, the decrease in the period of voxels enhanced the generation of cracks.

Figure 3 schematically summarizes the results. The horizontal axis indicates the laser irradiation condition: the right side corresponds to the higher density (smaller period of voxels) and higher pulse energy. The vertical axis indicates etching conditions: "up" corresponds to the higher temperature and longer period. Three thick lines mark the borders of the issues to be overcome. Corresponding double arrows mark the desirable side. The three double arrows point to the different directions. Therefore, the overlapping region of the three is small even if it exists. We have not yet found such an overlapping region. Three borderlines cross at a point in

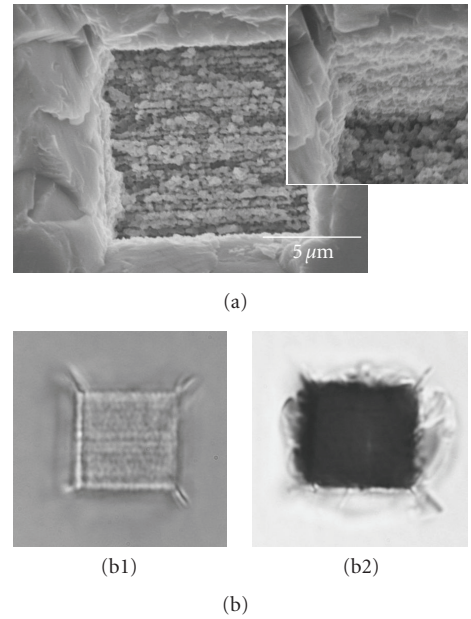


Figure 2: (a) SEM micrographs inside sapphire with a laser irradiation condition of $p_x = 0.2\,\mu$m and $p_z = 1.0\,\mu$m after etching at 100°C for 24 hours. The inset presents a close-up oblique view tilted at 20°. (b) Optical micrographs of the same sample as (a), (b1) before etching, and (b2) after.

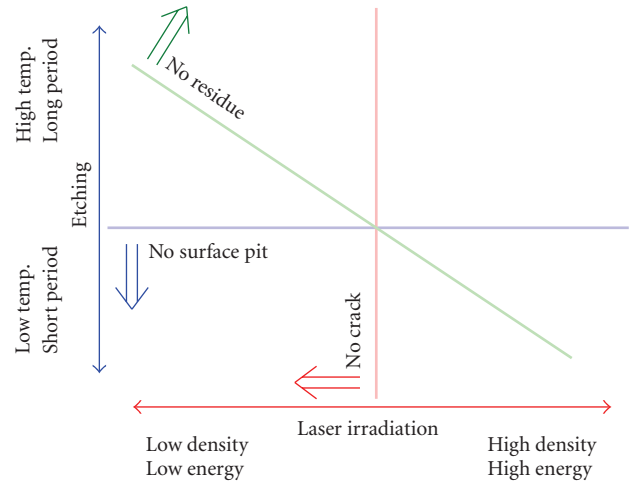


Figure 3: Schematic diagram of removal property of sapphire by femtosecond laser-assisted etching. Thick broken lines are borderlines of three issues; corresponding double arrows show the desirable region.

Figure 3, but the relative position of the lines has not been clarified yet. The existence of the overlapping region remains as an open question.

Another remaining problem is the roughness at the interface between etched and unetched regions. As shown in Figure 1(c), where complete volume etching was achieved with a generation of surface pits, the bottom of the etched cuboid is rough. At present, this roughness cannot be controlled during processing. A new processing strategy is

necessary for applications in which roughness hinders its use, as in optical applications.

## 4. Conclusion

Complete removal of the volume region by femtosecond laser-assisted etching inside sapphire was achieved. The increased etching temperature and increased density of laser irradiation points aided the progress of etching. Changes in the experimental parameters, however, caused undesirable phenomena of surface pits and cracks. The compatible region of experimental parameters, where complete etching is achieved without such problems, is expected to be small. For that reason, refinement of the experimental parameters or establishment of a new processing strategy is required.

## Acknowledgments

The authors would like to thank Professor Tatsuya Okada for fruitful discussion. This work was partly supported by KAKENHI (20360115), Nippon Sheet Glass Foundation for Materials Science and Engineering, and the Venture Business Laboratory of The University of Tokushima.

## References

[1] L.-S. Fan, Y.-C. Tai, and R. S. Muller, "Integrated movable micromechanical structures for sensors and actuators," *IEEE Transactions on Electron Devices*, vol. 35, no. 6, pp. 724–730, 1988.

[2] H.-B. Sun, S. Matsuo, and H. Misawa, "Three-dimensional photonic crystal structures achieved with two-photon-absorption photopolymerization of resin," *Applied Physics Letters*, vol. 74, no. 6, pp. 786–788, 1999.

[3] S. Kawata, H.-B. Sun, T. Tanaka, and K. Takada, "Finer features for functional microdevices," *Nature*, vol. 412, no. 6848, pp. 697–698, 2001.

[4] Y. Kondo, J. Qiu, T. Mitsuyu, K. Hirao, and T. Yoko, "Three-dimensional microdrilling of glass by multiphoton process and chemical etching," *Japanese Journal of Applied Physics*, vol. 38, no. 10A, pp. L1146–L1148, 1999.

[5] A. Marcinkevičius, S. Juodkazis, M. Watanabe, et al., "Femtosecond laser-assisted three-dimensional microfabrication in silica," *Optics Letters*, vol. 26, no. 5, pp. 277–279, 2001.

[6] R. S. Taylor, C. Hnatovsky, E. Simova, et al., "Ultra-high resolution index of refraction profiles of femtosecond laser modified silica structures," *Optics Express*, vol. 11, no. 7, pp. 775–781, 2003.

[7] Y. Bellouard, A. Said, M. Dugan, and P. Bado, "Fabrication of high-aspect ratio, micro-fluidic channels and tunnels using femtosecond laser pulses and chemical etching," *Optics Express*, vol. 12, no. 10, pp. 2120–2129, 2004.

[8] S. Juodkazis, K. Nishimura, H. Misawa, et al., "Control over the crystalline state of sapphire," *Advanced Materials*, vol. 18, no. 11, pp. 1361–1364, 2006.

[9] S. Matsuo, Y. Tabuchi, T. Okada, S. Juodkazis, and H. Misawa, "Femtosecond laser assisted etching of quartz: microstructuring from inside," *Applied Physics A*, vol. 84, no. 1-2, pp. 99–102, 2006.

[10] A. Crunteanu, G. Jänchen, P. Hoffmann, et al., "Three-dimensional structuring of sapphire by sequential $He^+$ ion-beam implantation and wet chemical etching," *Applied Physics A*, vol. 76, no. 7, pp. 1109–1112, 2003.

[11] A. Crunteanu, M. Pollnau, G. Jänchen, et al., "Ti:sapphire rib channel waveguide fabricated by reactive ion etching of a planar waveguide," *Applied Physics B*, vol. 75, no. 1, pp. 15–17, 2002.

[12] C. Grivas, D. P. Shepherd, T. C. May-Smith, et al., "Performance of $Ar^+$-milled Ti: sapphire rib waveguides as single transverse-mode broadband fluorescence sources," *IEEE Journal of Quantum Electronics*, vol. 39, no. 3, pp. 501–507, 2003.

[13] D. Wortmann, J. Gottmann, N. Brandt, and H. Horn-Solle, "Micro- and nanostructures inside sapphire by fs-laser irradiation and selective etching," *Optics Express*, vol. 16, no. 3, pp. 1517–1522, 2008.

[14] S. Matsuo, Y. Shichijo, T. Tomita, and S. Hashimoto, "Laser fabrication of ship-in-a-bottle microstructures in sapphire," *Journal of Laser Micro/Nanoengineering*, vol. 2, no. 2, pp. 114–116, 2007.

[15] Y. Cheng, K. Sugioka, and K. Midorikawa, "Microfluidic laser embedded in glass by three-dimensional femtosecond laser microprocessing," *Optics Letters*, vol. 29, no. 17, pp. 2007–2009, 2004.

[16] Z. Wang, K. Sugioka, and K. Midorikawa, "Three-dimensional integration of microoptical components buried inside photosensitive glass by femtosecond laser direct writing," *Applied Physics A*, vol. 89, no. 4, pp. 951–955, 2007.

[17] Y. Hanada, K. Sugioka, H. Kawano, I. S. Ishikawa, A. Miyawaki, and K. Midorikawa, "Nano-aquarium for dynamic observation of living cells fabricated by femtosecond laser direct writing of photostructurable glass," *Biomedical Microdevices*, vol. 10, no. 3, pp. 403–410, 2008.

[18] S. Matsuo, S. Kiyama, Y. Shichijo, et al., "Laser microfabrication and rotation of ship-in-a-bottle optical rotators," *Applied Physics Letters*, vol. 93, no. 5, Article ID 051107, 3 pages, 2008.

[19] P. L. Edwards and S. Huang, "Comparison of whisker growth sites and dislocation etch pits on single-crystal sapphire," *Journal of the American Ceramic Society*, vol. 49, no. 3, pp. 122–125, 1966.

Hindawi Publishing Corporation
Laser Chemistry
Volume 2008, Article ID 868767, 7 pages
doi:10.1155/2008/868767

*Research Article*

# Photosensitivity of the Er/Yb-Codoped Schott IOG1 Phosphate Glass Using 248 nm, Femtosecond, and Picosecond Laser Radiation

**Stavros Pissadakis and Irini Michelakaki**

*Institute of Electronic Structure and Laser, Foundation for Research and Technology-Hellas, N. Plastira 100, Vasilika Vouton, P.O. Box 1527, 71 110 Heraklion, Greece*

Correspondence should be addressed to Stavros Pissadakis, pissas@iesl.forth.gr

Received 13 August 2008; Accepted 17 September 2008

Recommended by Jacques Albert

The effect of 248 nm laser radiation, with pulse duration of 5 picoseconds, 500 femtoseconds, and 120 femtoseconds, on the optical properties and the Knoop hardness of a commercial Er/Yb-codoped phosphate glass is presented here. Refractive index changes of the order of few parts of $10^{-4}$ are correlated with optical absorption centers induced in the glass volume, using Kramers-Kroning relationship. Accordingly, substantially lower refractive index changes are measured in volume Bragg gratings inscribed in the glass, indicating that, in addition to the optical density changes, volume dilation changes of negative sign may also be associated with the 248 nm ultrafast irradiation. The Knoop hardness experimental results reveal that the glass matrix undergoes an observable initial hardening and then a reversing softening and volume dilation process for modest accumulated energy doses, where the Knoop hardness follows a nonmonotonic trend. Comparative results on the Knoop hardness trend are also presented for the case of 193 nm excimer laser radiation. The above findings denote that the positive or negative evolution of refractive index changes induced by the 248 nm ultrafast radiation in the glass is dominated by the counteraction of the color center formation and the volume modification effects.



## 1. Introduction

Phosphate glasses are promising host matrixes for the development of free-space and waveguiding optical devices, serving a diverse number of photonic applications. The pentavalent phosphorus can build flexible tetrahedra, where a double oxygen bond occupies one coordination corner, allowing the easy accommodation of other network modifiers, without affecting the glass polymerization chains. That microcoordination structure of the fundamental phosphoric glass matrix leads to specific macroscopic and spectroscopic properties, such as high solubility of rare earths without increasing quenching problems for laser excitation, low transformation temperatures, and potentially high transmissions in the deep ultraviolet wavelengths. Phosphate glasses have been employed as hosts for efficient waveguide [1] and fiber amplifiers [2] and lasers [3], biosensing devices [4], while recently, they have been used as platforms for inscribing into 2D photonic crystal structures [5]. Even though the above unique optical properties that phosphate glasses exhibit and the numerous applications serve, their photosensitivity has been examined in depth, only recently. The first studies on the phosphate glasses photosensitivity were carried out using femtosecond infrared [6] and near ultraviolet laser sources [7], in pristine or silver-doped matrixes. Later, other studies were presented including deep ultraviolet lasers, by means of 248 nm [8] and 193 nm [9] nanosecond excimer and 213 nm, 150 picoseconds Nd:YAG laser radiation [10]. In general, phosphate glasses appear to be of low photosensitivity with the index changes induced in those within the range of $10^{-4}$ and $10^{-5}$, while utilizing high intensities and rather prolonged exposures. Addition of codopand ions, such as Ag [8] or Ge [11], can substantially increase the photosensitivity and

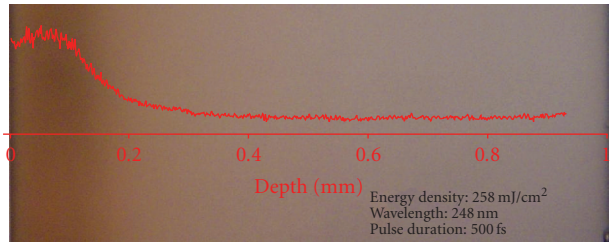


Figure 1: Optical microscope picture obtained from a side polished IOG1 phosphate glass sample, exposed using 248 nm, 500-femtosecond laser radiation and 36 000 pulses of 258 mJ/cm$^2$ energy density. The red line is a normalized gray scale absorption line obtained using image processing.

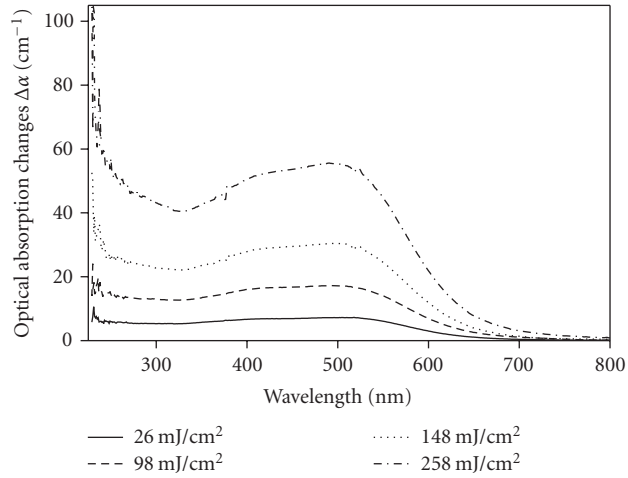


Figure 2: Optical absorption changes $\Delta\alpha$ for IOG1 glass samples exposed to different energy densities using 36 000 pulses of 500-femtosecond pulse duration. The absorption data have been normalized to coloration-damage depth as that was measured using optical microscopy imaging.

refractive index changes obtained by more than one order of magnitude. Moreover, the index changes induced in pristine glasses can be either of positive or negative sign, depending upon the exact composition of the exposed glass, the intensities, and energy densities used, as well as the accumulated energy doses dissipated in the glass volume [9, 12]. The origin of that interesting index engineering behavior is possibly associated with counteracting, radiation triggered, physical mechanisms. In particular, recent studies have revealed that in addition to the strong photochromic effects that occur in phosphate glasses under deep ultraviolet laser irradiation, significant volume modifications also take place, promoted by significant microstructural rearrangements undergone in the glass coordination [5, 9].

Herein, we investigate the photosensitivity of the high-performance rare earth doped IOG1 phosphate glass (manufactured by Schott, NY, USA) [13], after exposure to 248 nm, 5-picosecond, 500-femtosecond, and 120-femtosecond laser radiation. The IOG1 glass is optimized for being ion-exchangeable using $K^+$ and $Ag^+$ ions, for developing low loss, high-power lasers, and amplifiers [14]. Our target is to provide and correlate the laser-induced changes in the optical and structural data, for gaining a better insight in the underlying photosensitivity behavior of a commercial ultraphosphate glass matrix. The first part of the study presented herein investigates the effect of the exposure to such high photon energy and extreme intensity radiation on fundamental optical quantities of the glass such as that of the optical absorption and the refractive index. Moreover, the last part of the current study will include additional results on the effect of the irradiation on the Knoop hardness of the pristine and exposed glass.

## 2. Experimental

The IOG1 samples exposed here had a thickness of 1 mm and contained 2.3% wt. $Er_2O_3$ and 3.6% wt. $Yb_2O_3$. Energy dispersive x-ray (EDX) microanalysis measurements performed in similar IOG1 glass batches revealed the existence of other oxides such as $Al_2O_3$, $La_2O_3$, and $Na_2O$ [8]. The laser used for the exposures was 248 nm, hybrid Lambda-Physik laser emitting 5-picosecond and 500-femtoseconds pulses, at a repetition rate of 10 Hz. The flux contrast ratio between the emitted picosecond/femtosecond pulse and the nanosecond tail is greater than 95%. For obtaining 120-femtosecond pulses, the 500-femtosecond output was compressed using two reflection gratings which were positioned in parallel, with a spacing of approximately 6 cm between them [15]. All the exposures performed using 36 000 pulses. In the nongrating exposures, the beam was focused onto the sample using a spherical fused silica lens of 20 cm focal length. A circular aperture was used for selecting the optimum part of the beam, and an oscillatory $CaF_2$ plate was placed in front of the sample to spatially scan the beam for averaging irregularities. The glass samples were exposed to energy densities varying between 25 mJ/cm$^2$ and 258 mJ/cm$^2$. The spectrophotometric data were obtained by employing an UV-Visible spectrophotometer, scanning from 190 to 1500 nm.

The spectral data obtained for each sample were normalized to the damage depth induced by the radiation. This volume damage depth was estimated using optical microscopy imaging of the endface of polished samples and subsequent suitable image processing (see Figure 1).

The inscription of Bragg gratings was carried out by employing a 1070 nm period fused silica, phase mask in "almost" contact mode. The phase mask was of ±1 order design, while it was optimized for the 248 nm wavelength, exhibiting 0th order less than 1%. For assuring preferential inscription of the 535 nm period, the phase mask was thoroughly aligned with respect to the planar sample using an external He-Ne red beam. A rectangular aperture was used for selecting the optimum part of the beam and a fused silica 20 cm cylindrical lens for beam focusing. The samples were exposed to different energy densities which varied between 15 mJ/cm$^2$ and ≈50 mJ/cm$^2$, for the case

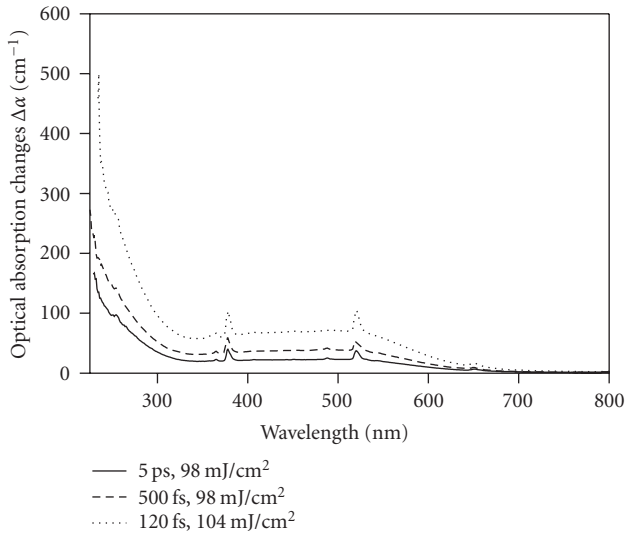


Figure 3: Optical absorption changes $\Delta\alpha$ for IOG1 glass samples exposed with different pulse durations using 36 000 pulses and similar energy density.

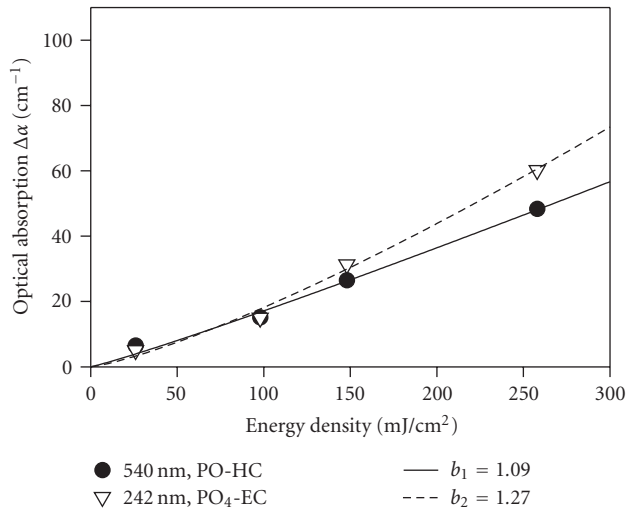


Figure 4: Spectral strength of the PO hole center (HC) located at 540 nm and that of the $PO_4$ electron center (EC) located at 242 nm versus energy density, for exposures using 248 nm, 500-femtosecond laser radiation.

of 500-femto second pulse duration. The volume gratings inscribed in the IOG1 glass were measured using a simple diffraction efficiency setup, employing a 632 nm He-Ne laser, while the gratings probed at Bragg angle. The refractive index changes induced in the glass were evaluated using standard coupled-mode theory for thick, phase-absorption gratings [16], considering a spatial coherence length of the order of the laser beam of $\approx 75\,\mu$m [17]. Knoop hardness measurements were performed using Matsuzawa, MXT70, digital microhardness indentation microscope, and applying a 50 gf load for 20-second indentation time. For reducing statistical errors, more than 15 indentations were applied on each sample examined. The exposed sample area was in general wider than 2 $mm^2$, allowing easy accommodation of the indentation traces. The Knoop hardness measurements performed in the pristine sample leaded to a hardness value of 381, a figure that is very close to the value that is provided by the manufacturer [13]. All spectral, refractive index, and hardness measurements were obtained a week after the laser exposures performed, for allowing defect and structural relaxations to reach a plateau state.

## 3. Results and Discussion

The changes in the optical absorption changes $\Delta\alpha$ of the exposed glass slabs for exposures of different energy densities using 500-femtosecond pulse duration, normalized to the penetration depth of the laser radiation at the 1/e target point, are presented in Figure 2. The exposures were performed using 36 000 pulses, while real time probing of the defect 540 nm band by employing a 2 mW 541 nm He-Ne revealed that color center saturation was easily reached shortly after the first 20 minutes of the exposure time, for all the pulse durations and energy densities used.

Also, the optical absorption changes $\Delta\alpha$ of the exposed glass for fixed energy density and variable pulse duration are presented in Figure 3. A significant absorption band related to PO bond hole center defects is formed between 220 nm and 700 nm. The spectral strength of the data presented (see Figure 1) denotes the occurrence of significant electronic changes induced into the exposed glass, by means of cleaving/deforming of the characteristic PO bond and the generation of PO-related centers by electron or hole retrapping [18].

The changes in optical absorption induced by 248 nm, 120-femtosecond, and 500-femtosecond laser radiation are substantially greater than that obtained using nanosecond pulses of similar energy density [8]; and on the same magnitude with those induced by 193 nm excimer laser radiation [9]. A point of disagreement with previous reports refers to the bleaching band located at the spectral vicinity of 240 nm [8]. In the spectral data presented in Figure 2, such bleaching feature does not exist. This may be attributed either to stoichiometric variations of the composition between the IOG1 samples exposed in different studies or to fundamental differences emerge from the underlying photosensitivity mechanism. We speculate that a bleaching band may be formed at that spectral location due to the annihilation of the $PO_4$ electron center; however, its strength can be screened by extensive electron retrapping generated by the longer wavelength bands [18]. Moreover, the accumulated energy density figures needed for inducing such optical density changes, using ultrafast 248 nm radiation, are significantly lower compared to that for corresponding exposures using 193 nm or 248 nm nanosecond radiation [9]. Another comment related to the high durability is that the phosphate glasses exhibit to the ultraviolet radiation. Extreme intensities of the order of $\approx 0.87$ TW/$cm^2$ (104 mJ/$cm^2$ at 120 femtoseconds) can be dissipated inside the glass matrix without triggering

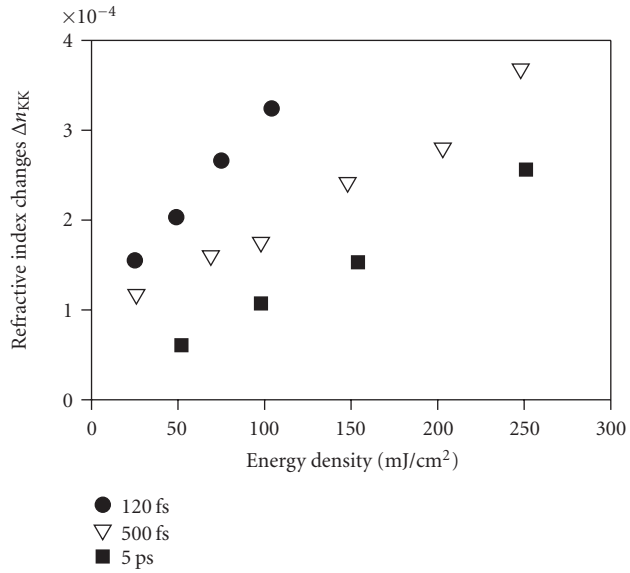


Figure 5: Refractive index changes $\Delta n_{KK}$ induced in the IOG1 phosphate glass using 248 nm, 5-picosecond, 500-femtosecond, and 120-femtosecond laser radiation versus energy density, estimated using Kramers-Kronig transformation.

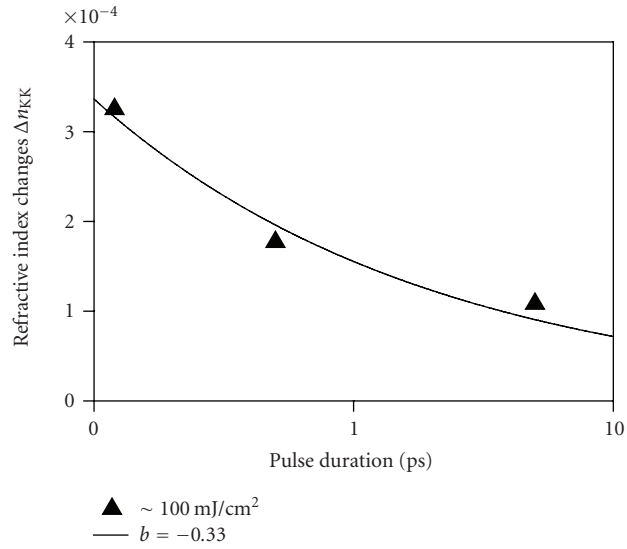


Figure 6: Refractive index changes $\Delta n_{KK}$ induced in the IOG1 phosphate glass versus pulse duration for fixed energy density dose of 248 nm laser radiation.

surface ablation or filamentation in the glass volume, while the corresponding figure for high-purity silicate glass is ≈0.2 TW/cm$^2$ (24 mJ/cm$^2$ at 120 femtoseconds).

The dependence of the radiation-induced optical density changes $\Delta\alpha$ upon the energy density of the exposure is presented in Figure 4. The data presented refer to two characteristic defect peaks that of PO hole center (HC) located at 540 nm and that of the $PO_4$ electron center (EC) located at 242 nm [18].

Both peaks increase with respect to the energy density of the exposure, while by fitting them to a simple exponential law of the form $\Delta\alpha \propto F^b$, where $F$ is the exposure energy density, the $b$ factor is evaluated to be slightly greater than unity (see $b$-data in Figure 4). The last indicates that the underlying color center generation process is linearly dependent upon the number of photons per area provided in the glass matrix.

Further, refractive index changes induced by the femtosecond radiation into the glass were estimated by using Kramers-Kronig transformation, from relaxed spectrophotometric data, for the wavelength of 633 nm. The refractive index differences $\Delta n_{KK}$, which are solely associated with color-centers formation (see Figure 5), were estimated to be of the order of few parts of $10^{-4}$, for all the pulse durations and the energy densities employed. These refractive index changes were calculated using the volume damage depths that were measured using optical microscopy imaging. For reference, the FWHM of these volume damage depths was varied between 300 $\mu$m for the 26 mJ/cm$^2$ exposure and 135 $\mu$m for the 258 mJ/cm$^2$ exposure, for the case of the 500-femtosecond radiation (see Figure 1). Accordingly, longer penetration depths up to 1 mm were measured for the case of the 5-picosecond

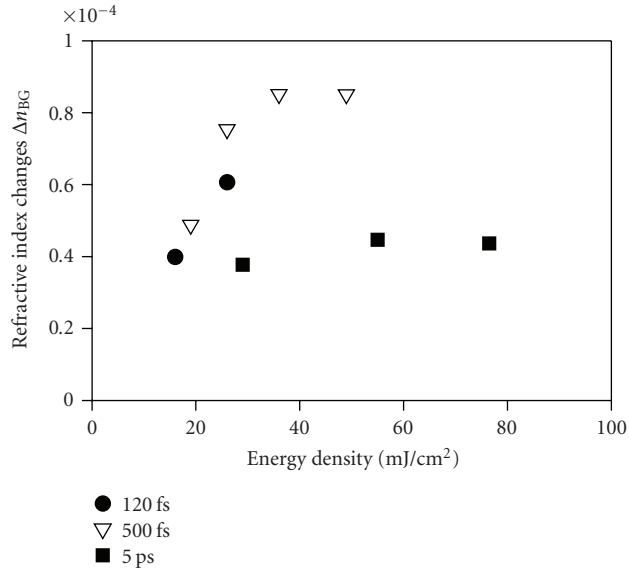


Figure 7: Refractive index changes $\Delta n_{BG}$ measured in Bragg gratings inscribed in the IOG1 glass using diffraction efficiency measurements.

exposures, while these depth figures become smaller for the case of 120-femtosecond irradiation (≈100 $\mu$m). Similarly, with the spectral strength data presented in Figure 4, the refractive index changes $\Delta n_{KK}$ of Figure 5 exhibit a linear dependence upon the laser energy density, confirming that the color center generation process and the mutually-related refractive index changes are possible single photon absorption products.

Also, the intensities dissipated inside the glass volume affect the absorption correlated refractive index changes $\Delta n_{KK}$, where the 120-femtosecond exposures progress these refractive index changes in a faster rate. However, this

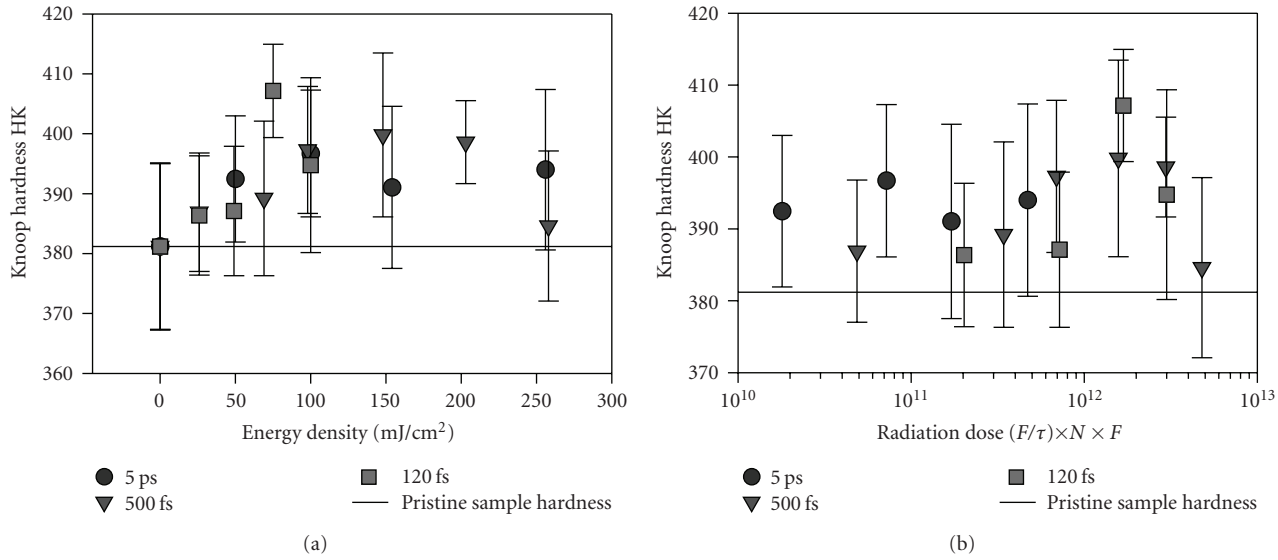


Figure 8: Knoop hardness measurements in pristine and exposed IOG1 phosphate glass versus (a) energy density and (b) energy dose for exposures using 5-picosecond, 500-femtosecond, and 120-femtosecond 248 nm laser radiation. $F$: energy density; $\tau$: pulse duration; $N$: number of pulses.

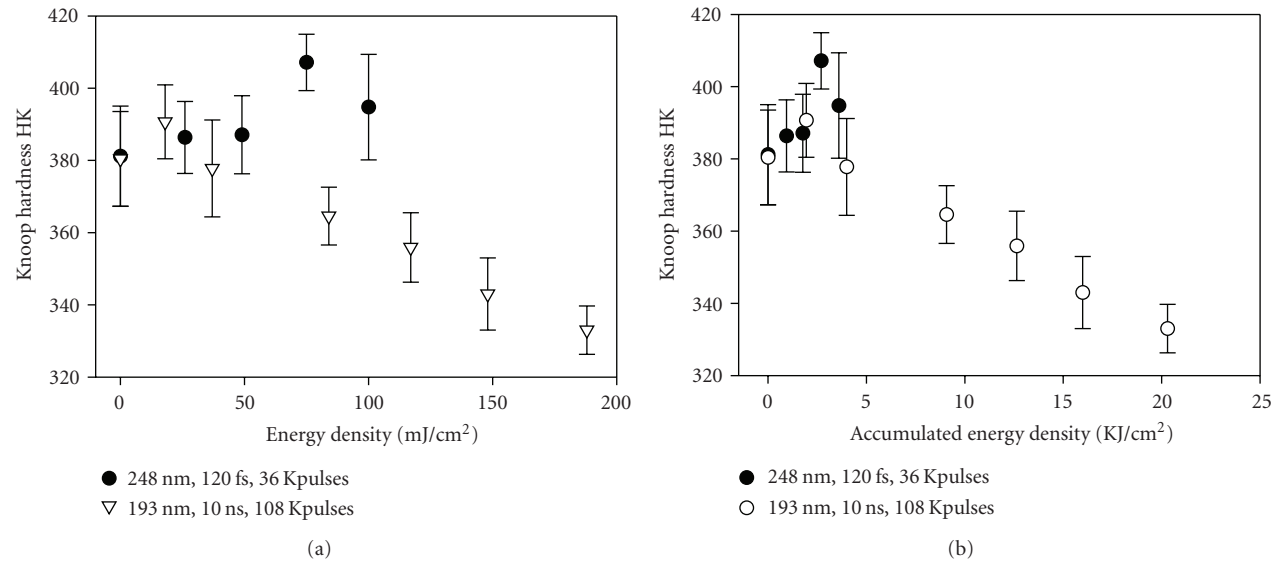


Figure 9: Knoop hardness measurements for IOG1 phosphate glass exposed using 120-femtosecond, 248 nm and 10 nanoseconds, 193 nm laser radiation versus (a) the energy density; and (b) the accumulated energy density of the exposure.

effect may be related with a reduction of the penetration depth due to extensive damage accumulation close to the glass surface vicinity, for greater exposure intensities applied.

In such a case, the photosensitivity products (optical defect concentration or refractive index changes) obtained will exhibit a sublinear dependence upon intensity, reducing the order of interaction below that of a single quantum for the 248 nm wavelength (see Figure 6).

Additional refractive index change measurements were carried out for Bragg gratings recorded in the Er/Yb-codoped IOG1 glass matrix (see Figure 7). The refractive index changes $\Delta n_{BG}$ obtained from diffraction efficiency measurements (Figure 7) are substantially lower than those estimated using Kramers-Kronig transformation, for exposures of the same energy density, while they exhibit a clear saturation trend. The above observation related to the absolute refractive index change magnitude indicates that an additional structural mechanism also contributes to the overall index changes measured in the grating structures. Yliniemi et al. reported that negative refractive index changes dominate the photosensitivity of the same glass using 193 nm excimer radiation [9], while we have found that similar negative refractive index changes may also occur for exposures using

213 nm, 150-picosecond radiation [10]. We believe that a negative refractive index change component also exists in the photosensitivity of the IOG1 phosphate glass using 248 nm picosecond and femtosecond-laser radiation. This negative sign refractive index component, that was revealed using the above correlated measurements (see Figures 5 and 7), may be associated with either localized stresses in the grating fringes [19] or absolute volume dilation.

For further identifying volume changes induced by the 248 nm laser irradiation into the IOG1 glass, we have performed Knoop hardness measurements on the exposed samples (see Figures 8(a) and 8(b)). The data of Figures 8(a) and 8(b) exhibit a nonmonotonous trend, for the three pulse durations employed.

In particular, for the cases of 500-femtosecond and 120-femtosecond irradiations, the Knoop hardness of the exposed samples undergoes an initial increase reaching a maximum value that is ≈6.8% greater than that of the pristine glass; while for increased doses [20] (see Figure 8(b)), the absolute hardness follows a declining trend, restoring to normal values. While the Knoop hardness changes induced using 5-picosecond pulses are rather noisy without following a clear trend for the exposures conditions applied, the results referring to the 500-femtosecond and 120-femtosecond pulse durations reach maximum for the same energy dose, indicating that the mechanisms triggered are of the same nature and strength. Changes in the hardness of the glass matrix are directly associated with elastic modulus changes and, therefore, radiation induced volume modifications [21, 22]. The nonmonotonous increase of Knoop hardness observed here can be initially attributed to volume compaction effects, which may related with the exhausting of a specific type of defect or with the passivation of surface singularities [23]. Accordingly, we believe that the decrease of hardness is related with the glass depolymerization proposed by Yliniemi et al. and observed in exposures using 193 nm nanosecond excimer laser radiation [9]. We have also performed micro-Raman spectroscopy using a 473 nm Ar-ion laser, in glass samples exposed using 120 femtoseconds, 100 mJ/cm$^2$, where the measurements show a ≈2.5% broadening of the two fundamental peaks located at 704 cm$^{-1}$ (POP symmetric bond) and 1184 cm$^{-1}$ ($PO_2$ symmetric bond), compared to that of the pristine glass; denoting the generation of a broad band of structural defects. Therefore, a glass depolymerization model based on the extensive cleaving of the fundamental PO bond may be used for explaining the volume dilation effects observed in the case of this ultraphosphate glass, when exposed to 248 nm picosecond and femtosecond radiations.

We believe that longer exposures employing 248 nm femtosecond radiation will succeed in lowering the Knoop hardness below the levels of the pristine sample. Such massive reduction of the surface hardness and the glass density has been observed in exposures using 193 nm excimer laser radiation (see Figures 9(a) and 9(b)), where the greater energy per photon progresses such reverse sign, structural, and volume modification effects much faster than the 248 nm radiation. These significant structural changes are induced for the case of 193 nm radiation without employing extreme sub-TW/cm$^2$ intensities, but by providing a photon energy that is close or slightly higher than the bandgap of the exposed material, while utilizing MW/cm$^2$ intensities. However, the massive decrease of the Knoop hardness and the accompanying strong volume dilation effects induced by the 193 nm exposures are observed in expense of increased accumulated energy densities; which in turn are manifold larger than those utilized for the 248 nm, 120-femtosecond irradiations (see Figure 9(b)). Finally, in Figure 9(b), we see that the Knoop hardness modifications induced by both wavelengths follow rather similar trends, while peaking at quite similar accumulated energy density value. Further work on the estimation of the elastic modulus of the glass exposed using 193 nm laser radiation and its correlation with the Knoop hardness and the exposure conditions are presented in detail elsewhere [24].

## 4. Conclusions

The photosensitivity of the Er/Yb-codoped IOG1 phosphate glass using 248 nm, 5-picosecond, 500-femtosecond, and 120-femtosecond laser radiation is presented here. We employed spectrophotometric measurements for identifying the absorption bands induced by the radiation; while later on, these spectral measurements were interpreted using Kramers-Kroning relationship for obtaining refractive index changes associated with this specific mechanism. The refractive index changes correlated with optical absorption centers induced in the glass volume are of the order of few parts of $10^{-4}$. Moreover, we employed Bragg grating recording in the glass volume for estimating the overall refractive index changes induced by the ultrafast radiation exposures. These measurements revealed that the overall refractive index changes formed are of substantially lower magnitude than those estimated using the Kramers-Kroning approach, indicating that, in addition to the optical density changes, volume dilation changes of negative sign are also associated with the 248 nm ultrafast irradiation. The Knoop hardness microindentation experimental results obtained show that the exposed glass matrix undergoes an observable initial hardening and then a reversing softening and volume dilation process for modest accumulated energy doses, wherein the Knoop hardness follows a nonmonotonic trend. Such observation justifies the lower refractive index changes gratings probed in volume Bragg grating reflectors, where the positive refractive index changes, due to color centers, are competed by the negative index changes induced by the volume dilation effects. We are working on a deeper investigation of the photosensitivity of phosphate glasses using ultraviolet nanosecond and femtosecond laser radiation, and the correlation of the results with those obtained for other well-studied glasses (i.e., Silicate and Germanosilicate amorphous matrices), using the same wavelengths and pulse durations. Also, gaining a better understanding on the volume damage and modification effects can be further exploited in the high yield selective chemical etching micro/nanoprocessing of the specific glass [5].

## Acknowledgments

Stavros Pissadakis gratefully acknowledges Leo Gilroy (Schott, NY, USA) for kindly providing the glass samples, as well as Vicky Vamvakaki and Nikos Chaniotakis (Laboratory of Analytical Chemistry, Chemistry Department, University of Crete) for performing the micro-Raman measurements.

## References

[1] D. L. Veasey, D. S. Funk, P. M. Peters, et al., "Yb/Er-codoped and Yb-doped waveguide lasers in phosphate glass," *Journal of Non-Crystalline Solids*, vol. 263-264, pp. 369–381, 2000.

[2] B. C. Hwang, S. Jiang, T. Luo, et al., "Erbium-doped phosphate glass fibre amplifiers with gain per unit length of 2.1 dB/cm," *Electronics Letters*, vol. 35, no. 12, pp. 1007–1009, 1999.

[3] J. Albert, A. Schüzgen, V. L. Temyanko, S. Honkanen, and N. Peyghambarian, "Strong Bragg gratings in phosphate glass single mode fiber," *Applied Physics Letters*, vol. 89, no. 10, Article ID 101127, 3 pages, 2006.

[4] M. Krauß and J. Leißner, "Bio-sensors for microbiological atmospheric pollution," in *Proceedings of the 7th ESG Conference on Glass Science and Technology*, Athens, Greece, April 2004, paper P-EI1.

[5] S. Pissadakis and C. Pappas, "Planar periodic structures fabricated in Er/Yb-codoped phosphate glass using multi-beam ultraviolet laser holography," *Optics Express*, vol. 15, no. 7, pp. 4296–4303, 2007.

[6] J. W. Chan, T. R. Huser, S. H. Risbud, J. S. Hayden, and D. M. Krol, "Waveguide fabrication in phosphate glasses using femtosecond laser pulses," *Applied Physics Letters*, vol. 82, no. 15, pp. 2371–2373, 2003.

[7] Y. Watanabe, G. Namikawa, T. Onuki, K. Nishio, and T. Tsuchiya, "Photosensitivity in phosphate glass doped with $Ag^+$ upon exposure to near-ultraviolet femtosecond laser pulses," *Applied Physics Letters*, vol. 78, no. 15, pp. 2125–2127, 2001.

[8] S. Pissadakis, A. Ikiades, P. Hua, A. K. Sheridan, and J. S. Wilkinson, "Photosensitivity of ion-exchanged Er-doped phosphate glass using 248 nm excimer laser radiation," *Optics Express*, vol. 12, no. 14, pp. 3131–3136, 2004.

[9] S. Yliniemi, S. Honkanen, A. Ianoul, A. Laronche, and J. Albert, "Photosensitivity and volume gratings in phosphate glasses for rare-earth-doped ion-exchanged optical waveguide lasers," *Journal of the Optical Society of America B*, vol. 23, no. 12, pp. 2470–2478, 2006.

[10] C. Pappas and S. Pissadakis, "Periodic nanostructuring of Er/Yb-codoped IOG1 phosphate glass by using ultraviolet laser-assisted selective chemical etching," *Journal of Applied Physics*, vol. 100, no. 11, Article ID 114308, 6 pages, 2006.

[11] S. Suzuki, A. Schülzgen, S. Sabet, J. V. Moloney, and N. Peyghambarian, "Photosensitivity of Ge-doped phosphate glass to 244 nm irradiation," *Applied Physics Letters*, vol. 89, no. 17, Article ID 171913, 3 pages, 2006.

[12] C. Pappas, *Fabrication of 1D and 2D relief Bragg reflectors in rare earth doped phosphate glass by employing holographic laser induced structural modification*, M.S. thesis, Physics Department, University of Crete, Heraklion, Greece, 2006.

[13] Schott Glass datasheets for IOG-1 glass.

[14] S. Yliniemi, J. Albert, Q. Wang, and S. Honkanen, "UV-exposed Bragg gratings for laser applications in silver-sodium ion-exchanged phosphate glass waveguides," *Optics Express*, vol. 14, no. 7, pp. 2898–2903, 2006.

[15] S. Szatmári and F. P. Schäfer, "Simplified laser system for the generation of 60 fs pulses at 248 nm," *Optics Communications*, vol. 68, no. 3, pp. 196–202, 1988.

[16] H. M. Smith, Ed., *Holographic Recording Materials*, Springer, Berlin, Germany, 1977.

[17] S. Kawata, I. Hikima, Y. Ichihara, and S. Watanabe, "Spatial coherence of KrF excimer lasers," *Applied Optics*, vol. 31, no. 3, pp. 387–396, 1992.

[18] D. Ehrt, P. Ebeling, and U. Nature, "UV transmission and radiation-induced defects in phosphate and fluoride-phosphate glasses," *Journal of Non-Crystalline Solids*, vol. 263-264, pp. 240–250, 2000.

[19] H. G. Limberger, P.-Y. Fonjallaz, R. P. Salathé, and F. Cochet, "Compaction- and photoelastic-induced index changes in fiber Bragg gratings," *Applied Physics Letters*, vol. 68, no. 22, pp. 3069–3071, 1996.

[20] D. C. Allan, C. Smith, N. F. Borrelli, and T. P. Seward III, "193-nm excimer-laser-induced densification of fused silica," *Optics Letters*, vol. 21, no. 24, pp. 1960–1962, 1996.

[21] Y. Bellouard, T. Colomb, C. Depeursinge, M. Dugan, A. A. Said, and P. Bado, "Nanoindentation and birefringence measurements on fused silica specimen exposed to low-energy femtosecond pulses," *Optics Express*, vol. 14, no. 18, pp. 8360–8366, 2006.

[22] D. B. Marshall, T. Noma, and A. G. Evans, "A simple method for determining elastic-modulus–to-hardness ratios using Knoop indentation measurements," *Journal of the American Ceramic Society*, vol. 65, no. 10, pp. c175–c176, 1982.

[23] W. Meisel, D. Sprenger, and P. Guetlich, "Surface versus bulk composition of a phosphate glass," *Surface and Interface Analysis*, vol. 22, no. 1–12, pp. 267–270, 1994.

[24] I. Michelakaki and S. Pissadakis, "Atypical behaviour of the surface hardness and the elastic modulus of a phosphate glass matrix under 193 nm laser irradiation," *Applied Physics A*. In press.

Hindawi Publishing Corporation
Laser Chemistry
Volume 2008, Article ID 976205, 6 pages
doi:10.1155/2008/976205

*Research Article*

# Three-Dimensional Modeling of the Heat-Affected Zone in Laser Machining Applications

**Martynas Beresna,[1] Titas Gertus,[2,3] Rolandas Tomašiūnas,[1] Hiroaki Misawa,[4] and Saulius Juodkazis[4]**

[1] *Institute of Materials Science and Applied Research, Saulėtekio 9, 2040 Vilnius, Lithuania*
[2] *Altechna Co. Ltd., Konstitucijos Avenue 23C-604, 08105 Vilnius, Lithuania*
[3] *Laser Research Center, Vilnius University, Saulėtekio 10, 10223 Vilnius, Lithuania*
[4] *Research Institute for Electronic Science, Hokkaido University, N21W10, Kitaku, Sapporo 001-0021, Japan*

Correspondence should be addressed to Saulius Juodkazis, saulius@es.hokudai.ac.jp

Received 5 May 2008; Accepted 16 September 2008

Recommended by Stavros Pissadakis

Thermal load as well as its three-dimensional (3D) spatial distribution has been estimated inside representative materials: glass (low thermal diffusion), silicon (semimetal properties), and sapphire (a crystalline dielectric of a high thermal conductivity) for typical laser processing and direct laser writing applications. The 3D temperature distribution allows to calculate thermal stress around the focal region. This provides an assessment tool for optimization of laser microprocessing conditions for controlled laser dicing and cutting applications.



## 1. Introduction

Laser processing is expanding fast into micro- and nanostructuring of complex multilayered and composite materials, heterostructures, and MEMS devices. Hence, precise account of energy delivery, heat-affected zone (HAZ), and thermal stress is of a paramount importance for high-precision fabrication and optical waveguide recording which usually have a narrow parameter space for optimization [1–9]. A high speed is required for efficient material processing by the *direct laser writing* (0.1–1 m/s for a linear scan), and it recently becomes achievable due to improvements in femtosecond laser sources which delivers large (~10 W) average power, at ~MHz repetition rate with a tens-of-$\mu$J pulse energy.

Picosecond and femtosecond lasers are the most prospective in the nano-microdrilling, dicing, and cutting applications where micrometer precision is required. At high repetition rates, thermal effects are pronounced and are usually responsible for crack formation in the case of in-bulk fabrication when nanosecond lasers are employed [10, 11]. For the waveguide recording, there are remarkable differences in defect and stress generation depending on pulse duration, scanning speed, and repetition rate [12, 13]. In the case of shorter pulses, the size and positioning of microcracks inside the bulk of transparent materials can be achieved with high precision avoiding damage of the entrance and exit surfaces. This allows to realize a, so-called, stealth dicing when the cracks inside workpiece are large enough for successful cleaving of the sample while there is no optical damage on both surfaces after laser irradiation [14, 15]. Similarly, cleaving of glasses can be controlled by designing a temperature field for a creation of a tensile stress which, first, forms and then guides a crack on the surface. There is a considerable interest in modeling of thermal fields inside the bulk of materials since they can be used for a controlled recording of waveguides, laser joining, and splitting applications in material processing.

Here, we explore numerically the temperature distribution inside bulk of a workpiece in different materials at realistic conditions of microprocessing by ultrafast (sub-1 ps) lasers. Combination of several laser pulses separated in time and space can be also modeled by the same approach for

practical 3D laser dicing and writing (photo-modification) applications.

## 2. Model

Recently, experimental results on laser welding and joining of glass [16, 17] have been quantitatively modeled by an in-bulk scanning of a rectangular heat source created at the focus of femtosecond laser beam [16]. Such a seemingly approximate description of the focal volume in the model nevertheless delivered good fit to the experimental data [16]. Hence, we use this model of the rectangular heat source for simulation of thermal field in different materials. Limitations of this approach are expected for focal spots of few micrometers in cross-section and at the very early stages of thermal diffusion, which were not considered here. It is also important that the model provides analytical solution, hence, the physical description and scaling rules of the laser processing can be qualitatively predicted for the more complex sample composition and geometry. For the quantitative modeling, however, the finite-difference time-domain (FDTD) simulations should be carried out for the actual sample geometry.

We use this model and calculate the extension of HAZ in glass, silicon, and sapphire. The dimensions of the heating source corresponds to tight focusing with numerical aperture NA $\simeq$ 0.5, which is a practical choice in laser microfabrication. We simulate the temperature field for a heat-source: a rectangular with a base area $(2a)^2$ and height $2h$ (in $z$-direction), scanned along $x$-direction at speed $v$ inside infinite material (Figure 1(a)). This model is realistic for actual laser processing, waveguide recording, and welding experiments when the 3D dimensions of the workpiece are much larger than dimensions of the heat-source (focal volume).

The temperature rise ($\theta$) at the time moment ($t$) at the location $(x, y, z)$ in quasi-steady state is [16]

$$\theta(x,y,z,t) = \frac{AQ}{64c_p\rho r}\sum_{i=0}^{\infty}\left(\mathrm{Erfc}\frac{\xi+iv\Xi^2/2-\delta}{\tau\sqrt{i\Xi^2/\tau^2+1}}-\mathrm{Erfc}\frac{\xi+iv\Xi^2/2+\delta}{\tau\sqrt{i\Xi^2/\tau^2+1}}\right)\times\left(\mathrm{Erfc}\frac{\psi-\delta}{\tau\sqrt{i\Xi^2/\tau^2+1}}-\mathrm{Erfc}\frac{\psi+\delta}{\tau\sqrt{i\Xi^2/\tau^2+1}}\right)\times\left(\mathrm{Erfc}\frac{\zeta-\eta}{\tau\sqrt{i\Xi^2/\tau^2+1}}-\mathrm{Erfc}\frac{\zeta+\eta}{\tau\sqrt{i\Xi^2/\tau^2+1}}\right), \quad (1)$$

where $\mathrm{erfc}(U) = (2/\sqrt{\pi})\int_U^{\infty}\exp(-u^2)du$, $A$ is absorbance of the laser pulse, $Q$ is the instantaneous laser energy, $2a$ is the diameter of the focus, $2h$ is the length of a heat source along $z$-axis, $c_p$ is specific heat, and $\rho$ is the mass density. The following nondimensional parameters are used in (1): $r^3 = a^2h$, $\xi = x/r$, $\psi = y/r$, $\zeta = z/r$, $\delta = a/r = 1/\sqrt[3]{n}$, $\eta = h/r = n^{2/3}$, $\tau = \sqrt{4\chi t}/r$, $\Xi = \sqrt{4\chi T}/r$, and $v = vr/(2\chi)$ (here $\chi$ is the temperature diffusivity).

## 3. Results and Discussion

We compare here axial temperature distributions for a high-power and high-repetition-rate heat source which models laser cutting, dicing, and waveguide recording when a focal spot is set inside the processed material. Materials with different thermal conductivity (thermal diffusivity) were modeled. The formulae given in Section 2 can be used for estimations of both axial and lateral cross-sections of the temperature field. In the following part, we present the temperature profiles along the beam scanning. The extension of lateral cross-section is closely matching that of the axial around the maximum temperature (see, Figure 1(b)). In order to compare thermal fields in very different materials, we used the same absorbance $A = 0.5$ which corresponds to a strong ionization of material, for example, at the optical breakdown conditions of dielectrics such as silica or sapphire [18, 19], and is relevant for laser processing by ultrashort pulses at high irradiance. For more quantitative estimations, the absorbance of material and its temporal evolution during the pulse of high irradiance should be known at the focal volume.

### 3.1. Temperature Field

Figure 2 shows the thermal profiles along the scan direction with heat source at $x = 0$ at different time moments within the period of laser pulsing inside glass. Similar conditions are created in glass-welding applications where high-temperature melts are essential for good quality joints [16, 17]. The spatial extension of the heated zone does not change significantly beyond a $\pm 5\,\mu$m range, only the maximum temperature is changing at the origin of the heat source. Trailing temperature distribution is recognizable at negative $x$ values.

Silicon differs from glass mainly by the thermal diffusivity which is $\chi = 0.8\ \mathrm{cm}^2/\mathrm{s}$ (for a glass $4.6\times10^{-3}\ \mathrm{cm}^2/\mathrm{s}$), while the specific heat and mass density are almost the same. This makes almost impossible to effectively heat and localize the hot spot inside silicon as it is shown in Figure 3. Geometrical parameters of the heat source (laser-heated focal volume) were the same as for glass at the same scanning speed of 10 cm/s. The heating power was increased 50 times to $Q = 10$ W and repetition rate was 1 or 10 MHz in order to heat up the focal volume (Figure 3). When repetition rate is larger (see Figure 3, curves $(2, 3)$), there is a significant spread of temperature beyond the acceptable $\pm 5\,\mu$m range. This would be critical for dicing of wafers with microelectronic chips at narrow street width. It is noteworthy that the heat capacity of solid and molten silicon is almost the same. This entitles a quantitative comparison of theoretical simulations and experiments in terms of thermal field. It should be noted that the optical properties change upon melting: the complex refractive index is changing from $n + ik = 3.69 + 6\times10^{-3}i$ (crystalline) silicon to $(3.9 + 5.5i)$ (liquid) silicon (for the silica native oxide, the refractive index is $1.45 + 4.6\times10^{-6}i$). The phase transition, the latent heat necessary to melt the focal volume, was not included in the used simple model. Hence, the obtained thermal field close to the melting point

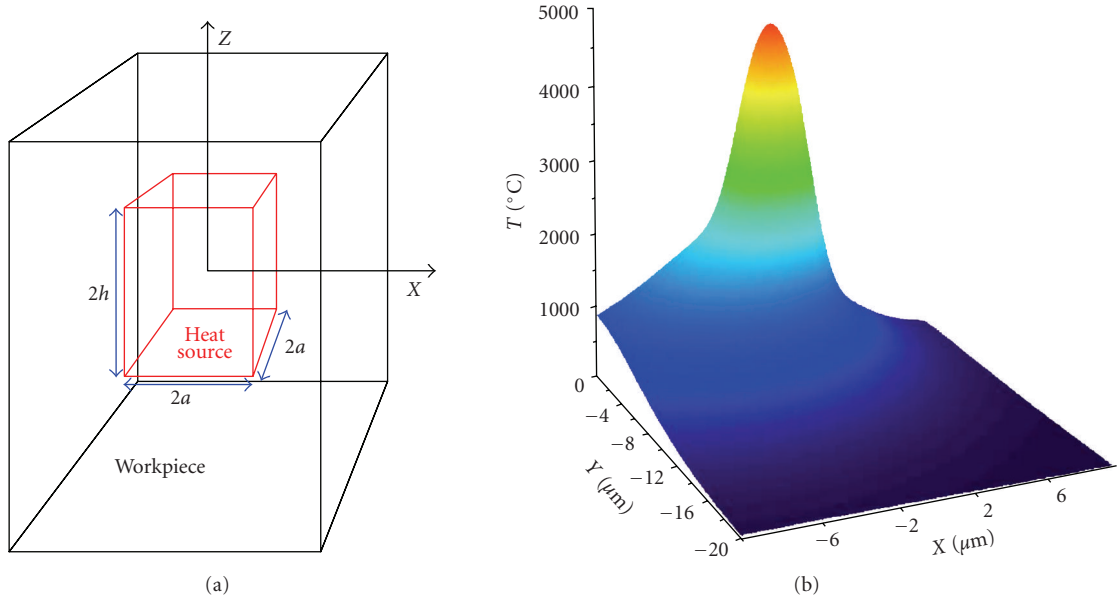


Figure 1: (a) Schematic presentation of the heat source with a square cross-section, $2a \times 2a$, on the $xy$-plane and $2h$ high. (b) The 3D temperature field in glass calculated by (1) with the same parameters as in Figure 2 at time moment $t = 0.1T$ ($T = 1/f$ where $f$ is the repetition rate) for $z = 0$.

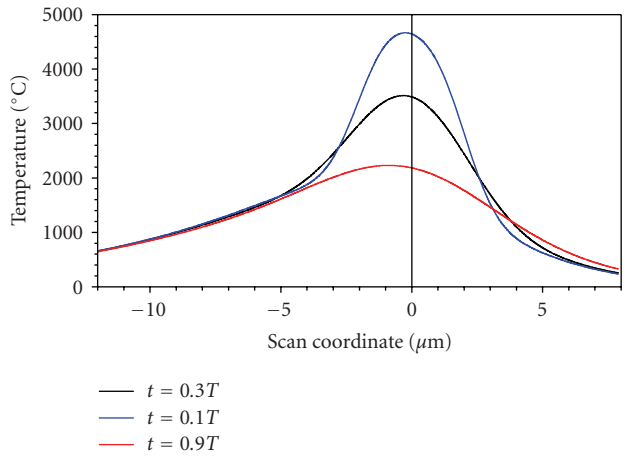


Figure 2: The axial temperature profile in glass at different time moments. Conditions: $Q = 0.2$ W at $f = 0.1$ MHz, $A = 0.5$ absorbance, 10 cm/s scan speed, the rectangular heat source is modeled by $2 \times 2 \times 20\,\mu m^3$ volume ($a \times a \times h$). Typical borosilicate glass parameters were taken from [16].

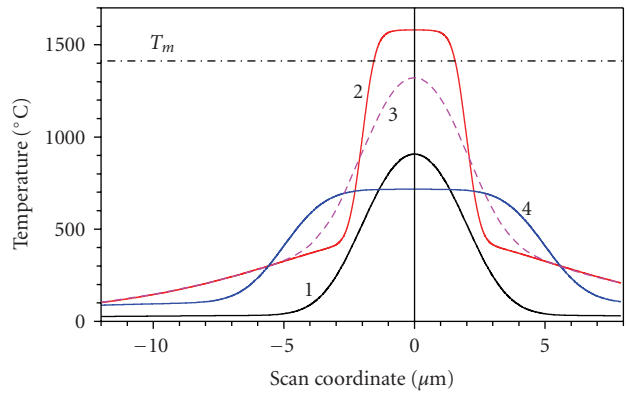


Figure 3: The axial temperature profile in Si. Conditions: $Q = 10$ W at $f = 1$ MHz (profiles: 1, 4) and 10 MHz (2, 3), $A = 0.5$ absorbance, 10 cm/s scan speed, time moment $t = 0.01T$ (1, 2, 4) and $0.1T$ (3), and dimensions of a rectangular heat source were $a = 2$, $h = 20\,\mu$m (1–3), and $a = 5\,\mu$m (4). Typical Si parameters: $c_p = 0.7$ J/(g K), $\rho = 2.329$ g/cm$^3$, $\chi = 0.8$ cm$^2$/s, and $T_m = 1412$°C is the melting temperature of Si.

is only approximate (Figure 3) since the increased absorbtion is not taken into account.

The in-bulk structuring of silicon remains a challenging task due to required high power and repetition rate; moreover, the wavelength of irradiation should be in the transparency region (a cutoff is at approximately 1.1 eV or 1120 nm in Si). Typical fs-lasers are usually operating at slightly shorter wavelengths. This makes them useful only for cutting and dicing of silicon by ablation.

Sapphire stands out from transparent dielectric materials due to its high thermal conductivity (though, inferior to diamond which has a higher thermal conductivity than many metals). In terms of temperature diffusivity relevant in this study, sapphire has a $\chi = 0.16$ cm$^2$/s value. Thus, it is expected to be able to localize heat more similar to silicon than glass. Figure 4 summarizes data, which show fast relaxation of maximum temperature.

The estimations given above are of qualitative nature since we are not considering here nonlinear effects of light propagation, filamentation, and self-focusing. However, general tendencies are depicted and can be used as first estimate of the thermal load to regions in close proximity of

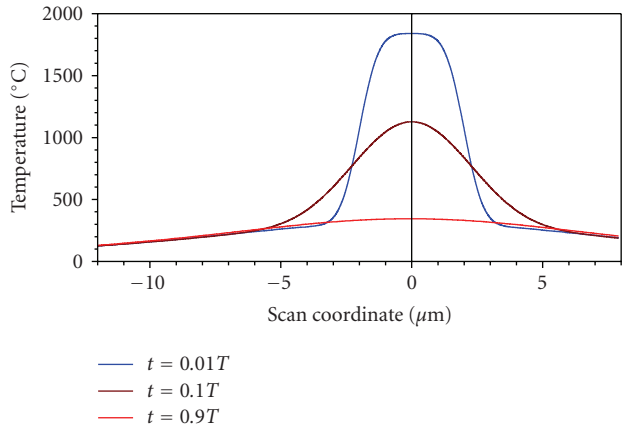


FIGURE 4: The axial temperature profile in sapphire at different time moments. Conditions: $Q = 5\,\mathrm{W}$ at $f = 1\,\mathrm{MHz}$, $A = 0.5$ absorptivity, 10 cm/s scan speed, the rectangular heat source dimensions were $a = 2$, $h = 20\,\mu\mathrm{m}$. Typical sapphire parameters [20]: $c_p = 0.761\,\mathrm{J/(g\ K)}$, $\rho = 3.9\,\mathrm{g/cm^3}$, $\chi = 0.16\,\mathrm{cm^2/s}$, and $T_m > 2050^\circ\mathrm{C}$ is the melting temperature of sapphire.

the irradiated laser spot. The most challenging task in laser processing of transparent materials is the evaluation of the amount of absorbed energy and the volume of its deposition. Recent success of this model [16] in description of glass welding encourages to apply it to other laser-processing tasks such as dicing, cutting, and waveguide recording in different materials.

## 3.2. Stress Confinement

With the known thermal field calculated numerically or analytically, one can estimate the stress acting inside materials due to thermal expansion. We discuss here a model where material is described by its average thermomechanical properties, hence, the model is better suited for glasses and amorphous materials rather than crystals. However, a qualitative mechanism of the stress confinement should be valid for crystals as well. It is noteworthy that the crystalline properties become more. important in crack propagation discussed in section 3.3.

For example, for a linear heat source scanned along $x$-direction inside isotropic medium, the stress along $y$-axis is given by [14]

$$\sigma_y(x) = \sigma_{\max}\left(e^{(x/l)}\mathbf{K}_1\left(\frac{|x|}{l}\right)\operatorname{sign} x - \frac{l}{x}\right), \tag{2}$$

where $\sigma_{\max} = q\mu\alpha(1+\nu)/(2\pi d\kappa)$ [Pa] is the maximum stress for the heating power $q$ [W], $\mathbf{K}_1$ is the modified Bessel function of the first kind and order, $\nu$ is the Poisson ratio, $l = \kappa/(c\nu)$ is the length of thermal diffusion expressed via the specific heat capacity density $c$ and the thermal conductivity $\kappa$, $\nu$ is the velocity of the heat source, $d$ is the thickness of sample (in this case equal to the length of the heat source). This expression (2) links the absorbed heat to the generated stress. In the case of a heating source of finite dimensions, the temperature field can be calculated by (1) and then integrated by the same way as in the case of (2) according to [14]

$$\sigma_y(x) = \mu(1+\nu)\alpha\left[\int_0^l T(x,\xi)d\xi - T(x)\right]. \tag{3}$$

It should be noted that analytical result is not available in the case of a heat source of finite dimensions and (3) should be integrated numerically.

The stress field around waveguides recorded by the femtosecond direct laser writing inside Nd-doped yttrium aluminium garnet (YAG) can be engineered to exert compressive and tensile stresses on the order of ±1 kbar, respectively (up to +5 kbar for compression). Such photomodification can create the following: (i) waveguiding regions due to augmented refractive index $\Delta n = ((n^2-1)(n^2+2)/2n)(P/E)$, here $P$ is the pressure and $E$ is the Young modulus, and, (ii) the spectral properties of Nd transitions can be effectively modified via pressure [21, 22]. The combined effects of refractive index and emission changes can be utilized for the creation of efficiently lasing waveguide laser-written in Nd:YAG ceramics [23].

## 3.3. Crack Propagation

Laser dicing, splitting, and cutting applications rely on a seeding of photo-modification which alters material strength and serves as a crack generator. The critical stress required for the surface or in-bulk crack formation is discussed in what follows.

The theoretical strength of material, in terms of stress, can be estimated from the work necessary to increase the atomic intraplane distance by 25% at which cleaving of a crystal occurs [24]:

$$\sigma_{\mathrm{th}} = \sqrt{\frac{\gamma E}{a_0}} \simeq \frac{E}{2\pi}, \tag{4}$$

where $E$ is the Young modulus, $\gamma$ is the surface energy per area, and $a_0$ is the atomic intraplane distance. When crack is present inside material, the stress concentration at the crack tip depends on the crack shape and size [24]:

$$\sigma_{\max} = 2\sigma\sqrt{\frac{l_c}{l_\rho}}, \tag{5}$$

where $2l_c$ is the length of the crack (assumed to be elliptical), $\sigma$ is the applied stress, and $l_\rho$ is the radius at the crack tip. Crack propagation ensues at the fracture stress when $\sigma_{\mathrm{th}} = \sigma_{\max}$, or [24]

$$\sigma_F = \sqrt{\frac{2\gamma E l_\rho}{3\pi a_0 l_c}}. \tag{6}$$

Since the material failure (strength limit) for the tensile stress is approximately ten times lower as compared with that for a compressive load (4) scanning of two or several heat sources, the laser foci, spatially separated across (or along) the scanning direction is prospective for the controlled cleaving and dicing with a literarily zero street width. The

absorbed laser power (the heat source) depends on the linear and nonlinear absorption at the focus, that is, on irradiance and ionization level at the focus. The cooling of the two or more spatially and temporally separated laser foci can generate tensile stresses for the controlled cleaving at the optimized conditions of laser machining.

The thermal diffusion length $L_D = \sqrt{\chi t}$ ($t$ is an effective irradiation duration or pulse duration) and the absorption depth ($\sim 1/\alpha(\lambda)$) defines a typical feature size of laser micromachining via the absorption at the wavelength $\lambda$ (linear and nonlinear absorption with the absorption coefficient $\alpha$ which is intensity-/irradiance-dependent) [25]. The minimum feature sizes of the in-bulk modification or ablation smaller than both $1/\alpha$ and $L_D$ are achievable via control of processing parameters: velocity of scan, laser repetition rate, and pulse energy.

The laser heating necessary to achieve fracture strength limit in compression requires very high laser power and a high temperature gradient [19], hence, it is considered impractical for the laser processing of multilayered and multicomponent workpieces. Ultrashort pulses favor creation of a fast heating due to strong nonlinear absorption and rapid thermal quenching [18]. Both factors facilitate a stress generation. Generation of compressive and tensile stresses with a particular patterns made of several spatially (e.g., by using Gauss-Bessel beams/pulses [26]) and temporally shaped beams/pulses is expected to deliver practical solutions for the surface and in-bulk laser machining as well as for other direct laser writing applications. Since the temperature field is not symmetrical around its maximum along the scanning direction (Figure 1), it may provide an explanation to the recently observed nonreciprocity effect in femtosecond laser recording in a non-centrosymmetric lithium niobate [27].

## 4. Conclusions

The knowledge of the 3D temperature field provides a possibility to estimate stresses inside the workpiece under laser fabrication. The 3D localization of temperature inside glass, silicon, and sapphire has been calculated and discussed for practical irradiation conditions in direct laser writing/dicing/cutting applications. Strong thermal gradients can be exploited for generation of tensile stress created by several heating sources (irradiation spots/patterns) and are prospective for the controlled laser cleaving. Thermal stress sources can be created by either of the following or their combination: by a cumulative fast repetition laser irradiation, by usage of ultra-short laser pulses, or by implementation of fast laser-spot (sample) scanning. The femtosecond direct laser writing can be used for the in-bulk localization of stresses and photo-modification for photonic applications [23, 27].

## Acknowledgments

Financial support by a 20070305-1 grant from "Mokslininkų Sąjungos Institutas" is highly acknowledged. S. Juodkazis is grateful to Tecdia Co., Ltd. and to the Grant-in-Aid no. 19360322 from the Ministry of Education, Science, Sports, and Culture, Japan, and to a visiting professor invitation at the Institute of Materials Science and Applied Research, Vilnius University, Lithuania.

## References

[1] K. M. Davis, K. Miura, N. Sugimoto, and K. Hirao, "Writing waveguides in glass with a femtosecond laser," *Optics Letters*, vol. 21, no. 21, pp. 1729–1731, 1996.

[2] M. Will, S. Nolte, B. N. Chichkov, and A. Tünnermann, "Optical properties of waveguides fabricated in fused silica by femtosecond laser pulses," *Applied Optics*, vol. 41, no. 21, pp. 4360–4364, 2002.

[3] H. Zhang, S. M. Eaton, J. Li, and P. R. Herman, "Femtosecond laser direct writing of multiwavelength Bragg grating waveguides in glass," *Optics Letters*, vol. 31, no. 23, pp. 3495–3497, 2006.

[4] A. H. Nejadmalayeri and P. R. Herman, "Rapid thermal annealing in high repetition rate ultrafast laser waveguide writing in lithium niobate," *Optics Express*, vol. 15, no. 17, pp. 10842–10854, 2007.

[5] Z. Wang, K. Sugioka, Y. Hanada, and K. Midorikawa, "Optical waveguide fabrication and integration with a micro-mirror inside photosensitive glass by femtosecond laser direct writing," *Applied Physics A*, vol. 88, no. 4, pp. 699–704, 2007.

[6] S. Pissadakis, R. Böhme, and K. Zimmer, "Sub-micron periodic structuring of sapphire by laser induced backside wet etching technique," *Optics Express*, vol. 15, no. 4, pp. 1428–1433, 2007.

[7] S. Yliniemi, S. Honkanen, A. Ianoul, A. Laronche, and J. Albert, "Photosensitivity and volume gratings in phosphate glasses for rare-earth-doped ion-exchanged optical waveguide lasers," *Journal of the Optical Society of America B*, vol. 23, no. 12, pp. 2470–2478, 2006.

[8] S. Juodkazis, V. Mizeikis, S. Matsuo, K. Ueno, and H. Misawa, "Three-dimensional micro- and nano-structuring of materials by tightly focused laser radiation," *Bulletin of the Chemical Society of Japan*, vol. 81, no. 4, pp. 411–448, 2008.

[9] S. Juodkazis, V. Mizeikis, and H. Misawa, "Three-dimensional structuring of resists and resins by direct laser writing and holographic recording," in *Photoresponsive Polymers I*, vol. 213 of *Advances in Polymer Science*, pp. 157–206, Springer, Berlin, Germany, 2008.

[10] E. Vanagas, J.-Y. Ye, M. Li, M. Miwa, S. Juodkazis, and H. Misawa, "Analysis of stress induced by a three-dimensional recording in glass," *Applied Physics A*, vol. 81, no. 4, pp. 725–727, 2005.

[11] S. Juodkazis, H. Misawa, E. Vanagas, and M. Li, "Thermal effects and breakdown in laser microfabrication," in *Proceedings of the 4th International Congress on Laser Advanced Materials Processing (LAMP '06)*, pp. 6–60, Kyoto, Japan, May 2006.

[12] W. J. Reichman, D. M. Krol, L. Shah, et al., "A spectroscopic comparison of femtosecond-laser-modified fused silica using kilohertz and megahertz laser systems," *Journal of Applied Physics*, vol. 99, no. 12, Article ID 123112, 5 pages, 2006.

[13] M. Watanabe, S. Juodkazis, J. Nishii, S. Matsuo, and H. Misawa, "Microfabrication by a high-fluence femtosecond exposure: mechanism and applications," in *Photon Processing in Microelectronics and Photonics*, K. Sugioka, M. C. Gower, R. F. Haglund, et al., Eds., vol. 4637 of *Proceedings of SPIE*, pp. 159–168, San Jose, Calif, USA, January 2002.

[14] S. Juodkazis, H. Misawa, and I. Maksimov, "Thermal accumulation effect in three-dimensional recording by picosecond pulses," *Applied Physics Letters*, vol. 85, no. 22, pp. 5239–5241, 2004.

[15] S. Juodkazis and H. Misawa, "Laser processing of sapphire by strongly focused femtosecond pulses," *Applied Physics A*, vol. 93, no. 4, pp. 857–861, 2008.

[16] I. Miyamoto, A. Horn, J. Gottmann, D. Wortmann, and F. Yoshino, "Fusion welding of glass using femtosecond laser pulses with high-repetition rates," *Journal of Laser Micro/Nanoengineering*, vol. 2, no. 1, pp. 57–63, 2007.

[17] W. Watanabe, S. Onda, T. Tamaki, and K. Itoh, "Direct joining of glass substrates by 1 kHz femtosecond laser pulses," *Applied Physics B*, vol. 87, no. 1, pp. 85–89, 2007.

[18] E. E. Gamaly, S. Juodkazis, K. Nishimura, et al., "Laser-matter interaction in the bulk of a transparent solid: confined microexplosion and void formation," *Physical Review B*, vol. 73, no. 21, Article ID 214101, 15 pages, 2006.

[19] S. Juodkazis, K. Nishimura, S. Tanaka, et al., "Laser-induced microexplosion confined in the bulk of a sapphire cystal: evidence of multimegabar pressures," *Physical Review Letters*, vol. 96, no. 16, Article ID 166101, 4 pages, 2006.

[20] S. Juodkazis, K. Nishimura, H. Misawa, et al., "Control over the crystalline state of sapphire," *Advanced Materials*, vol. 18, no. 11, pp. 1361–1364, 2006.

[21] S. Kobyakov, A. Kamińska, A. Suchocki, D. Galanciak, and M. Malinowski, "$Nd^{3+}$-doped yttrium aluminum garnet crystal as a near-infrared pressure sensor for diamond anvil cells," *Applied Physics Letters*, vol. 88, no. 23, Article ID 234102, 2 pages, 2006.

[22] G. A. Torchia, P. F. Meilán, A. Rodenas, D. Jaque, C. Mendez, and L. Roso, "Femtosecond laser written surface waveguides fabricated in Nd:YAG ceramics," *Optics Express*, vol. 15, no. 20, pp. 13266–13271, 2007.

[23] G. A. Torchia, A. Rodenas, A. Benayas, E. Cantelar, L. Roso, and D. Jaque, "Highly efficient laser action in femtosecond-written Nd:yttrium aluminum garnet ceramic waveguides," *Applied Physics Letters*, vol. 92, no. 11, Article ID 111103, 3 pages, 2008.

[24] T. H. Courtney, *Mechanical Behavior of Materials*, McGraw-Hill International Editions: Material Science/Metallurgy Series, McGraw-Hill, New York, NY, USA, 2nd edition, 2000.

[25] S. Nolte, C. Momma, H. Jacobs, et al., "Ablation of metals by ultrashort laser pulses," *Journal of the Optical Society of America B*, vol. 14, no. 10, pp. 2716–2722, 1997.

[26] A. Marcinkevicius, S. Juodkazis, S. Matsuo, V. Mizeikis, and H. Misawa, "Application of Bessel beams for microfabrication of dielectrics by femtosecond laser," *Japanese Journal of Applied Physics*, vol. 40, no. 11A, pp. L1197–L1199, 2001.

[27] W. Yang, P. G. Kazansky, and Y. P. Svirko, "Non-reciprocal ultrafast laser writing," *Nature Photonics*, vol. 2, no. 2, pp. 99–104, 2008.